Statistical-Dynamical Channel Modeling of Outdoor Optical Wireless Links

Dissertation submitted by

MUHAMMAD SALEEM AWAN

to the Faculty of Electrical Engineering and Information Technology

Graz University of Technology, Austria

in partial fulfillment of the requirements for the degree of

Doctor of Philosophy (Ph. D)

at the

Institute for Broadband Communication

Graz, May 2010

Supervisor and 1st Reviewer: Prof. Dr. Erich Leitgeb

2nd Reviewer: Prof. Carlo Capsoni

Declaration - EIDESSTATTLICHE ERKLAERUNG

Ich erklaere an Eides statt, dass ich die vorliegende Arbeit selbststaendig verfasst, andere als die angegebenen Quellen/Hilfsmittel nicht benutzt und die den benutzten Quellen woertlich und inhaltlich entnommenen Stellen als solche kenntlich gemacht habe.

Graz, am:————- (Unterschrift)————————..

STATUTORY DECLARATION

I declare that I have authored this thesis independently, that I have not used other than the declared sources / resources and that I have explicitly marked all material which has been quoted either literally or by content from the used sources.

Graz, dated:————- Signature————————..

Dedication

To my loving parents, to whom I owe, the love and the strive for wisdom and knowledge.

CONTENTS

LIST OF FIGURES

LIST OF TABLES

Acknowledgements

In the name Of God (Allah) the Most Gracious (Al-Rahman) the Most Merciful (Al-Raheem), The Lord of the Heavens, Earth and that is in between. All praise be to Allah, the Cherisher and Sustainer of the worlds. Peace and prayer be upon our beloved Prophet, Muhammad, his family, and all of his companions. Praise be to Allah for His majesty, bestowal of favors, knowledge, ability, wisdom and power. Verily all praise, grace and sovereignty belong to my Allah Al-Raheem. I would not have been capable of completing this dissertation without blessings of Allah Al-Raheem, the only Grantor of graces.

I am highly obliged to my colleagues Marzuki, Paul Brandl, Farukh Nadeem, Bernhard Geiger, Andreas Merdonig, Muhammad Saeed Khan, Christia Meidiana, Pirmin Pezzei, Thomas Plank and to all other colleagues at Institute of Broadband Communications (IBK) who helped me and gave their valuable suggestions. My gratitude also goes out to my Pakistani colleagues in Graz, Austria especially to Muhammad Sarwar Ehsan, Shahzad Saleem, Syed Nadeem Ahsan, Hasnat Ahmad, Tajamal Hussain, Zahid Hussain Abro who have helped me through discussions, guidance and providing their nice company. Special thanks goes to Prof. Carlo Capsoni and Roberto Nebuloni of Politecnico di Milano (Italy), Prof. Fary Z. Ghassemlooy of Northumbria University (UK), Prof. Steve Hranilovic of McMaster University Canada) and Laszlo Csurgai Horwath of BME Budapest (Hungary) of whom critical reasoning and helpful suggestions helped me improve my work during the course of my Ph. D research.

Last, but not least, the acknowledgement is due to Prof. Dr. Erich Leitgeb who being my advisor for the Ph.D work, has helped me in numerous ways during the course of this work, and provided me all required resources to accomplish the task. His dedication to his work was always exemplary, and he was the main driving force (and the co-supervisor) behind most of the research accomplished during the course of the thesis. Dr. Erich Leitgeb has always provided me the necessary guidance and help. His encouragement in different aspects of the work contributed to my personal and professional development. I would also like to thank Prof. Carlo Capsoni for agreeing to act on my examination committee, and his valuable suggestions helped refine the work.

I would also like to acknowledge the financial support of the Higher Education Commission of Pakistan which made this work possible and the Europe-wide network of excellence in Satellite Communications (SatNEx) played a vital role in the dissemination of the research results. The support of OEAD office is also gratefully acknowledged with special thanks to Christina Duss and Petra Mellak-Herzog, who always welcomed me with smiling faces and co-operated up to their best possible level.

I am thankful from core of my heart especially to my parents, brothers, sisters, my wife

and childrens, friends and my well-wishers who prayed for my success and have remained the binding force in my life all through this work. During the thesis, a lot of people have been very supportive and therefore are due my biggest thanks. Thanks to anybody I missed who deserves a mention!. May Allah Al-Raheem give reward to all those who helped me and prayed for me during my research. Ameen.

Muhammad Saleem Awan

TU Graz, Graz, May 2010

Abstract

The growing need for Earth observation and monitoring systems has stimulated considerable interest in free-space optical wireless (FSO) systems because of the huge bandwidth requirements. However, terrestrial FSO links are severely impacted by weather conditions especially dense fog to a larger extent while, rain and snow to a lesser extent. For the proper deployment of FSO technology requires a better understanding of the free-space channel transmission characteristics as they have major influence on the transmission link properties like link availability, reliability and quality of service. This thesis provides new insight on the fog microphysics, its characterization and the fog attenuation modeling. A comprehensive analysis of the measured fog attenuations is presented by building the discussion through comparison of recorded attenuations at Graz (Austria), Milan (Italy), Nice (France) and Prague (Czech Republic). It was observed that fog attenuations in radiation fog environments are much stable when compared with advection fog attenuations, because of the difference in the microclimate and the microphysics involved. The work further proposes novel approaches to compute the exponential distribution, and modified gamma distribution parameters from the measured fog attenuations recorded at Graz and Prague. The newly computed distribution parameters are compared, analyzed and validated against the representative fog events on the basis of statistical analysis, and new fog drop size distribution computation methods are proposed which best approximate the attenuation behavior at a particular location.

Zusammenfassung

Der steigende Bedarf an Erdbeobachtungs- und -monitoringsystemen und der damit verbundene Bandbreitenbedarf fuehrte zu grossem Interesse an optischen Freiraumuebertragungssystemen (FSO). Leider sind terrestrische FSO Verbindungen durch dichten Nebel stark, durch Regen und Schnee hingegen schwach in ihrer Zuverlaessigkeit eingeschraenkt. Fuer einen erfolgreichen Einsatz von FSO Technologien ist das Verstaendnis der zugrundeliegenden Ausbreitungseigenschaften von grosser Bedeutung, da diese grossen Einfluss auf die Verfuegbarkeit, Zuverlaessigkeit und Dienstguete haben. Diese Arbeit bietet neue Einblicke in die Mikrophysik des Nebels, dessen Charakterisierung und die Modellierung der Nebeldaempfung. Eine umfangreiche Analyse von gemessenen Nebeldaempfungen ist durch den Vergleich von Aufzeichnungen aus Graz (Oesterreich), Mailand (Italien), Nizza (Frankreich) und Prag (Tschechische Republik) gegeben. Es wurde beobachtet, dass die Nebeldaempfung in kontinentalen Klimaten stabiler ist als in maritimen Umgebungen, was auf die Unterschiede im Mikroklima und der Mikrophysik zurueckzufuehren ist. Anhand der Messergebnisse aus Graz und Prag entwickelt die Arbeit neue Methoden zur Berechnung der Parameter der Exponential- bzw. der modifizierten Gamma-Verteilung, die zur

Beschreibung der Nebeldaempfung herangezogen werden. Die erhaltenen Verteilungsparameter wurden verglichen und analysiert, sowie mittels representativer Nebelereignisse auf der Basis statistischer Methoden validiert. Ebenfalls wurden neue Methoden zur Berechnung der Tropfengroesseverteilung entwickelt, um die Daempfung an bestimmten Orten besser zu approximieren.

1 INTRODUCTION

Tremendous advances made in the design of electro-optical components and systems coupled with huge progress achieved in the information processing capabilities helped improve the optical communication transceivers. We can witness today many state of the art optical wireless systems being employed in many short-range to long-range terrestrial, ground-space and space-space communication application scenarios. This thesis presents investigations on the statistical-dynamical channel modeling of terrestrial Free-Space Optical (FSO) links in different climatic conditions such as fog, snow, rain and clouds. These climatic factors can have a significant impact on the transmission of optical beams in the free-space atmosphere. FSO links may experience a complete loss of signal caused by the effects of dense fog. Moreover, sudden changes in temperature and pressure causing scintillations may distorts the amplitude of the target signal. Therefore, any optical wireless system that relies on the propagation of optical beams in free-space must, therefore, be designed to take these factors into account. The main emphasis of this work has been on characterizing the terrestrial atmospheric channel for FSO links for different harsh environmental conditions. This would help optical wireless system designers in fields such as meteorology, telecommunications, radar, and aircraft guidance systems face the challenge of predicting and compensating for these potentially serious weather-related effects. The work is multidisciplinary and involves knowledge about FSO, atmospheric physics, meteorology and statistics among many others.

1.1 Brief History of Optical Communication

Free-space optical wireless communications, also referred to as FSO, is a very poplar subject in today's technological marketplace. The communication methods that employed optical transmissions existed in their primitive form for centuries throughout the known human history; well before the work of Claude Chappe, a French inventor who first demonstrated a practical semaphore system in the year 1792. His system was a series of semaphores mounted on towers, where human operators relayed messages from one tower to the next. However, the information transmitted by optical means thus remained very limited until the appearance of optical telegraph at the end of 18^{th} century when telecommunications really started. Thus enabled individuals to communicate over long distances. The quality of service (QoS) remained low due to the lack of reproducibility and reliability of both transmitters and the receivers; of the men and the materials; and the changing nature of the air a transmission channel [1].

Optical transmission came to be available for the communication system after the laser as a light source was invented. As a coherent light source being not in a nature, first working laser (already described as stimulated emission by Albert Einstein 1905) i.e., a Ruby Laser in 1960 by Theodore Maimann, was a milestone for the optical technology and paved the way to another solution in the form of optical telecommunication based on optical fibers [1]. With the almost simultaneous developments of low attenuation optical fibers and semiconductor lasers emitting in continuous mode at room temperature in 1970-71, led to an explosion of wired optical telecommunications. Optical fiber transmissions unquestionably dominates fields of terrestrial long-distance transmissions, starting at about 10 km for metropolitan networks and up to several thousand kilometers as for cables and the trans-oceanic transmissions and thus has become an integral and indispensable part of the information superhighway system across the whole globe [2]. The network infrastructure, based on silica single mode glass fibers in buried cables, is already deployed for most countries, e.g Europe, North America or Japan. Longer distance directive radio links for terrestrial applications are only used for very special cases, but radio frequency is used as the main medium for shorter distances non-directive applications like the access segment of networks, successful examples are the digital cellular telephone network (GSM, UMTS), WLAN for data transmission in smaller cells, or DVB-T for digital television broadcasting [2, 3].
The transmission capacity of wired communication systems from telegraph systems to Dense Wavelength Division Multiplexing (DWDM) based state of the art fiber systems has been constantly increasing, approximately getting a double about after every two years. Innovation in electro-optic components, to perform system functions analogous to those carried out in electrical and electronic domain, and the introduction of single mode fibers has further accelerated this trend at an average rate of doubling every 18 months. Prior to optical communications, electrical coaxial cables were used to transmitted data signals at a maximum bit rate of 565 Mbit/s over 1 km distance between electrical regenerators. But with the introduction of single-mode fibers and lasers the transmission capacity reached up to 2.5 Gbit/s over distances of 100 km without regenerators. Next extraordinary achievement was made in the early 1990s with the development of optical amplifiers Erbium Doped Fiber Amplifiers (EDFA). Later the DWDM systems were designed that combine many optical channels in the frequency domain, allowing the simultaneous amplification of optical signal from all the channels. Finally, the transmitted stream signal is demultiplexed at the receiver end [4].

1.2 Overview of Optical Wireless Communication

FSO has the great potential to solve problems for bridging the last mile access network gap to provide broadband internet access to rural areas and for disaster recovery. The carrier frequencies in the range of 300 THz, allows very high data rates by the optical

links. Among other advantages license free communication, easy installation, avoiding electromagnetic pollution and wiretapping safety are few to name. Some of the possible applications are web browsing, electronic commerce, streaming audio and video, teleconferencing, real-time medical imaging transfer, enterprize networking, work sharing, and high speed interplanetary links. Initially it was mainly considered as a solution to the last mile access problem but now it is being investigated for high speed data transfer applications involving links between fixed and mobile platforms e.g., High Altitude Platforms (HAPs), Unmanned Aerial Vehicles (UAVs), Geostationary (GEO) and Low Earth Orbits (LEO) satellite terminals. Famous optical wireless links experiments in last few years like Optical ground Station (OGS)-ARTEMIS, JPL-OCTL, Altair UAV-to-Ground, Stratospheric Optical Payload Experiment-STROPEX, Airborne Laser Optical Link - LOLA, Optical Downlink Experiment like KIODO and TerraSAR-X LCT-ATM Laser Link are few good examples showing the importance of such links for future broadband communication requirements. Nevertheless, widespread popularity of FSO communication systems is hindered by its susceptibility to certain weather conditions and atmospheric variations. In any communication system, transmission is influenced by the propagation channel, and the propagation channel for FSO communication is atmosphere. Among all atmospheric effects, fog is the most critical weather condition. Fog is characterized by several physical parameters such as liquid water content, particle size distribution, fog temperature and humidity. Since the size of fog particles is comparable to the transmission wavelength of optical and near infrared waves, it causes attenuation due to Mie scattering, which in turn reduces availability for considerable amount of time.
One of the most promising of the new access technologies is Optical wireless, a line of sight (LOS) broadband communication technology, that employs pulse-modulated beams of visible or infrared light (in the terahertz spectrum of the electromagnetic radiations) to transmit information robustly through the atmospheric free-space using optical transceivers to form point-to-point communication links. Normally, the range of optical frequencies usually employed for FSO lies within 20 THz to 375 THz frequencies band of the electromagnetic spectrum of the radiations (Fig. 1.1).

The concept of transmitting information through the air by means of modulated light signal is quite old; and although significant advances have been made over the past ten years, the concept remains relatively simple; a narrow beam of light is launched at a transmission station, transmitted through the atmosphere, and subsequently received at the receive station (Fig. 1.2). The latest developments in the design and field application of Free-Space Optics (FSO) have come about in response to a need for greater bandwidth and improved communication systems. FSO systems are generally designed as bandwidth and protocol-transparent physical layer connections [6]. FSO links are generally directed line-of-sight links with recent developments aiming at providing optical Multi-Input Multi-Output (MIMO) functionality for the next generation high speed optical networks [7, 8]. Nowadays, FSO communications technology is identified as an attractive alternative to complement existing microwave (mmW) and radio frequency (RF) communication links for the backhaul traffic [9]. This technology has some inherent prime advantages like

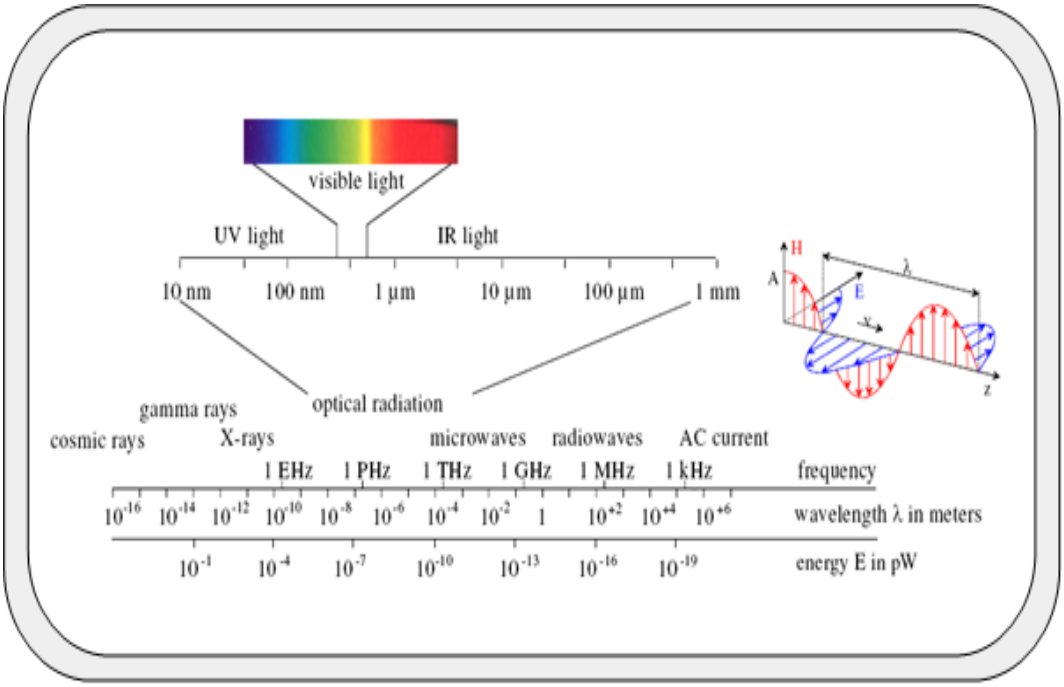

Figure 1.1: Electromagnetic wave spectrum [5]

higher data rates exceeding easily 100 Gbit/s using WDM techniques, security aspects, EMC/EMI immunity, frequency regulation issues, low terminal size and weight, small aperture sizes and low power consumption. It is anticipated that FSO technology will acquire an important role in satellite networks besides opening up opportunities in emerging technological advancements such as hybrid optical/RF or optical/mmW diversity, MIMO for the next generation of optical WLAN, and diversified applications such as short range communications (few mm) like optical links in a PC to a very long range communications (thousand of km), for example, links between OGS and the GEO satellite [10, 11]. Currently, FSO is finding niche applications both in military as well as commercial services sectors; as the FSO provide flexibility of establishing links on fixed as well as on mobile platforms depending upon the user requirements and the dedicated application scenarios [13, 14]. The optical links may also include a metropolitan network using air-to-air laser communication between office buildings, a long distance optical link between an optical ground station and a building or satellite platform, or an inter-satellite link and bridges the last mile connectivity gap throughout metropolitan networks [15]. To develop the next generation of optical wireless terminals with reduced mass, size and power consumption, and increased data transmission rate several studies were made in the last ten years [16, 17, 18]. The optical terminal design has been specifically optimized for point-to-point fixed as well as mobile platforms links between spacecrafts located at LEO/GEO orbits, and between high altitude platforms (HAPs) e.g., stratospheric platforms/aircrafts/UAVs and spacecrafts in GEO orbit (Fig. 1.3).

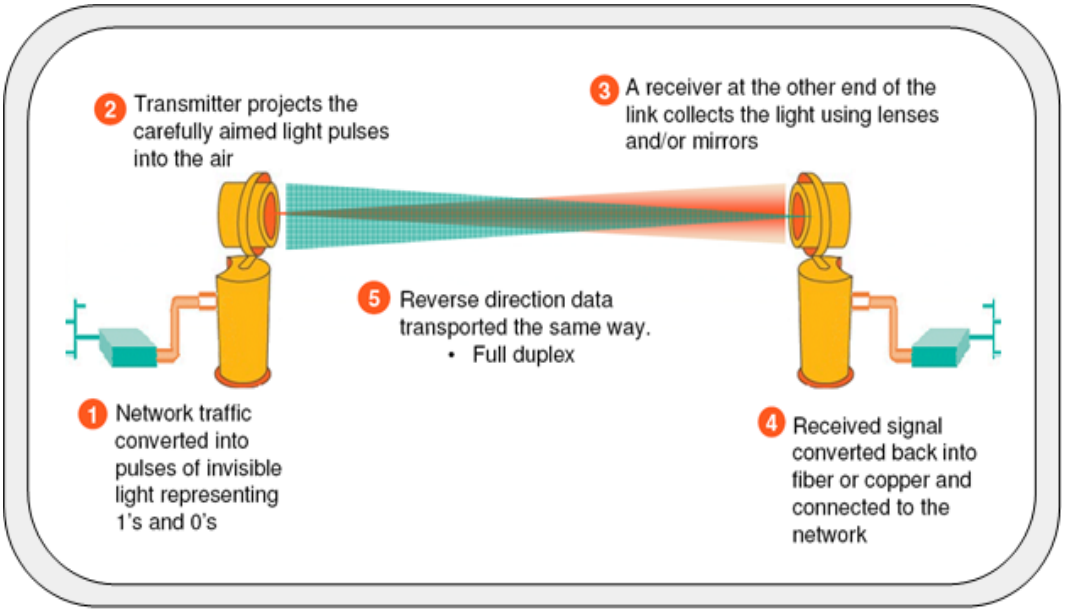

Figure 1.2: Operating principle of an optical wireless system [12]

Unlike the previous space-space scenarios, optical link between an OGS and a GEO satellite entails long-distance propagation through the atmosphere. FSO system performance depends on internal as well as external parameters; internal parameters relate to the design of the FSO system and include optical power, wavelength, transmission bandwidth, divergence angle, and optical loss on the transmit side and receiver sensitivity, bit error rate (BER), receiver lens diameter and receiver field of view (FOV) on the receiver side. External parameters relate to the environment and include visibility range and atmospheric attenuation, scintillation or atmospheric turbulence, deployment distance, window loss, and pointing loss. Overall optimum FSO system design is highly dependent upon the intended application, required availability, and cost point. By far the most important application of the FSO is to provide broadband Internet connectivity to the customer premises. With the advent and adoption of free-space optics, light will be able to deliver the optical capacity through the air, enabling completely optical wireless connectivity [20]. In recent years, extensive work is being carried out to make the optical wireless systems more suitable for short range as well as for relatively longer distance communication applications like e.g., optical ground stations OGS and terminals in space (un-manned aerial vehicles UAVs, high altitude platforms HAPs and LEO/GEO satellites) [13, 21]. Fig. 1.4 illustrates future optical communication network for near-earth application scenarios made up of optical communication terminals.

Free-space optics (FSO) links involving optical ground stations (OGS) are highly influenced by the earth atmosphere due to the interaction of the optical wave with particles of different size and shape. Fog, clouds, rain and snow cause significant signal attenuation thus limiting the performance of such links (Fig. 1.5). The major drawbacks of free-

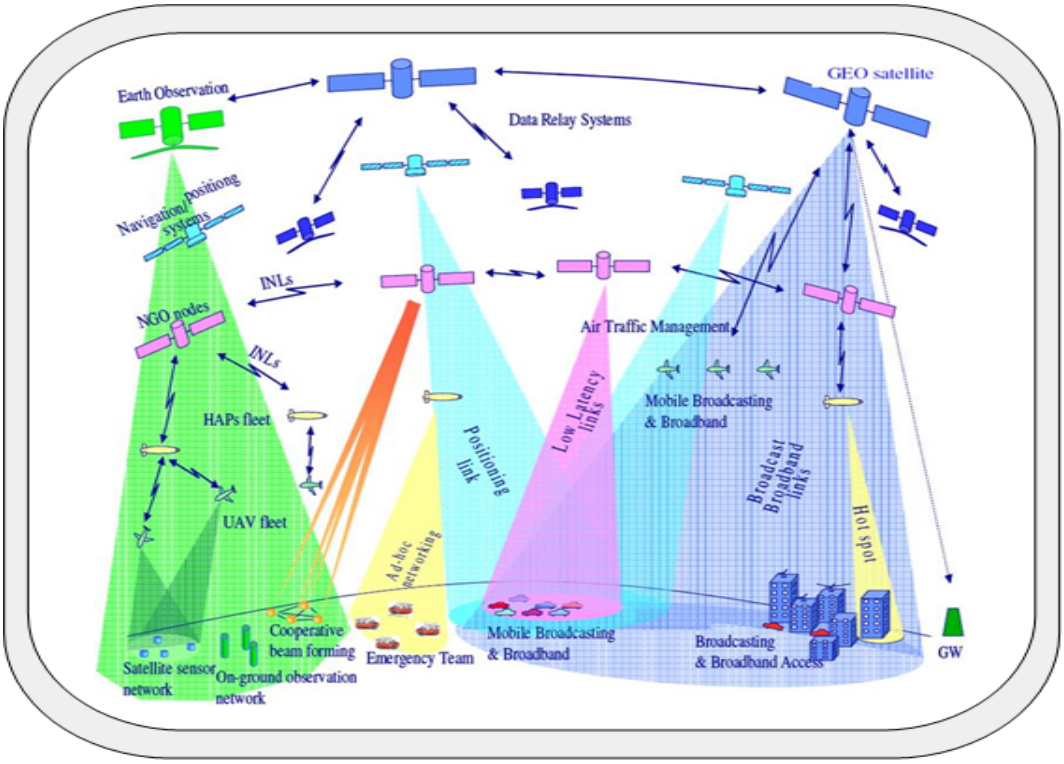

Figure 1.3: Application scenarios of optical wireless systems [19]

space optics are propagation impairments produced by the interaction of the optical wave with the earth atmosphere. As a result, special techniques have to be developed to cope with the atmospheric effects. Absorption and scattering on atmospheric particles as fog, rain, snow and clouds result in such effects as wave front distortion, beam wandering and beam spreading, that in turn are responsible for significant signal loss (Fig. 1.5). Moreover, even in the absence of atmospheric particles, air turbulence introduces propagation impairments resulting in an increased BER [23]. Measurements showed that optical turbulence decreases exponentially with altitude and that significant turbulent activity can be found up to 25 km altitude. The effects of optical turbulence are stochastic in space and time, producing signal fades on a timescale of several milliseconds in fixed applications [24, 25]. Fade levels can exceed 20 dB in extreme cases depending on the propagation path and on the link range. The FSO links in the troposphere (i.e. the lower part of the atmosphere up to 10-12 km above ground) are mostly affected by clouds and fog. Nonetheless, the contribution of hydrometeors is not negligible. Optical attenuation can be up to 130 dB/km in moderate continental fog environments [26] and up to 480 dB/km in dense maritime fog [27]. Rain can cause attenuations up to 20-30 dB/km at a rain rate of 150 mm/h [28], whereas specific attenuation through falling snow can well exceed over 45 dB/km [29]. Finally, attenuation values due to clouds can be much higher than 50 dB/km [30]. High attenuation due to clouds can be mitigated by ground station diversity to minimize

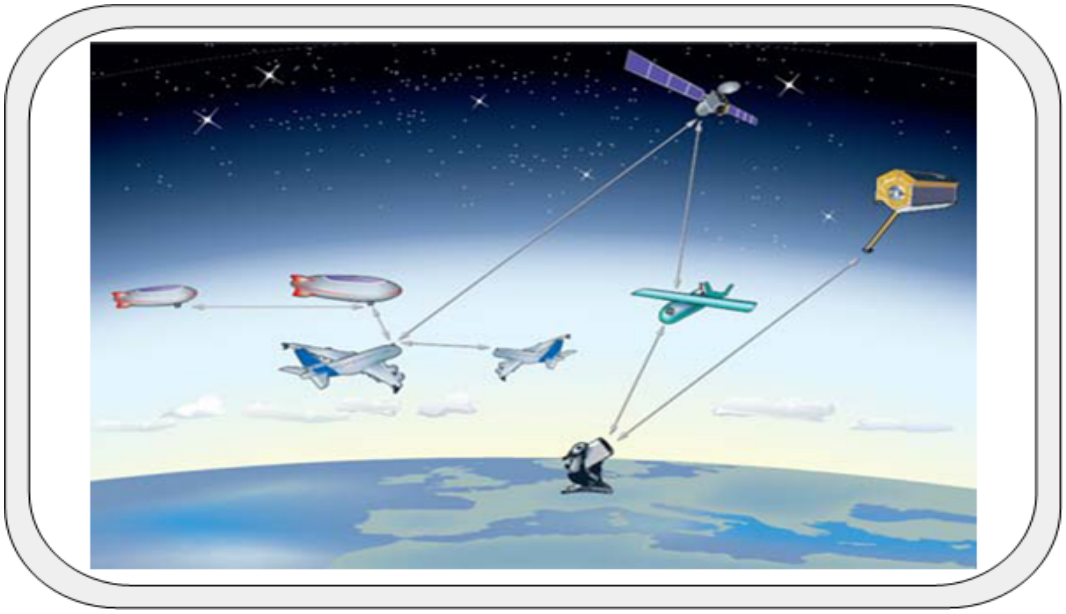

Figure 1.4: Near-earth application scenarios of optical wireless systems [22]

the probability of cloud coverage [31, 32]. Additionally, using a longer wavelength (e.g. 10μm instead of 1.55μm) leads to lower cloud attenuation, increasing link availability for thin clouds. Long-distance links are affected mainly by the optical turbulence and there exist no wavelength window in the optical spectrum that can avoid losses induced by turbulence [24]. However, intensity fluctuations and the corresponding BER ($> 10^{-9}$) can be decreased by using a longer wavelength since fluctuations decrease as $\lambda^{-7/6}$. The short fades due to turbulence can be mitigated by multi-site diversity, higher power single mode lasers and different error control techniques. More generally, atmospheric effects can be mitigated by adaptive optics: for instance, the directivity of the antenna can be improved by applying the appropriate wave front compensation to the transmitted signal [7, 33].

Despite great potential of FSO communication for its usage in the next generation access networks, its widespread deployment has been hampered by reliability and availability issues related to atmospheric variations. It is interesting to note that though this technology has been named Free-space Optics, much of its utilization has been in terrestrial atmosphere where light communication suffers all sorts of channel degradation effects which are usually absent in actual free-space channel scenario (Fig. 1.3). This factor is perhaps the only drawback associated with FSO communications and one of the main reasons for its limited deployments in many regions of the world.

Light attenuation through terrestrial atmosphere is caused by various physical phenomena: absorption, scattering, beam wandering, beam spreading and wavefront distortion etc. Absorption and Scattering of light occurs when transmitted FSO beam interacts with particles

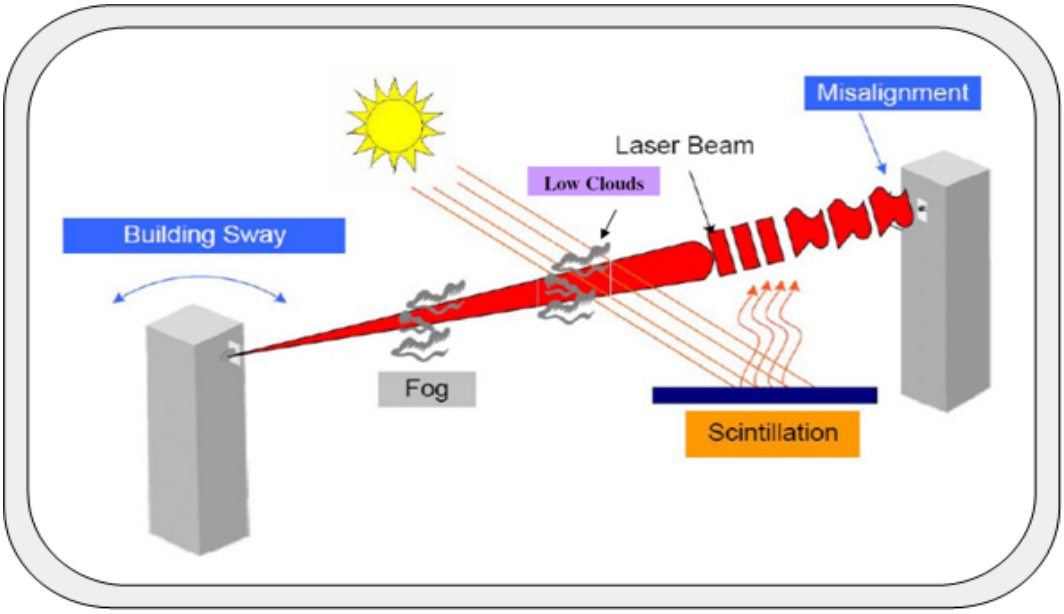

Figure 1.5: Major atmospheric effects affecting a terrestrial optical wireless system [34]

of smoke and dust, droplets of fog, haze, smog and rain, flakes of snow etc., suspended in the atmosphere. During this interaction of light with particles and droplets, light is both absorbed and scattered in different directions. As a result of these interactions, light continuously loses energy while traveling in the forward direction, thus restricting the maximum length of the link as well as presenting new challenges for optimum detection of received signal. Absorption can be controlled by transmitting light at such chosen bands of spectrum where absorption effect is minimum and we can ignore this loss without affecting the practical results significantly. However no such band is found where scattering loss can be minimized. Beam diversion results because of atmospheric turbulence whereby light traveling through different pockets of the atmosphere at different temperatures suffers changes in its direction due to variation in the index of refraction of medium along the link. This can result in the beam wandering away from reception element causing loss of power at receiver. This is stochastic effect and can be taken care of by high power single mode lasers and multi-site diversity of receiving elements. Adaptive optics can also be used to improve the directivity by applying wavefront compensation to optical signal. The biggest challenge to FSO communication today is to counter the deleterious effects of fog on the transmitted optical signals. Fog microphysics tells us that specific attenuation (dB/km) depends largely on particle or droplet size distribution (PSD) or (DSD) of fog droplets in atmosphere. This attenuation is caused in major part by scattering by fog droplets or aerosol; and attenuations by molecular/aerosol absorption and molecular scattering effects are negligible in comparison. Thus light traveling through foggy atmosphere undergoes scattering by droplets and this is the major source of attenuation of the optical signal. There are three types of scattering: Rayleigh Scattering, Mie Scattering and the

Geometrical (non-selective) Scattering. Rayleigh Scattering occurs when light is scattered by particles much smaller than the wavelength. However, when particle size become comparable to the wavelength Mie scattering is the predominant effect. Geometrical scattering occurs when size of the interacting particles is much larger than the transmitted wavelength. Today most of FSO communication takes place in bands where absorption effect is minimum and scattering effects are modeled by Mie Scattering Theory exclusively.
The choice of the transmission wavelength for FSO links depends not only on the characteristics of the atmospheric channel, but also on factors such as the optical background noise and the technologies developed for lasers, detectors and spectral filters. As a result of recent technology developments, optical sources and detectors operating at short-wave infrared and long-wave infrared have become available [35]. Furthermore, ground to space laser communications could benefit from modulation schemes less sensitive to atmospheric effects (e.g., polarization-based modulation schemes) and non-traditional areas such as optical/radiofrequency (RF) or optical/microwave (mmW) diversity. The transmission of high intensity ultra-short laser pulses through fog and clouds has recently been demonstrated [36]. Amplification of optical signals in the atmosphere in a similar way like optical amplification is performed using optical fibers could also be envisaged.

1.3 Motivation

In the past decade, the world has witnessed a dramatic increase in the traffic carried by the telecommunication networks. Internet traffic is approximately doubled every six months, and there is clearly a need for high-speed, reliable network infrastructure to accommodate this rapid increase. Optical fiber systems provide the means to achieve high bit rates in the core and the metropolitan-area network level. However, the fiber has still a long way to go, before it reaches the customer premises (the Fiber-to-the-Home, the FTTH concept). Indeed, fiber installation costs can be quite expensive, and hence an investment to bring the fiber in the access network is not likely to be economically viable due to poor internal rate of return.
Free-Space Optical (FSO) wireless access technology is by far the only most viable solution, for creating a three-dimensional global communications grid of inter-connected ground and airborne terminals, and it emerged as a promising access technology to address the needs encountered as a result of the massive expansion of the global telecommunications networks. The huge amount of data exchange between satellites and ground stations demands enormous bandwidth capacity that cannot be provided by strictly regulated, scarce resources of the Radio Frequency (RF) spectrum. The spatially confined laser beams has the potential of providing virtually unlimited bandwidth to the end user with data/information security guaranteed at the physical layer. Motivation to further investigate this area of research comprehensively is acquired for many pros and cons of this access technology that make it very challenging and interesting and are listed as under:

- Can serve as a high-bandwidth bridge (the "last mile") between the local area networks (LANs) and the medium area networks (MANs) or wide area networks (WANs).
- Using the same antenna size, the power can be focussed much better at optical frequencies. In the link budget, the antenna gain is much higher. For space applications over long distances, which will use directive links, this means, much more power can be transmitted. Provided that transmitter and receiver are aligned well, and provided that the lenses or mirrors surface has a very high quality, to be able to come close to the diffraction limit.
- The narrow optical beam width allows a much high data rates, either inter-satellite links, or links from ground station to satellites, as compared to RF.
- As terrestrial optical communication shows, it is comparatively easy to go for very high data rates, provided sufficient receive power is available. For the same bit error rates, higher data rates in optical communication with direct detection require less increase in receive power, as compared to RF communication. (For very sensitive optical technologies, this is not the case).
- The same transmission protocols can be used than for fiber-optic cables. As protocol conversions always means delay and latency time, reducing conversions is an advantage for all real-time applications. The prototype demonstrations from several suppliers have reported that capacities in the range of 100 Mbps to 2.5 Gbps and in laboratory demonstrations as high as 40 Gbps, are achievable.
- Optical transmission can operate close to the quantum limit. The distribution of secure keys, based on pairs of entangled photons, may be an important application for the future. Such a distribution service is possible from a space platform.
- Low start-up and operation costs, mostly due to the fact that Optical wireless transmission is not regulated by the Federal Communication Commission (FCC), and does not require expensive licensing of the spectrum needed.
- The optical satellite terminals can be small in structure and lightweight. As an example, the deployment of the high-gain antenna dish of the Galileo-probe on its way to Jupiter failed. This can always happen to large structures, which have to be deployed in space, as there is not enough space in the rocket fairing. Optical terminals achieve very high directivity with comparatively small apertures.

Optical technology is expected to revolutionize our communication system architectures especially the ground-space and in-space communication system architecture and one can witness a linear increase in the trends of data rate for Earth observation satellites with the every coming year. Fig. 1.6 and Fig. 1.7 below shows a recent history and future trends of increase in data rates storage capacity and the number of bits per pixel of stored image data for our Earth observation missions, respectively [10]. It is clearly evident that with the availability of state of the art electro-optical components now a days, a linear increase in

the sensor resolution can be seen. With the memory size well over 1 Tbytes and digitized bits more than 13 bits, Gbps-class laser communication is inevitable for data download from Earth observation satellites in the near future.

However, Optical wireless systems are not without challenges as the promised enormous

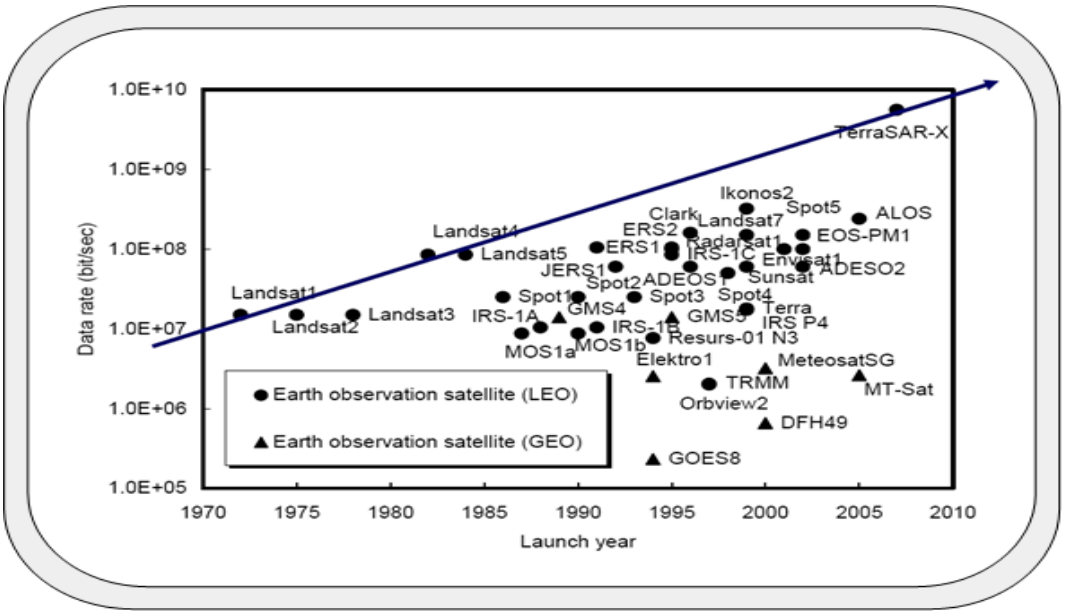

Figure 1.6: Trends of data rates for Earth observation satellites [10]

data rates are only available under clear weather conditions, and atmospheric phenomena such as clouds, fog, and even turbulence can degrade the performance, dramatically. While turbid media such as clouds and aerosols cause pulse broadening in space and time, turbulence presents itself as scintillation and fading. To exploit the great potentials of free-space optical wireless at its best under all adverse weather conditions, prudent measures must be taken in the design of transmitter and receiver and to the precise and realistic modeling of the free-space atmospheric channel. Especially the free-space atmospheric channel for terrestrial applications or ground-space applications (such that if it entail propagation of the optical signals through the earth atmosphere) poses a greatest challenge to the transmission of free-space optical signals in conditions like fog, snow, rain and clouds. The transmitted optical beam interacts with the particles of the medium and results in many complex phenomena like scattering, absorption and extinction etc. Of all atmospheric effects fog is by far the major limiting factor as it causes substantial attenuation of the transmitted optical signal. Moreover, observing legally mandated upper limits to the intensity of the transmitted optical beam is also a major concern in the usage of such systems. These two challenges highlight one of the critical design trade-offs that must be resolved to field a successful optical wireless system such that the system must transmit enough power, within the allowable eye-safe limits, so that the FSO link may render a very high availability for a high percentage of the time.

Many models were proposed in recent years by scientists to predict attenuation of optical

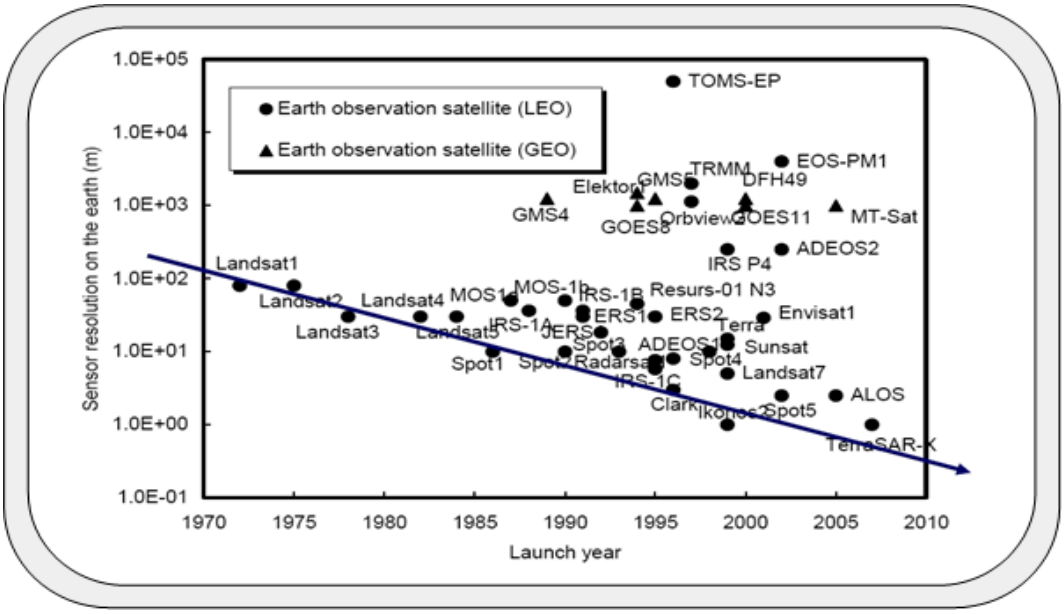

Figure 1.7: Trends of sensor resolution for Earth observation satellites [10]

signal through different atmospheric conditions in general and for fog especially. Most of these models are empirical derived through curve fitting techniques of the experimental data values obtained in the some field experiments. However the utility of these models is limited as they may not depict some of the most important parameter from communication system design perspective. It is now a well established fact that fog behavior is not the same at different locations around the globe due to variability of environmental conditions and due to the difference in the behavior of various fog types and thus attenuation experienced by the light beam is a random phenomenon. Moreover, the concentrations of matter in the atmosphere, which result in the signal attenuation vary spatially and temporally, and depends on the current local weather conditions. This makes the understanding task somewhat very tedious and interesting. However, almost all empirical models proposed up to date have been able to suggest, at best, average specific attenuations in certain environmental condition for a given optical link. The other types of models proposed are based on microphysical properties of a particular phenomenon. However, applicability of such models is somehow limited due to the fact that most of such microphysical parameters are not measured usually at the sight of installation of optical links. Moreover, simulating these parameters behavior is very complex and time consuming and yet again, these values serve only to indicate average attenuation per unit length of link and do not explain changes in attenuation. Thus from an engineering point of view there is a dire need for a better understanding of different atmospheric effects and their influence on the transmitted optical beams in free-space such that their attenuation behavior could be statistically probable with sufficient accuracy while stochastic parameters be able to enhance the understanding

of a system designer/engineer about a certain limiting process. Such an understanding is vital to exploit and utilize randomness in the apparently stationary behavior, especially like fog, in order to propose better strategies to overcome or at least lessen the severity of light attenuations through fog.

1.4 State of the Art Literature Review of Free-Space Optical Communication Systems

The access network performs a critical function in the overall telecommunication network by bridging the "last mile" and thereby providing a cost-effective means for users to utilize the network and its broad array of services. FSO technology is one of the most promising and emerging access technology having tremendous potential to offer fiber-like bandwidth and the lowest cost per bit of information transmitted. In order to successfully design and field an optical wireless system, a number of critical design trade offs related especially to the free-space atmospheric channel, the specification of a particular wavelength for transmission and the transmitter and receiver design must be resolved [37, 38].
In the communication world, FSO is one area which need be researched comprehensively. The theory behind free-space optical communications is well represented in the literature [6]. The effect of fog and other impairments on the performance of the systems have remained an actively researched area and different kinds of solutions have been proposed to combat such conditions. The selection of an appropriate wavelength to provide optimum performance has been a major point of disagreement [39]. Availability and reliability analysis for FSO systems has been extensively carried out [9, 31] to prove their importance in the evolving broadband network. Hybrid FSO-RF links promises very high availabilities [40, 41], and the development of an intelligent switch-over is an open problem [42].
Currently, optical wireless systems are mainly being used for short range communication applications like the Last-mile access. FSO has demonstrated the application potential in many areas such as line-of-sight communications, satellite communications and the last mile solution in a fiber optics networking. Optical wavelength having wavelengths 0.8 μm, 1.5 μm, 3.5 μm and 10 μm are now commonly available and are currently being used in state-of-the-art free-space laser communication systems [43, 44]; unfortunately the system performance is imposed by atmospheric turbulence [13]. To reduce atmospheric effect in free-space laser communication systems, several techniques have been used, such as adaptive optics, aperture averaging, coding techniques and multiple transmitters [4, 30]; however, significant improvement has not been achieved yet. Such systems are in use for long distances and the most accurate solutions with acquisition and tracking for space applications [45, 46]. Due to the availability of sensitive electro-optic components, multiple aperture transmitter and receiver optical schemes are being researched and employed in order to increase availability and reliability [47]. On the other hand efficient power estimation and equalization techniques are being researched along with utilizing robust

modulation and coding techniques and employing adaptive optics to increase the data rates [48, 49]. For designing high performance links, efforts are being made to possibly design an intelligent switchover between FSO and redundant RF link [50]. Recent research has successfully demonstrated 80 Gb/s free-space optical communication demonstration between an aerostat and a ground terminal [51]. For these links, a very precise beam pointing and tracking system is used to maintain beam alignment and dynamic wave front compensation [52, 53]. In recent times, FSO links are being investigated for certain innovative application scenarios like high data rate optical links between earth station and the satellite or the HAPs in addition to last-mile access solution [44, 51, 54].

1.5 Thesis Contribution, Scientific Focus, and Organization

Because of the quality of the transmitter and detection systems today, the limiting factor in overall system performance of a FSO system is the propagation medium. One of the potential challenges currently faced by the FSO industry in order to improve its link availability and reliability is the modeling of the terrestrial free-space optical channel for adverse weather conditions like fog, snow and clouds. Especially, a thorough insight of the atmosphere and various mechanisms of signal attenuation are required to improve its performance and acceptability. Modeling the atmospheric channel for different fog conditions is a problem of great complexity due to a number of dynamic atmospheric parameters that affect the channel performance and the disagreement over the mathematical modeling of these phenomena [1, 55]. All these important models and many others helped in understanding the complex behavior of fog attenuation to some extent, in general, but could not provide a major breakthrough. Since most of these models are empirical models and contributed a little in overcoming, or at least limiting the fog attenuation factor.
The investigations in statistical-dynamical channel modeling of the terrestrial FSO links for adverse weather conditions (especially dense fog) are of great importance because the future access networks will rely heavily on the terrestrial and ground-space FSO networks. An in-depth analysis of the measured optical attenuations data collected in rain, snow and different fog conditions provides a useful insight about these effects on the installed FSO systems. Based on the measured attenuation data, in particular radiation fog conditions, few prediction models are proposed and evaluated in detail in chapter 4 and chapter 5, and are thus the main contribution of this thesis. These prediction models are mainly based on Mie scattering theory and usually employ one of the two drop size distributions i.e., the two parameter exponential distribution or the three parameter modified gamma distribution. It is hoped that the proposed models and their subsequent analysis presented will be useful in improving the propagation tools and data of integrated telecommunication, navigation and Earth observation systems and the proposed prediction models can be disseminated later into ITU-Recommendations. Moreover, the results of this work are important for the scientific community towards better understanding of the FSO related problems and crit-

ical overview of different models previously presented. The originality and significance of this thesis contributions is reflected by publication of parts of this thesis in several peer reviewed conference proceedings and journals (as mentioned in Appendix A).
This thesis focuses on the statistical-dynamical channel modeling of the outdoor FSO links especially for fog conditions. Thus, only optical attenuations of the laser beam in different fog conditions are of interest. Furthermore, because the free-space optical channel modeling is a wide and many-fold topic, the span of this thesis has been restricted only to model the most common weather conditions like fog/clouds, rain, and snow for terrestrial FSO scenario. The signal behavior therefore is derived from the optical received power reaching the receiver. This implies that ultimately only optical power attenuations will be of concern. In addition, influence of temperature, relative humidity, liquid water content, particle size distribution and particle density is also investigated and evaluated in sufficient details.
Given these findings, more specific questions were formulated:

1. How can we characterize and quantify the fog, rain and snow related optical attenuations related to terrestrial FSO links? Can the fog related optical attenuations be quantified on the basis of their dependence on its seasonal and diurnal life cycle? What are the overall conditions and mechanisms associated with the formation, evolution and dissipation of fog, and how significantly they influence the propagation of optical signals in free-space? How detrimental are the rainfall and snowfall related optical attenuations and how good are the different models (empirical and analytical) in predicting the optical attenuations in comparison to actual measured attenuations?

2. How variable is the fog microphysics and corresponding DSD at different locations but with similar fog environments, and what is its influence on the propagation of optical signals in free-space? How can we relate optical attenuations with the fog density and thus in turn to amount of liquid water content? Can we rely on liquid water content parameter besides visibility range in order to predict optical attenuations accurately?

3. On the basis of actual measured attenuation data from different locations, can we predict the DSD parameters optimally? On the basis of such DSD parameters estimated can we predict optical attenuations for FSO links at different locations but similar fog environments?

These questions represent the core motivation for the following research and each is addressed in a distinct chapter of this dissertation,

- Chapter 2 presents the theoretical background related to the propagation of optical radiations in the free-space atmosphere in order to thoroughly assess the performance of terrestrial optical links. In this chapter various physical and optical characteristics of the free-space channel are described. Additionally, various existing channel models (deterministic as well as empirical) commonly employed in case of

free-space optical links, are also mentioned along with their pros and cons for certain communication applications.

- Chapter 3 describes measured optical attenuations and their analysis for different atmospheric conditions especially fog (radiation and advection), rain and dry snow conditions. This chapter further provides a detailed comparison about optical attenuations recorded at Graz, Milan and Prague, especially for continental (radiation) fog environments. In the subsequent section, an analysis of the measured attenuations is provided on the basis of seasonal and diurnal variations.
- Chapter 4, deals with investigations on microphysical properties of fog. Firstly, the fog phenomena is discussed with focus on the fog formation, its maturity and dissipation. Then its influence on the terrestrial free-space optical links is discussed on the basis of actual measured attenuation data. Then in the second section, fog density measurement sensor setup is explained followed by the analysis of the fog density measurement results from two locations Graz (Austria) and Budapest (Hungary). This section is followed by an empirical model that deals with relationship between measured optical attenuations and the corresponding values of temperature and relative humidity. In the final section, prediction model dealing with fog drop size distribution (DSD) and liquid water content (LWC) from measurement of fog density is discussed followed by analysis and comparison of fog density with the actual measured attenuation data.
- Chapter 5 is focussed on fog attenuation prediction methods. In the first section, a model based on Mie scattering theory and modified gamma droplet distribution is proposed that is based on Marsaglia method to compute DSD parameters. Next sections deals with the methodology to retrieve fog related DSD parameters, especially Modified Gamma and Exponential distribution parameters. This is accomplished by using standard iterative procedure of optimally determining the distribution parameters corresponding to the two representative fog events recorded at Graz (Austria) and Prague (Czech Republic). This method is complemented by an appropriate performance analysis and comparison of the retrieved DSD parameters for both DSDs mentioned.
- Chapter 6 provides the overall conclusion of this work by outlining major achievements and the future work directions.

2 CHANNEL MODELING

The performance of terrestrial free-space links is primarily dependent upon the climatology and the physical characteristics of its installation location. In general, weather and installation characteristics that impair or reduce visibility also affect the free-space link performance. Severity and duration of the atmospheric effects affect the distance and the availability of the links. Significant success is not till achieved in overcoming the detrimental behavior of adverse atmospheric conditions on the optical signal transmitted in the case of FSO. Especially, modeling the attenuation effects of different fog, snow and cloud conditions still remain the major challenge to the widespread applicability and acceptability of this access technology. The free-space atmospheric channel always play an important role in limiting the performance of optical wireless systems in adverse weather conditions, however, in clear weather conditions optical wireless technology surpasses any other competitive access technology in terms of data transmission efficiency. Characterizing the free-space channel for different adverse weather conditions for such links is a major issue for the research community [56]. Disagreement also exists among researchers on the modeling of the free-space channel for various weather conditions and a variety of impairments are possible to model the attenuation effects caused by phenomenon like rain, snow, fog, different kinds of dust and smoke particles (aerosols). This chapter focusses on the description of some important atmospheric attenuators, the necessary theoretical background concerning their attenuation behavior and on the various modeling approaches of such factors.

2.1 Light Wave and Photons

Light has an enormous potential to transmit large data volumes and the high optical frequencies make it possible to utilize very broad bandwidth in an energy-efficient manner. Light, as well as RF signals are electromagnetic transversal waves, which can propagate in free space. The signal is a wave in the electric field $\overrightarrow{E}$ as well as in the magnetic field $\overrightarrow{H}$. For far field considerations, in sufficiently long distance to the transmitter, both fields have well known relations to each other. For the $\overrightarrow{E}\,field$, the relation is:

$$E(x,t) = Acos2\pi(\frac{t}{\tau} - \frac{x}{\lambda} - \vartheta_1) \tag{2.1}$$

where A is the signal amplitude, t is the wave period in time (corresponding to the frequency f with $f = \frac{1}{\tau}$), λ is the wave period (wavelength) in space and ϑ_1 is the start phase.

As Equation (2.1) indicates, the wave can be seen as a spatial wave (over distance x) and as a temporal wave (over time t). Wavelength and frequency are related according to:

$$v = \lambda \cdot f \tag{2.2}$$

where v is the velocity of light in vacuum c = $2.99792458 \times 10^8 \frac{m}{s}$. The $\overrightarrow{E} - wave$ and the $\overrightarrow{H} - wave$ are related with the wave impedance Z by the following Equation:

$$Z = \sqrt{\frac{\mu_0 . \mu_r}{\varepsilon_0 . \varepsilon_r}} \tag{2.3}$$

where
$\varepsilon_0 = 8.854 \times 10^{-12} \frac{As}{Vm}$ is the electric field constant called vacuum permittivity
$\varepsilon_r = 1$ is the relative static permittivity or dielectric constant in vacuum
$\mu_0 = 4\pi \times 10^{-7} \frac{N}{A^2}$ is the magnetic field constant called permeability in free-space
$\mu_r = 1$ is the relative permeability constant of water
In the far field, this impedance becomes real, $Z_0 \cong 377\Omega$.
While for RF communication the voltage is modulated and radiated as electric field by an electrical dipole antenna, or (rarely) current is modulated and radiated as magnetic field by a loop antenna, due to the high frequency these parameters are not accessible for classical optical communication. In this case, the optical power P_{Opt}, or as it is usually termed, the light intensity I is modulated over time (if intensity modulation (IM) is used).

$$P_{Opt}(t) = \int I(X_0, t) dA. \tag{2.4}$$

The power is the integral over the illuminated area A in this case. As Max Planck found in 1900, that energy is granular or quantized i.e., made of individual units called quanta. The relationship for quantization of energy is given by:

$$E_{PH} = h \cdot f \tag{2.5}$$

where h = 6.625×10^{-34} Js is the Planck's constant. The quantum formula of the energy Equation (2.5) allows to re-write the formula for optical power, simply adding up a number of the elementary particles of the electromagnetic wave, i.e., the photons.

$$P_{Opt}(t) = n(t) \cdot E_{PH} = n(t) \cdot hf \tag{2.6}$$

Here $n(t)$ is the rate of photons, generated over time, and E_{PH} is the energy of a single photon. As can be seen, the energy of a photon increases with the frequency of the electromagnetic wave. This means, transmitted power at higher frequency shows more of the single particle properties and also interact with matter, whereas lower frequency rather behaves according to the wave model. It is interesting to note in optical communication, that

the (spontaneous) generation and detection of photons is a statistical process, which can be described by the Poisson distribution:

$$p(n|T) = \frac{(rT)^n e^{-rT}}{n!} \tag{2.7}$$

$p(n|T)$ is the probability, to count a number of n photons in the time period T, and r is the average count rate. If for the case of data transmission, the time period T for "light state" is chosen to a fixed value, and the average count rate in this period is $N = rT$, Equation (2.7) can be simplified to:

$$p(n) = \frac{N^n}{n!}.e^{-N} \tag{2.8}$$

Assuming digital optical data transmission using Intensity Modulated with equal probability of "light state" and "dark state" (e.g. Manchester coding, 2PPM, etc.) a bit error is observed for the case, that no photon is detected during the "light state" period. The probability for this case is:

$$p(0) = \frac{N^0}{0!}.e^{-N} = \frac{1}{1}.e^{-N} \tag{2.9}$$

On the other hand, a requirement of a certain bit error rate (BER) like 10^{-9} (means one bit error for 10^9 transmitted bits) requires an average count of photons over time for "light state", which is:

$$p(0) = 10^{-9} \equiv e^{-N} = \frac{1}{e^N} \tag{2.10}$$

$$10^9 = e^{-N}|ln \tag{2.11}$$

$$N = ln(10^9) \cong 20.7 \tag{2.12}$$

This means, an average count of 11 photons per bit is necessary, if light and dark states have equal probability. So, not considering any other receiver noise contribution, the limitation of quantum noise for classical optical communication requires a minimum average optical receive power $\overline{P_{MIN}}$ of:

$$\overline{P_{MIN}} = floor(\frac{N}{2}).R_b.E_{PH} \tag{2.13}$$

where N is the average count of photons per bit to achieve a certain BER, R_b is the bit rate and E_{PH} is the photon energy. This is a clear derivation and a good approximation for a limit, which due to different noise contributions in practical cases usually cannot be achieved. This means, the minimum required optical receive power is dependent on the light wavelength due to the particle properties of light. Longer wavelengths have less quantum noise and allow lower receive powers for direct detection with a photodiode.

2.2 Free-Space Atmospheric Channel

The outdoor free-space atmospheric channel for optical wireless links (terrestrial and ground-space links) is impaired mainly by absorption and scattering phenomena as a result of its strong interaction with aerosol particles of different types and shapes present in between the transceiver terminals. This interaction results in a wide variety of complex phenomena like frequency selective attenuation, free space loss, clear air absorption, scattering and scintillation noise induced due to atmospheric turbulence (Fig. 1.5). The outdoor free-space optical links usually employ high-power lasers operating in class 3B band or above for maximum coverage at high data-rates. Due to the existence of direct LOS path between the transmitter and the receiver, the problems associated with multi-path propagation are eliminated. As a result, very high data rates can be transmitted over a relatively larger distance when compared with non-directed diffused systems (Fig. 2.1).
Frequency selective absorption at specific optical wavelengths comes from the interaction

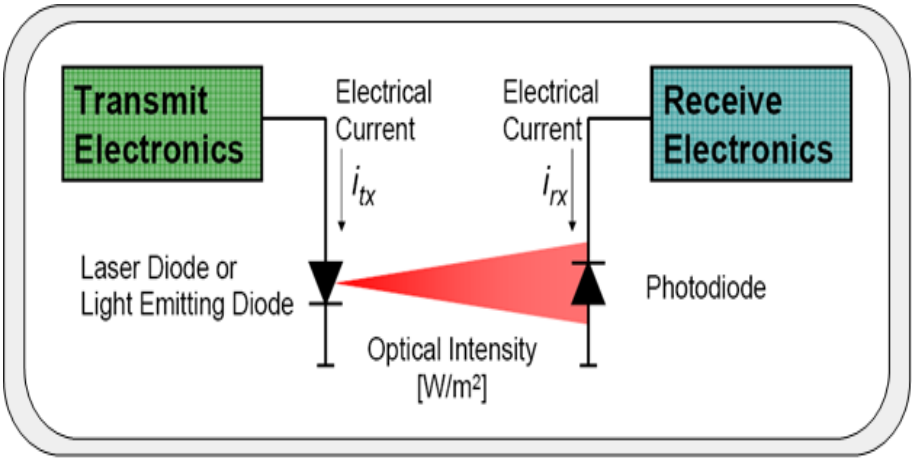

Figure 2.1: Free-Space Optical Wireless System [57]

between the photons and atoms or molecules that leads to the extinction of the incident photon, elevation of the temperature, and radiative emission. Atmospheric scattering results from the interaction between the photons and the atoms and molecules in the propagation medium. Scattering causes angular redistribution of the radiation with or without modification of the wavelength. Scintillation is caused by thermal turbulence within the propagation medium that results in randomly distributed cells having variable sizes (10 cm - 1 km), temperatures, and refractive indices causing scattering, multi-path and variation of the angles of arrival. In addition, background radiation effect and sunlight can also affect the FSO performance significantly. All atmospheric effects interfering with the transmitted optical beam for FSO links can be divided into following four broader categories:

- Attenuation: reduction in received optical power caused by absorption and scattering on molecules and aerosol particles etc.
- Scintillation: fluctuation in received signal power
- Beam wander: mispointing
- Beam spreading: reduction in antenna gain

In the subsequent sections, free-space atmospheric channel for outdoor links is discussed in detail with special focus on its structure, composition and different attenuating effects. Later on, different channel models (empirical, deterministic and statistical) that were previously employed in order to efficiently characterize the outdoor free-space optical channel.

2.2.1 Composition of the Atmosphere

To characterize the properties of atmospheric transmission affecting optical wireless systems operating in free-space, the gaseous constituents of the atmosphere are classified into two broader categories i.e., constituents in the form of gases that are in majority and the ones that are in minority.
The atmospheric constituents in the form of major gases like O_2, N_2, Ar., are found in abundance and distributed uniformly (concentration do not vary significantly with time) up to an altitude of 100 km, in proportion to a fixed volume (with a variation of less than 1%), to an altitude of more than 15 km depending on the latitude. In the visible and infrared atmospheric transmission at earth (up to 15 μm), alone among these constituents, this CO_2 absorption bands are important. Note that O_2 has a relatively narrow absorption band in the visible spectrum around 0.7 μm due to the magnetic dipole moment, whereas it has strong absorption in the ultraviolet band.
Atmospheric constituents like CO_2, H_2O, O_3 although are in minority but impact the optical propagations significantly. They are found in variable proportions by volume and their concentration varies according to:

- The location (latitude, altitude, or sea mainland)
- Environment (urban, rural and maritime),
- Weather

The main component of this category is the water vapor H_2O. Its concentration depends on the climatic and meteorological parameters. For example, in marine areas its concentration can reach up to 2% while its value above 20 km altitude is zero. To quantify the amount water vapor H_2O in the air, the concentration is measured from the atmospheric humidity, which we define by the following quantities:

- The number of millimeter of precipitable water w_0 per km.
- Absolute humidity (g/m^3): mass of water-vapor per unit volume of air and its below given relation can be derived from Ideal gas law,

$$A.H = 2170 \times [\frac{pH_2O}{T}] \tag{2.14}$$

- Relative humidity (%): ratio of water-vapor partial pressure measured in units of kilo-Pascals (kPa) to the saturation vapor pressure $E_s(T)$ (also measured in kPa) and is given by the following relationship,

$$R.H = [\frac{pH_2O}{E_s(T)}] \times 100\% \tag{2.15}$$

where

$$E_s(T) = 2.4096(\frac{300}{T})^5 10^{(10-2950.2/T)} \tag{2.16}$$

The concentration of Ozone O_3 varies depending on the altitude (maximum 25 km), latitude and season. It offers significant absorption in the ultraviolet and infrared regions around the wavelength of 9.6 μm.

2.2.2 Aerosols Composition and their Classification

Atmospheric aerosols are tiny particles of solid or liquid suspended in the Earth atmosphere that vary not only in their chemical composition but also in size (0.001 to 100 μm) and shape (spherical, ellipsoid, rods., etc.). Aerosols exist even in the clearest weather conditions and their presence in the atmosphere significantly influence the climate, either directly by altering the radiative balance of the planet, or indirectly by modifying the optical properties of clouds due to a change in their microphysical properties. They can significantly alter transmission of optical radiation, as evidenced by the important example of reduced visibility due to the presence of pollution or fog. Actually, the visibility parameter is a measure of how an object can be seen through the air and hence characterizes the opacity of the atmosphere (see Section 2.4.2). Generally, simple shapes of the aerosols are assumed for model calculations; however shape distribution functions are also required. Whereas, size distribution functions specify the concentration of a particle as a function of its radius. Atmospheric particles can be categorized into two broader classes:

- aerosols; consist of very small size particles like smoke, smog, cosmic dust, clouds, fog, volcanic ash etc.
- hydrometeors; mainly consist of water-dominated particles in the solid or liquid forms like fog, haze, mist, rain, snow, sleet, hail and many types of clouds etc.

The nature of aerosols depends strongly on the environment: urban, rural or maritime. As For example in a marine particles consist mainly of water and crystals salt, whereas in rural areas they consist partly of dust raised by wind. The size distribution of these aerosols is quite similar in the lower troposphere and near the ground. Only their concentrations and mean radii differ depending on the altitude.

Aerosols Classification

Aerosols are airborne particles that have variable drop speeds in the atmosphere (e.g., a particle of 0.01 μm average speed of fall of 0.3 m/month while for a particle of 10 microns that speed goes to 0.3 m/minute). This limits the variation in size of these particles between 0.001 to approximately 100 μm. Indeed, particles smaller than 1 nm are considered ions. For ions rate of chemical variations is an important parameter and they disintegrate very rapidly and so are unstable. For the particles whose size exceeds 100 μm (0.5 m/second), the sedimentation rate is large enough, which causes their precipitation. According to their formation process we classify aerosols into two categories:

- The primary aerosols; that are emitted directly into the atmosphere as particulate like volcanic ash, sea spray, desert dust, industrial dust etc.
- Secondary aerosols; that are formed as result of chemical transformation of a gas phase into particulate phase by various processes e.g., sulfate, organic compounds, etc.

The optical properties (refractive index) and microphysical (size distribution, shape and the composition of particles) of aerosols depend strongly on their origin (source and mechanism production). The form of aerosols is often irregular, liquid aerosols are spherical while solid aerosols are found in various forms (cubic, cylindrical, agglomerated etc.). Equivalent diameter term is often used to describe the size of these particles. This diameter corresponds to diameter of a sphere having the same physical properties as if the particles are irregular. Several spherical particles of equivalent diameters are currently used include by example the optical equivalent diameter, the aerodynamic equivalent diameter and the diameter by volume equivalent. According to the size of the radius r of the particle (assumed spherical), we distinguish three classes:

- Aitken particles and ultra-fine particles (nucleation mode): these are very fine aerosols in the size range between 0.001 and 0.1 μm, they are the core part of the condensation and formation processes of clouds and fogs.
- Fine particles (accumulation mode) are particles that belong to the size range between 0.1 and 1 μm, atmospheric aerosols of this mode are much greater in quantity than the particles of other modes.

- The larger particles (coarse mode) are particles whose size varies between 1 and 100 μm, the particles are essentially elementary particles, they are much less in number than other particles and they can remain in the atmosphere in the free state only for a limited period, in a region located in the vicinity of emission sources.

2.3 Atmospheric Channel Effects

The overall performance of free-space optical wireless systems is degraded due to the influence of various atmospheric effects on the transmission of electromagnetic waves. The quality and availability of these links is reduced with the increase in severity and duration of these effects. Effects of the atmosphere can be separated into pure losses and random distortions of the transmitted optical wave. Pure losses emerge as a result of absorption or scattering processes of the atmospheric particles and these processes are highly wavelength dependent. Whereas, the random distortions deform the phase front of the optical wave and this happens due to changes in the refractive index of the turbulent air as a result of temperature gradients in the atmosphere. The all electromagnetic radiations used in any communication system are affected by the atmosphere as shown by Fig. 2.2 below. Moreover, a good understanding of atmospheric phenomena such as fog, haze, mist,

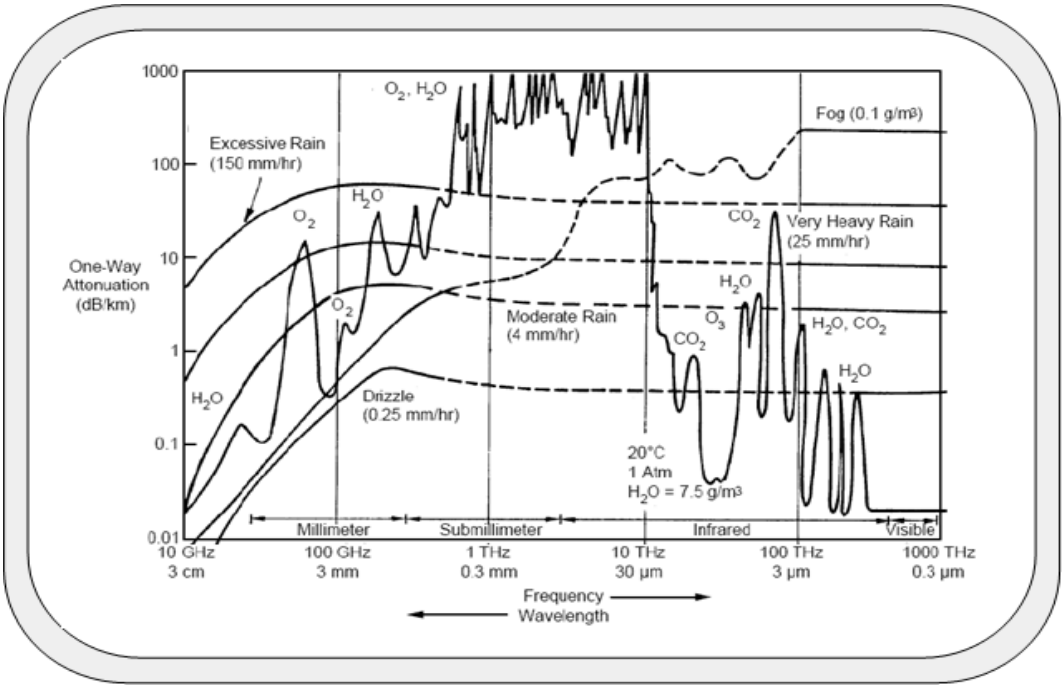

Figure 2.2: Typical Spectrum of atmospheric attenuations [58]

snow, rain and clouds and their effect on the performance of a FSO link is of great importance while designing the transmitter and the receiver of such a system. By understanding weather parameters such as humidity, visibility range and temperature, together with the features of an FSO system and its deployment characteristics, it is possible to model atmospheric propagation.
For that reason in recent years, we find in literature a growing number of scientific publications on benchmarking and increasing the free-space optical wireless system reliability [59, 60, 61]. However, Fog still remains a major source of concern for terrestrial FSO systems and is considered the main mechanism of signal degradation for electromagnetic radiations transmitted in the wavelength range of visible and infrared band. Thus, a relationship between the characteristics of fog like density and visibility range etc., and the optical attenuations of the signal transmitted is very important, in order to predict outdoor FSO system performance, prior to its physical installation at a particular location. In this chapter, different empirical and theoretical expressions, which are a function of wavelength and visibility range, are being presented that predict the atmospheric attenuation of laser radiation in the visible and infrared wavelength range.

2.3.1 Absorption

Absorption is a factor highly dependent on transmitted wavelength and occurs as a result of the absorption of a transmitted light photon by the gas molecules of the terrestrial atmosphere. The photon energy absorbed by the gas molecule raises the kinetic energy of the gas molecule. Thats the reason why absorption process is essentially responsible for the heating of the Earth atmosphere. The theory of gaseous absorption is now fairly well-developed and well-understood. A number of methods exist to predict optical signal attenuations by atmospheric absorption over a wide range of frequencies with good accuracy.
We distinguish absorption process from the following three processes:

- The electronic transitions due to absorption of photons whose energy is exactly equivalent to the transition between two levels of the molecule based on rules of the existence of quantum energy states. The electronic transitions are responsible for the emission spectrum and absorption in the UV and visible bands.

- The transitions due to the vibration of atoms which are responsible for the emission spectrum due to thermally heating of the H_2O, CO_2 etc., molecules and the absorption spectrum observed against infrared transmissions.

- The transitions due to rotation of molecules and the fine structure of vibrational bands that results in the emission spectrum and the absorption spectrum at free-space optical transmissions at infrared wavelengths.

In the context of electromagnetic radiations, when atmospheric particles absorb light, this absorption provokes a transition (or excitation) in the particle atoms (typically the electrons) from a lower energy level to a higher one. Only those light photons are absorbed that can cause electron transitions from one energy level to another. The excited electrons come back to their original unexcited states through discrete emissions of radiation. Thats the reason why absorption is a quantum effect (a selective phenomenon) and is a strong function of transmission wavelength and the gases and pollutants that are present in the atmosphere and results in relatively transparent atmospheric transmission windows, and relatively opaque atmospheric absorption bands (called atmospheric blocking windows) as shown in Fig. 2.4, which presents the transmittance of light through the atmosphere due to molecular absorption for wavelengths up to 15 μm. Beer-Lambert law, as illustrated in Fig. 2.3, relates the transmitted power $P(\lambda,0)$ with the power received $P(\lambda,d)$ at distance d by the following relation,

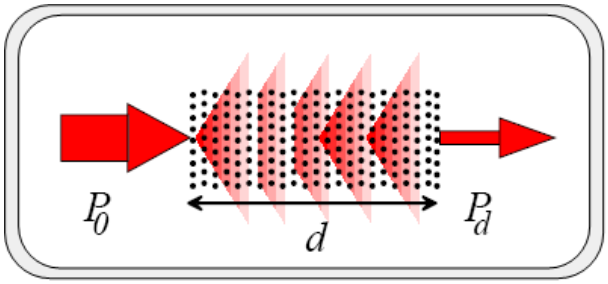

Figure 2.3: Illustration of the Beer Lambert Law [15]

$$T_r(\lambda,d) = \frac{P(\lambda,d)}{P(\lambda,0)} \tag{2.17}$$

where λ is the transmission wavelength and T_r is the total atmospheric transmittance. Transmittance is usually expressed as a number between 0 and 1. Sometimes, it is expressed as $\%Transmittance$ which simply means $100T_r$. Beer-Lambert Law relates the transmittance of light to absorbance by taking the negative logarithmic function, base 10, of the transmittance observed by a sample, which results in a linear relationship as,

$$Absorbance = 2 - Log_{10}(T_r) \tag{2.18}$$

According to Beer-Lambert law absorbance is directly proportional to the path length and the concentration of the particles and is measured in absorbance units (Au). For example, $\sim$1.0Au is equal to 10% transmittance, $\sim$2.0Au is equal to 1% transmittance, and so on in a logarithmic scale. The absorption spectrum is represented by the variation of the spectral absorption coefficient. The nature of this spectrum is due to the variations of possible energy levels inside the gas mass generated essentially by the electronic transitions, the vibrations of the gas atoms and rotations of the gas molecules. The apparent increase in the

pressure or temperature of the gas molecules due to some possible effects tends to widen the spectral absorption lines by excitation of new possible energy levels.

The atmospheric molecules are characterized by their index of refraction that in turn

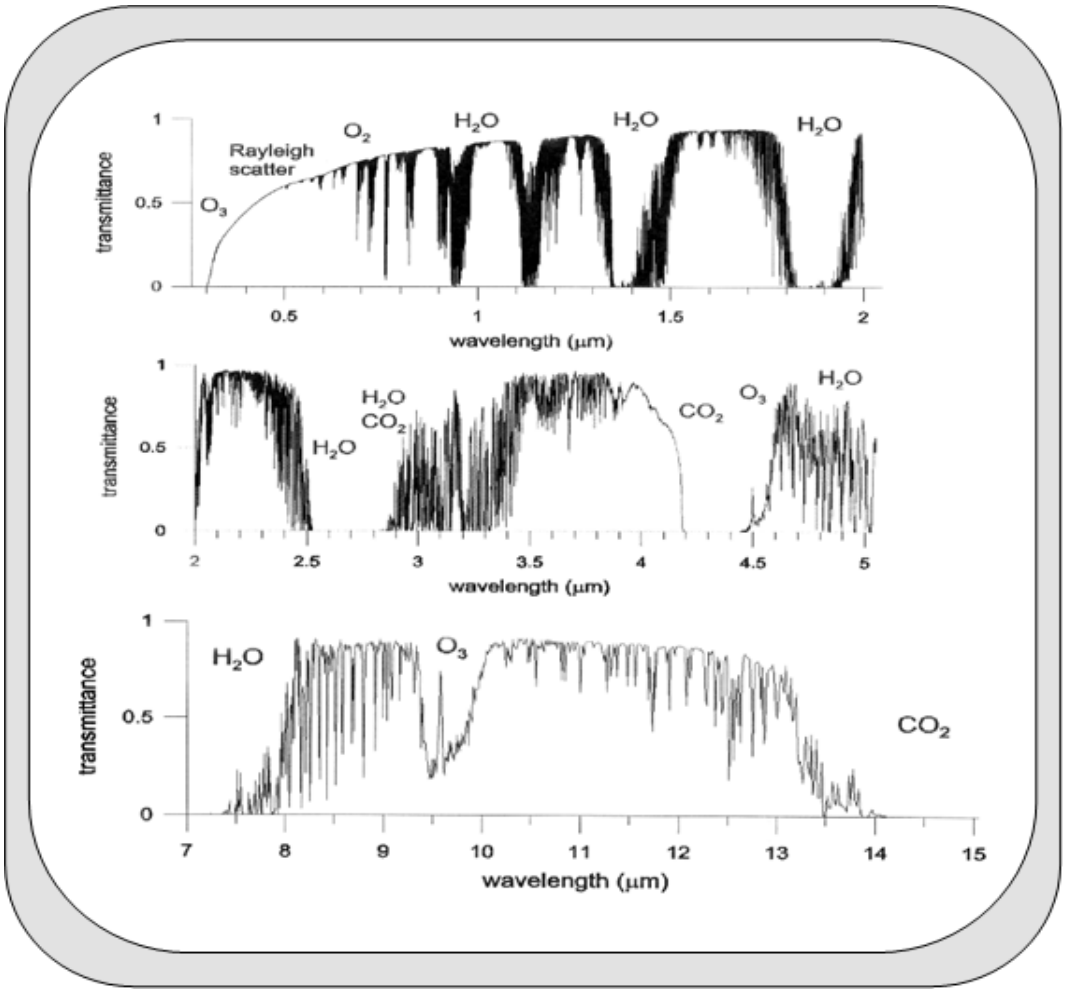

Figure 2.4: Atmospheric propagation spectrum up to 15 μm wavelength range [56]

depends on the chemical composition of the particle. Basically this refractive index is a combination of real and imaginary parts of the refractive index and so is a complex function. The real part of this refractive index contributes mainly towards attenuation due to scattering phenomena whereas the imaginary part mainly contributes towards attenuation due to absorption. The decrease in the power density of the transmitted optical beam due to absorption process is usually named as attenuation due to absorption and the wavelength at which most power of the propagated light beam is absorbed by a particular impurity in free-space is usually termed as the absorption peak. Looking from the free-space optical

wireless perspective we can categorize absorption phenomena into two regimes; molecular absorption and the aerosol absorption (details given in the following sections). Fig. 2.5 shows atmospheric transmissions spectra for optical wavelengths in the near-IR spectral range under clear weather conditions (e.g., visibility range $>$ 15 km), as the near-IR wavelength region (750 nm to 1550 nm) is the most commonly used optical wavelengths band for commercially available FSO systems. Upon comparing Fig. 2.4 and Fig. 2.5, in particular for near-IR wavelengths region, one can notice that there exists certain transmission windows for which the attenuations are $<$ 0.5 dB/km while the high transmission for these wavelengths are evident through the value of transmittance that easily exceeds a value of 0.8. Hence due to lesser absorbance by water particles for laser wavelengths in near-IR band, the optical attenuations are significantly reduced thereby increasing the transmittance of the signals that is exponentially related to the concentration of the aerosol particles and the path length. This suggests that these particular wavelength bands (within the 0.7 - 10 μm) can be exploited for use in FSO systems to avoid most of the losses due to absorption, especially for marine or relatively humid environments.

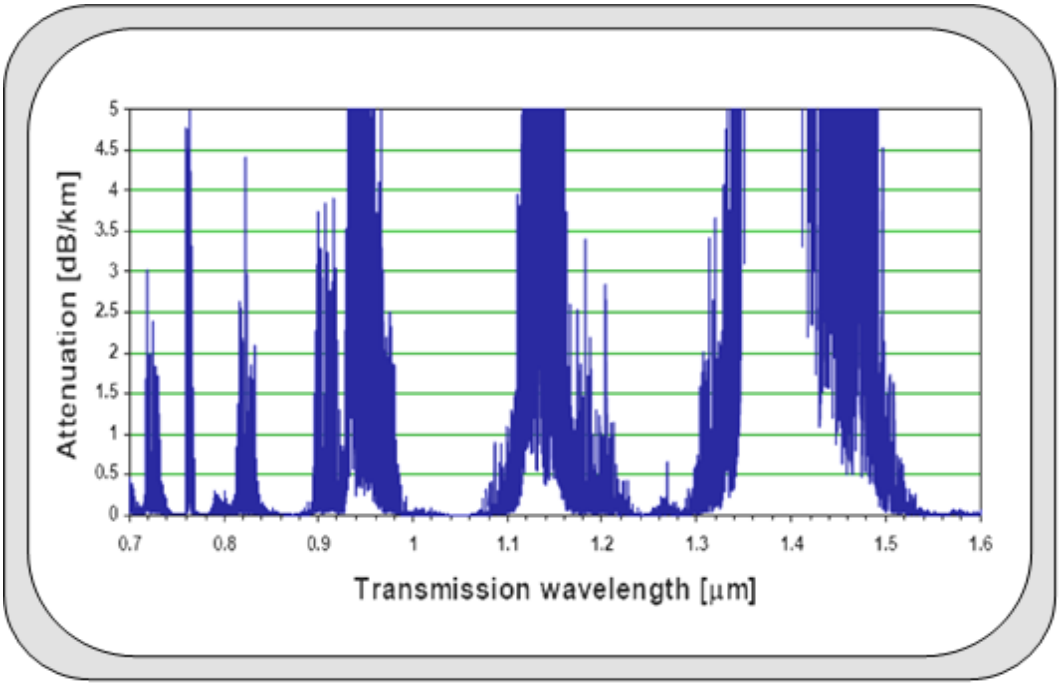

Figure 2.5: Typical Atmospheric transmissions spectra for clear weather conditions [6]

Molecular Absorption

Attenuation under clear-air conditions is mainly the attenuation due to the absorption by gaseous molecules. Atmospheric absorption at specific optical wavelengths results from the interaction between photons and atoms or molecules (N_2, O_2, H_2, H_2O, CO_2, O_2, etc,) which leads to the absorption of the incident photon and an elevation of the temperature. Although the Earth atmosphere is considered to be highly transparent for the near-infrared and visible wavelengths yet it can cause severe absorption at ultraviolet wavelengths (below 200 nm) due to O_2 and O_3 molecules and so can essentially block all optical transmission for wavelengths below 200 nm. The absorption in near-infrared wavelength region occurs primarily due to water vapors which are always present even in clear weather conditions. Whereas attenuation contribution of gas absorption e.g., CO_x and NO_x, is quite small as compared to the overall absorption caused by water molecules. But this is not the case for long-infrared wavelength range (> 2000 nm), where gas absorption (e.g., CO_x and NO_x) dominates the absorption properties of the Earth atmosphere.
Usually, for wavelengths normally available for use in FSO systems ($0.7 - 10$ μm), appropriate lasers can be selected in windows of transmittance that can avoid most of the losses due to absorption. Most of the typical commercial FSO systems operate in windows around 850 nm and 1550 nm because of the reason that reliable, inexpensive and high performance components are readily available on affordable prices as they are also extensively used in fiber optic communications. There also exist some more transmission windows in the transmission spectrum in the ranges between $3 - 5$ μm and $8 - 14$ μm, but at the moment the availability of components for these wavelengths is very limited and also are much expensive. There are a number of fundamental parameters that determine the absorption caused by the molecular resonance and are:

- Possible energy states for each molecular species
- The probability of transition from a lower energy level E_i to a higher energy level E_f
- The intensity of resonance lines
- The natural profile of each line

Following are the global transmission windows for the optical transmissions in free-space:

- From 0.4 to 1.4 μm for Visible and very near Infrared
- From 1.4 to 1.9 μm and 1.9 to 2.7 μm for Near Infrared
- From 2.7 to 4.3 μm and 4.5 to 5.2 μm for Mean Infrared
- From 8 to 14 μm for Far Infrared
- From 16 to 28 μm for Extreme Infrared

Generally, the profile of each absorption line is modified by the Doppler Effect when the molecules are moving with regard to the incident wave and by the collision effect due to the interaction of the molecules. These phenomena lead to a spectral widening of the natural line of each atmospheric molecule which can be explained in the form of the Voigt profile. Basically, the Voigt profile is a spectral line profile in which a spectral line is broadened by two types of mechanisms, one of which alone would produce a Gaussian profile usually as a result of the Doppler broadening, and the other would produce a Lorentzian profile. The general profile of the absorption line in the form of the Voigt profile is basically the convolution of both the Lorentzian (f_l) and the Doppler profiles (f_d) and is represented mathematically as below:

$$f_V = f_l \otimes f_d \tag{2.19}$$

The coefficient of molecular absorption α, for an isolated absorption line depends on the wave number $k(cm^{-}1)$, pressure P (mbar) and temperature T (K). The wave number k and wavelength λ (μm) are linked by the relationship:

$$k = \frac{2\pi * 10000}{\lambda} \tag{2.20}$$

The absorption coefficient is written as:

$$\alpha(\sigma, P, T) = S(T).f(\sigma, P, T) \tag{2.21}$$

where S(T) is the intensity of the absorption line at a temperature T and f (σ, P, T) is its global Voigt profile. The intensity of the absorption line is written as follows:

$$S(T) = S_0(\frac{T}{T_0})^{\xi} exp[\frac{-E}{K}(\frac{1}{T} - \frac{1}{T_0})] \tag{2.22}$$

Here, T_0 is the normal temperature i.e., 273.15 K, S_0 is the intensity of the line at T_0, E is the energy of low transition, ξ is a numerical constant whose value is 1 if the molecule is linear and K is the Boltzmann constant $1.3806568 \times 10^{-23}$ (JK^{-1}). Related to the absorption line profile, there are two cases dependent on the altitude:

- In the lower atmosphere: the widening of the line profile is then mainly due to collision process, in which case the line profile will take the form of Lorentz:

$$f_l(\sigma, P, T) = \frac{\delta\sigma_l}{\pi(\sigma - \sigma_0)^2 \delta{\sigma_l}^2} \tag{2.23}$$

  where σ_0 is the position of the absorption line and half-width at half height $\delta\sigma_l$ depends on the pressure and temperature and is written as follows:

$$\delta\sigma_l = \frac{P}{P_0}(\frac{T}{T0})^{0.5} \delta{\sigma_l}^0 \tag{2.24}$$

  here P_0 = 1013 mb and $\delta{\sigma_l}^0$ is the half-width at half height at P_0 and T_0.

- At the high altitude: the widening of the line is due to the Doppler effect. Its profile is given by the following relationship:

$$f_d(\sigma,T) = \frac{1}{\sqrt{\pi}\delta\sigma_d} exp[-(\frac{\sigma-\sigma_0}{\delta\sigma_d})^2] \tag{2.25}$$

with

$$\delta\sigma_d = \frac{\sigma_0}{c}(\frac{2KT}{m})^{0.5} = 3.58\times10^{-7}\sigma_0\sqrt{\frac{T}{M}} \tag{2.26}$$

where c is the speed of light, M the molar mass and m is the mass per molecule.

Aerosol Absorption

Aerosols are atmospheric particles like dust, organic material, pollutants, ice, water droplets etc. They are frequently found in the atmosphere in variable sizes from sub-micrometer to a few tens of micrometers and these aerosols also vary in shapes from spherical to irregular geometries. In the terrestrial atmosphere they differ in distribution, components, and profile concentration; and consequently impact the propagating laser beams in free-space in different ways. For example, in maritime environment, the aerosols are primarily made up of droplets of water (foam, fog, drizzle, rain), of salt crystals and various particles of continental origin. Type and density of continental particles depend on distance and characteristics of the neighboring coasts. From Mie scattering theory, the aerosol absorption coefficient is given by:

$$\alpha_a(\lambda) = 10^5 \int_0^\infty Q_a(\frac{2(\pi)r}{\lambda}, n'')(\pi)r^2 n(r)dr \tag{2.27}$$

with n'' representing the imaginary part of the refractive index of the aerosol particles, and Q_a the Mie normalized absorption cross section. Mie theory allows to determine the electromagnetic field absorbed by homogeneous spherical particles and to evaluate absorption Q_a cross sections dependent on the particles size, imaginary part of the complex refractive index and on the incident radiation wavelength.

2.3.2 Scattering

In the context of free-space optical beam propagation, scattering is defined as the dispersal of a beam of light particles into a range of directions as a result of its physical interactions with the atmospheric particles. When an atmospheric particle intercepts an electromagnetic wave, part of the wave energy is removed by the particle and re-radiated into a solid angle centered at it. The re-radiation or scattering behavior depends on the characteristics of the particle like size of the particle in relation to the incident wavelength, its complex

index of refraction (especially its real part), and its isotropy (the property of molecules and materials of having identical physical characteristics in all directions). If all these above mentioned parameters are known, the scattering pattern of the particle can be predicted with sufficient accuracy.
The size of the atmospheric particle defines the type of symmetry of the scattered energy with reference to the direction of propagation of the incident light beam. We can further subdivide the scattering process into three distinct scattering regimes, as discussed below, on the basis of the size of particle and its interaction with the incident radiation. If the size of the particle is equal (comparable) to the wavelength of the incident light ($\lambda/10 \leq r \leq 10\lambda$), the scattering by the particle presents a large forward lobe and small side lobes that start to appear and this type of scattering is called Mie scattering. As the size of the particle becomes smaller, the backward lobe becomes larger and the side lobes disappear. When the size of the particle is approximately 10 percent the size of the wavelength of the incident beam ($r < \lambda/10$), the backward lobe is symmetrical with the forward lobe. This type of scattering is termed as Rayleigh scattering. The third type of scattering is referred as Geometrical scattering and occurs if the size of the particle is 10 times greater than the incident wavelength ($r > 10\lambda$). In this type of scattering some very complex and irregular shape scattering patterns are formed as a result of incident wavelength and atmospheric particle interaction. In general, forward scattering becomes more significant when particle sizes exceed the incident wavelength. Fig. 2.6 shows illustration of the re-distribution of radiation once a particle is hit by an electromagnetic wave. It is

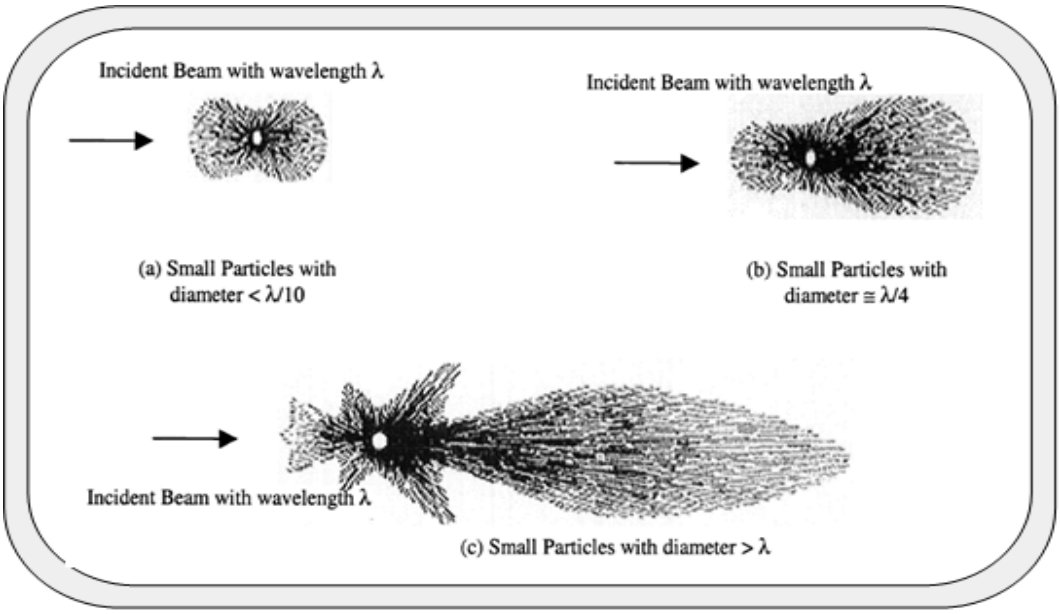

Figure 2.6: Illustration of scattering patterns for three different scattering regimes [37]

interesting to note that most of the light that reaches our eyes comes indirectly by means of scattering process. Fine atmospheric particles standing in the path of free-space optical beams abstract energy from the incident wave and re-radiate it in different directions. The received power at a distance d from the transmitter is given by the Beer-Lambert law and the total transmittance Equation (2.17) can be re-written as,

$$T_r(\lambda,d) = \frac{P(\lambda,d)}{P(\lambda,0)} = e^{-\gamma(\lambda)d} \tag{2.28}$$

In this equation, $\gamma(\lambda)$ is the attenuation of the total extinction coefficient per unit of length. This parameter is dependent on the transmission wavelength and the density of the atmospheric constituents along the line of sight. From above equation, the loss L in dB that an optical beam experiences is given by [30],

$$L = -10Log_{10}T_r \tag{2.29}$$

Generally, $\gamma(\lambda)$ is given by,

$$\gamma(\lambda) = \alpha_m(\lambda) + \alpha_a(\lambda) + \beta_m(\lambda) + \beta_a(\lambda) \tag{2.30}$$

where $\alpha_{m,a}(\lambda)$ are molecular and aerosol absorption coefficients and $\beta_{m,a}(\lambda)$ are molecular and aerosol scattering coefficients respectively.

Rayleigh Scattering

Rayleigh scattering refers to scattering by molecular and atmospheric gases of sizes much less than the incident wavelength. It varies as the fourth power of the incident wavelength with overall constant dependent on the index of refraction. The scattering by the atmospheric gas molecules (Rayleigh scatter) contributes to the total attenuation of the electromagnetic radiation. The expression for the molecular scattering coefficient $\beta_m(\lambda)$ is given by:

$$\beta_m(\lambda) = 10^3 \frac{24\pi^3}{\rho\lambda^4}\left[\frac{n'(\nu)^2-1}{n'(\nu)^2+2}\right]^2\left[\frac{6+3\sigma}{6-7\sigma}\right] \tag{2.31}$$

where σ is the depolarization factor of air ($\sigma \cong 0.03$), ρ is the polarization density of the molecules (mol.$cm^{-}3$), and $n'(\nu)$ is the real part of the refractive index of air having frequency ν. The molecular composition of the atmosphere allows to obtain an approximate value of $\beta_m(\lambda)$,

$$\beta_m(\lambda) = \frac{A}{\lambda^4} \tag{2.32}$$

where

$$A(km^{-1}\,\mu m^4) = 1.09 \times 10^{-3}\left(\frac{PT_0}{TP_0}\right) \tag{2.33}$$

Here P(mbar) is the atmospheric pressure and $P_0 = 1013$ mbar, and T(K) is the atmospheric temperature and $T_0 = 273.15$ K. As an example, for a wavelength $\lambda = 8\mu m$, atmospheric pressure $P = 1013$ mbar and temperature of $T = 300K$, the value of molecular scattering coefficient $\beta_m(\lambda) \approx 2.47 \times 10^{-7}(km^{-1})$. Under the same atmospheric conditions for a wavelength of $\lambda = 550nm$, the value of molecular scattering coefficient becomes $\beta_m(\lambda) \approx 10^{-3}(km^{-1})$. It can be inferred that the molecular scattering is negligible for infrared wavelengths and the Rayleigh scattering is relevant primarily for the ultraviolet to the visible region of the electromagnetic spectrum.

Mie Scattering

The determination of the properties and optical characteristics of atmospheric aerosols as well as clouds and fog requires a good understanding of the interaction of light with particles. The theory of electromagnetism (arrived at its maturity in the late 19^th century) provides a standard treatment for simple cases, namely the interaction of spherical, homogeneous and isotropic light particle with the propagating light beam. This specific case was treated by Gustav Mie [62]. It should be noted that scattering and absorption are dynamic, local phenomena and tend to vary widely from location to location in severity.
Scattering caused by relatively larger size particles of fog, rain, snow and clouds etc., is classified as Mie scattering. Mie theory best describes the scattering phenomena by aerosol particles of sizes comparable to the incident wavelength. For practical purposes, optical losses due to Rayleigh scattering are considered almost negligible when compared to losses due to Mie scattering in the wavelength range 0.5 μm to 2 μm. Generally, according to the Mie theory, the aerosols scattering coefficient depends on the particle concentration, size distribution, cross-section, and incident radiation wavelength. Basically, Mie theory is an analytical approach to describe the propagation of light in the scattering medium by combining processes of scattering and absorption variations. The calculated parameters such as scattering cross sections and absorption can characterize the properties of scattering and absorption of the medium for a given wavelength.
In the treatment of Mie scattering we assume that the frequencies of incident radiation are identical and distributed. All effects involving transitions by quantum scattering centers will not be considered. We also assume that particles are independent. This assumption means that the scattering centers are not positioned on a structure or a specific order which prevents the systematic phase shifts give rise to interference phenomena. In clouds, fog and rain, we usually assume that the particles are distributed randomly in the volume studied, or, in other word, there is no phase consistency between the fields absorbed or scattered by individual particles. Furthermore, the concentration of droplets is generally low enough that we can consider that particles are not coupled together. Finally, we assume that the scattering caused by N particles is just N times l larger than the scattering caused by single particle. The interaction of electromagnetic radiation with an absorbing sphere whose size

is greater or equal to the wavelength is well described by Mie theory, which was particularly well presented in several references in the literature [56, 62, 63]. We employ the Maxwell's equations and the principle of energy conservation to determine the effective scattering cross section, absorption and extinction and the scattering efficiency, absorption and extinction as a function of the wavelength of the radiation, the particle size and its complex refractive index. For example, consider the free-space optical transmissions through fog. All the fog particles actually consist of an accumulation of water spheres with a particular drop size distribution, the effect of the individual drop must be summed over a unit volume keeping in mind the assumptions already mentioned above. Then, from Mie theory the aerosol scattering co-efficient $\beta_a(\lambda)$ is given by:

$$\beta_a(\lambda) = 10^5 \int_0^\infty Q_{Ext}(\frac{2(\pi)r}{\lambda}, n')(\pi)r^2 C(r)dr\ [km^{-1}] \tag{2.34}$$

where n' is the real part of the refractive index of the fog particles, λ is the incident wavelength in μm, r is the radius of fog particle in cm. The scattering efficiency Q_{Ext} is defined as the scattering cross-section normalized by the particle cross-sectional area, and $C(r)$ is the particle size distribution which usually is the Modified Gamma distributions. Fig. 2.7 shows a simulation of scattering efficiency of water particles as a function of fog particle radius against 950 nm optical transmissions.

However, to simply describe the action of aerosol in the atmosphere for the free-space

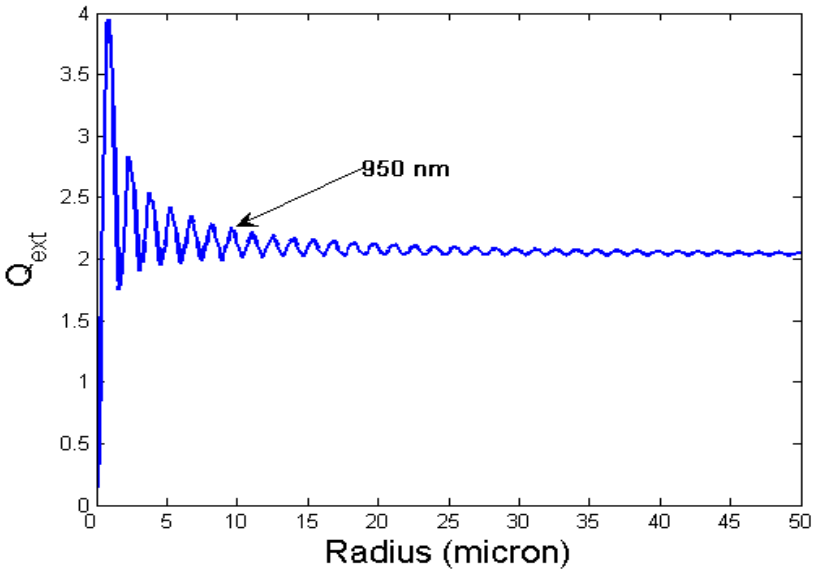

Figure 2.7: Simulated scattering efficiency Q_{Ext} of water particles

optical communication, it is convenient to use the following practical relationships commonly used to describe the scattering coefficient $\beta_a(\lambda)$, in horizontal path with constant

aerosol concentration:

$$\beta_a(\lambda) = C_1 \lambda^{-\delta} \; [km^{-1}] \tag{2.35}$$

where C1 and δ are constants that depend upon the aerosol characteristics like density, particle size distribution and λ is the wavelength of interest in μm. The constant δ is related to the atmospheric visibility range (see Section 2.4.2) and varies from 1.0 to 1.6 (from poor visibility to clear line-of-sight). The constant C1 is related to the visual (or meteorological) range V (in kilometers) as:

$$C_1 = \frac{3.91}{V}(0.55)^{\delta} \; [km^{-1}] \tag{2.36}$$

Since the Earth atmosphere has maximum transmission at 0.55 μm wavelength, therefore visual range is measured at this wavelength. The scattering coefficient $\beta_a(\lambda)$ then becomes:

$$\beta_a(\lambda) = \frac{3.91}{V}(\frac{\lambda}{0.55})^{-\delta} \; [km^{-1}] \tag{2.37}$$

Geometrical Scattering

Geometrical or Non-selective scattering applies to particle sized larger than the incident wavelength. In this case, Mie theory is approximated by the principles of reflection, refraction and diffraction. The name non-selective refers to the fact that scattering is independent of wavelength. Geometrical or non-selective scattering occurs in snow, hail, rain and cloud droplets, where the size of the particles is much higher than the incident light wavelength. Table 2.1 below summarizes scattering processes for typical atmospheric particles with their radii λ = 850 nm.

Type	**Radius(μm)**	**Size parameter (X_0)**	**Scattering process**
Air Molecules	0.0001	0.00074	Rayleigh
Haze particle	0.01 - 1	0.074 - 7.4	Rayleigh - Mie
Fog droplet	1 - 20	7.4 - 147.8	Mie - Geometrical
Rain	100 - 10000	740 - 74000	Geometrical
Snow	1000 - 5000	7400 - 37000	Geometrical
Hail	5000 - 50000	37000 - 370000	Geometrical

Table 2.1: Scattering processes for most common atmospheric effects at λ = 850 nm

2.3.3 Extinction

Absorption and scattering processes are mainly responsible to the loss and redirection of the energy of an optical beam when intercepted by suspended particles in the atmosphere.

Their combined effect is termed as extinction. Actually, absorption and scattering take out the energy from the forward propagating beam direction. Extinction process is a linear effect in both intensity of optical radiation and in the amount of atmospheric matter, provided the physical conditions like temperature, pressure, composition etc., is held constant [2]. Equation (2.30) represents the mathematical formula to calculate the combined losses due to absorption and scattering processes. The optical thickness of a medium between two points h_1 and h_2 is defined as:

$$\tau_0(h_1,h_2) = \int_{h_2}^{h_1} \gamma_{ext,\nu}(\rho)d\rho \tag{2.38}$$

here ν is the frequency of the given optical beam and ρ defines the density (path-integrated distribution) of atmospheric constituents along the line of sight. By knowing the optical thickness τ_0 and the optical beam initial intensity I_0, the resultant reduction in the intensity of optical beam after propagation between two points h_1 and h_2 is given by:

$$I_\nu = I_0 e^{-\tau_0} \tag{2.39}$$

2.3.4 Atmospheric Turbulence or Scintillation Losses

The atmospheric temperature at a given location is never constant, it fluctuates both in the temporal and spatial domains. This may cause deterioration in the quality of the received signal. Fluctuations in the intensity and phase of the received signal may lead to increased link error probability, particularly in link ranges of the order of the 1 km or over. The fluctuation is a function of the atmospheric wind speed and the atmospheric pressure. This small variation (0.01 to 0.1 degrees) in the air temperature brings with it, a spatial and temporal variation in the refractive index of the atmospheric optical channel. The channel thus behaves like a pathway filled with optical prisms whose sizes and refractive indices are constantly changing. The implication of this is that, the received signal irradiance/power fades in sympathy with the fluctuation of the temperature along the propagation path. Fig. 2.8 shows an illustration of the effect of atmospheric turbulence on the free-space optical beam. The modeling of this irradiance fluctuation has received considerable attention in literature with a number of models now in place to describe this phenomenon across different regimes [16]. Lognormal distribution has been widely used to model the probability density function (PDF) of the irradiance and to study performance of coded free-space optical links [65, 66] over the turbulent channel. A Lognormal channel model due to its simplicity can only be applicable in weak turbulence conditions. Many statistical models like the K distribution, I-K distribution, and Log-normal Rician channel have been proposed to describe atmospheric turbulence channels [67, 68]. Recently modified Rytov theory has been used to propose a Gamma-Gamma PDF as a tractable mathematical model for atmospheric turbulence [69, 70].

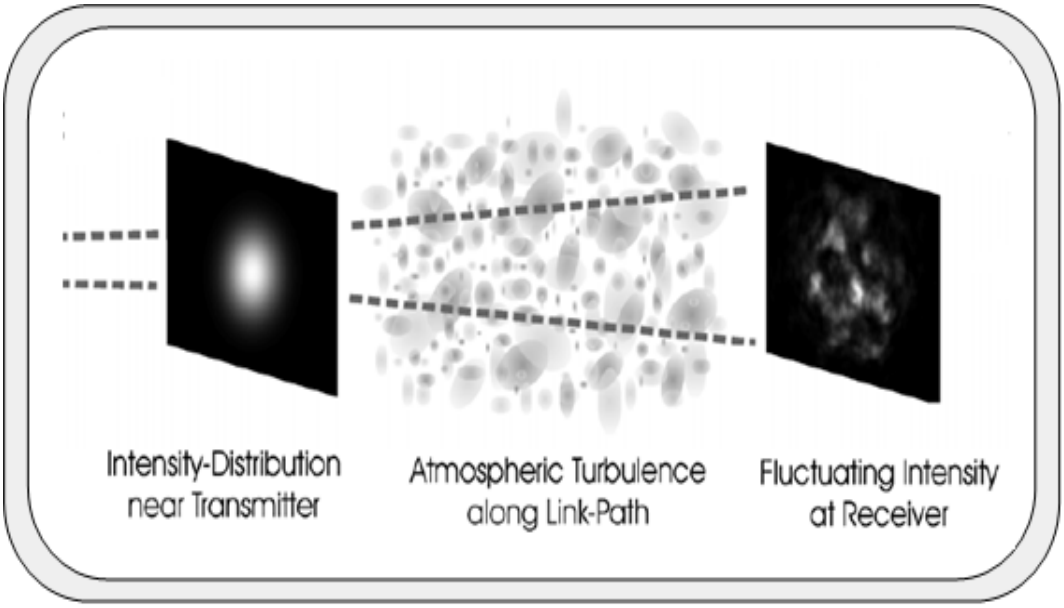

Figure 2.8: Illustrating the atmospheric turbulence effect [64]

Physical Description of Scintillation Effect

Minute fluctuations of refractive index along the optical channel path due to random thermal inhomogeneities induced by atmospheric turbulence result in the reduction of beam intensity. The solar energy (turbulence energy) affects major portions of the air cells (eddies), through unequal heating of different parts of the underlying surface, in the atmosphere of minimum size L_o called the outer scale. Since bigger air cells are usually unstable so they disintegrate and their energy is transferred adiabatically to the smaller air cells. The fragmentation process continues until the size of air cell reaches a critical minimum value called the inner scale l_o and it marks the air cell size at which the drag force becomes larger than the inertial forces. Thereafter, the air cell's energy gets destroyed via viscous dissipation, and the air cells lose their identities. Fig. 2.9 gives an illustration of the deviation of the optical beam under the influence of turbulent cells.

The strength of the optical turbulence has traditionally been measured by the Rytov variance σ_1^2 defined by,

$$\sigma_1^2 = 1.23 C_n^2 k^{\frac{7}{6}} L^{\frac{11}{6}} \tag{2.40}$$

where C_n^2 is the refractive index structure parameter, k is the wave number and L the propagation distance. Some researchers consider the worst case scenario and use the coefficient value of 23.17 in the above equation. The constant of refractive index structure C_n^2 is basically a measure of the fluctuations in the refractive index, and is very sensitive to even small scale temperature variations. C_n^2 typically range from $10^{-17} m^{-\frac{2}{3}}$ to $10^{-13} m^{-\frac{2}{3}}$ from weak turbulence to strong turbulence conditions, respectively. Fig.2.10 shows the simu-

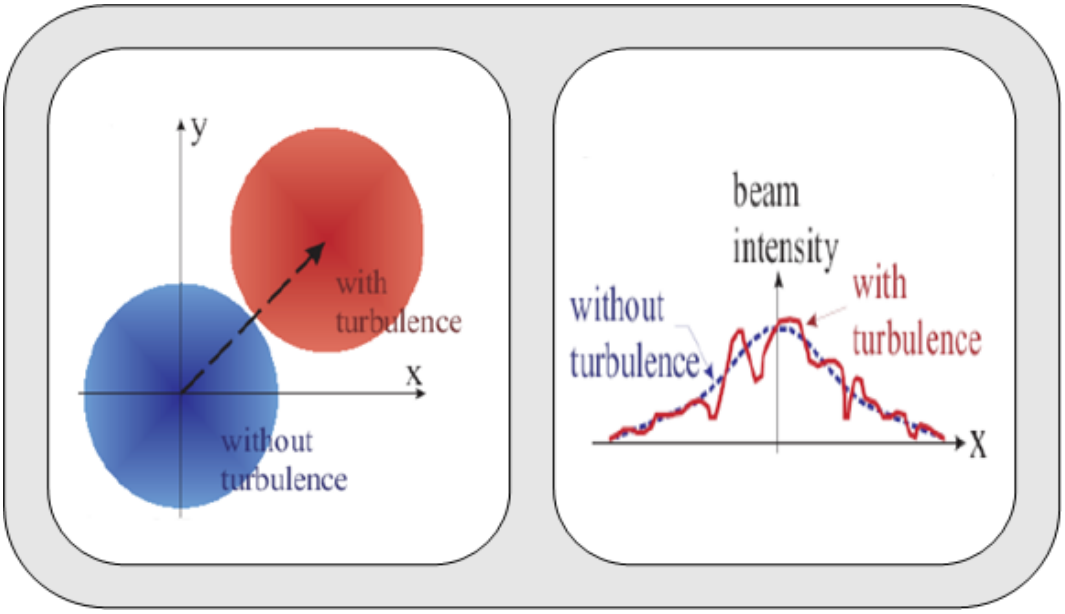

Figure 2.9: Optical beam deviation under influence of turbulence cells [71]

lation of variation in attenuation for different strengths of the refractive index parameter.

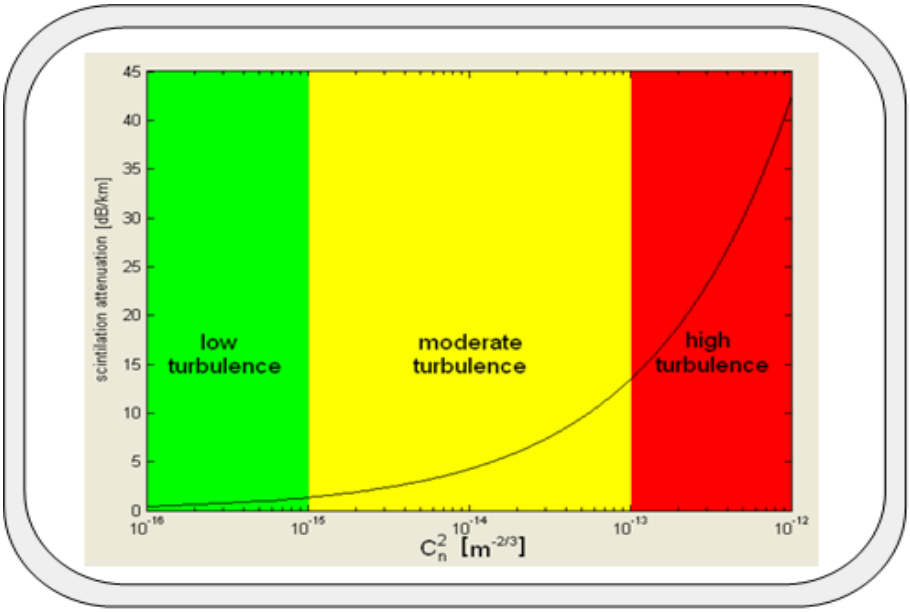

Figure 2.10: Scintillation attenuation based on C_n^2 [72]

Time Scale Description of Scintillation Effect

Generally, when an optical beam is transmitted in free-space, random fluctuations (scintillations) occur in the intensity of the optical beam. These scintillations result in Slow fading (e.g., if the coherence time is on order of 10 ms while bit period is on order of 1 ns) of the optical signal. The length and the depth of the resultant fades have to be estimated in order to overcome the detrimental behavior of scintillations. The coherence length of these fluctuations ranges from few milliseconds to tens of milliseconds, justifying a frozen atmospheric model for high-speed communications. Usually, the fading time is much longer than one bit duration and the data signal is affected by very slow fading [23, 48]. A slow-fading condition may be considered and in the event of weak turbulence, the intensity of the optical field can be modeled with Log-normal distribution. Leitgeb et. al determined a scintillation fade of 4 dB attenuation depth with 20 ms of fade length [73]. Zhu et. al proposed a detection scheme for free-space optical wireless systems [65]. In this scheme the correlation length of intensity fluctuations, d_0 is assumed greater than the receiver aperture D_0, and the receiver observation interval T_0 during each bit interval is considered less than the turbulence correlation time t_0.
In a recent article [74], Shannon capacities for the free-space optical link have been presented using an accurate scintillation model based on Gamma-Gamma probability distribution model to predict the intensity fluctuations of the optical signal. This statistical representation not only fits the channel scintillation accurately, but its parameters can be related to the physical conditions of turbulence proposed by [67]. While [75] states "the outcome of propagation through the medium may be modeled as the sum of many independent complex optical fields, leading to a complex Gaussian field at the receiver" and considers a frozen atmospheric model, with coherence length of turbulence induced intensity fluctuations in the range of few to tens of milliseconds.

2.3.5 Beam Spreading and Beam Wandering

Random fluctuations in the refractive index of the Earth atmosphere are causing random changes in the signal-carrying laser beam intensity (irradiance) called scintillations. Scattering caused by atmospheric turbulence leads to the spread and increase in the radius of a finite optical beam such that the beam spreading is beyond the spreading predicted by diffraction and a continuous random motion of the beam centroid about the receiver. These both effects are illustrated in Figure (2.11). These both effect causes a decrease in the mean intensity of the beam at the receiver and could result in the random signal loss of signal at the receiver and result in increased system bit error rate due to signal fading [2, 76]. We can determine the beam spot radius using the small angle approximation e.g., Table 2.2 shows spot diameter values for different values of beam divergence for a link distance of 1

km. The spot size value can be measured by the following relationship:

$$SpotSize(m) = Angle(milliradians) \times Range(km) \tag{2.41}$$

Two types of beam spread can actually be defined, one being the short-term beam spread

Divergence	Range	Beam Diameter
0.5 mrad	1.0 km	$\sim$ 20.0 inches ($\sim$ 0.5 m)
1.0 mrad	1.0 km	$\sim$ 39.37 inches ($\sim$ 1.0 m)
2.0 mrad	1.0 km	$\sim$ 6.5 feet ($\sim$ 2.0 m)
4.0 mrad ($\sim \frac{1}{4}$ degree)	1.0 km	$\sim$ 13.0 feet ($\sim$ 4.0 m)

Table 2.2: Effect of beam divergence on beam spot size [24]

and the other type is the long-term beam spread, whether one considers the beam spot at a given instant of time or the average of all its positions taken over a longer time period. Beam spreading, long-term and short-term, is actually the spread of an optical beam as it propagates through the atmosphere. Therefore, in this context we consider short-term

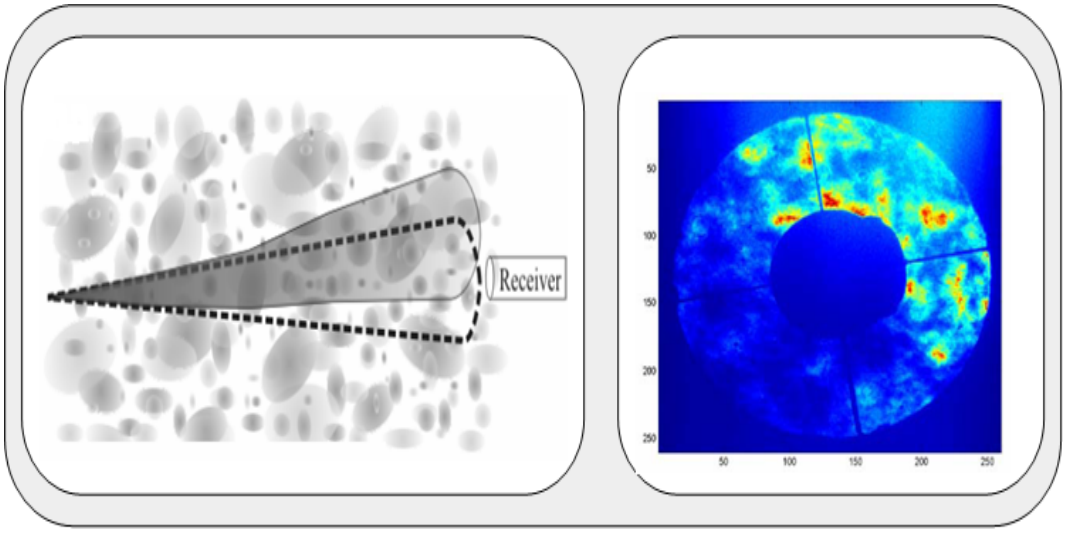

Figure 2.11: Illustrating effect of beam wandering and beam spreading [77]

beam radius and long-term beam radius, the latter being always larger. If we consider W to be the radius of the unperturbed beam, W_{ST} the radius of the short-term beam and W_{LT} radius of the long-term beam or effective radius then:

$$W \leq W_{ST} \leq W_{LT} \tag{2.42}$$

The long-term beam is described by the effective beam radius W_{LT}, which is given by:

$$W_{LT} = W^2[1 + 1.625(\sigma_R^2)^{6/5}\Lambda] \tag{2.43}$$

where σ_R^2 is the optical beam intensity variance. Knowing the long-term beam radius W_{LT} and the mean square of the short-term beam centroid radius $\langle r_C^2 \rangle$, short-term beam radius can be:

$$W_{ST} = [W_{LT}^2 - \langle r_C^2 \rangle] \tag{2.44}$$

here r_C is the deviation of the short-term beam centroid from the optical axis. Whereas, mean square of the short-term radius is given by:

$$\langle r_C^2 \rangle = 2.87 C_n^2 L^3 W_0^{-1/3} \tag{2.45}$$

so Equation 2.44 becomes

$$W_{LT} = W^2[1 + 1.625(\sigma_R^2)^{6/5}\Lambda - 2.87 C_n^2 L^3 W_0^{-1/3}] \tag{2.46}$$

Beam wander arises when small turbulent whirl bigger than the beam diameter cause slow, but large displacements of the transmitted beam. The main factor responsible for beam wander is refracting large-scale turbulence. Beam wander can be predicted using geometrical optics approximation. It is observed that narrow beams are likely to suffer more from turbulence-induced deviation and this effect can be reduced by controlling the transmitter beam radius W_0 i.e., the radius of the collimated beam at the transmitter. Equation 2.45 is derived from the Rytov theory and is based on phase-front statistics whose validity can be extended even to the strong-fluctuations regime.

2.3.6 Background Radiation

The main source of background radiations affecting the optical beams at the receivers end are Sun, Moon, planets (including Earth), scattering atmosphere. In certain situations, background radiations can significantly degrade the performance of free-space optical links, like for example, if the maximum background power exceeds the information signal power thereby disrupting the normal operation of the photo-detectors. The background radiations arrive at the optical receiver after being scattered in many ways in the free-space atmospheric channel due to the following effects [78]:

- Specular reflections
- Scattering due to hydrometeors
- Scattering from solid objects
- Scattering by the receiver elements of the optical system

Specular reflections illuminate the receiver by highly collimated sunlight through reflections from flat surfaces like polished surfaces, window panes etc. Usually this kind of reflections are of short duration and are dependent on the distance and the size of the reflecting surface and its reflectivity at the operating wavelength of the receiver. Scattering

due to hydrometeors like fog, snow, rain and clouds etc., results in a very narrow main power lobe in the direction of radiation propagation and this may cause severe damage if the Sun-receiver-transmitter angle is also small. Such scattering situations may arise if the sunlight scattering aerosol is either over the communication path but the path itself is relatively clear or if the sunlight scattering aerosol is also within the communication path. The third kind of situation arises if the Sun illuminated solid object having diffusely reflecting surfaces lie within the receiver field of view. But this kind of background effect of radiations cannot affect the link availability appreciably. In the fourth kind of situation, the scattered radiation power density can be estimated from the experimental data and with a properly designed receive optical system the effects can be ignored.

2.3.7 Solar Influence

Free space optical links for high speed communications must take into account the link degradation environmental effects that results in interference of light beams coming from sun in the optical receiver instantaneous field of view and hence can cause link disruptions, even with significant optical filtering. The effect of solar influences can be divided further into two parts, namely solar background effect and direct sunlight effect. Figure (2.12) represents a typical solar radiation spectrum. It is clearly observable from that the spectrum of the solar radiation is close to that of a black body with a temperature of about 5800 K. About half of the spectrum lies in the visible short-wave part, while the other half mostly in the near-infrared part of the electromagnetic spectrum and some part also lies in the ultraviolet region of the spectrum.

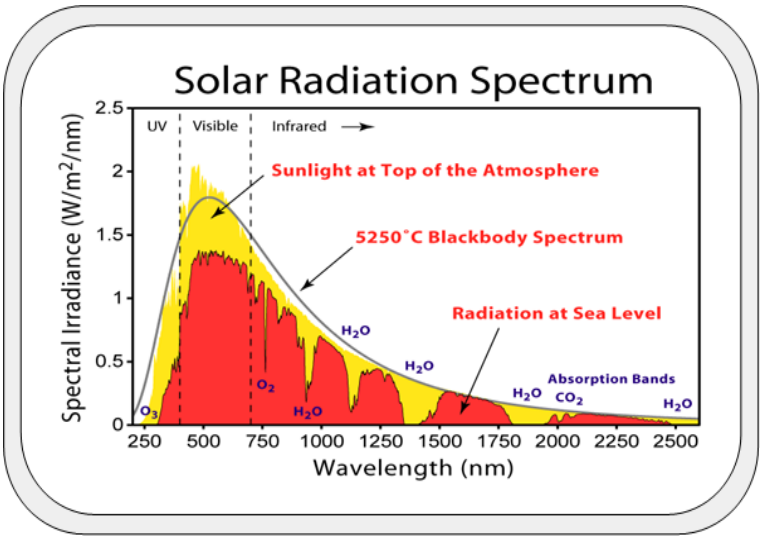

Figure 2.12: Solar radiation spectrum [79]

Solar Background Effect

In practice, the sunlight reflections in the background can cause high amounts of signal attenuation, if we consider uniform scattering in the atmospheric channel. Sun is a region-radiator and the scattering of sunlight can cause reduction in the optical signal power at the receiver. The following formula is considered in order to calculate the solar background power [78]:

$$P_B = B * S_R * \eta_R * \Omega_R * \Delta B_w \tag{2.47}$$

where P_B is the background power (W), B the brightness (lx), S_R the effective area (m^2), η_R the transmittance, Ω_R the receiver field of view (sr) and ΔB_w is the bandwidth of the receiver (nm).

Direct Sunlight

Direct sunlight has much detrimental influence on the FSO system performance. In extreme cases can even cause total link outage and thus considerably affect the FSO link availability. It is seen through experiments that direct sunlight does not cause irreversible degradation of receiver sensors used in the FSO systems. In the simulation, this is effect is mitigated by introducing a user defined parameter dependent on the precisely defined exact geographical position given in degrees of latitude as well as the orientation of the FSO unit with reference to its elevation. The sun is assumed to be located at infinitely far away distance, so an FSO unit cannot come closer to the sun, it just may change its direction. The distance between the transmit and receive units is well known and constant (user-defined) so the calculations are based on this parameter. Additionally the earth surface is assumed to be plane because of the proportionally short length of FSO communications paths. The elevation of the sun across the earth surface and the azimuth can be calculated by the use of astronomical formulas such as [80]:

$$\sin(\theta) = \sin\delta \sin\varphi + \cos\delta \cos\varphi \cos(t) \tag{2.48}$$

where θ is the elevation of the sun, δ declination of the sun and φ geographical latitude, all in degrees. t is the hour angle, calculated as:

$$t = 15 * (12 - h)$$

where h is the local time at moment of consideration.

2.4 Optical Wireless Channel Models

The ability to communicate between any two nodes using electromagnetic wave propagation in a physical medium is highly dependent on the transmission properties of that

environment. How far a transmit signal will reach before it eventually becomes too weak for the detector to sense its received power is directly a function of the propagation environment and the nature of the signal. Modeling the propagation environment properties are essential to being able to design reliable communication systems with adequate transmitting and receiving apparatus that fulfills the service objectives of the service operators. Characterization of the different kinds of fog and corresponding attenuations with respect to different environments, in a way, that better communication systems can be designed which counteract these attenuations more efficiently is of prime significance. Earlier research emphasized on the time domain characterization of fog attenuation, however, still there is a need of extensive elaborations, and there is a little in the form of documentation, recommendations and standards to estimate availability, reliability and quality of service of terrestrial FSO links. Below is a brief summary of some approaches that were considered in the past to model the free-space optical channel to simulate or predict the optical attenuations.

2.4.1 Deterministic Models

Due to rapid advances in computing capabilities, ray tracing techniques have become one of the most popular methods for characterizing propagation in complicated environments. These techniques were initially attractive because of their extremely accurate path loss predictions in dense urban areas, undulating terrains, and maze-like indoor environments. In order to mitigate the detrimental behavior of different weather conditions various approaches were considered to model the free-space channel attenuation effects. One such strategy is the deterministic models for the optical wireless links. Examples are deterministic model based on Mie scattering that requires microphysical information about a certain weather effect. The second type model is based on Ray tracing technique requiring a very complex trigonometric and geometric techniques. In short, although deterministic models offer excellent accuracy and are able to provide additional parameters such as small-scale fading or delay spread but the main disadvantage of such models is sometimes prohibitively large computation time.

Mie Scattering Based Model

The problem of light scattering by a particle, in some cases can be solved analytically. The exact solution to scattering of light by an isotropic and a homogeneous spherical particle was initially given by Gustav Mie in 1908. Besides the fact that this theory is analytical, it allows us to describe, among other things, all hydrometeors and the different types of aerosols present in the atmosphere as spherical particles.
To apply Mie scattering theory, we assume that aerosol particles are spherical in shape and are suspended in space while acting independently with a complex refractive index

[63]. To calculate the expected signal attenuation over an atmospheric path, the fact that in actual all the particles are not spherical in shape does not seem to have a large impact on the accuracy of the results calculated using Mie scattering theory [62]. The detailed description about Mie scattering based attenuation prediction technique is already described under Mie Scattering section above.

Ray Tracing Based Model

Deterministic propagation models for optical wireless links generally rely on ray-tracing (a high frequency approximation method) techniques. Its not a single cohesive mathematical technique but a collection of methods that rely on geometric optics, the uniform theory of diffraction and other scattering mechanisms which can predict electromagnetic scattering from objects in the propagation environment. The concept of using ray tracing modeling technique can be found in [81, 82].
The notion of this technique is to describe optical beam propagation by different rays that travel from the transmitting node to the receiving node and are subject to reflection, scattering and diffraction as they interact with the objects in the propagation environments. Since a ray tracing model tracks ray trajectories, it not only provides site-specific time dispersion information but it is possible to predict root mean square (RMS) delay spread, power delay profiles, angles-of-arrival, realistic mobile fading, and virtually any other channel parameter. The computations are performed with help of the universal theory of diffraction (UTD). In order to evaluate the accuracy of a ray tracing prediction, there are three main areas of error to consider:

- propagation modeling errors
- kinematic errors
- database errors

Propagation modeling errors arise from the geometrical optics models considered to describe optical beam behavior. Kinematic errors (or path finding errors) are determined by the ability of a ray tracing algorithm to find accurate radiation paths and this is the most time-consuming part of a field-prediction. For this purpose either the ray tracing or the ray launching algorithm is used. The database errors stem from the limitations of a numerical description of the channel. The biggest drawback of this technique is, however, large computation time and the fact that it is not accurate everywhere as it does not provide a complete and accurate calculation of the electromagnetic field at all locations in the propagation environment.

2.4.2 Empirical Models

Empirical models are based on observations or measurement of signal performance in real propagation environments. Such models use predictors or specifiers that have been found through statistical analysis and are correlated with the quantity to be predicted. The weakness of many empirical models that have been put forth so far lies in the lack of proper statistical significance testing in the propagation measurement analysis. The accuracy and usefulness of empirical models is highly dependent on the propagation environment in which original data for the model was gathered and on its universal applicability. These models fundamentally use the experimentally measured data to infer a relationship between the propagation circumstances and the expected signal power levels. Since they use statistical specifiers that are inherently non-causal, non site-specific, have no direct relationship with the quantity being measured and do not take into account the unique features of a given propagation environment. Examples of empirical models, from the perspective of terrestrial FSO links, are attenuation predictions based on visibility range, wavelength dependent attenuation model and optical depth dependent models etc. The biggest advantage of empirical channel models is that they are very easy to use and do not usually require complex computations about a certain effect.

Visibility Range Dependent Models

Visibility is defined as being the distance to an object at which the image contrast drops to a certain percentage of the original contrast of the object, equivalent to a certain transmission threshold τ_{TH} over the atmospheric path. Unfortunately, two definitions for this threshold exist, 2% and 5%. Nowadays, 5% transmission threshold is more commonly used for example at the airports to denote the "runway visibility range" *RVR* [27, 83]. Another subjective term, the *visibility range*, is more commonly adopted terminology that is used in meteorology nowadays instead of RVR, and is the actual distance at which a person can discern an ideal dark object against the horizon sky [84]. The visibility range terminology will be used hereafter, whenever visibility is referred. The visibility range is technically measured at the center of sensitivity for the human eye (where the sensitivity of the human eye is maximum), at 550 nm with a spectral band width of typically 250 nm. An international code of visibility range for different climatic conditions is given in Appendix D (Table D.1). The Koschmieder formula relates visibility range with optical extinctions as:

$$V(km) = \frac{\ln(\frac{1}{\tau_{TH}})}{\lambda_0} = [\frac{\ln(\tau_{TH})d}{\ln(\tau_{MEAS})}] \tag{2.49}$$

The total extinction coefficient γ_e and visibility range are related by:

$$V(550nm) = \frac{\ln(\frac{1}{\tau_{TH}})}{\gamma_e(550nm)} = \frac{-\ln(0.05)}{\gamma_e(550nm)} = \frac{3.0}{\gamma_e(550nm)} \tag{2.50}$$

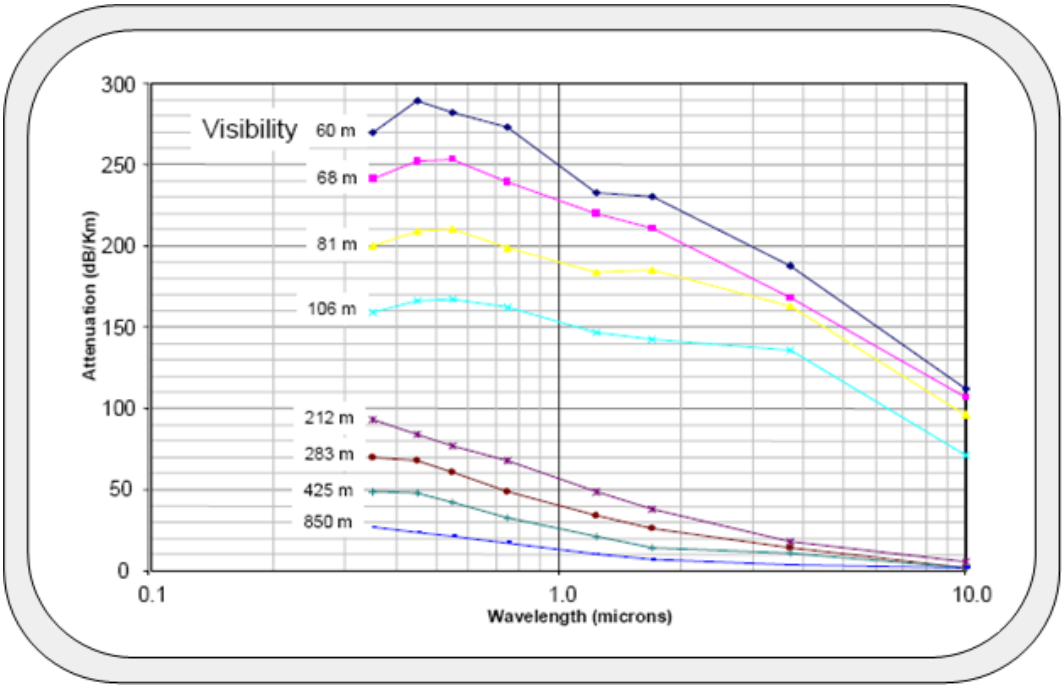

Figure 2.13: Simulating optical attenuations against visibility range [16]

Different empirical models have been proposed that relate visibility range with optical attenuations. Examples are, Kim [40], Pierce [85], Kruse [86], Al-Naboulsi [87] models, and CCIR model [58]. Fig. 2.13 provides the simulated results for the optical attenuations corresponding to a certain visibility range values at different optical wavelengths. It can be observed that under dense fog conditions for a visibility range of 60 m, the optical attenuation at 10 μm was typically half (around 125 dB/km) of that at 1.55 μm. These results indicate that under very dense fog conditions over a 200 meter link distance, an optical link established with a 10.6 μm system with 46 dB of link margin would still have 23 dB of margin left when a similarly margined optical link operating at 1.55 μm system goes down.

In order to approximate optical attenuations through a certain weather condition based on visibility range estimate, there are two most widely used models: the Kruse model and the Kim model both relate total extinction coefficient $\gamma_e(\lambda)$ to visibility range V. For a detail about Kruse and Kim models along with their approximations of parameter q for different visibility ranges, and the derivation of their model equations for the two transmission thresholds please refer to Section 3.2.3.

Al Naboulsi [87], proposed model to predict the fog attenuation in visible and IR regions is based on Mie theory and is built from two types of particle size distributions. He calculated the attenuation from FASCOD for various values of visibility at a given wavelength. Then, with a linear regression technique, he approximated these values by an analytical

expression to describe relationship between fog attenuation and visibility:

$$\gamma(\lambda) = \frac{a(\lambda)}{V + b(\lambda)} \tag{2.51}$$

Where $a(\lambda)$ and $b(\lambda)$ are parameters that depend on wavelength. For wavelengths located between 690 nm to 1550 nm and visibility between 50 m and 1000 m, fog attenuation for two types of fog (advection and radiation) can be expressed as:

$$\gamma_{adv}(\lambda) = \frac{0.11478\lambda + 3.8367}{V} \tag{2.52}$$

$$\gamma_{rad}(\lambda) = \frac{0.18126\lambda^2 + 0.13709\lambda + 3.7502}{V} \tag{2.53}$$

Whereas, the specific attenuation coefficient is:

$$a_{spec}(dB/km) = \frac{1000}{\ln 10} \cdot \gamma(\lambda) \tag{2.54}$$

Since Al Naboulsi does not take into account all distributions present in nature and their dynamic and temporal evolutions, it is essential to experimentally check the model capacity to represent the fog attenuation. This model underestimates attenuation at 1550 nm in a radiation fog, reducing visibility to 50 m.
Pierce [85] proposed that attenuation in fog should be treated as virtually wavelength independent from the visible to the near IR and a more appropriate formula is:

$$\Gamma(V;\lambda) = \frac{\kappa}{V}(dB/km) \tag{2.55}$$

Where V is the visual range and $8.5dB < \kappa < 17dB$. [85] concluded that the scattering analysis shows that visibility is related more closely to near forward scattering, rather than to attenuation.
According to Bataille [88], who used the polynomial approach to calculate the molecular and aerosol extinction coefficients for 830 nm, 1060 nm, 1330 nm, 1540 nm, 3.820 μm, and 10 μm laser lines as they correspond to atmospheric transmission window for which transmission systems exist. Since his model was difficult to simulate, so this model could not attract applicability. The specific extinction coefficient σ_n is obtained by:

$$\begin{aligned}\sigma_m = &-\ln(A_1 + A_2 H + A_3 H^2 + A_4 H^x + A_5 V^{-1/2} \\ &+ A_6 V^{-y} + A_7 H V^{-1/2} + A_8 (H/V)^y + A_9 H^z/V \\ &+ A_{10} H V^{-1})\end{aligned} \tag{2.56}$$

Where V is the visibility in km, $H(g/m^3)$ is the absolute humidity, x, y, z are real numbers used to optimize the polynomial for each studied wavelength. Their values are adjusted

when the maximum relative error between FASCOD and the polynomial is lower than 5%. Coefficients $A_i(i = 1,10)$ for the different studied waves. Bataille [88] showed in his measurements that attenuation decreases with increasing the wavelength. The maritime environment gives the most severe attenuation while the rural environment presents the least attenuation. The CCIR formula used for calculating optical attenuation for aerosols applies more particularly in the visible spectrum around 0.6 μm [58]:

$$\alpha(dB/km) = \frac{17}{V} \tag{2.57}$$

The visibility range dependent different attenuation models namely, the CCIR model, Bataille model, Naboulsi Advection fog model, Naboulsi Radiation fog model, Kruse model and Kim model are simulated for comparison against a transmission wavelength of 850 nm. The visibility range values against which they are simulated extend from 50 m to 1000 m. The corresponding plot is shown in Fig. 2.14 below. It is important to mention here that the CCIR model simulated is equivalent to the Pierce model with value of parameter κ taken as 17 dB. From Fig. 2.14 it is visible through comparison that, in general, all the mentioned models behave closely the same and there seems no special reason to prefer one particular empirical model over the others against visibility range below 1000 m. It is noticeable that for a visibility range region around 100 m the Kruse and Kim models delineate maximum up to approx. 20 dB/km in comparison to the other models mentioned. However, this gap in approximated attenuations narrows down linearly with the increase of visibility range.

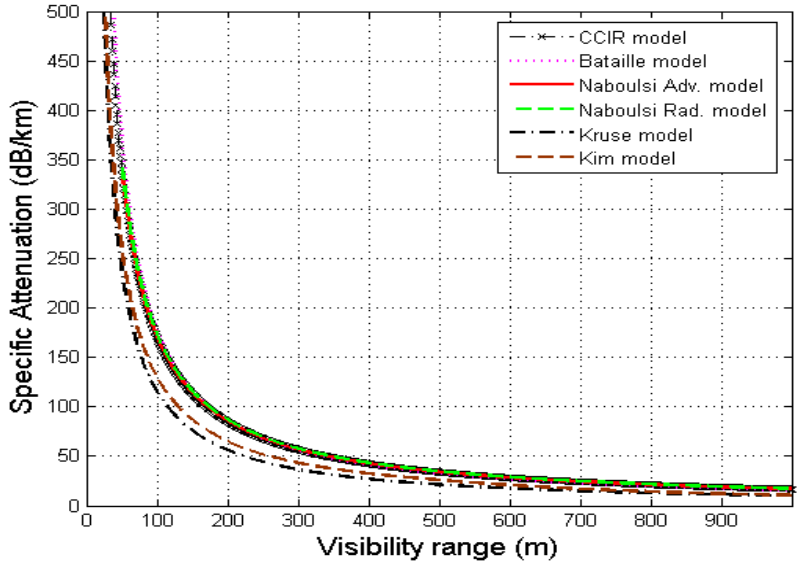

Figure 2.14: Simulations of visibility range dependent empirical models

Wavelength Dependent Models:

The free-space propagation path has different characteristics for the different FSO scenarios. These atmospheric characteristics are highly dependent on the transmission wavelength, for example, at some wavelengths scattering is more dominant mechanism of signal power loss than the absorption phenomena [38]. Similarly, attenuation losses due to water vapor absorption depend also on the wavelength and it is observed that longer wavelengths may suffer few dB of attenuation than the shorter wavelengths. Hence, selection of a certain wavelength for a particular communication scenario is very important as it has many important consequences. For free-space optical transmissions in the troposphere, especially in conditions like fog, snow, rain and clouds, the atmosphere highly interacts with the transmitted beam and hence plays a very detrimental role to the optical signal transmissions. In terrestrial scenarios, longer wavelengths are found to perform better and hence provide better link availability and reliability as compared to the shorter wavelengths [16, 32]. Considering the space-space optical communication scenarios e.g., optical link between GEO-GEO or GEO-LEO, here the free-space optical link do not suffer from atmospheric effects. Therefore, shorter wavelengths are found to be more suitable than the longer wavelengths [43].
There are different methods available that confirm wavelength dependency. Analytical model such as Mie scattering theory based fog attenuation predictions using Modified Gamma Distribution (Equation 3.3), and empirical model based on Kruse, Kim and Al-Naboulsi models (See for reference Section 2.4.2 and Section 3.2.3 and Fig. 2.13 for fixed visibility range conditions).

Optical Depth Dependent Models:

Ketprom [55] considered that the optical signal experiences multiple scattering while propagating through the atmosphere before being received at the receiver. He used the idea of optical depth which indicates the thickness of fog. Optical depth generally indicates the average number of interactions that light will incur when propagating through a multiple scatter channel. The atmospheric transmittance (as given in Equation (2.28)) and the optical depth τ_0 (as defined in Equation (2.38)) are related to transmission path between h_1 and h_2 by the following relationship,

$$T_r = e^{-\int_{h_1}^{h_2} \gamma(\rho) d\rho} \tag{2.58}$$

and

$$\tau_0 = \int_{h_1}^{h_2} \gamma(\rho) d\rho \tag{2.59}$$

The beam loss (L) in dB as given in Equation (2.29) for transmittance then can be related to optical depth as well,

$$L = -10Log_{10}T_r = 4.34\tau_0 \tag{2.60}$$

Therefore, for an optical depth of about 0.7 the signal power loss is about 50 %, which corresponds to a loss of 3 dB. Ketprom analyzed the OOK modulated light transmission through dense fog by using vector radiative transfer (RT) theory, which is based on the assumption of power conservation and is applicable for studying multiple scattering effects [55]. He solved the vector RT equation for a band limited signal to obtain the specific intensity of a received signal in the frequency domain. His results show the frequency response of the channel, as frequency response represents the characteristics of the channel as a function of frequency. The frequency response of the channel has the characteristics of low pass filter while the phase of the fog channel displays nonlinear characteristics at low frequency and is dependent on the optical depth. The Fourier transform of the frequency response is the impulse response that characterizes the fog channel in the time domain. To obtain the expected received signal, he convolved the impulse response with the transmitted signal.

$$y(t) = x(t) \otimes h(t) + n(t) \tag{2.61}$$

Where expected received signal is $y(t)$, is the convolution of the transmitted signal $x(t)$ and impulse response of the fog channel $h(t)$ plus the additive Gaussian noise $n(t)$.

2.4.3 Statistical Models

Statistical models give an explicit representation of the channel statistics in terms of parametric distributions, and are based on known probability density functions, which are also used in the terrestrial mobile communication systems.
Analytical and empirical models have been found to have certain limitations and sometimes are not feasible to apply for a certain communication scenario due to their complexity, relatively larger computation time, and over or under estimation of certain atmospheric effect. On the other hand, physical-statistical modeling is a hybrid approach, which builds in the advantages of both empirical and physical models while avoiding many of their disadvantages. Therefore statistical-dynamical model provides an alternate strategy to model the behavior of atmospheric effect on free-space optical wireless transmissions and study it in terms of random variables and their associated probability distributions. Physical-statistical models derive fading distributions directly from distributions of physical parameters. The input knowledge consists of electromagnetic theory and sound physical understanding. Hence, physical-statistical models require only simple input data such as input distribution parameters. The environment description is entirely objective, avoiding problems of subjective classification, and capable of high statistical accuracy. The models are based on sound physical principles, so they are applicable over very wide parameter

ranges, and the required computational effort can be very small. The results could be inferred from the evaluation of long-term experimental data collected at selected locations where the optical wireless links has to be installed and then appropriate FSO system could be designed and installed that meets certain availability and reliability requirements for a carrier grade communication technology.
On the basis of statistical evaluation of the experimental data gathered from different locations we can develop *prediction models, availability models* and *reliability models*. From the perspective of FSO systems, the prediction model means the numerical prediction model that uses current weather conditions as input into the mathematical models of the atmosphere to predict the optical attenuations. The availability models generally define the ability of FSO systems to perform their required operation under given conditions at a stated instant of time. While reliability models express the characteristics of the FSO system with a probability that a FSO system will perform its required operation under given conditions for a stated period of time and guarantee that no operational interruptions will occur during this time period. The meteorological conditions on experimental paths can be identified by means of data obtained from a nearest weather station located near the optical link site. The records of attenuation events caused by weather effects can be compared then with the concurrent meteorological situation to identify the reason of the attenuation events by processing only the strictly concurrent attenuation events with hydrometeor occurrences. This statistically processed data is ranked in accordance with the individual types of hydrometeors and required first order and second order statistics like cumulative distributions of attenuation, fade durations, certain event intensity and its duration, inter-fade duration and certain event inter-event duration statistics can be inferred.

2.5 Summary about Channel Modeling

Good knowledge of the propagation medium, its optical characteristics and the aerosol particles present, is necessary to understand the effects of environment on the free-space propagation of light signals in order to quantify the corresponding attenuations and losses it will suffer in terms of energy or optical power. The effect of atmosphere on the propagation of laser radiation is firstly due to its chemical composition and on the other hand due to the presence of different types of particles or aerosols that are suspended in air. The different weather conditions such as fog and the presence of different types of precipitation can significantly reduce optical radiation transmission in atmospheric free-space. In this chapter, the influence of atmosphere on the propagation of optical radiation is discussed. This influence is reflected in terms of optical properties of the atmosphere (absorption coefficients and extinction) that are strongly linked to the index of refraction. The interaction of light with molecules, that make up the atmosphere and aerosols with a theoretical perspective, is discussed while focusing on the absorption in general and light scattering in particular. In addition, some detail about the optical turbulence or scintillation effect and

its related influences is also provided. Scintillation occurs mainly due to the temperature variations in clear sky conditions, and is of much significance for long distance ground-space FSO links. In the last part, few analytical and empirical models are also discussed as they identify the potential advantages and limitations of the atmospheric optical links for certain communication application scenario. These models are discussed with reference to optical attenuations as a function of key parameters such as radiation wavelength, the different weather conditions etc., that come into play and influence the performance of the FSO systems. All the discussion made under this chapter is necessary for our understanding of various mechanisms of optical signal losses in the free-space atmosphere and for the purpose of suggesting improvements in the existing optical wireless systems.

3 OPTICAL TRANSMISSIONS AND ATTENUATION MEASUREMENT RESULTS

In order to fully exploit and utilize the advantages offered by the FSO technology and to design fixed or mobile FSO links for terrestrial or ground-space communication scenarios, it is necessary to understand the losses and the mechanisms of losses that affect the optical signal transmissions through the atmospheric free-space. This chapter focuses on the discussion about the attenuation results and their possible comparison with results collected at different locations. However, the main focus of this chapter will be discussion and analysis of the fog attenuation measurements, but in the last section few rain and snow attenuation events are also discussed and analyzed.

Optical Attenuation in the Presence of Precipitation

In meteorology, precipitation is a class of hydrometeors and it is any product of the condensation of atmospheric water vapor that is pulled down by gravity and deposited on the Earth's surface. The main forms of precipitation are fog, rain, snow and clouds. When an optical beam propagates through clear sky conditions, even then some optical signal attenuation takes place due to the absorption by atmospheric particulates (gaseous constituents of the atmosphere in particular Oxygen and water vapors). The presence of precipitation in the Earth atmosphere considerably increases the amount of optical signal attenuation and is dependent on the size of the particles, particle concentration and form, and the chemical composition.
The terrestrial FSO links are mostly affected by low clouds, fog and snow. Fog being the most detrimental of all effect with attenuation levels as high as 480 dB/km in dense maritime fog environments [27], around 120 dB/km in continental fog environments [26]. Optical attenuations may easily exceed 50 dB/km in low clouds [30], while through rain the attenuations are not that significant as heavy rain showers can cause specific attenuations up to 30 dB/km at a rain rate of 150 mm/h [64]. However, measurements showed that optical attenuations through falling dry snow can easily reach 45 dB/km [29]. This potentially limits the achievable optical link range with very high reliability to less than 500 m during such conditions and thus requires a detailed characterization of each climatic conditions for terrestrial FSO link of different path lengths.

Atmospheric Effects Attenuation Modeling

In the recent years, there is a growing trend to investigate various possibilities of modeling the free-space atmospheric channel for different communication scenarios in order to enhance the capabilities of the FSO links [16, 74, 89]. In late 90's, when FSO started gathering momentum as a potential access technology, the research mostly revolved around studying the influence caused by fog attenuations on the terrestrial FSO links by comparing fog attenuations for different wavelengths [20, 40] and proposing better models relating visibility range to fog attenuation [85, 87]. The phenomenon of fog has been actively researched for many decades but with varying interests [90, 91]. However, driven by niche applications of FSO technology in many ground & space and fixed & mobile communication scenarios with the need of more bandwidth demands the research activity soon started towards characterizing various atmospheric phenomena considered detrimental (like fog, rain, snow, clouds and atmospheric turbulence) to the propagation of optical signal in free-space [27, 29, 69, 47]. Since terrestrial FSO systems are more vulnerable to certain fog conditions, therefore, the more focus remained on characterizing different fog conditions for terrestrial FSO link scenarios by investigating the time-series analysis of fog attenuations [92, 93, 94]. In this chapter, optical attenuation results are discussed for terrestrial FSO links in radiation and advection fog conditions in further detail with possible comparison with measurement attenuation data available from other locations. In addition, results about optical attenuations measured in rain and dry snow conditions are also presented and analyzed. Moreover, with ever growing demand of ground-space optical links, clouds play a decisive role on the optical link availability. Because of the un-availability of optical attenuations measured through clouds, optical attenuations are simulated for different cloud types using predictions generated using Mie scattering theory and the prediction model given in ITU-R P. 1622 recommendation.
The terrestrial FSO links must deal with the atmosphere just above the surface of the earth, where it has maximum density due to the gravitational force. Atmospheric attenuation can be distinguished as molecular absorption, Rayleigh-scattering, and aerosol-scattering. Molecular absorption is an effect of electron- and nucleus-resonance of atmospheric molecules, Rayleigh-scattering is caused by the atmospheric molecules acting as dipole-antennas, and aerosol-scattering is caused by droplets and particles that are larger than the wavelength that is influenced. Atmospheric attenuation of FSO systems is typically dominated by fog but can also be due to low clouds, rain, snow, dust, and various combinations thereof. Molecular absorption may be minimized by appropriate selection of the optical wavelength.

3.1 Experimental Setups

In this section experimental setups of terrestrial FSO links installed at Graz, Milan and Prague (in continental fog conditions) and La Turbie, Nice (in dense maritime fog conditions) are discussed. The mission of these attenuation measurement campaigns at different locations was to study the influence of fog on the optical signals transmitted in the atmospheric free-space channel. However, during these campaigns few rain and snow events also occurred at Graz, Milan and Prague on these FSO links, the attenuation results will be discussed in the appropriate sections to follow.

3.1.1 Experimental Setup at Graz, Austria

Graz provides dynamic weather conditions with thunderstorms in summer; heavy fogs at the end of autumn; frequent drizzle, storm, snow and haze in winters. The longest measurements campaign at the continental city of Graz started on 29^{th} September, 2005 and continued until 1^{st} March 2006. The considered data span over 156 days and 21 major fog events were measured during this period each having life span of at least half hour. The latest attenuation measurement campaign started at the end of September 2009 and is continuing till to-date. The purpose of this latest campaign is to analyze the behavior of measured fog attenuations with respect to variations in fog density. In order to measure fog density, temperature and relative humidity a fog sensor device is built by colleagues of Budapest University of Technology and Economics and is installed next to the receiver terminal.
In Graz, two independent links were established between the University buildings, a shorter one operating over 79.8 m free air distance, and a longer one operating over 800 m free air distance. The shorter link allows measurements of specific attenuation as high as 310 dB/km. For optical impressions, a Webcam in addition, takes pictures every minute. The operating temperature for the systems was maintained at a constant level by using small heating devices inside the system to reduce any temperature influences on the receiver diode. Thus, it was ensured that the system was stable against any thermal drift. The FSO transceivers installed at Graz are a self-developed system and is basically it consists of an optical transmitter and receiver system, each equipped in a waterproof housing mounted on a tripod with mechanical options for alignment.
In the transmitter, two independent LED-based light sources and optical systems are implemented. One is operating at 850 nm center wavelength and 50 nm spectral width at a full angle beam divergence of 2.4 degrees, the second one is operating at 950 nm center wavelength and 30 nm spectral width at a beam divergence of 0.8 degrees. The same transmitter optics for 850 and 950 nm have been used, but with different light sources having different active (light emitting) areas. This results in different divergence angles. To have approximately the same power for both wavelengths at the receiver, only 1 LED

(L7558-01) at 850 nm is used which emits about 8 mW average optical power in total, however, the average emitted power after the lens is about 3.5 mW, the rest being radiated in a wider angle. For the 950 nm wavelength, 4 LEDs (SHF495P) are used each emitting 1 mW to produce the same average power at the receiver. Thus, for both the wavelengths, the average received optical power after a distance of 30 m is -17 dBm.
Each light source is 100 percent *Amplitude-shift keying* (ASK) modulated by the driver electronics circuit with an individual carrier frequency provided by a crystal oscillator. ASK is a form of modulation that represents transmitted digital data as variations in the amplitude of a carrier wave such that the amplitude of the carrier signal varies in accordance with the bit stream (modulating signal) by keeping frequency and phase constant. Basically, all optical digital transmission systems use this modulation scheme on the physical layer (with very few exceptions). A square-wave with 50 percent duty cycle is used to switch the light source on and off. The square wave can be produced easily with typical FSO transmitter drivers and the receive band-pass filters cut away any higher order harmonics.
For the system 6 MHz is used for the 950 nm light source and 5.5 MHz for the 850 nm light source. This allows associating the received power of each optical wavelength with the signal strength of a modulation frequency. The choice of the receiver filters was motivated by two factors, firstly, to utilize frequencies which appear in most type of data transmission (1- 10 MHz range), and secondly, on the availability of ceramic bandpass filters. Crystal resonators were chosen for the transmitter, at 6 MHz (commercially available) and at 5.5 MHz (self designed) with very similar characteristics to avoid any modulation frequency dependent attenuation effect. Accordingly, the receiver consists of a single optical system of 98 mm lens diameter with 1.7 degrees full acceptance angle for both wavelengths without optical bandpass filter, a Si-photo-PIN-diode (SFH203FA) with a spectral range of 800 to 1000 nm, a trans-impedance amplifier followed by an RF gain stage and then the modulation carrier frequencies are separated by electrical bandpass filters, rectified and decoupled by a DC amplifier. The resulting DC output voltages correspond to the optical power received from each of the two optical wavelengths. To record the measurement data, a conventional computer with an A/D conversion card (National Instruments PCI-6023E) operating under LabView software is used. The card operates at a maximum of 200 kilosamples per second and is a 12-bit, 16-input analog-to-digital converter. The measured DC voltage value of every channel is stored as a time series in a table.
Among the advantages of this RF Marker transmission measurement concept compared to systems using non modulated light and optical bandpass filters at the receiver is the point that the same optical system and front end is used for two (or in principle for a number of) optical wavelengths and so - except for chromatic aberration (which may be neglected) - to have equal optical properties for the wavelengths, it allows excellent suppression of ambient light and it allows to measure light transmission under similar conditions as used by FSO systems which also operate by on-off-keying to modulate the light. Due to the fact, that optical filters can be replaced by filters in the electrical domain, the system can be built quite cost effective, which may allow a wider range of applications.

Before any practical fog measurement was performed, the system was calibrated in the lab to determine the relation between the received optical power and the output DC voltage level. The crosstalk between the two wavelength channels was found to be sufficiently low (less than 0.01 Volts DC for all measured points) in the linear range of the input stage amplifier, resulting in a maximal output change of 0.19 dB(opt) for both channels in case of 25 dB difference in the input power. Non modulated ambient light up to 0.1 mW (more than the maximum daylight receiving power for this system) is completely suppressed, resulting in output power change of less than 0.005 dB(opt). The dynamic range of the system exceeds 25 dB(opt) for each of the two channels and is limited mostly by the resolution of the data logger and the DC amplifier offset.
For the measurement campaigns, the link distance was selected carefully as a compromise between accuracy and allowable attenuation range, depending on the expected maximum fog attenuation. The FSO link at Graz for a link distance of 79.8 meters allowed specific attenuation measurement up to 310 dB/km. The data was processed and evaluated after the measurement in MATLAB, resulting in the diagrams shown in the following sections. With the aim to measure and characterize fog, the measurement campaigns were carried out consecutively for 2 years in Graz. In the winters of 2004 and 2005. The first measurement campaign, which was started in late October 2004 and continued till March 2005, did not yield any significant results because of the much less probability of fog formation that winter. The second much more successful campaign was started on 27^{th} September, 2005 and continued until 1^{st} of March 2006.

3.1.2 Experimental Setup at Milan, Italy

The 319-m optical link in Milan, Italy is installed within the campus Leonardo of Politecnico di Milano. The experimental set-up consists of a commercial optical link Terescope 3000 formed by two identical transceivers, which can transmit both data up to 155 Mbps and a single carrier at 785 nm. The Terescope 3000 system was manufactured by Optical Access (now MRV). The transmitters on each side of the link are assembled in triangular shape and use three identical and independent semiconductor laser diodes having nominal output power of 10mW and the beam divergence is 2.5 mrad. The data are sampled every 1 s. Visual range is measured by an optical transmissiometer (Model 6100) manufactured by Belfort Instrument while the meteorological quantities (temperature, relative humidity, solar radiation, rain rate etc.) are measured by a weather station manufactured by Davis. The visual range meter and the weather station are placed near one of the two terminals of the optical link. Almost continuously from 2003 to 2006, this set-up has been collecting data.

3.1.3 Experimental Setup at Prague, Czech Republic

At Prague, Czech Republic the experimental FSO link operates at 850 nm wavelength on a channel length of about 850 m. Transmitted power of this FSO system is +16 dBm, divergence angle is 9 mrad, receiver aperture is 515 cm^2 and the recording fade margin is about 20 dB. Optical calibration was performed before deploying the device. The calibrated Received Signal Strength Indicator (RSSI) signal of the FSO link has been recorded continuously on a PC hard disc. The relative received signal level was derived from the RSSI signal and processed statistically. All attenuation events were classified according to the meteorological conditions causing the corresponding attenuation event.
The meteorological conditions were recorded using a BW video camera images of the space between the transmitter site and the receiver site. The data obtained from an automatic meteorological station located near the receiver site. The automatic meteorological station is equipped by VAISALA sensors for measurement of temperature, humidity and pressure of air, velocity and direction of wind, and 2 tipping-bucket raingauges with differing collecting areas for the measurement of rain intensities. VAISALA PWD11 equipment is used for the visibility measurement. Meteorological conditions during fading events have been recorded.

3.1.4 Experimental Setup at Nice, France

The measurement setup in France consisted of a transmissiometer to measure visibility at 550 nm center wavelength, an infrared link for transmission measurement at 850 and 950 nm and a PC based data logger to record the measured data. In addition, temperature, humidity, and ambient light were recorded in longer time intervals. It is important to mention that the same FSO link equipment was used at Nice as that used at Graz. For the two measurement campaigns (Graz and Nice), the link distance was selected carefully as a compromise between accuracy and allowable attenuation range, depending on the expected maximum fog attenuation. Provided a dynamic range of 25 dB for the system at each wavelength, at La Turbie, Nice a link distance of 28.3 m did allow measuring specific attenuation of up to 880 dB/km.

3.2 Fog Attenuation

To assess the availability and reliability of FSO links in the troposphere for different fog conditions, the two broad classes of models can be envisaged to estimate fog attenuation,

- Microphysical models, that require the knowledge of the structure of fog and of the scattering properties of fog particles [55, 63]

- Empirical methods, based on the conversion of some easy-to-measure atmospheric parameter, as visibility range, into optical attenuation

In the following discussion it is assumed that fog intensity is uniform all along the entire transmission path. As far as optical transmission through fog is considered, scattering prevails over absorption, because the refractive index of water has a negligible imaginary part. In principle, the attenuation measurements allow us to find the size and distribution of the sizes of particles present per unit volume, their shape and orientation, and their chemical composition. In case if we know the physical properties like refractive index, we may find the Mie extinction or scattering cross-section. Because scattering is the main mechanism of the optical signal loss in case of terrestrial FSO links, the type of scattering governed by the optical signal interactions with smog, smoke, mist, haze and fog droplets is the Mie scattering.
With Mie scattering the angular intensity distribution becomes more complex with more energy transmitted in the forward direction. It is interesting to analyze in more detail the effect of temperature variations on the complex refractive index and complex permittivity of water as these two parameters affect Mie scattering calculations. The complex refractive index and complex permittivity were calculated using the method provided by P. S. Ray [95] and are plotted for wavelengths up to 10 μm in Fig. 3.1 and Fig. 3.2, respectively. The real part of the complex refractive index corresponds to scattering while the imaginary part corresponds to absorption.
There are no appreciable variations in the complex refractive index, indicating negligible

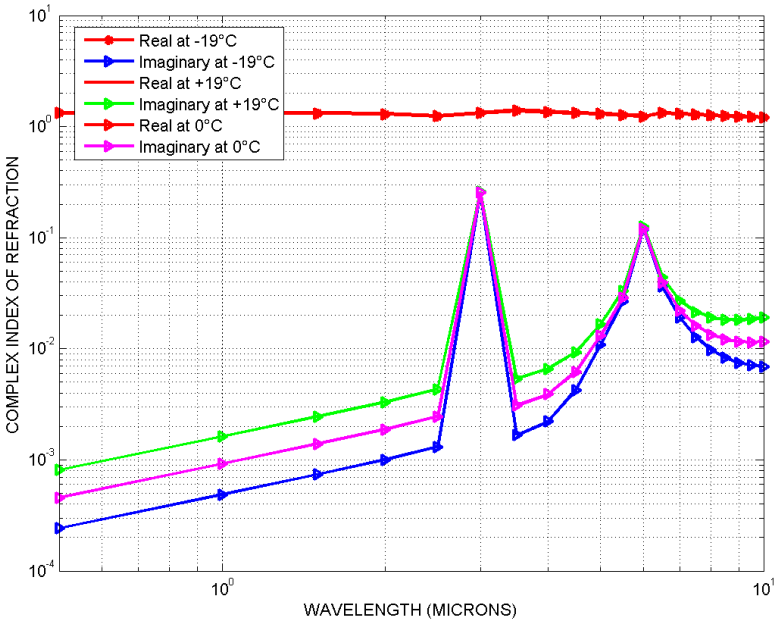

Figure 3.1: Complex refractive index of water for three different temperatures [96]

attenuation by absorption effect. This justifies the assumption that for optical transmission through fog, the losses due to absorption can be ignored as compared to the scattering loss. The refractive index is insensitive both to temperature variations (from -19 °C to +19 °C) and to wavelength variations (from 0.550 μm to 10 μm), its real part changing from 1.330 to 1.342. We recall that temperature remains almost stable during a fog event and that fog keeps the temperature of the surrounding air steady since its main constituent is a liquid water droplet, which has an high specific heat capacity (i.e. the amount of heat per unit mass required to raise the temperature by one degree Celsius). The complex permittivity is also computed for a temperature ranging from -19 °C to +19 °C (Fig. 3.2). There are no significant changes in its real and imaginary parts for wavelengths up to 10 μm. The real part of the complex permittivity is comprised between 5.3272 and 5.359.

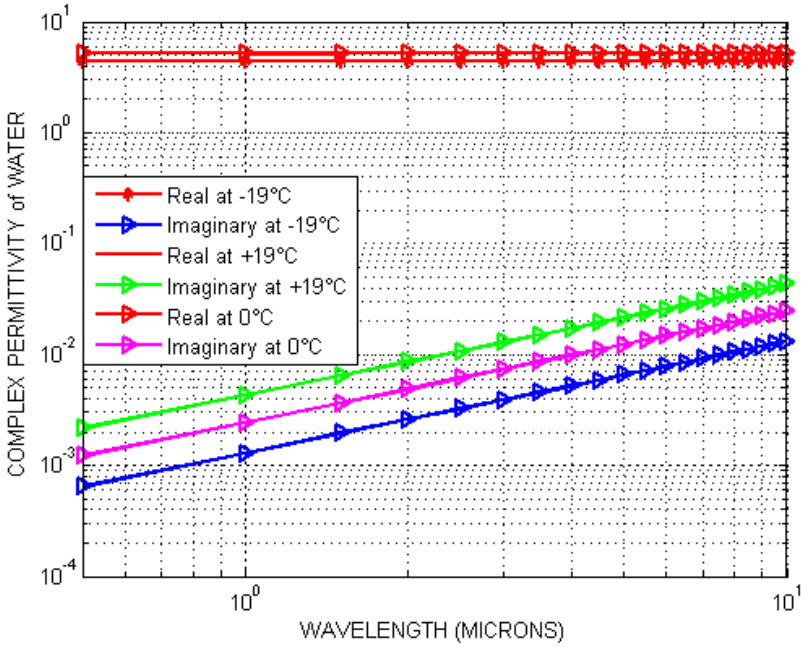

Figure 3.2: Complex permittivity of water for different temperatures [96]

3.2.1 Optical Scattering - Multiple Scattering based Model

In order to calculate extinction of the optical signal only, multiple scattering effect can improve the transmission of the signal but cannot make it more severe. Since it is assumed that all the energy that is scattered out of the transmitted optical beam is permanently lost when the total extinction cross-section is calculated. But when multiple scattering effects are considered then such consideration allows to recover back that lost energy into the

receiver's field of view through available computational methods. It is possible though that multiple scattering may either retain the same wavelength dependence like single scattering or may further refine it out. Hence if multiple scattering even occurs to some extent in the atmosphere in the presence of fog conditions particularly, then it will not change much the resulting attenuations as observed in case of single scattering assumptions [85]. In actual, the calculations of optical attenuations considering multiple scattering effects yield attenuation values that are lower than those attenuation values that assume single scattering [12].
If individual fog particles don't have a high forward scattering efficiency and their number concentration is low enough, path attenuation through fog can be calculated through the single scattering theory, which assumes that the energy absorbed or scattered by a particle is definitely lost. However, if this is not the case, the contribution of scattered light to the amount of energy transmitted through the medium cannot be neglected. Multiple scattering is governed by the radiative transfer equation, which descends from energy conservation. At very dense concentration (the volume occupied by particles should be much larger that 1% of the total volume), the diffusion approximation describes well the process in terms of a random walk of the photons in the medium.
No experimental evidence of multiple scattering effects has been found in the case of optical transmission through moderate fog [97]. Simulations based on a model of random walk of photons through the atmosphere [98] show that in the case of thick fog (visibility range less than 250 m), the path attenuation in the first optical window is a few percent smaller (on a dB scale) than the one predicted by a single scattering model.

3.2.2 Optical Scattering - Single Scattering based Microphysical Model

Fog attenuations can be predicted based on method given by Mie scattering theory based on microphysical parameters of fog particle such as DSD. In order to apply Mie scattering towards prediction of optical attenuations for fog conditions, following assumptions are made that does not seem to have a large impact on the accuracy of the results calculated [62, 63],

- The scattered light has the same wavelength as of the incident light
- The fog particles are spherical in shape and are acting independently with a complex refractive index in free-space
- Only single scattering takes place and the multiple scattering effects are negligible

If individual particles don't have a high forward scattering efficiency and their number concentration is low enough, path attenuation can be calculated through the single scattering theory, which assumes that the energy absorbed or scattered by a particle is definitely lost. However, if this is not the case, the contribution of scattered light to the amount of

energy transmitted through the medium cannot be neglected. If γ is the attenuation of the total extinction coefficient per unit length then it can be represented in the form as,

$$\gamma(\lambda) = \alpha_a(\lambda) + \alpha_m(\lambda) + \beta_a(\lambda) + \beta_m(\lambda) \tag{3.1}$$

Where α_m and α_a are the molecular gas and aerosol absorption coefficients; β_m and β_a are the molecular gas and aerosol scattering coefficients, respectively. While calculating the contributions towards overall fog attenuation, the attenuations introduced by molecular gas scattering and absorption coefficients, and aerosol absorption coefficients can be ignored when compared with the attenuation contribution by fog droplets (aerosol scattering coefficient), so:

$$\gamma(\lambda) \cong \beta_a(\lambda) \tag{3.2}$$

or,

$$\gamma(\lambda) \cong \beta_a(\lambda) = 10^5 \int_0^\infty Q_d(\frac{2(\pi)r}{\lambda}, n')\pi r^2 C(r)dr \; [km^{-1}] \tag{3.3}$$

Here, $\gamma(\lambda)$ is the specific attenuation measured in dB/km calculated by summing up the attenuation effect of all individual fog droplets present per unit volume per unit of radius increment. n' is the real part of the complex refractive index of the fog particles and Q_d is the normalized Mie scattering cross-section and the factor πr^2 is introduced here for denormalizing with respect to the geometrical cross-sectional area of the fog droplets. In Fig. 3.3, modified gamma drop size distribution (hereafter MGDSD) profiles for moderate and dense continental as well as maritime fog conditions are plotted. The corresponding MGDSD parameters of continental fog only are listed in Table 3.1 [99, 100]. The parameters N_r and LWC in Table 3.1 show the fog droplets number density and the liquid water content, respectively. Whereas, m, N_0 and Λ are the three parameters of MGDSD representing shape parameter, the intercept or the normalization constant and the slope or gradient of the fog particles DSD, respectively.

Fig. 3.4 shows the specific attenuation for selected wavelengths at 10 °C using Equation

Fog Type	**m**	N_0	Λ	N_r cm^{-3}	**LWC** g/m^3	γ **dB/km**
Moderate Continental	6	607.5	3	20	0.016	37.66
Dense Continental	6	2.37	1.5	100	0.063	124.82

Table 3.1: Standard values of modified gamma distribution parameters for continental fog conditions [99]

(3.3) for moderate continental fog. There are slight indications of wavelength dependent attenuation for optical links under continental fog conditions i.e., at longer wavelengths the attenuations are smaller when compared with shorter wavelengths.

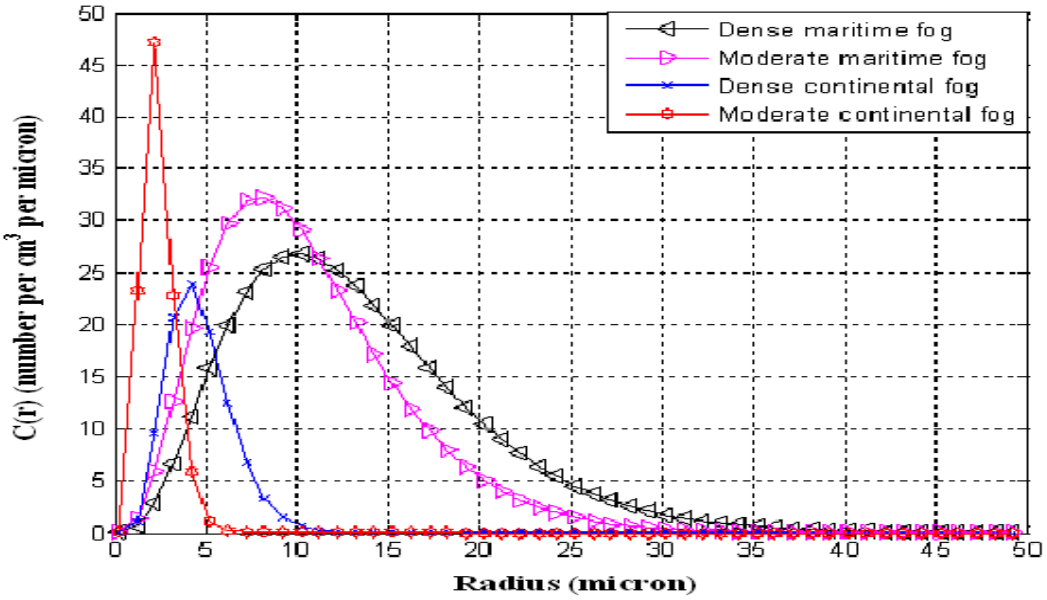

Figure 3.3: Modified gamma DSD for different fog conditions [101]

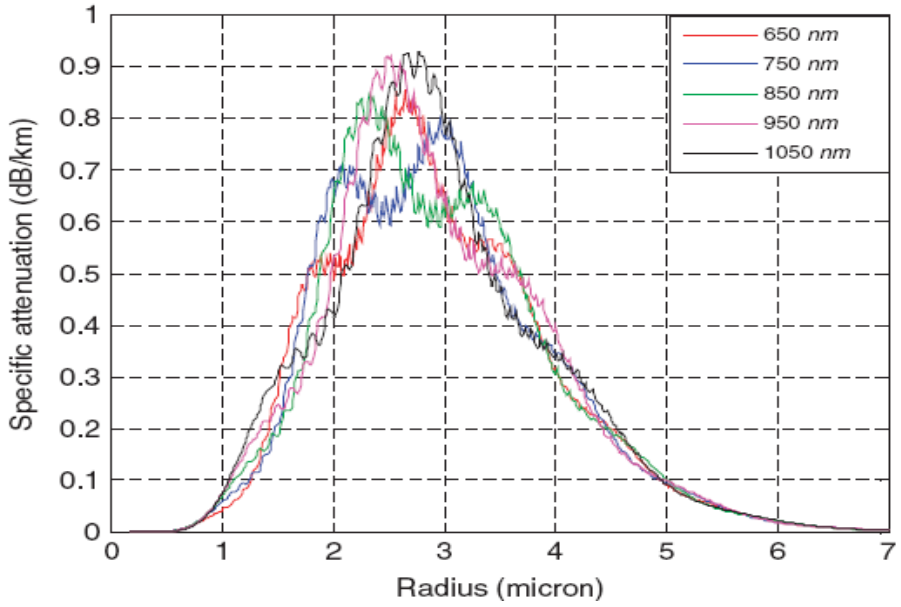

Figure 3.4: Predicted specific attenuation at 10 °C [101]

3.2.3 Visual Range based Empirical Model to Predict Fog Attenuations

With the exception of the magnitude of visibility range, the physical properties of fog are not commonly measured while installing terrestrial FSO link. The visibility range

parameter has long been used to quantify the effect of particles in the atmosphere (fog and aerosols) on the transmission of optical waves, visible and near-infrared 2.5 μm. Indeed, in this area of the spectrum, the attenuation coefficient is approximated by the scattering coefficient of particles in the atmosphere since [102],

- Scattering by atmospheric molecules (Rayleigh scattering) is negligible,
- Absorption by aerosols or fog particles is negligible because the imaginary part of refractive index of these particles is very weak in this area of the spectrum.

To determine the optical contrast, consider the example of the following object (Fig. 3.5), Viewing this object from a distance z, under "perfectly clear" conditions, the contrast can

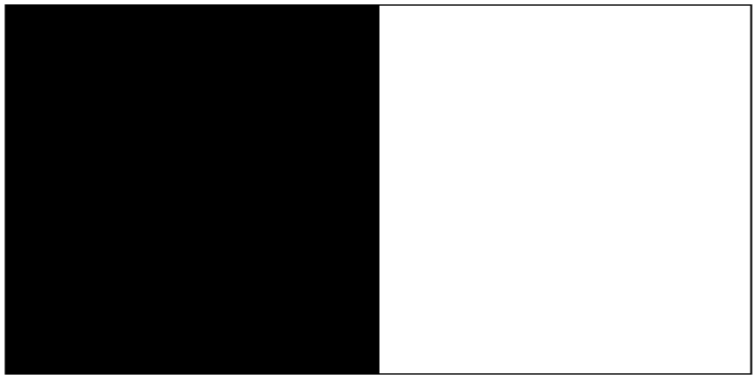

Figure 3.5: Example of object used to measure the optical contrast

be defined in terms of apparent irradiance from dark and bright patch. If the irradiance for the dark and bright patches are $I_b(z)$ for the black and $I_w(z)$ for the white part, respectively, then the contrast at distance z is given by [85],

$$C(z) = \frac{I_w(z) - I_b(z)}{I_b(z)} \tag{3.4}$$

Considering distance z to be very large, in that case $I_w(z) \geq I_b(z)$ so that the optical contrast C(z) is necessarily a number between 0 and infinity. At a distance z = 0, the above equation becomes,

$$C(0) = \frac{I_w(0) - I_b(0)}{I_b(0)} = \frac{I_w - I_b}{I_b} \tag{3.5}$$

Then by dividing the above two equations we have,

$$\frac{C(z)}{C(0)} = \frac{I_w(z) - I_b(z)}{I_b(z)} \times \frac{I_b(0)}{I_w(0) - I_b(0)} \tag{3.6}$$

Then according to the definition of visibility range, if the $C(z)/C(0) = 2\%$, then Z = V. Assuming the irradiance of the black patch I_b as compared to the white patch I_w, then

above equation becomes,

$$\frac{C(z)}{C(0)} = \frac{I_w(z)}{I_w} \tag{3.7}$$

On the other hand we know that,

$$I_w(z) = I_w(0)exp[-\beta_V z] \tag{3.8}$$

Where β_V is the optical attenuations scattering coefficient due to aerosols in the visible spectrum. Indeed, it is in a transmission window implying that molecular absorption is negligible. It is the same for aerosol absorption since for the visible and near Infrared radiations, the imaginary part of refractive index of particles in the atmosphere is negligible. For z = V we can write,

$$\frac{C(z=V)}{C(0)} = \frac{I_w(z=V)}{I_w} = exp[-\beta_V V] = 0.02 \tag{3.9}$$

or,

$$\beta_V V = -\ln(0.02) = 3.912 \tag{3.10}$$

or in terms of decibel units, Equation (3.8) becomes,

$$I_w(z) = I_w 10^{-\gamma_z/10} \tag{3.11}$$

and hence finally we get,

$$\gamma = -\frac{10\log(0.02)}{V} = \frac{17}{V} \tag{3.12}$$

Based on the qualitative approach, Kruse empirically established changes in the overall scattering coefficient similar to that of aerosols outside the strict visible spectrum, especially in the near infrared, from the following empirical formula [62, 102],

$$\beta(\lambda) = C_1\lambda^{-q} + C_2\lambda^{-4} \tag{3.13}$$

Here C_1 and C_2 are the constants determined by the concentration of aerosols and the distribution of their sizes. The first term on the right side of Equation (3.13) corresponds to scattering by aerosols, while the second term corresponds to the Rayleigh scattering that becomes negligible as compared to the first term for $\lambda \geq 0.4\mu$m . Thus the Equation (3.13) becomes,

$$\beta(\lambda) \simeq \beta_a(\lambda) = C_1\lambda^{-q} \tag{3.14}$$

For a wavelength $\lambda = 0.55\mu$m, the above equation becomes,

$$\beta(0.55\mu m) \simeq \beta_a(0.55\mu m) = \beta_V = C_1(0.55\mu m)^{-q} \tag{3.15}$$

Considering a contrast ratio or transmission threshold $\tau_{TH} = 2\%$ for wavelengths (λ) between 0.4 μm to 2.5μm, the final equation for the extinction coefficient thus becomes [12],

$$\gamma(V,\lambda) = \frac{17}{V}[\frac{\lambda}{550}]^{-q} \ [dB/km] \tag{3.16}$$

and for a 5% transmittance threshold the extinction coefficient is given by,

$$\gamma(V,\lambda) = \frac{13}{V}[\frac{\lambda}{550}]^{-q} \ [dB/km] \tag{3.17}$$

In Equations (3.16) and (3.17), V is the visual range in km, λ is the transmission wavelength in nm, γ is the total extinction coefficient and q is the size distribution coefficient of scattering. The wavelength dependency in this expression is given by "q" parameter, which was proposed by Kruse [86] as,

$$q = \begin{cases} 1.6 & \text{if V} > 50 \text{ km} \\ 1.3 & \text{if 6 km} < \text{V} < 50 \text{ km} \\ 0.585V^{\frac{1}{3}} & \text{if V} < 6 \text{ km} \end{cases}$$

Kruse relation predicts lesser attenuation for longer wavelengths and fails to correctly estimate the atmospheric attenuation for visibility below 1 km (high attenuation conditions). Indeed, the visibility parameter is easily measured and stored from weather stations or airports, allowing a geo-local assessment of performance of these FSO systems from the variation of this parameter. From Equations (3.16) or (3.17), depending upon the transmission contrast with Kruse approximations of visibility range values, it is obvious that irrespective of any weather conditions use of longer wavelengths for transmissions incur lesser atmospheric attenuations. This implies that future FSO systems be developed that operate preferably at longer wavelengths like at 1550 nm or at 10 μm [103, 104, 105]. However, there is a serious drawback of Kruse approximations which, although, hold well for clear weather conditions but fails to give the explanation for visibility ranges especially lesser than 500 m (dense fog conditions) and thus require an extrapolation for visibilities below 1 km. Another limitation of Kruse approximations is that it does not account for the various types and classes of aerosols.
In the literature Mie scattering, transmission measurements and simple observations indicate atmospheric attenuations are independent of the transmission wavelength and thus allow to assign a fixed value to the parameter q for low visibility values (below 500 m), as approximated by I. I. Kim et.al. [106]. According to Kim, the "q" parameter has following values based on visibility range estimates,

$$q = \begin{cases} 1.6 & \text{if V} > 50 \text{ km} \\ 1.3 & \text{if 6 km} < \text{V} < 50 \text{ km} \\ 0.16V + 0.34 & \text{if 1 km} < \text{V} < 6 \text{ km} \\ V - 0.5 & \text{if 0.5 km} < \text{V} < 1 \text{ km} \\ 0 & \text{if V} < 0.5 \text{ km} \end{cases}$$

One major difference between the Kruse and Kim models is that Kruse assumes a wavelength dependency while Kim assumes wavelength independent attenuation for very low visibility range conditions like dense fog (visibility range $\leq$ 500 m). That means in dense fog conditions, FSO system operating at 1550 nm wavelength will undergo the same

amount of optical attenuations like if operating at 690 nm or 780 nm wavelengths. Moreover, for visibility ranges $\geq$ 500 m the Kim and Kruse models suggest the same kind of behavior i.e., lesser attenuations for longer wavelengths.

3.2.4 Time Series Analysis and Comparison of Measured Continental or Radiation Fog Attenuations

Fog still remains the major hurdle in establishing high availability terrestrial FSO links operating over long distances because of high attenuation of the optical signal transmitted. The time series analysis of the fog attenuation characteristics for continental fog are already presented and discussed based on experimental attenuation data recorded at Graz [26, 80, 94]. The time series analysis shows that the specific attenuations inside continental fog conditions may reach up to 150 dB/km in relatively stable fog conditions having little changes in specific attenuation over time. In this section the results of optical transmission measurements in Milan and in Graz, tailored to investigate the impact fog attenuation on terrestrial FSO links are discussed and compared. shows the specific attenuation over a scale of minutes for both Graz and Nice, the differences among the two fog types are clear, with the maritime fog having greater attenuation and faster changes in the attenuation levels.
The measurement database considered in this work consists of six winter months both for Graz and Milan but in different years. Fig. 3.6(a) - (c) show the profiles of visual range, laser attenuation and the differences in specific attenuation during a fog event that occurred at Milan on 11^{th} and 12^{th} January 2005, respectively. In Fig. 3.6(b), two profiles are shown: the measured laser attenuation (red curve) and the attenuation as estimated from visual range (blue curve). The system goes into outage every time the measured attenuation exceeds the allowable dynamic range for atmospheric losses; the dynamic range of the receiver is 21 dB ($\sim$ 66 dB/km). The optical attenuation, as estimated from visual range through the Kim and Kruse models, as discussed in the previous section, Fig. 3.6(b), has a maximum value of 154.13 dB/km, while its median value is 34.55 dB/km, nearly equal to the median value found for the sequence of measured specific attenuation (34.98 dB/km).

Indeed, if we compare the two time profiles in Fig. 3.6(b), we see that there is a good agreement between measurements and estimates except in the case of the peak attenuation in the morning of 12^{th} January, when the estimated values are much higher (this behavior could be ascribed to the sharpness of visual range decrease that may be a symptom of non-uniform visual range conditions along the path. In fact, during this short event the two curves have a similar profile, but the measured attenuation curve is slightly delayed in time) [96]. Fig. 3.7(a) - (b) are relative to a heavy fog event that occurred in Graz on 2^{nd} February 2006 showing the time series profile of optical attenuations at 850 nm and 950 nm and the corresponding changes in attenuations at 950 nm, respectively. The peak, mean and median values of specific attenuation, derived from actual measurements made

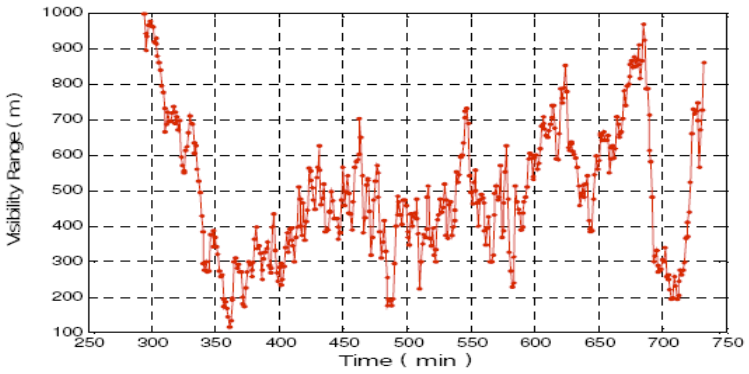

(a)

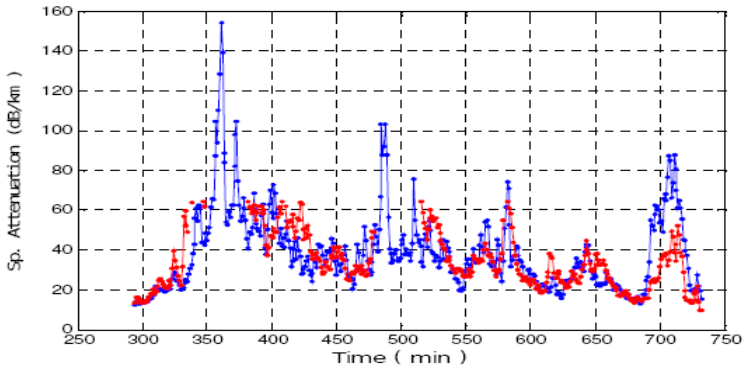

(b)

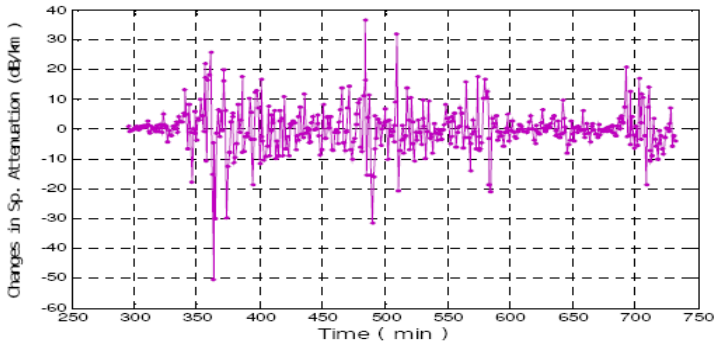

(c)

Figure 3.6: Time series profiles of a fog event at Milan, Italy

by the transmissiometer, are 224, 130 and 80.24 dB/km, respectively.

These are the largest attenuation values measured during the experimental campaign. Fig.

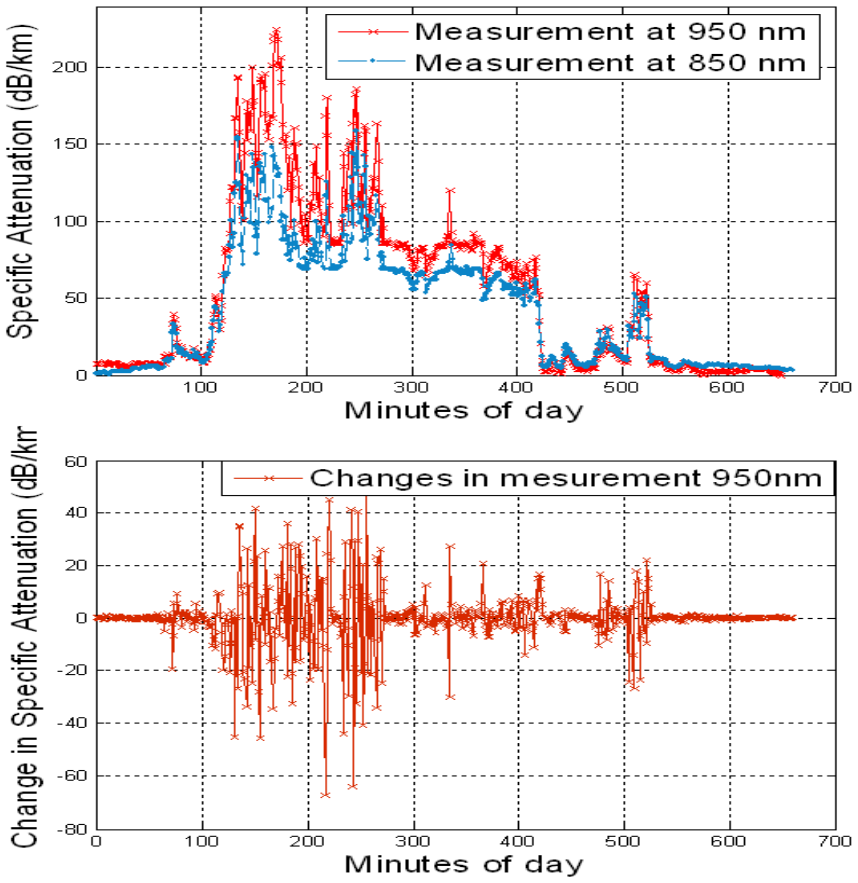

Figure 3.7: Time series profile of a fog event at Graz, Austria

3.6(c) and Fig. 3.7(c) show the variations in specific attenuation observed in Milan and in Graz, as obtained by subtracting the attenuation at the n^{th} sampling time to the one at the $(n+1)^{th}$ sampling time [96]. When attenuations are comparable in the two cases, similar values of attenuation variations were detected. During the measurement period, from September to February, 20 events were recorded in Milan (see Table 3.2), during which

- no precipitation was detected, and
- path attenuation exceeded the value corresponding to 1 km visual range (see (7)) for more than 30 min.

The above visual range value is conventionally used as the upper limit for fog occurrence, according to the International Visual range Code. In seven cases, the attenuation exceeded the dynamic range of the receiver. The value of 60 dB/km corresponds to a visual range around 250 m, which is roughly the limit for moderate fog, lower values being associated

with thick fog and dense fog. In about half of fog events detected in Milan, the maximum specific attenuation exceeded 60 dB/km. On the whole, specific attenuation was in excess of 60 dB/km during about 0.86% of the measurement time, a non-negligible value at all. Two-year measurements showed that the above value of specific attenuation was exceeded during 0.3% of time, confirming that the winter months are the most challenging for optical propagation in the measurement area. A similar analysis has been carried out on Graz data, the results of which being reported in Table 3.3. Differently from Milan, measurements in Graz were not continuous due to limitations of data storage; hence some episodes could not be detected during the measurement period. In Graz, only two events have maximum specific attenuation less than 60 dB/km, while all but two have a 99% specific attenuation above it [96].
Graz and Milan are the two continental locations and at both locations the radiation fog frequently occurs during winter months. It is interesting to compare our attenuation results, for the two locations, in order to get an insight into the radiation fog microphysics and its related characteristics for the two locations as observed by the two FSO links installed. For this purpose Fig. 3.8 shows a plot of the specific attenuation values detected in the two sites which are compared for the median specific attenuation against the 99^{th} percentile of each fog event. It can be noticed that Milan moderate fog data exhibit a certain degree of correlation between the two selected values of the attenuation distribution. On the other side, Graz data are much more scattered: even the events that exhibit median specific attenuation values similar as the ones in Milan have a 99th percentile spreading from 50 to more than 200 dB/km. Therefore, not only fog intensity is higher in Graz than in Milan but also the physical process of fog formation, growth and dissipation seem to be different. The above differences can be explained as follows. Despite Milan and Graz are located in the same temperate area, there are two major differences that are expected to affect to some extent measurements,

- The climate during winter is colder in Graz, where daily temperature minima are often below 0 °C, while in Milan temperature rarely falls below 0 °C, and
- Milan is a large city and despite the measurement site is located about 3 km from the center of the city, the microclimate is that of a dense urban area. On the other side, Graz is a midsize town, with the optical link being located in a suburban environment with no tall buildings and many wide open areas around.

Therefore, it is reasonable that fog episodes are heavier in Graz than in Milan [96].

3.2.5 Time Series Analysis and Comparison of Measured Maritime or Advection Fog Attenuations

Like continental fog environment, studying the behavior of optical signal propagation in maritime fog environment is also very important. In this section optical signal attenuation

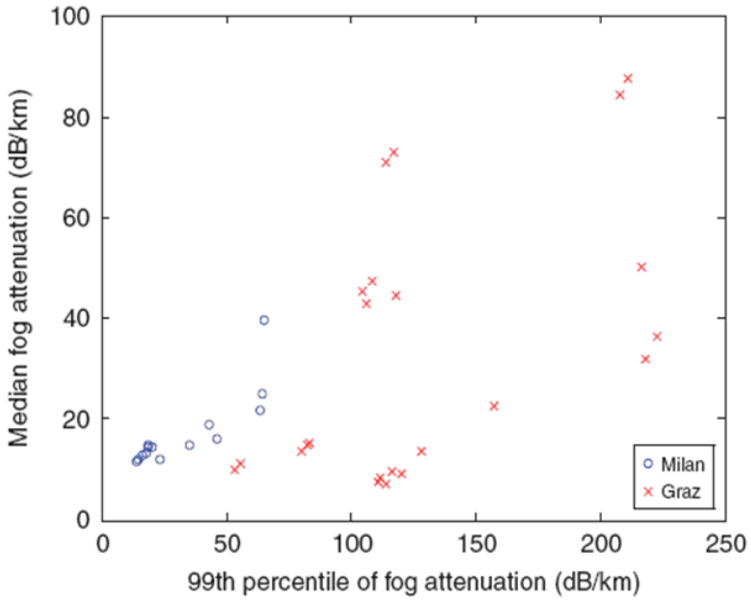

Figure 3.8: Median laser attenuation against attenuation at the 99th percentile as detected in Milan and Graz during fog events

predictions and analysis of the measured attenuations in dense maritime fog conditions is presented. Optical signal attenuations in dense maritime fog environment can be predicted to a good approximate by employing Mie scattering theory dealing single scattering assumption and considering the MGDSD for the dense maritime fog droplets. Fig. 3.9 shows a plot of the predicted specific attenuation value for dense maritime fog at Nice, calculated using Mie theory and standard modified gamma distribution parameters. The plot shows no wavelength dependency for simulated wavelengths from 650 nm to 1050 nm at 10 °C temperatures. Even with the change of temperature, no wavelength dependency was found.

Dense maritime fog attenuations were measured on a very short distance FSO link (about 28.3 m) during year 2004 at Nice under COST 270 short term scientific mission. The measured attenuation results are already presented and analyzed in detail in the literature [27, 92] on the basis of visibility range dependent empirical models. It was observed that dense maritime fog may reduce the FSO link distances up to 28 meters only. The observed changes in attenuation using 950 nm wavelength, and corresponding histogram showing the probability of changes to higher or lower attenuation levels from one second to the next are presented in Fig. 3.10 below. This mentioned plot shows the time series of changes in specific attenuation (left), and the histogram of changes in attenuation (right) for a dense maritime fog event over a minute scale.

From the analysis of actual measured optical attenuations against a very dense and settled

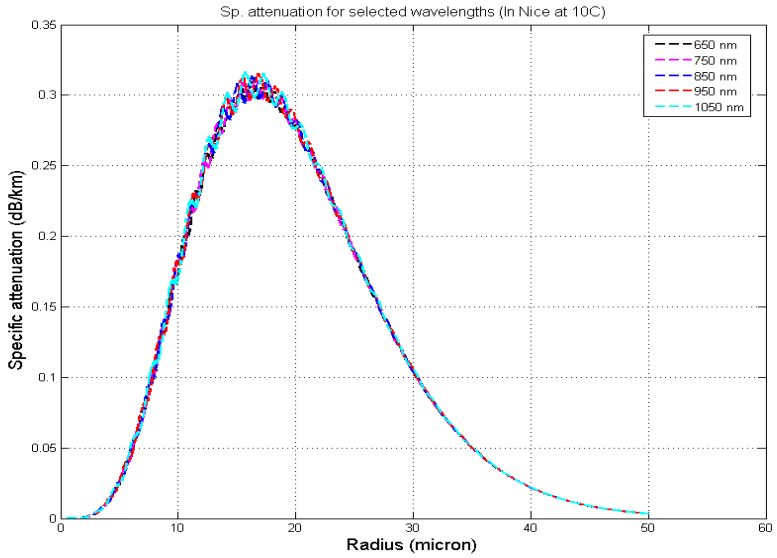

Figure 3.9: Predicted specific attenuation at 10 °C for dense maritime fog conditions

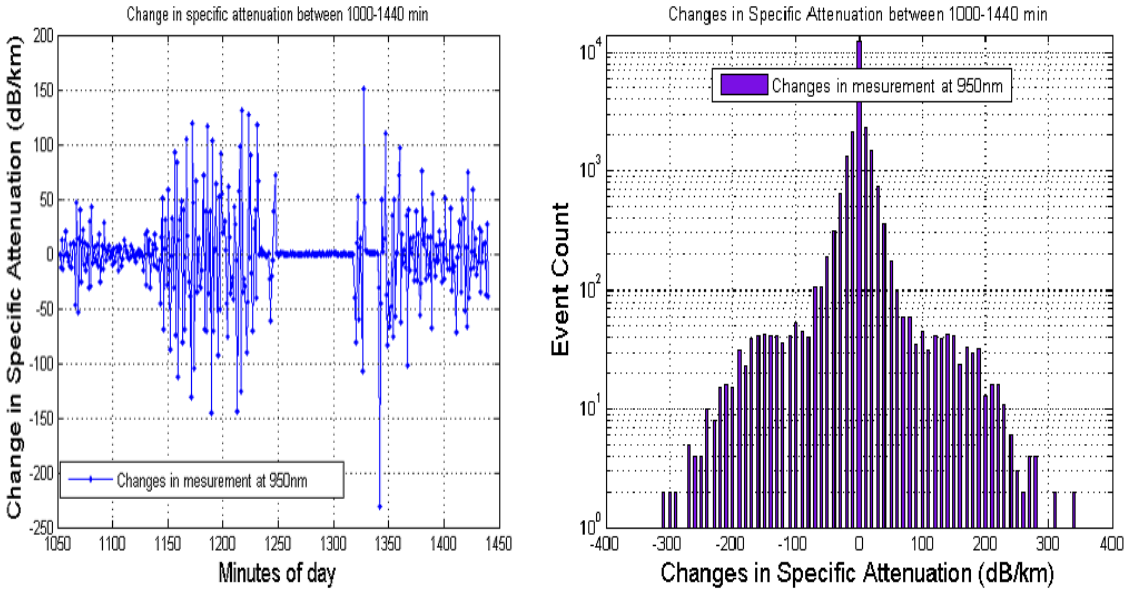

Figure 3.10: Time series profile of dense maritime fog attenuations

maritime fog event over a 28 m FSO link, we observe from the changes in attenuations and the corresponding histogram plots that the mean specific attenuation is about 388.92 dB/km over a minute scale. The peak attenuation value measured on a original time resolution of 1 value per second is about 760 dB/km. But when averaged over a minute scale the peak attenuation value is about 480 dB/km. Analyzing the changes in attenuation over a second

scale reveals that dense maritime fog attenuations have a mean of -0.0158, a variance of 1372.3, and a standard deviation of 37.0445. The observed changes occur very rapidly on a second scale reaching up to +/- 300 dB/km, and when these changes in attenuation are averaged over a minute scale then the value is about +/- 200 dB/km. That means even if the mean and averaged attenuation could be compensated by the margin of the installation, still the high variability of attenuation can cause link disruptions. As we have observed through simulation of complex refractive index of water for different temperature that no significant changes in the real part of complex refractive index and complex permittivity are observed even with the temperature variation of $\pm$ 20 °C as can be seen in Fig. 3.1 and Fig. 3.2, above. The main reason for these sudden changes in optical attenuations can be the influence of wind speed and direction and the inherent property of inhomogeneous characteristics of the maritime fog.
Fig. 3.11 shows the comparison between Kim and Kruse models for changes in specific attenuations for the same dense maritime fog event as mentioned above. The attenuation values shown here are derived from the visibility range values recorded by the transmissiometer and are not the actual measured attenuation values. The visibility range values vary from 26 m to 1000 m corresponding to this particular fog event and so are simulated for this range to compute corresponding optical attenuations as shown in Fig. 3.11. Statistical evaluation of the computed attenuation data by this approach is known as the zero hypothesis. The Kruse model has the mean of the histogram around 32.13 dB/km and the variance 27.75 dB/km, while Kim model has the mean of the histogram around 7.20 dB/km and the variance about 23.36 dB/km. Besides the mentioned spreading of the attenuation data, even if there remains some spreading then it is quite clearly evident that for dense maritime fog no wavelength dependency can be expected for the investigated wavelengths between 550 and 1050 nm. In the Fig. 3.11, it is clearly evident that the Kim's model is more accurate and appropriate while modeling optical attenuations against dense maritime fog conditions when visibility range is usually very limited less than few hundred meters.

3.2.6 Critical evaluation of measured attenuation results on the basis of 2 and 5 percent transmission thresholds

In the literature two different values of transmission threshold are considered to define the visibility range; namely the 2% and 5% thresholds. Kruse et al., Kim et al., Pierce et el. and Nebuloni et al., considered 2% threshold [86, 40, 85, 107], whereas Gebhart et al., Al Naboulsi et al. and Kolka et al. consider 5% transmission threshold [27, 87, 83]. According to current definition of visibility range the value of transmission threshold is taken as 5% [94, 92, 108]. In this section, a comparison between simulated results based on 2% and 5% thresholds for Kruse and Kim models is made and then measured fog attenuation data is analyzed for the two mentioned thresholds. In Fig. 3.12, Kim model and Kruse model at 2% and 5% transmission thresholds are simulated for optical wavelengths in the

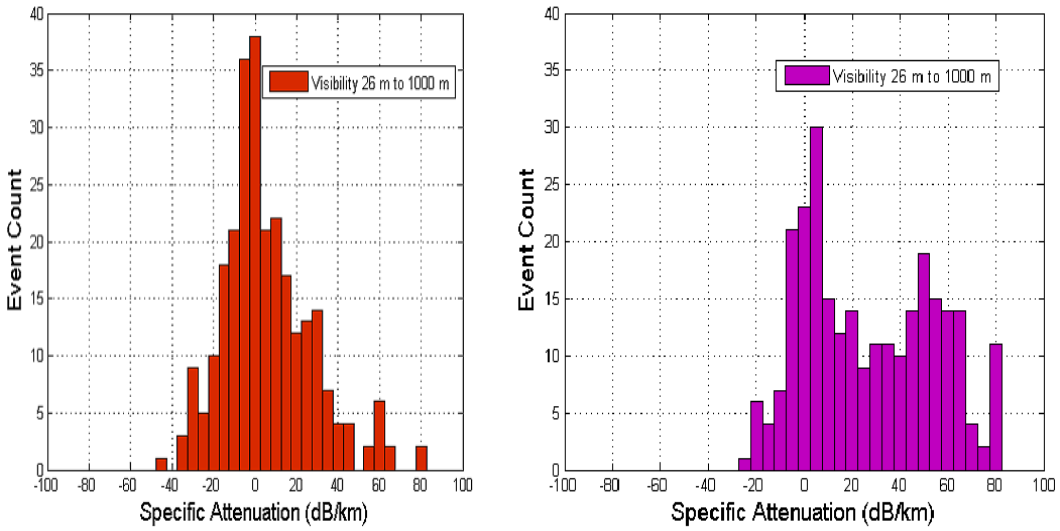

Figure 3.11: Comparing Kim(left); and Kruse models (right) for dense maritime fog

range between 550 nm to 10 μm. The plots as shown in Fig. 3.12(a, b) and Fig. 3.12(c, d) are simulated for Kim model at 2% and 5% thresholds, respectively. In Fig. 3.12(e, f) Kruse model is simulated for 2% and 5% thresholds. In simulations of Kim model for the two mentioned thresholds, there is no advantage of any particular optical wavelength up to a visibility range of 500 m. For visibility range $>$ 500 m, however, the longer wavelength performs much better as compared to the shorter wavelengths in terms of incurred optical attenuations. Thats why it is preferred that for relatively long distance FSO links, longer wavelengths be used as they provide much better mitigation against atmospheric effects. However, by Kim model for short distance optical links having visibility range $<$ 500 m, there is no advantage of using any particular wavelength over the other wavelengths. Simulations of the Kruse model for 2% and 5% thresholds show that there is enough advantage of using longer wavelengths even for short distance FSO links $<$ 500 m. For example by Kruse model, we may get approximately 40 dB/km (for 2% threshold), and 50 dB/km (for 5% threshold) less attenuations when employing 10 μm wavelength as compared to 1550 nm wavelength against a visibility range of about 100 m, respectively.

The Table 3.4 below shows the comparision of Kruse and Kim models at 200 m and 800 m visibility range for 850 nm, 950 nm, 1550 nm and 10 μm wavelengths. So for example, using 10 μm wavelength against a visibility range of 800 m the optical attenuations are almost twice (200%) as high at 2% as they are at 5% thresholds for Kruse and Kim models. Whereas, for a visibility range of 200 m with the same wavelength the optical attenuations predicted are much greater i.e., approx. 270% as high as at 2% thresholds in comparison to 5% thresholds of the both Kruse and Kim models.

Now the comparision of measured fog attenuation data (of moderate continental fog and dense maritime fog) is being presented for both Kruse and Kim models with 2% and 5% transmission thresholds. As already mentioned that the fog environment at Milan (Italy)

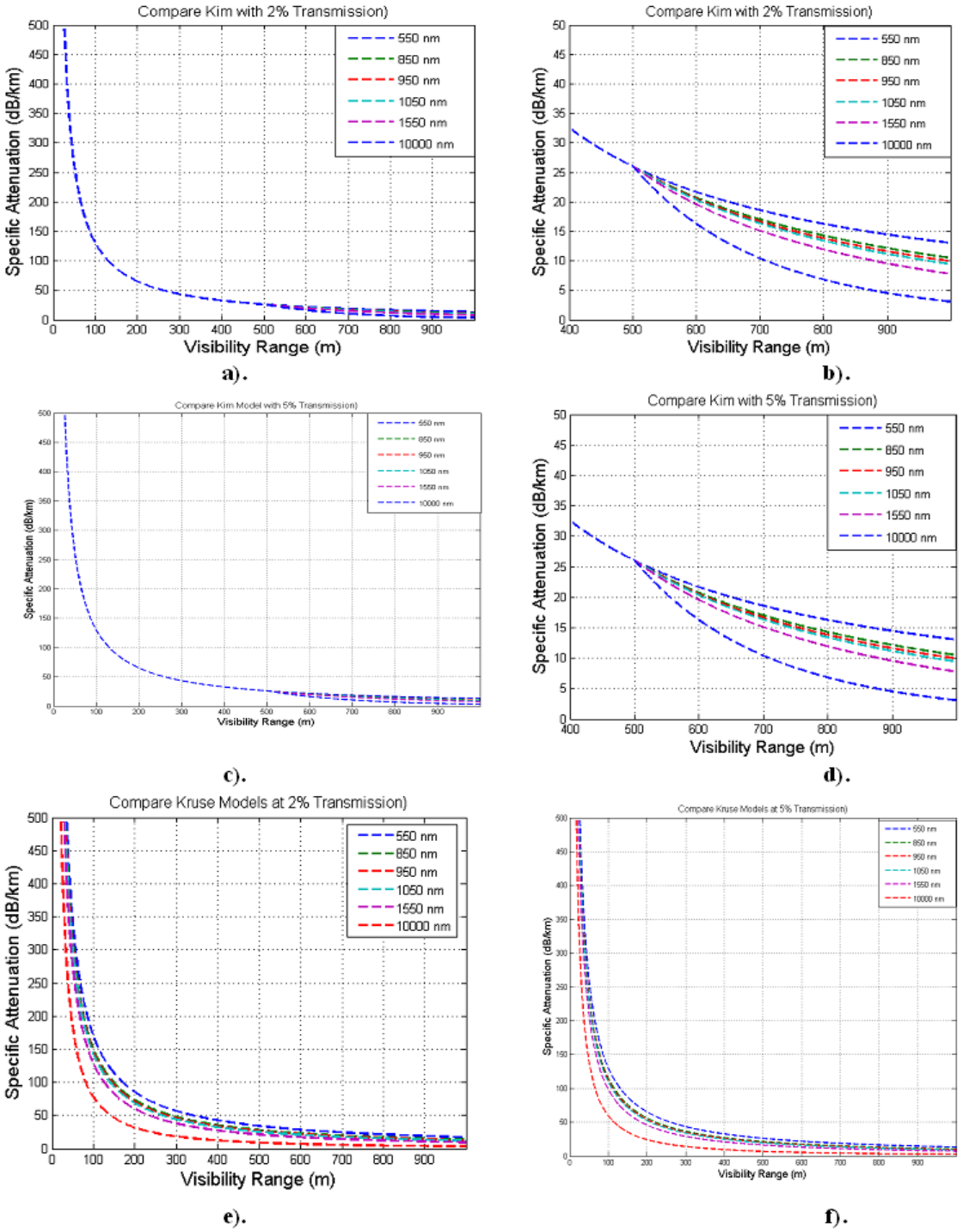

Figure 3.12: Kruse and Kim models simulations at 2% and 5% transmission thresholds

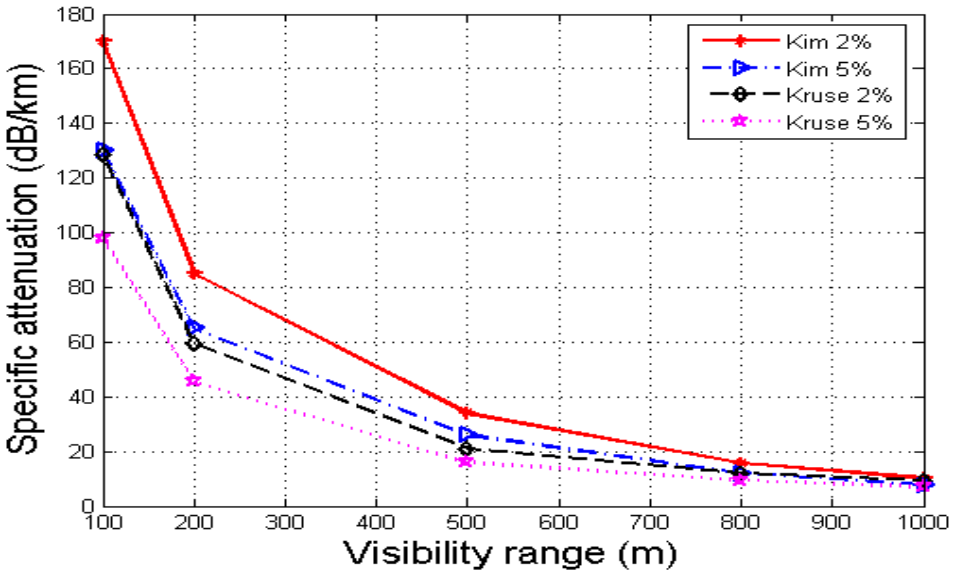

Figure 3.13: Comparison of predicted optical attenuations using Kim and Kruse models for 2% and 5% thresholds at 1550 nm optical wavelength

and Prague (Czech Republic) is of moderate continental fog type, whereas that of La Turbie, Nice (France) is of dense maritime fog, so we analyze this data to see whether it fits to any particular model at a particular transmission threshold. Although a large fog attenuation data set for Graz (Austria) of continental fog environment is also available but the corresponding visibility range values are missing as it was not measured in the field. In Fig. 3.14 the fog attenuation data measured at Milan on 11^{th} Jan. 2005 was re-arranged as a series of specific attenuation (dB/km) over visibility range . Every red dot means one measured value per minute and every plus symbol means optical attenuation value estimated from visibility range. It is important to mention here that fog attenuation values are measured at Milan assuming Kim model for 2% transmission threshold. It is visible through this plot that for attenuation values measured corresponding to visibility range values between 200 m - 500 m are bit more scattered as compared to those attenuation values that correspond to visibility range between 500 m - 1000 m. This spreading between measurement points and the calculated curve can be explained by considering the varying particle size distribution in the fog over time, as the measurement data is now re-arranged and not dependent on time any more. The visibility range values $<$ 500 m correspond to dense fog conditions, typically. Therefore, in such situations the particle concentration may change very rapidly with time depending upon the wind speed and direction and hence may cause relatively larger spread in the measured data points. The plot as shown in Fig. 3.14, the measured data points do not seem to suggest any real reasons for preferring one empirical model over the others. However, for visibility range values $<$ 800 m the data points are more centered around Kim and Kruse models with 2% transmission threshold but for vis-

ibility range $>$ 800 m the data points converge over Kim and Kruse models with 2% and 5% transmission thresholds.

Wavelengths (nm)	Visibility Range (m)	Kim (2%) dB/km	Kim (5%) dB/km	Kruse (2%) dB/km	Kruse(5%) dB/km
850	200	85	65	73.239	56.006
950	200	85	65	70.504	53.915
1550	200	85	65	59.632	45.601
10,000	200	85	65	31.513	24.098
850	800	18.648	14.261	16.776	12.829
950	800	18.036	17.793	15.793	12.077
1550	800	15.573	11.909	12.106	9.2574
10,000	800	8.9016	6.8071	4.3984	3.3635

Table 3.4: Comparision of attenuations at different optical wavelengths considering 2% and 5% thresholds for a visibility range of 200 m and 800m

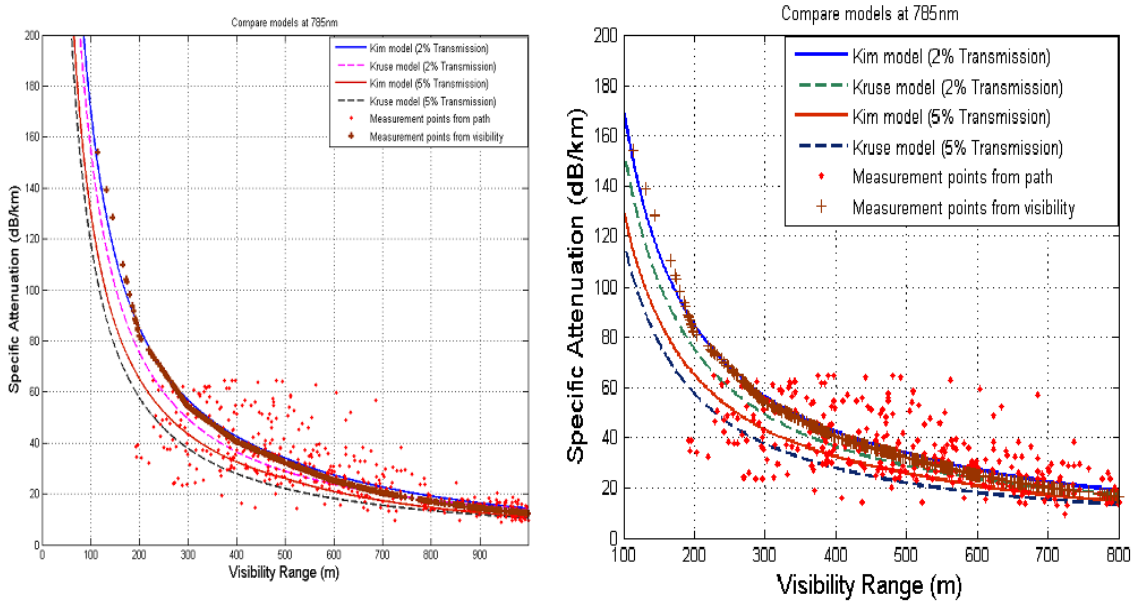

Figure 3.14: Milan's measured fog attenuation data comparison using Kruse and Kim models (left); zoom in view (right)

In Fig. 3.15, the measured attenuation data is also compared with Kim and Kruse models with 2% and 5% transmission thresholds for the moderate continental fog event measured on 28^{th} Sept. 2007. The transmission threshold considered for Prague case was 5% using Kruse model. The measured attenuation data points are marked with red stars. Here again

large deviation between data points and the Kruse model with 5% transmission threshold is observed for visibility range values < 400 m and it goes on decreasing with the increase of visibility range till 1000 m. It is easily observable that the data points are more concentrated around Kruse model with 5% transmission threshold as compared to the other models and so is the preferable model for the fog conditions at Prague. Moreover, the observed scatter of the data points may be attributed to the varying DSD of the fog particles with the variations in wind speed and direction and to the sensitivity of the instruments in measuring the observed attenuations.

Fig. 3.16 shows the comparison of measured optical attenuations at 950 nm wavelength

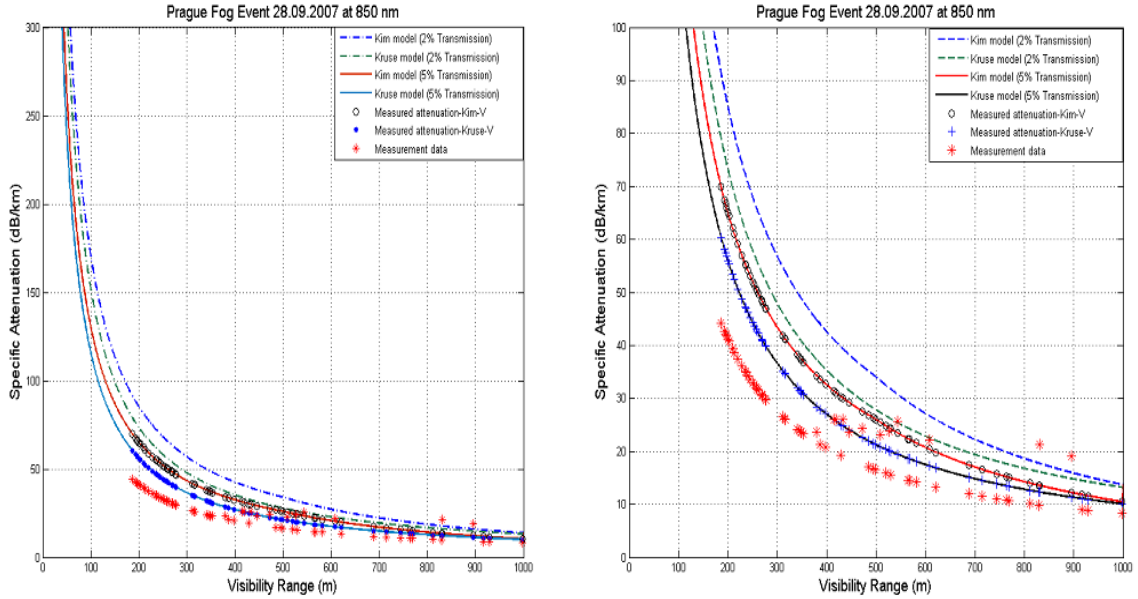

Figure 3.15: Prague fog event attenuation data comparison with Kruse and Kim models (left); zoom in view (right) collected at 850 nm wavelength

with Kruse and Kim models for the dense maritime fog case. The plot shows the data points marked as red against Kruse model (left) and Kim model (right) at 5% transmission threshold. It is clearly evident that the Kim model is more suitable than the Kruse model for measured data points against visibility range < 500 m as the data points are more concentrated around Kim model than the Kruse model for this range. However, for visibility range conditions > 500 m the data points seem to be more concentrated around Kruse model than the Kim model. Therefore, Kruse model is the preferable model in dense maritime fog conditions having visibility range > 500 m to 1000 m.

Hence, we may safely conclude that in moderate continental fog environments no particular model is preferable over the other. However, it is better to use Kim model with 5% transmission threshold as Kim model better differentiates the visibility range conditions < 500 m. In dense maritime fog case it was observed that at 5% transmission threshold Kim model is more appropriate for dense fog conditions but for moderate maritime fog

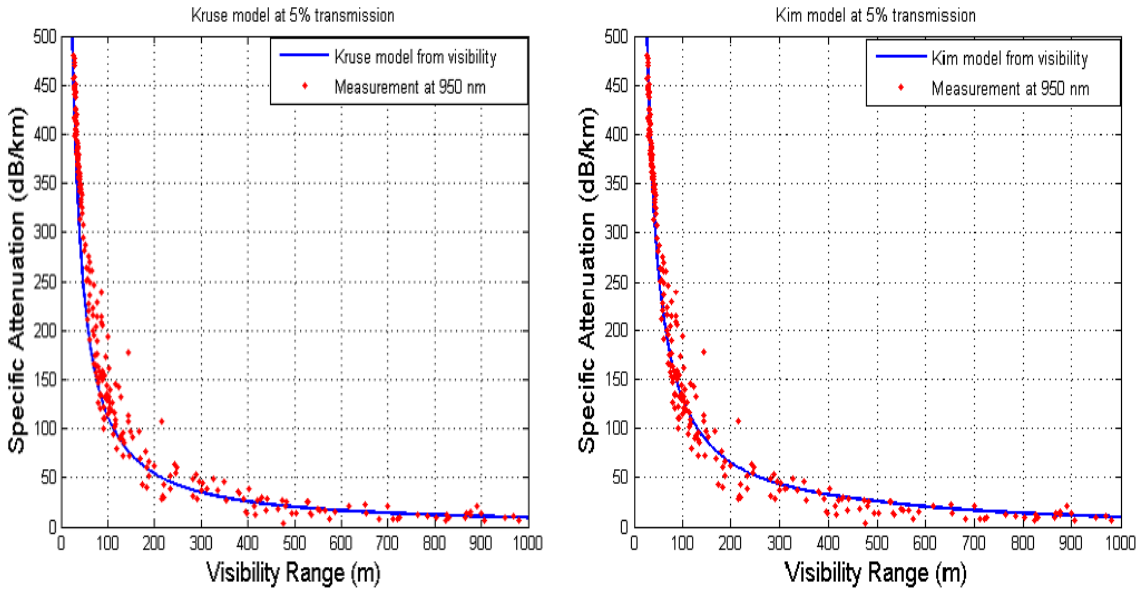

Figure 3.16: Dense maritime fog attenuations comparison using Kruse and Kim models

conditions Kruse model seems better choice.

3.2.7 Impact of Fog's Seasonal and Diurnal Variability on Optical Transmissions

For FSO link design and installation the extreme attenuations determine the requirements to get the acceptable link unavailability. The character of the various types of fog can be further explained by examining the temporal distributions of fog occurrence frequencies for each fog type. Frequencies are calculated using Equation 4.2, 4.3 and 4.4 applied to events of each type. It is interesting to see the seasonal and diurnal behavior a particular fog on the terrestrial FSO links. In this section, seasonal and diurnal behavior of continental fog and dense maritime fog is evaluated from the perspective of optical signal attenuations measured on experimental FSO links installed at Graz (continental), Milan (continental) and Nice (maritime). This information is particularly useful in the link budget designs for future FSO links at locations having such kind of fog environments.
For our analysis of the fog attenuation data the time series of total attenuations A_t is considered, which is the attenuation due to the different hydrometeors like water vapors, clouds, fog and rain etc. If we denote the cumulative distribution of total attenuations by $P_{A_t}(x)$, which is the probability that at an arbitrary time interval t_0 the total attenuation exceeds x dB so that the optical link remains unavailable. This is given by the following relationship (Equation 3.18),

$$P_{A_t}(x) = P[A_t(t_0) > x] \tag{3.18}$$

Where x is the normalized link margin such that x=x*/L (dB/km) and its value also represents the highest value of the atmospheric attenuation, and x* is the link margin whose upper bound is determined by the dynamical range of the receiver having a typical value of about 30-40 dB [109]. The percent availability of the FSO links such that it fulfils the quality of service (QoS) requirements i.e., received optical power falls below the threshold limit of the receiver sensitivity. It can be expressed by Equation 3.19 below,

$$Availability = (1 - P[A_t(x)]) \times 100 \tag{3.19}$$

When the received optical power at the receiver end falls below the sensitivity threshold of the receiver i.e., the total atmospheric attenuations or losses are more than the link margin of the optical link then a fade occurs. These fades can be described as short term fades or the long term fades. Short term fades can be due to small duration optical power interruptions at the receiver end. The causes may be atmospheric scintillations or some object flying through the optical beam link. On the other hand the long term fades occurs due to precipitation like rain, fog, snow etc., and their duration can be in an hour or more than an hour.

Seasonal variations of optical attenuations

Graz has a continental fog environment and fog is a very common phenomena especially in winter starting from September till mid of March. The longest fog attenuation measurement campaign over a 80 m FSO link took place in Graz that started at the end of September 2005 and lasted till start of March 2006 i.e., almost 5 complete months. Some 21 major fog events were recorded that had minimum duration of greater than half an hour during this time period. Usually moderate kind of continental fog occurs in Graz but few dense continental fog events were also recorded over the 80 m link distance showing optical signal attenuations easily exceeding 100 dB/km. The frequency and persistence of the continental fog, like most other meteorological effects, shows a marked seasonal dependence. Especially, in winter the probability of occurrence of continental fog at Graz is much higher as relative humidity reaches more than 80% and temperature remains close to 0°C. The continental fog attenuation data of five winter months (Oct. 2005 Ű Feb. 2006), on a 80 m FSO link installed at Graz, is plotted for CDF exceeded (%) against optical attenuations and is given in Fig. 3.17 below [109, 110].

This plot clearly shows that the specific attenuations are comparatively higher in January 2006 as compared to the other months. Whereas October 2005 shows relatively lower values of signal attenuations since normally in October fog starts to evolve due to favorable meteorological conditions. In the months of December and January usually the air remains saturated enough most of the time with enough cooling such that relatively dense continental fog accumulates, as is clearly evident from this plot. In order to see the variability of fog attenuations over this mentioned period, a contour plot is drawn of the recorded

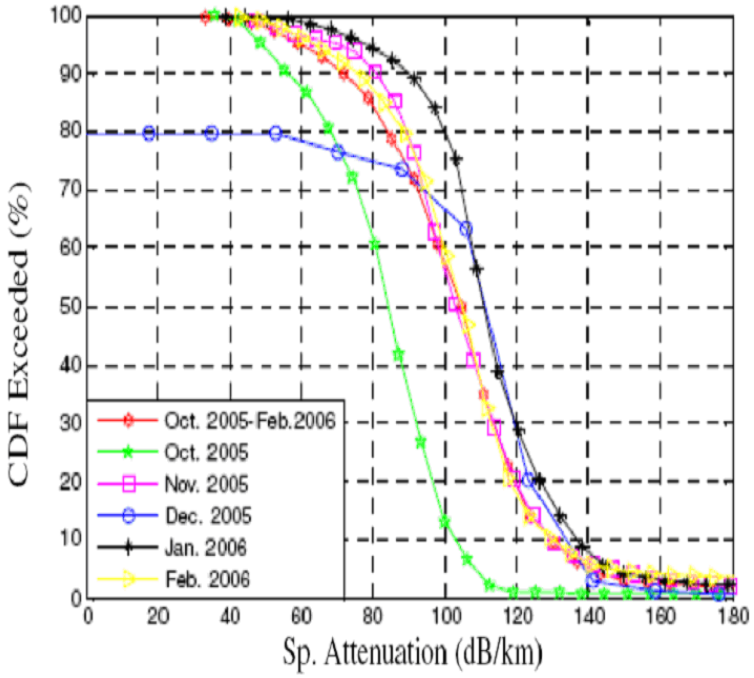

Figure 3.17: Monthly variation of continental fog attenuations at Graz

continental fog attenuations data measured on a second time scale. The contour plot as given in Fig. 3.18, identifies the time intervals that have the highest and lowest values of fog attenuation during the above mentioned campaign [109, 110].

From this contour plot, it is evident that few individual events of very dense continental fog occurred depicted by very high attenuations in dB/km. However, due to the very random high attenuations, it is difficult to conclude any particular time slots when the fog attenuations are particularly high. But from this plot, it is clear that especially in October to end of January the overall attenuations are on the higher side with attenuations in the range of 120 dB/km-180 dB/km on a second scale. The optical signal attenuations are comparatively lesser in September and February as compared with the other months in winter. The possible explanation of this behavior is that usually in these months (i.e., winter starting months and the ending months of winter) the climatic conditions are characterized by relatively lower relative humidity values around 70-80 and relatively higher temperatures approaching 10 degrees Celsius. So there is a very high likelihood of a less severe fog occurrence i.e, a kind of light continental fog or moderate continental fog with visibility range most of the time well over 500 m.

Just for the sake of completion, Fig. 3.19 shows the moderate continental fog attenuations measured over 319 m FSO link installed at Milan, Italy operating at 785 nm optical wavelength. The measured fog attenuations for winter months (Nov. to Feb.) are compared with optical attenuations (without fog) for summer months (May-July) in this mentioned plot. It is clearly observable that attenuations are particularly high in winter months (in the

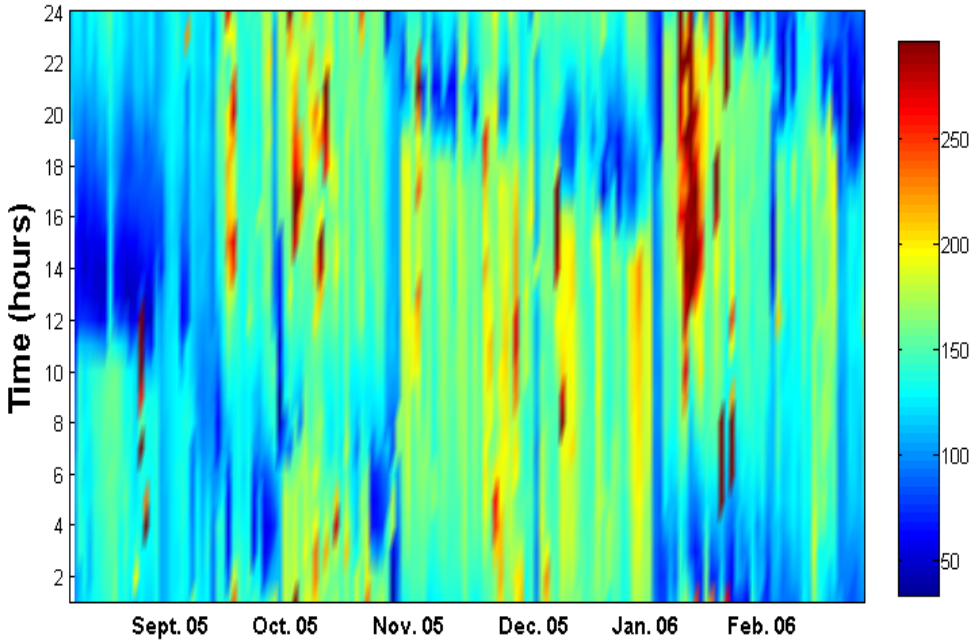

Figure 3.18: Contour plot of continental fog attenuations for Graz

presence of fog conditions) than the summer months (without fog); almost twice as high in winter than in summer months [109, 110].

For a more detailed study of seasonal variations of optical attenuations inside continental fog conditions a plot representing cumulative distribution frequency (CDF) of optical attenuations for the FSO link installed at Milan is given in Fig. 3.20 [111]. Milan is a big city and has an urban continental environment. The continental fog attenuation data is of two years (i.e., Apr. 2004ŰMar. 2006) for Milan. The attenuation data is for 785 nm optical wavelength transmitted on a 319 m FSO link. The optical signal attenuations are greater than 30 dB/km for about 1% and are greater than 60 dB/km for about 0.3% of the yearly time. Similar attenuation behavior like Graz can be noticed for the Milan case as the specific attenuations are highest for the month of January and are lowest in comparison for the month of June. Moreover, attenuations are very low in comparison from April to September than from October to March. This suggests variable achieveability of availability and QoS figures for terrestrial FSO link corresponding to seasonal dependence of continental fog attenuation behavior.

In short, the temporal distribution of continental or radiation fog events, represented by events recorded at Graz and Milan indicate that radiation fog events sparsely occur in summer (April to September) and has minimum frequency of their occurrence, but these fog events occur quite frequently with a very high frequency in winter months (September to end of February) (see Figs. 3.19 & 3.20) [109, 110].

- Winter (Nov-Feb)

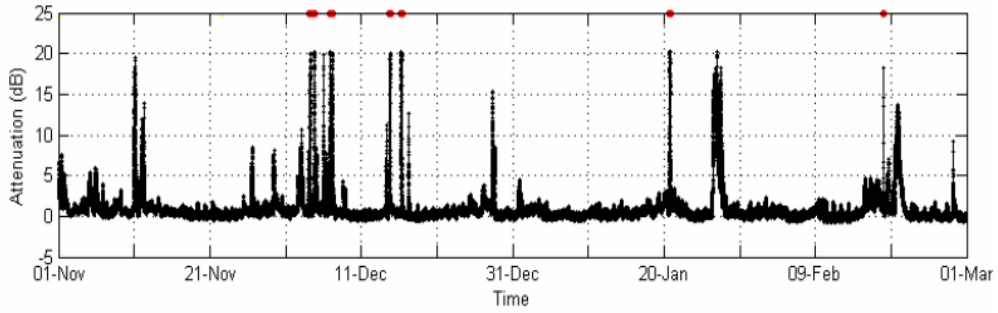

- Summer (May-Jul)

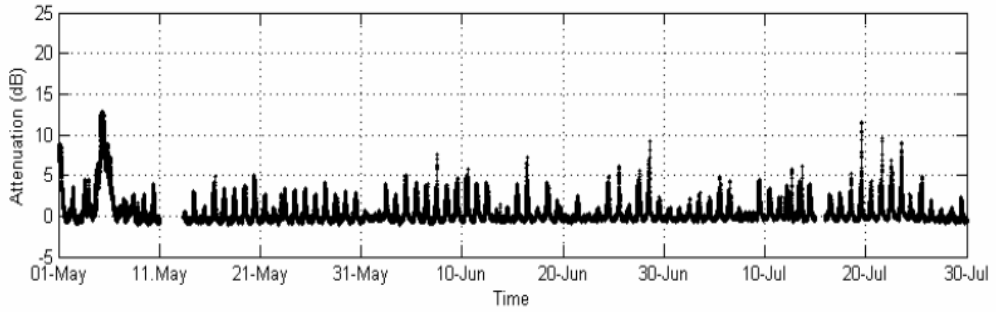

Figure 3.19: Seasonal variations of continental fog attenuations for Milan, Italy [111]

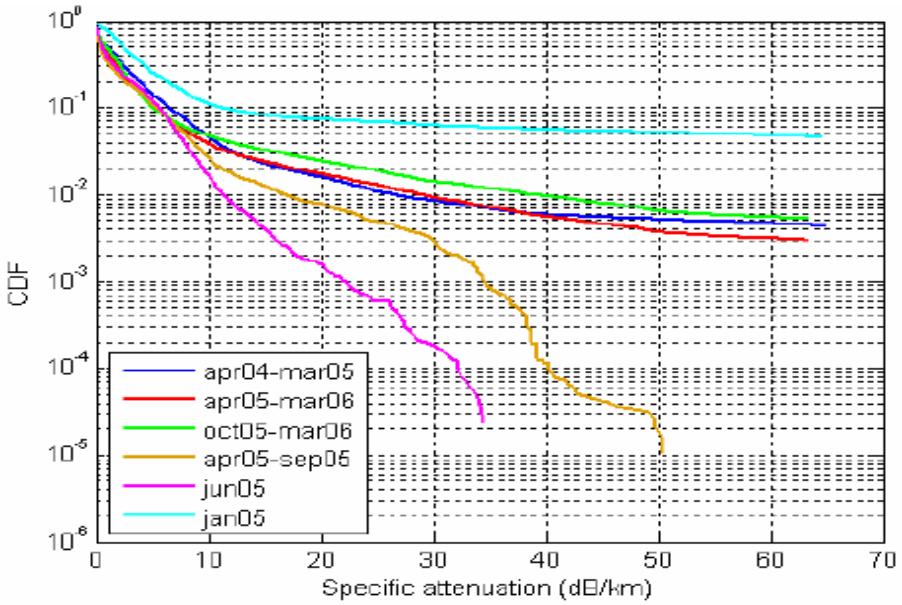

Figure 3.20: CDF of continental fog attenuation's seasonal variation at Milan [111]

Diurnal variations of optical attenuations

Apart from observing the seasonal dependence of continental fog attenuations and maritime fog attenuations, an analysis about the optical attenuations diurnal behavior would further reveal more interesting insights about the trend of optical attenuations. We analyze the diurnal behavior of continental fog attenuation values measured on a minute scale recorded in Graz and Milan, and dense maritime fog attenuations recorded at Nice in for four non-overlapping time intervals of 6 hour each i.e., 00:00-06:00, 06:00-12:00, 12:00-18:00, and 18:00-24:00.
As evident from the contour plot of optical attenuations measured at Graz (Fig. 3.18), normally radiation fog events tend to begin during the the night hours and especially in the second half of the night [109, 110]. This is clearly evident during month of September. A larger proportion of these fog events begin earlier in the night during the peak in October and January. But then from November till end of December, most of these fog events begin in the second half of the night. Moreover, in October and January few very dense fog events occur sporadically with optical attenuations reaching well over 150 dB/km on a second scale. The duration of such very dense fog events is normally not very long and may last up to 3-6 hours depending upon the climatic conditions and geographical locations. The behavior of optical attenuations diurnal variations in terms of CDF exceeded $(\%)$ against optical attenuations recorded at Graz can be seen in Fig. 3.21 [109, 110]. As can be clearly seen that major contribution of optical attenuations comes from radiation fog occurring in the evening and night hours than in the early and late morning hours. The optical attenuations are particularly highest during the time interval of 12-18 hours as compared to the other three remaining six hour intervals and thus this time interval can be termed as the worst time interval in terms of optical attenuations at Graz. Whereas, optical attenuations are least in the time interval of 00-06 hours in comparison to the remaining three time intervals.
Diurnal variations behavior of optical signal attenuations inside radiation fog conditions at Milan was also investigated. The plot showing such variations for the same four non-overlapping time intervals of 6 hour i.e., 00:00-06:00, 06:00-12:00, 12:00-18:00, and 18:00-24:00 is shown in Fig. 3.22. The data set for diurnal variations analysis for the Milan case comprises of 2 winter months i.e., January 2006 and February 2006. The plot shows optical attenuations reaching up to maximum 66 dB/km using 785 nm optical wavelength. This is due to the limitation imposed by the used optical transceiver dynamic range such that the receiver cannot detect higher values of optical attenuations than this given limit. The maximum value of specific attenuations reached up to 154 dB/km, computed using visibility range dependent empirical formula given by Kruse and Kim models. The radiation fog diurnal behavior here at Milan is similar like that for the Graz case as the optical attenuations exceeding 10 dB/km are highest for the 18-24 hour time interval then followed by optical attenuations for the 00-06 time interval. Whereas, the attenuations are least during the 12-18 hours time interval. Hence by analyzing the diurnal behavior of

optical attenuations for continental or radiation fog case at two geographically separated locations (Graz & Milan), it can be safely concluded that diurnal behavior is almost the same and it follows the same trend for the both locations. However, the peak level of optical attenuations may vary from location to location that is dependent on the microphysics and the vicinity of the location.

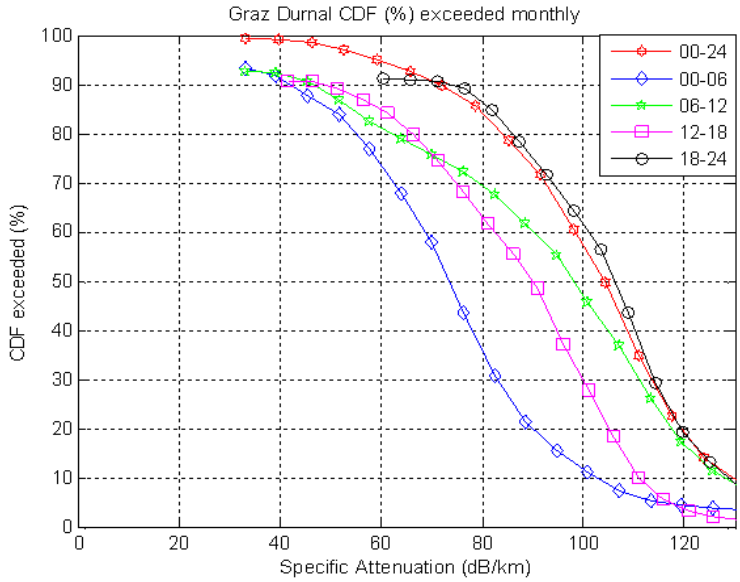

Figure 3.21: Diurnal behavior of continental fog attenuations at Graz

On a diurnal time scale, formation of advection or maritime fog takes place mostly during nighttime hours. Especially, in summer there is a higher probability of the occurrence of this type fog formation, right after the sunset with decreasing solar radiation in the evening, and it is complemented by significant frequencies throughout the rest of the night. During the night-time ground surface temperature cools down that reduces the turbulent mixing of warmer and colder air masses and as a result a stable layer of maritime fog establishes itself over the land surface. This cooler and less turbulent boundary layer causes an inland propagation of the advection fog layer under the influence of an onshore push from the remnants of the sea breeze. Contrary to the radiation fog formation trend, advection fog formation in winter usually takes place in the middle part of the night. Whereas, during the daytime the inland propagation of a coastal fog layer is determined by competing influences associated with solar warming of the landmass [112]. The inland advection of maritime fog through the generation of a sea-breeze circulation is enhanced by differential heating between the landmass and the ocean. The solar warming over land results in dissipation of advection fog due to the convectively-driven mixing of warm dry air with the advancing marine layer.

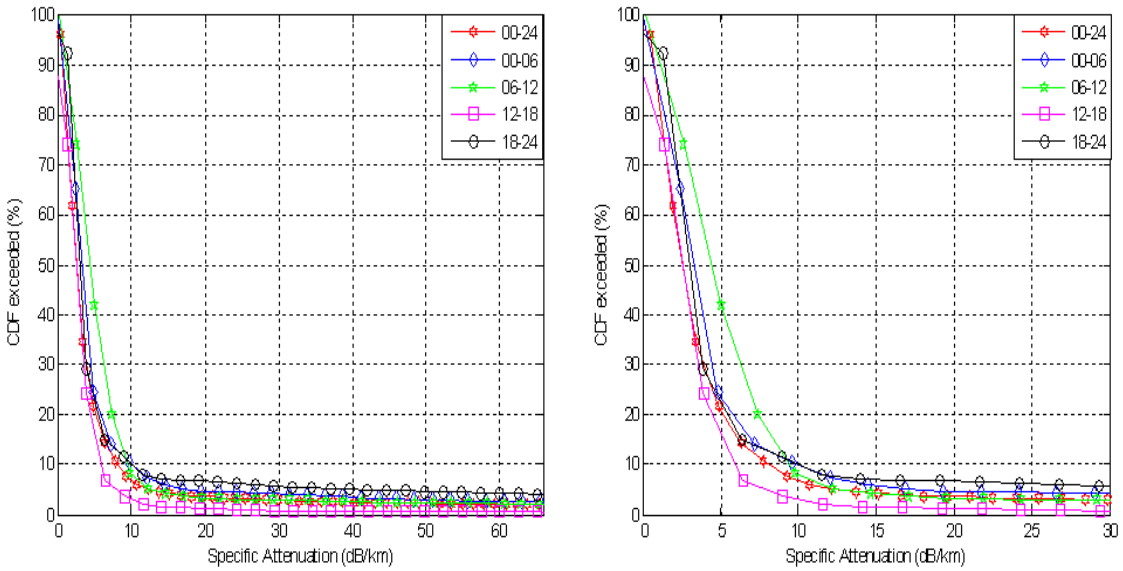

Figure 3.22: Diurnal behavior of continental fog attenuations (left) measured at Milan

In order to observe the diurnal behavior of optical attenuations for the maritime or advection fog case, we consider optical attenuation data consisting of eight consecutive days of summer i.e., from 24.06.2004 to 01.07.2004 recorded at La Turbie near Nice, France. The corresponding plot showing diurnal variations of optical attenuations at Nice is shown in Fig. 3.23 [109, 110]. The specific attenuation values shown are recorded on a seconds time scale. The diurnal variations of optical attenuations are analyzed in four equal six hour time intervals same like Graz and Milan cases. The plot shows the cumulative exceedance probability or CDF $(\%)$ exceeded against specific attenuations in dB/km.

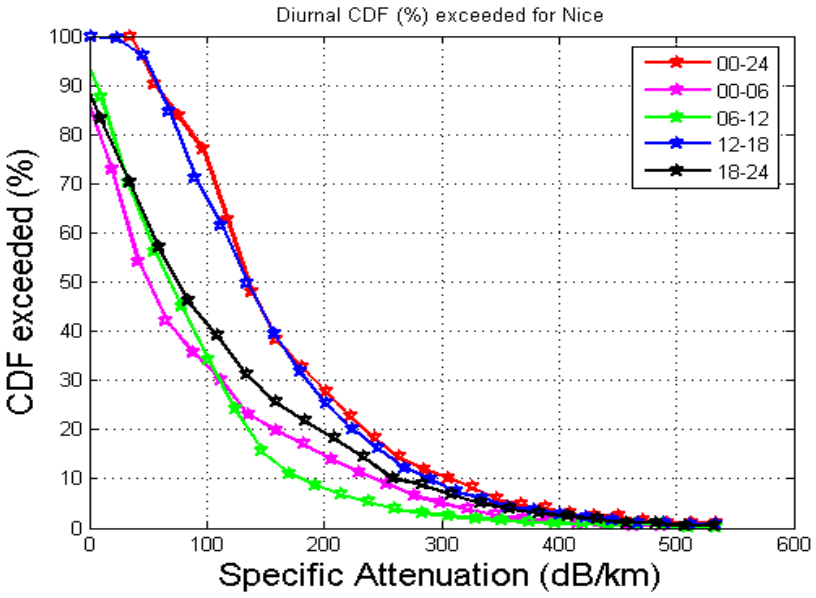

Figure 3.23: Diurnal behavior of maritime fog attenuations measured at Nice

As evident from this plot, the optical signal attenuations at Nice are highest in the 12-18 hours time interval followed by 18-24 hours time interval. Whereas, the optical attenuations are significantly lower in the 06-12 hours time interval. The cumulative statistics showing the behavior of dense maritime fog are derived from a limited samples from eight days of attenuation measurements. Therefore, they do not necessarily represent the typical diurnal behavior for maritime fog modeling studies.

ID	Initial date	Initial time	End date	End time	Duration	Max	Mean	50%	90%	99% [a]
1	24.10.2004	06:54:00	24.10.2004	11:15:00	4:21	49.52	34.48	16.21	24.87	45.79
2	25.10.2004	01:04:00	25.10.2004	03:38:00	2:26	23.84	15.07	11.84	15.65	23.55
3	25.10.2004	05:45:00	25.10.2004	12:41:00	6:56	39.13	25.24	14.81	22.46	35.27
4	25.10.2004	13:03:00	25.10.2004	13:36:00	0:33	13.87	12.03	11.62	13.47	13.87
5	25.12.2004	17:18:00	25.12.2004	17:51:00	0:33	16.38	13.38	12.90	15.05	16.38
6	29.12.2004	07:04:00	29.12.2004	07:44:00	0:40	63.99	55.87	24.87	59.96	63.99
7	07.01.2005	18:19:00	07.01.2005	22:23:00	4:04	-	-	-	-	-
8	07.01.2005	22:37:00	08.01.2005	01:03:00	2:26	-	-	-	-	-
9	11.01.2005	22:47:00	12.01.2005	06:10:00	7:23	-	-	34.98	-	-
10	12.01.2005	06:55:00	12.01.2005	07:29:00	0:34	20.28	15.99	14.61	18.07	20.28
11	12.01.2005	08:10:00	12.01.2005	08:51:00	0:41	18.57	15.25	14.78	17.28	18.57
12	13.01.2005	18:44:00	14.01.2005	13:28:00	18:44	-	-	-	-	-
13	14.01.2005	17:21:00	15.01.2005	00:52:00	7:31	-	-	-	-	-
14	15.01.2005	19:10:00	15.01.2005	20:40:00	1:30	43.46	35.05	19.04	39.39	43.23
15	18.01.2005	00:35:00	18.01.2005	01:09:00	0:34	17.67	14.25	13.10	16.76	17.67
16	18.01.2005	16:20:00	19.01.2005	03:14:00	10:54	64.78	52.33	21.74	47.45	63.65
17	19.01.2005	09:49:00	19.01.2005	10:58:00	1:09	-	-	44.69	-	-
18	25.02.2005	00:29:00	25.02.2005	01:12:00	0:43	14.61	12.49	12.18	13.78	14.61
19	25.02.2005	07:32:00	25.02.2005	08:48:00	1:16	18.24	15.08	14.31	17.05	18.17
20	28.02.2005	04:01:00	28.02.2005	08:56:00	4:55	-	-	39.44	58.28	65.11

Table 3.2: Fog episodes detected in Milan from September 2004 to February 2005

[a] The last five columns show laser attenuation values measured during fog: maximum and mean specific attenuations are shown, along with the 50%, 90% and 99% percentiles of the attenuation distribution. When fog attenuation exceeded the dynamic range of the laser receiver, any or all of the above values could not be calculated

ID	Initial date	Initial time	End date	End time	Duration	Max	Mean	50%	90%	99% [a]
1	29.09.2005	02:00:00	29.09.2005	03:12:34	1:12	81.09	21.28	13.642	78.63	80.32
2	29.09.2005	03:42:29	29.09.2005	05:11:10	1:29	84.25	22.5	15.378	79.95	83.20
3	29.09.2005	05:50:06	29.09.2005	07:29:59	1:40	83.94	22.1	14.921	79.31	82.11
4	25.10.2005	03:00:00	25.10.2005	04:32:04	1:32	109.62	41.11	45.228	93.25	104.17
5	25.10.2005	05:33:51	25.10.2005	07:03:12	1:29	113.14	40.05	43.045	95.434	106.35
6	25.10.2005	10:23:39	25.10.2005	10:59:59	0:37	118.61	43.06	47.441	97.616	108.53
7	26.10.2005	01:30:00	26.10.2005	02:31:40	1:31	117.8	34.24	7.108	109.64	114.3
8	26.10.2005	03:17:37	26.10.2005	03:59:59	0:43	119.42	38.71	9.439	111.97	116.63
9	11.11.2005	14:00:00	11.11.2005	18:32:32	4:32	55.918	14.38	11.18	52.051	55.365
10	12.11.2005	07:25:09	12.11.2005	11:00:00	3:35	53.287	15.83	10.075	50.947	53.018
11	22.11.2005	03:57:23	22.11.2005	05:59:59	2:03	111.8	29.17	7.318	108.490	110.7
12	29.11.2005	03:17:06	29.11.2005	05:59:59	2:43	121.74	40.13	9.33	115.7	120.53
13	30.11.2005	06:30:46	30.11.2005	07:31:35	1:01	112.78	31.62	8.457	109.6	111.78
14	13.12.2005	21:00:00	13.12.2005	23:37:38	1:37	128.31	45.39	13.421	119.18	127.99
15	09.01.2006	05:00:00	09.01.2006	06:11:43	1:11	115.5	58.59	70.837	109.77	114.35
16	09.01.2006	22:00:00	09.01.2006	23:52:15	1:52	117.65	53.48	73.127	112.06	117.21
17	10.01.2006	01:13:25	10.01.2006	04:59:59	3:47	118.78	17.82	44.69	115.48	117.61
18	30.01.2006	21:00:00	31.01.2006	00:38:26	3:38	159.01	37.13	22.51	125.29	157.4
19	31.01.2006	15:00:00	31.01.2006	18:06:55	3:07	218.92	62.26	50.121	207.96	216.73
20	01.02.2006	04:51:59	01.02.2006	07:02:07	2:10	224.2	85.26	87.676	198.22	210.98
21	01.02.2006	20:00:00	01.02.2006	22:24:52	2:24	213.1	83.42	84.35	197.58	207.65
22	02.02.2006	21:00:00	02.02.2006	22:48:36	1:48	224.96	53.87	36.562	199.99	222.69
23	03.02.2006	05:43:48	03.02.2006	07:59:59	2:16	213.94	78.67	32.02	195.46	218.15

Table 3.3: Fog episodes detected in Graz from September 2005 to February 2006

[a] See footnote of Table 3.2 for further explanation

3.3 Rain Attenuations

The rain is formed from the water vapor in the atmosphere. It consists of drops of water, the shape and number vary in time and space. The shape of drops depends on their size: they may be considered as spheres to a radius of 1 mm and beyond by flattened spheroids: ellipsoid from the revolution of an ellipse around its short axis. Usually an equivalent radius is considered which is the sphere having the same volume when we talk about rain droplet. Attenuation by rain is mainly due to the phenomenon of scattering as it occurs for aerosols. For optical and infrared transmissions in free-space, the wavelength is far below the diameter of raindrops and hence the drops cause significantly lower attenuation, much smaller than from fog. The type of scattering due to rainfall is called non-selective or geometrical scattering and is wavelength independent. The value of the scattering cross-section normalized, Q_d, is equal to 2 regardless of the wavelength (field of geometrical optics). The rain droplet size cannot exceed 5.5 mm because at this limit the surface tension that hold the rain droplet intact is weakened and the rain droplet is subdivided.
From the perspective of systems communications, rain is characterized by a statistical description of the perturbations induced by hydrometeors on a route determined in space and time. The intensity of rain (R) measured in mm/h, is the basic parameter used to describe the rain, locally. Its measurement is made either directly on the ground through rain gauges or similar devices whose integration time is recommended for a minute or indirectly by means of weather radar. These both techniques are particularly well suited to analyze the structure of the rain. There are two types of rain:

- The extended or stratiform rainfall have large spatial extent (hundreds kilometers), duration at a given location is long up to several hours and intensity is moderate (less than a few mm/h). The intensity of rain there is, however, not uniform, even if the spatial variation is small. Radar measurements show consistency vertical to the isotherm 0 °C.
- The convective rainfall, generally associated with frontal are of limited spatial extension, duration is usually short-term (minutes) but can be very intensive. The thunder storm events are an example of this type rain. The "horizontal" variability of the intensity of rain is very strong. There is the presence of isolated areas of very high intensity ($>$ 100 mm/h) is commonly called "Rain cells, whose characteristic size can range from 500 m to 10 km for "supercells". The knowledge of the size of these cells is obviously critical for the attenuation calculations.

In addition to the spatial distribution, knowledge of the occurrence is necessary to complete modeling of rain. The probability of exceedance, often expressed as a percentage, is the probability that a level of intensity R is exceeded or equaled. For example if the probability of overflow is 0.1%, this means that the intensity will be exceeded for R 0.012 months per year i.e., approximately 8 hours. Global maps of rain intensity exceeded for a given percentage of the year average can be found in ITU Recommendation [113].

3.3.1 Prediction of Rain Attenuations

The first model is an empirical model that relates visibility range with the optical attenuations due to rainfall [114]. Since rainfall also impairs visibility range, therefore visibility range parameter can be used to predict optical signal attenuations, irrespective of the type of rain, to a good approximation. Atlas gave the following relationship between visibility range (V) and light attenuation (γ) in rain,

$$\gamma_{rain} = \frac{2.9}{V} \tag{3.20}$$

The second model is a microphysical model based on rain droplet size distribution. The amount of optical signal attenuation not only depends on the size and number of the rain droplets that intercept the path of the radiation but also on the rainfall rate [37, 114]. The optical attenuation linearly increases with rainfall rate, whereas, the mean of the raindrop sizes increases with the rainfall rate. The expression of scattering coefficient by rain is given by,

$$\gamma_{rain} = \int_0^\infty 2\pi r^2 C(r) dr \tag{3.21}$$

where C(r) is the rain droplet size distribution (characterized by the equivalent radius). This distribution results from complex processes such as coalescence or bursting. The most commonly used empirical distribution is the Marshall and Palmer Distribution (distribution M-P) [115],

$$C(r) = 2N_0 exp(-2r\gamma) \tag{3.22}$$

Where,

$$\gamma = \alpha R^{-0.21} \tag{3.23}$$

Here R is the rainfall intensity in mm/h, α is a constant that has a value of 4.1, while γ (mm^{-1})and N_0 = 8000 $mm^{-1}m^{-3}$ are the experimentally determined constant that depend on the type of rain under study. When the size of irregularities due to precipitation becomes significant compared to the wavelength, the optical signal will be attenuated by the phenomena of reflection and refraction. The attenuation A_{rain} (dB/km) is independent of the wavelength and is a function of rainfall intensity R (mm/h) according to the following equation,

$$A_{rain} = aR^b \tag{3.24}$$

where a = 0.365 and b = 0.63. This last expression shows that for the visible and the infrared waves the extinction is independent of the wavelength. In 1968 Joss et al. have proposed a new coefficient of extinction by rain with parameters N_0, which vary depending on the type of rain studied, which lead to another expressions of the extinction coefficient [116]. Indeed, the M-P distribution is an average distribution and the use of high frequency optical transmissions in free-space requires further analysis. This distribution underestimates the very small drops of drizzle on one hand and on the other hand of storms. The

values of parameters N_0 depending on the type of rain, either if it is convective rain storm or continuous rain showers or drizzle, are given for these three types of rain in Table 3.5 [116].

The corresponding values of the parameter A, of the Equation (3.24), are tabulated in

Rain Parameters	Rain Type		
	Drizzle	**Continuous Showers**	**Strong Showers**
N_0 $(mm^{-1}m^{-3})$	3×10^4	7×10^3	14×10^2
$\gamma(mm^{-1})$	$5.7R^{0.21}$	$4.1R^{0.21}$	$3.0R^{0.21}$

Table 3.5: Rain parameter values of N_0 and γ for the studied rain types

Table 3.6 below, against three ranges of rain rate or intensity of precipitation [88]. The optical attenuation due to rain, as a function of rain intensity or precipitation rate R (mm/h), can be found by the following relationship [103, 37],

$$\gamma_{rain} = 1.076R^{\frac{2}{3}} \qquad \text{dB/km} \tag{3.25}$$

where R is the rain rate in mm/hr.

There exist another model that employs modified gamma distribution to model the rain droplets [28]. If Q_d denotes scattering cross-section of the rain droplets of radius r, and C(r) the MGDSD, then the optical attenuation can be calculated by the following relationship,

$$\gamma_{rain} = 4.34 \int_{r_1}^{r_2} Q_d(r)C(r)dr \qquad \text{dB/km} \tag{3.26}$$

Rain Parameters	Rain Type		
	Drizzle	**Continuous Showers**	**Strong Showers**
Intensity (mm/h)	$R < 3.8$	$3.8 < R < 7.6$	$R > 7.6$
Parameter A	0.509	0.319	0.163

Table 3.6: Values of parameter A depending on the type and intensity of rain

3.3.2 Time Series of Rain Attenuation Measurements

In this section, the influence of rain events on the propagation of optical signals transmitted in free-space is being discussed. Fig. 3.24 shows the measured time series of temperature, rainfall intensity, relative air humidity and number of transmission error seconds (ES) detected along an optical link against a rain event that occurred at Budapest. Measurements

were performed at Budapest, in October 2002 using a 2.3 km optical link at 0.785 μm. The test signal was a PCM31 format pseudo-random signal, measured with a Wavetek EDT-135 type E1 analyzer. During the rain event there were no errors on the optical link, as there was no significant reduction in visual range. After the rain ceased, the temperature decreased while the humidity increased, leading to the formation of fog, which, in turn, produced transmission errors. This measurement confirms that to estimate the attenuation of free space optical links the drop size, air humidity and the temperature may provide valuable information.

Fig. 3.25 presents a simulation of specific attenuation for different rain rates (using model

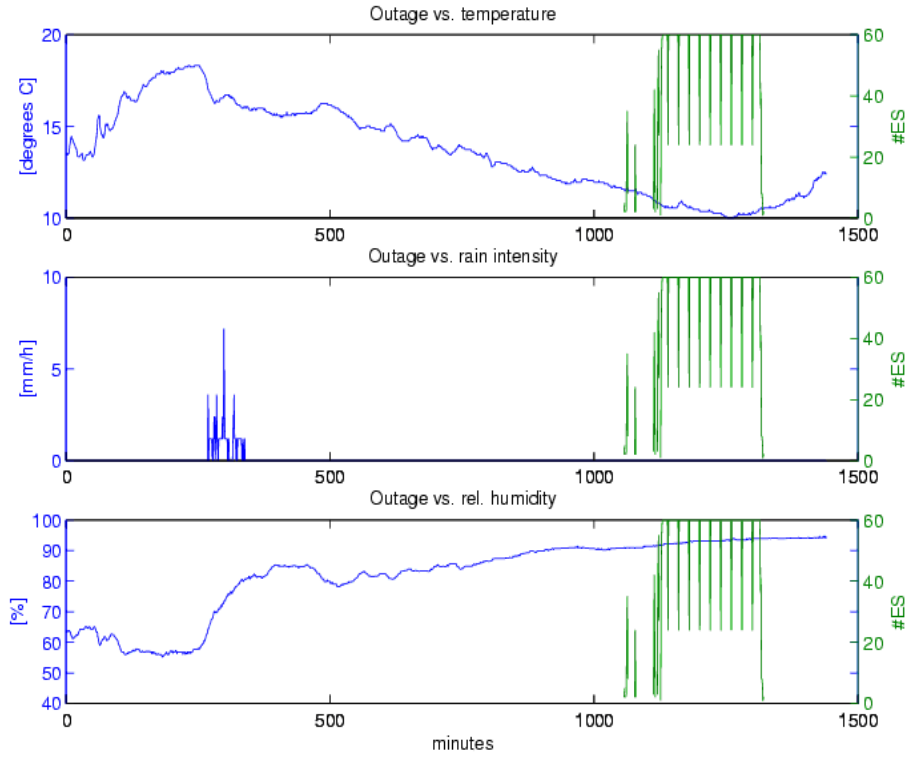

Figure 3.24: Time series of temperature, rain intensity and relative air humidity, against number of error seconds (plotted in green) detected along an optical communication link over a 2.3 km path

given in Equation 3.25). From this simulation it is observable that even with heaviest rain showers at a rain rate of 150 mm/h, the maximum attenuation can reach up to 30.38 dB/km. Consider a moderate rain rate (R = 1 mm/h) that remains uniform for about 10 minutes time and usually occur during continental rain in middle Europe may results in an attenuation of only about 1.076 dB/km. For heavy thunderstorms, attenuation can easily exceed 10 dB/km making availability questionable if the system setting has a very small error margin. The same holds for heavy snowfall (more than 5 cm and uniform over 3 hours), where attenuations of more than 45 dB/km could be possible [29]. Depending on

the time of the year and the geographic location, these values can be exceeded. It may also happen that the weather events discussed occur simultaneously, i.e. fog with rain or fog with snow [94].

The time series of a representative rain event that is recorded at Milan, Italy on a 319

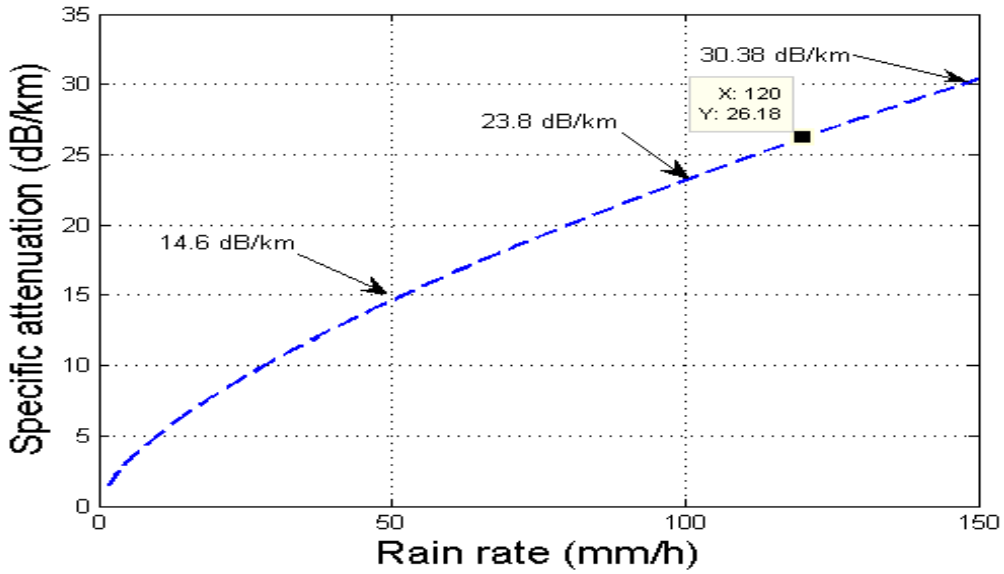

Figure 3.25: Simulation of rain rate vs specific attenuation

m optical link operating using 785 nm wavelength is shown in the Fig. 3.26 [117]. This sample rain event was recorded at Milan during year 2005-2006 measurement campaign. In this plot rain rate measured for the rain event is plotted against the specific attenuation and the corresponding visibility range recorded. It is visible through the plot that the maximum specific attenuation of about 23 dB/km was observed at a rain rate of 0.9 mm/hr and corresponding visibility value of about 735 m. With a maximum observed rain rate of 3 mm/h, the corresponding value of specific attenuation is about 1.47 dB/km against a visibility range value of approximately 4359 m. The specific attenuation for this particular rain event changes at a rate of $\pm$ 0.7 dB/km averaged on a minute scale. Comparing the attenuation results measured with the simulation results as shown by Fig. 3.25, we notice a kind of discrepancy in the observed values i.e., less attenuations for higher rain rate and higher attenuations for lesser rain rate. However, by considering the visibility range values recorded in parallel and comparing them with the measured attenuation results then we may explain this discrepancy. As we observed that with a rain rate of 0.9 mm/hr the corresponding visibility was about 734.19 m, so converting this visibility range into optical attenuations using Kruse and Kim models with 2 % and 5 % transmission thresholds results in attenuations of about 13.26 dB/km, 15.57 dB/km and 17.35 dB/km and 20.38

dB/km, respectively. Then comparing the rain rate of 0.9 mm/hr with corresponding attenuations as shown in Fig. 3.25 yields in attenuations up to approx. 2 dB/km, and thus the total attenuations with rain and light fog combined reach up to 15.5 dB/km and 19.35 dB/km using Kruse model for 2 % and 5 % thresholds and 17.5 dB/km and 22.37 dB/km using Kim model with 2 % and 5 % thresholds, respectively. Hence we may safely conclude that this rain event was accompanied by a some kind of light fog event that resulted in higher attenuations (up to 23 dB/km). Whereas, the attenuation results obtained with a rain rate of 3 mm/hr correspond to a visibility range of about 4359 m suggesting that there was no fog in this case and thus resulted in attenuations up to 1.5 dB/km as expected.

Another sample rain event discussed here is recorded at Prague for the transmission of 850

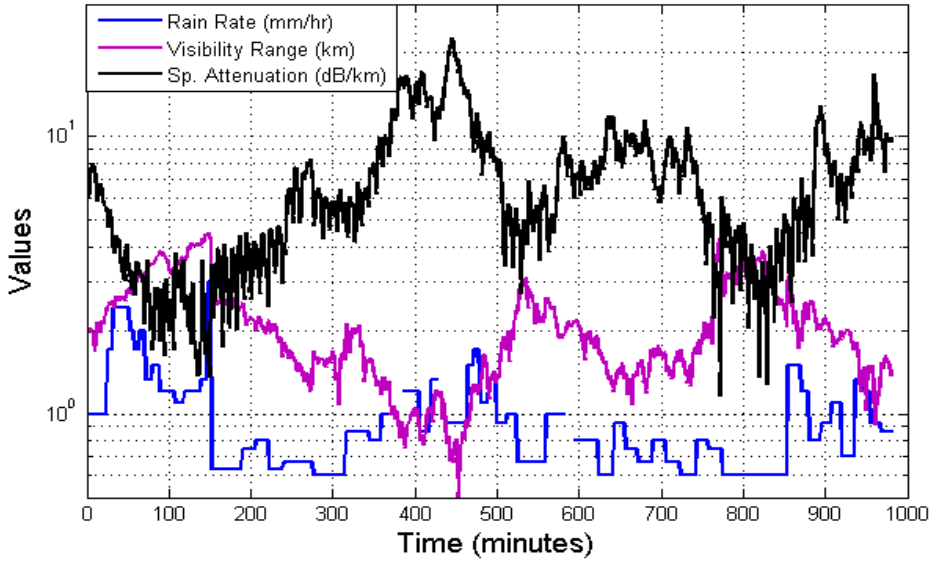

Figure 3.26: Time series of recorded rain events at Milan, Italy

nm pulses on 850 m link. Fig. 3.27 shows the sample rain event that occurred during the attenuation measurement campaign of year 2006 Ű 2007 on 18.09.2006 at Prague [117]. The minimum measured visibility during this particular rain events is 1000 m. While the maximum rain rate during this particular rain event (of Prague) was recorded to be about 44 mm/hr and maximum specific attenuation reached was 8.5 dB/km. The maximum specific attenuation of about 8.5 dB/km reached against a rain rate of approximately 21 mm/h, whereas, the specific attenuation value of 6.35 dB/km corresponds to a maximum rain rate of about 44 mm/h. This behavior of rain attenuations is somewhat similar to the rain attenuations behavior as observed in the last discussed case of Milan representative rain event. Comparing the attenuation results measured with the simulation results as shown by Fig. 3.25, it can be noticed that attenuations of 8.5 dB/km can be expected with a rain rate of

21 mm/hr but the attenuations at 44 mm/hr are too small i.e., 6.35 dB/km. Possibly this may be due to the reason that majority of rain droplet sizes, with a 44 mm/hr rain rate were either too small or too big and were not comparable to the 850 nm wavelength employed for the FSO link. The changes in specific attenuations recorded during this rain event were about $\pm$ 1.70 dB/km averaged on a minute scale. From the analysis of this particular recorded rain event it was noticed that the rain attenuation occurs for percentages of time smaller than 0.66%. However, since the data samples related to rain effects on FSO links are very limited so they do not necessarily represent the typical behavior of rain and thus no concrete conclusions can be drawn.

From the comparison of the mentioned two rain events, it is observed that rain event

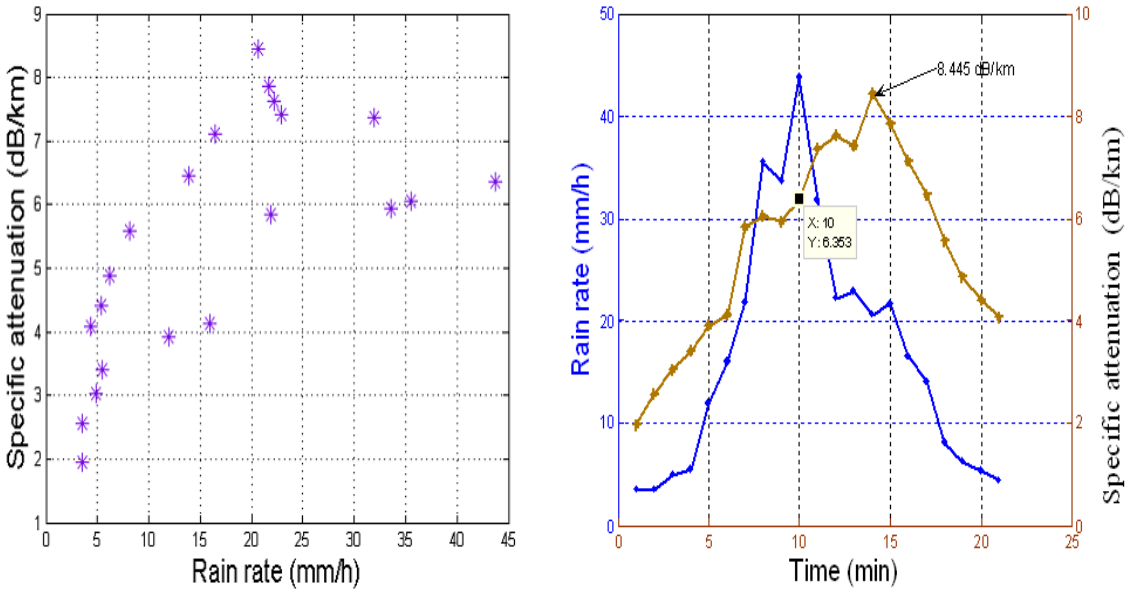

Figure 3.27: Rain rate vs measured specific attenuation (left); time series of rain rate and specific attenuation against a rain event at Prague

effects are variable from location to location and the type of environment. These effects are dependent mainly on the rain drop sizes, their chemical composition and their orientation since small rain droplets are usually spherical in shape and correspond to very small rain rates and hence reduce visibility range more as compared to relatively larger size rain droplets who result in relatively heavy rain showers but result in comparatively greater visibility range.

3.4 Snow Attenuations

Snow also causes non-negligible attenuation of the transmitted optical signal in free-space. When precipitation rates are compared, the snowfall rate is usually lesser than the rainfall rate. Fig. 3.28 shows the visibility range dependent comparison of fog, snow and rain models for optical transmissions at 950 nm [118].

It is evident from the Fig. 3.28 that the role of fog and snow conditions is extremely

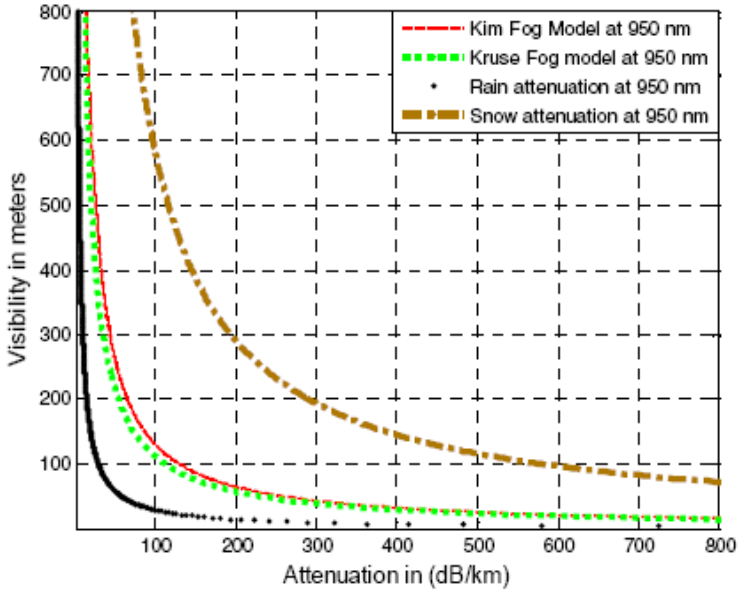

Figure 3.28: Simulating empirical models for fog, rain and snow conditions

important for the reliable operation of terrestrial optical links as these two conditions can introduce very high attenuations to the transmitted optical signals for reduced visibility range conditions. There exist few snow attenuation prediction models that can be used in order to model the optical signal attenuations.

3.4.1 Prediction of Snow Attenuations

The first model is an empirical model that relates visibility range with the optical attenuations [119]. Since snowfall also impairs visibility range, therefore visibility range parameter can be used to predict optical signal attenuations, irrespective of the type of snow, to a good approximation. O'Brien gave the following relationship between visibility range (V)

and light attenuation (γ)in falling snow,

$$\gamma_{snow} = \frac{58}{V} \tag{3.27}$$

The second model deals with the microphysical properties of snow. The model is given by the following relationship [29],

$$\gamma_{snow} = 0.3619 \frac{\rho_w R}{C_3 v_t} \qquad \text{dB/km} \tag{3.28}$$

where v_t is the terminal velocity of the snowflakes and ρ_w is the water density in g/cm^3, R is snowfall rate in mm/hr, C_3 is the thickness of snowflakes in g/cm^2. Although snowflakes have a very complicated shape but they do not exhibit any preferred dimension. So assuming their spherical shape seems reasonable and gives us a very realistic attenuations profile in case of FSO links.
The third model relates optical signal attenuation as a function of wavelength λ (nm) to the snowfall intensity S (mm/h). The attenuations due to snowfall are modeled based on categorization into dry and wet snow types and the specific attenuation is given by the following relations:

$$\gamma_{snow} = aS^b \qquad \text{dB/km} \tag{3.29}$$

Here parameters a and b categorize snowfall type and for the two types of snow have values as,

- For wet snow below 500 m of elevation:

$$a = 1.023 * 10^{-4}\lambda + 3.7855466 \qquad b = 0.72$$

- For dry snow above 500 m of elevation:

$$a = 5.42 * 10^{-5}\lambda + 5.4958776 \qquad b = 1.38$$

From the simulations based on dry snow and wet snow classification (Fig. 3.29) and also indicated by Equation (3.29) that the specific attenuation by dry snow is much higher than specific attenuation caused by wet snow [118]. Moreover, for both snow types no optical wavelength dependency is observed, that means, there is no advantage of using longer wavelengths in dry and wet snow environments as it was seen in case of fog conditions. This suggests to use shorter wavelengths for free-space optical links in areas with high snow rates as lower wavelengths have high availability of components. The intensity of precipitation of snow (precipitation rate) is the fundamental parameter used to describe the snow, locally. Its measurement is recorded at meteorological stations. In case if only snow attenuations are known then the snow rate (S) can be estimated from specific snow attenuations by a model given by [115].

$$\gamma_{snow} = 0.00349 \frac{S^{1.6}}{\lambda^4} + 0.00224 \frac{S}{\lambda} \tag{3.30}$$

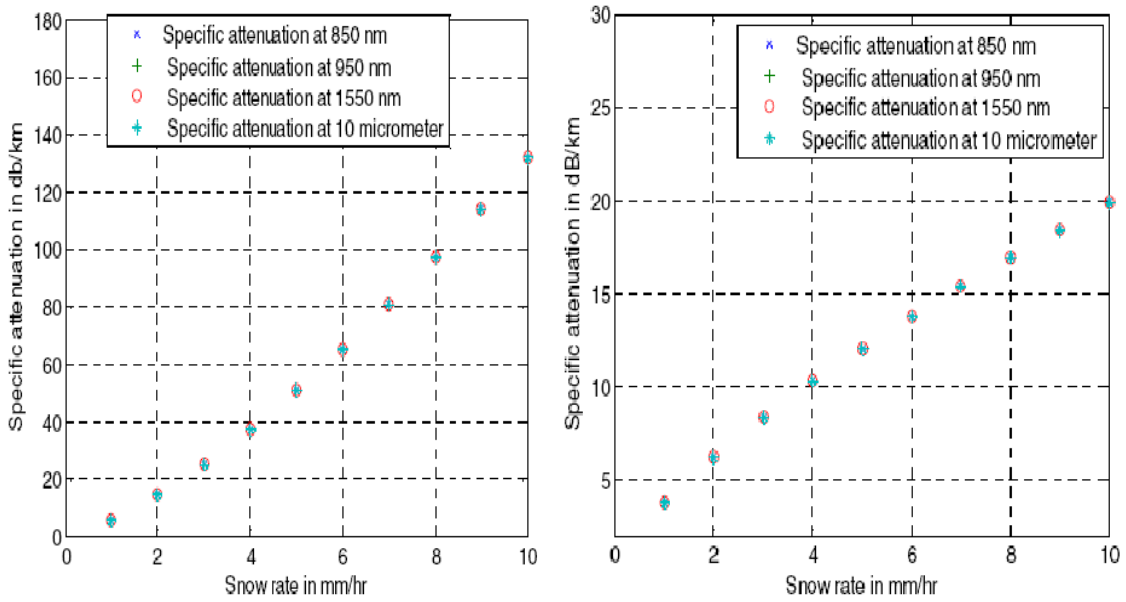

Figure 3.29: Simulating optical attenuations for dry snow (left) and wet snow (right)

3.4.2 Time Series of Snow Attenuation Measurements

A time series of attenuations of the three major dry snow events is being presented in this section. The three snow events were recorded on a 79.8 m optical link installed at Graz. The longest snow event occurred in Nov. 2005 measurement campaign and it lasted for three days as it started on 25^{th} Nov. 2005 and ended on 28^{th} Nov. 2005. While the remaining two major snow events occurred during our year 2009 measurement campaign and the two took place on 01^{st} and 2^{nd} Feb. 2009. The time series of all the three events optical attenuations in dB/km using 950 nm optical wavelength for transmission is shown in Fig. 3.30 below, Since during these campaigns snow rate could not be measured so we estimated the snow rate using the model given by T. Oguchi and is given in Equation (3.30). The snow rate was estimated against the longest snow event i.e., of the Nov. 2005 snow event and the time series of this snow event is plotted in Fig. 3.31 below [118]. This mentioned snow event had a peak value of 50 dB/km specific attenuation against a snow rate of about 5 mm/hr. But against a maximum value of snow rate of about 6.5 mm/hr estimated, the measured snow attenuation recorded was 47 dB/km. This shows that snow attenuations can vary depending upon the size of the snowflake, amount of equivalent liquid water content and the snowfall rate.

The maximum attenuation in case of dry snow we measured is about 68 dB/km against the dry snow event of 2^{nd} Feb. 2009. The changes of specific attenuations of the Nov. 2005 dry snow event were around $\pm$ 10 dB/km on a second scale [26]. Whereas, the

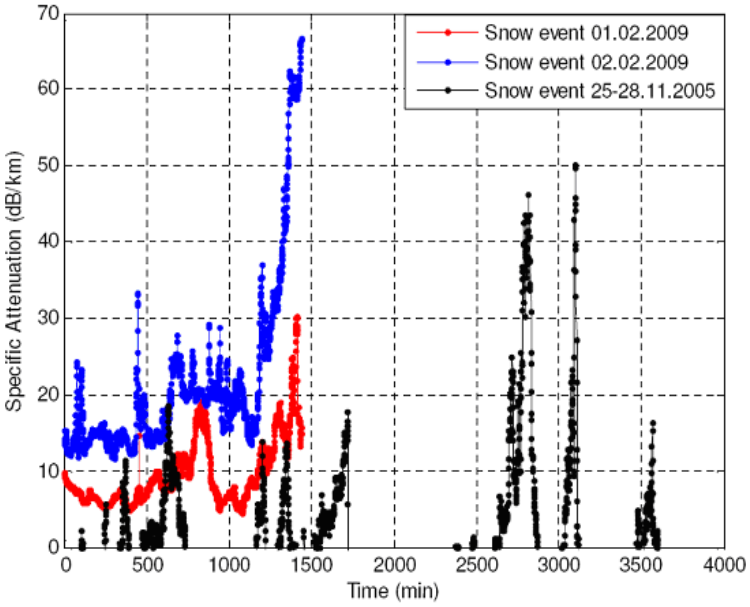

Figure 3.30: Time series of three snow events recorded over a 79.8 m FSO link

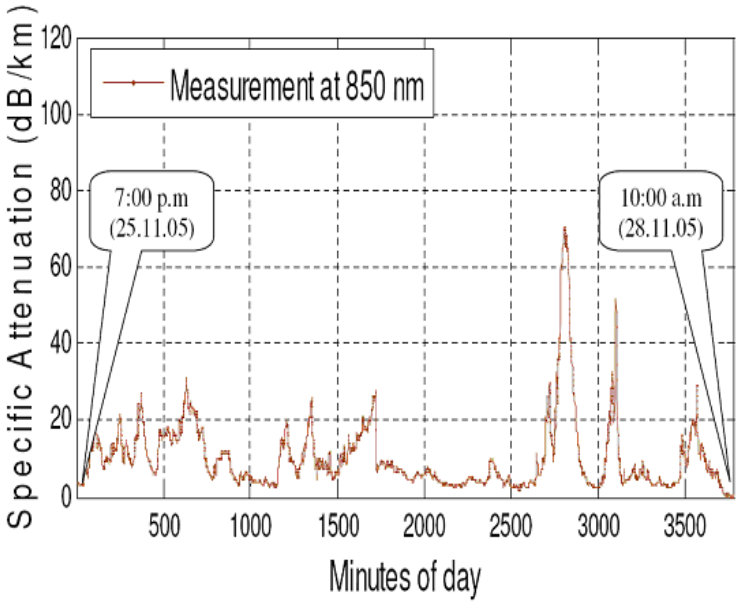

Figure 3.31: Snow attenuations estimated from snowfall rate for snow event of Nov. 2005

observed variations in specific attenuations due to dry snow effects for the 01^{st} and 2^{nd}

Feb. 2009 snow events were about ± 7 dB/km and ± 6 dB/km, averaged on a seconds scale [118, 120]. A corresponding plot of all three dry snow event attenuations showing the cumulative exceedance probability percentage is presented in Fig. 3.32 below. From this plot it is evident that the attenuations were much higher of the 2^{nd} Feb. 2009 snow event as compared to the other two snow events of 01^{st} Feb. 2009 and the Nov. 2005.
The simulations for wet snow are not performed here as wet snow has negligible effect in

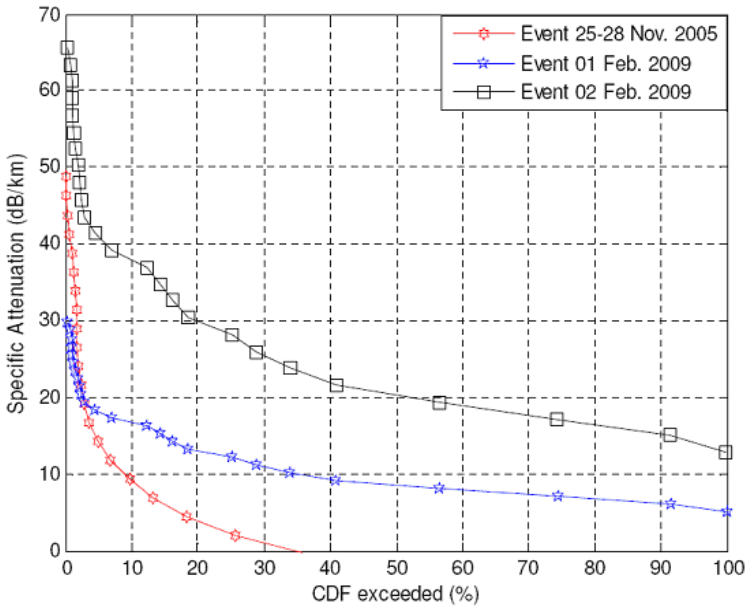

Figure 3.32: Cumulative exceedance percentage of three observed snow events

terms of snow attenuations on the performance of FSO link.

3.5 Summary about Attenuation Measurements

To make optimal use of the huge unlicensed bandwidth offered by FSO links for our future transmission requirements, it is necessary to have appropriate propagation related data in order to properly plan FSO communication system design for different communication scenarios (e.g., terrestrial, ground-space and space-space). As we noted, there exist very limited experimental data of atmospheric attenuations in terms of the geographical and meteorological parameters. For this purpose experimental FSO links has been installed at Graz, Milan, Prague (under the continental fog conditions) and Nice (under dense maritime fog condition) as these locations has a quite high occurrence of fog. Besides numerous issues related to the environment, measurements of attenuations, as a function of visibility

range, at different wavelengths were made on the FSO links installed at these mentioned locations. The next step was to characterize and parameterize the measured attenuations for the two most prevalent fog types in order to quantify the spectral dependence of attenuation for the terrestrial FSO links. At the mentioned sites besides Graz, the fog attenuations were recorded in parallel to the measurement of important meteorological parameters like temperature, visibility range and relative humidity etc. Nevertheless, the comparisons of measured optical attenuations were made with the already well established prediction models based on visibility range to see which model best fits the optical extinctions for the three continental fog locations (Graz, Milan and Prague). The results were applied to an experimental link of 80 m installed at Graz, Austria, 319 m FSO link at Milan, Italy and 850 m FSO link at Prague, Czech Republic. We noted an excellent agreement between predictions generated through visibility range estimate and the experimental attenuation data recorded. It is concluded that the terrestrial FSO system can be deployed successfully for distances less than a kilometer and the results obtained at Graz, Milan and Prague fully confirm this feasibility. It was further noted that generally we cannot prefer one particular empirical model over the others for thick to light fog conditions as all models perform equally well. However, for dense fog conditions Kim model seems to perform well as compared to the other models as it describes the low visibility range conditions and related optical attenuations well. Recall that the spectral dependence of attenuation in case of very low visibilities (lower kilometer) is always the source of much debate. The variability in fog attenuations was also observed at the three continental fog locations, and is also probably due to the difference in the type of FSO equipment, the sensitivity of measurements and the nature of the fog which is particularly inherent of the geographical vicinity. We further noticed that the continental fogs are stable and homogenous at large in comparison to maritime fog which are very inhomogeneous. It is a well established fact now that the wind and the DSD has a very strong influence on the homogeneity of the advection fog. Besides the analysis of fog related optical extinctions, few rain and snow events were also evaluated and their impact on the free-space optical signals is studied. It was found out that rain attenuations are not much significant as compared to snow and fog attenuations. The snow and rain attenuations are particularly sensitive to their particular fall rates, and the corresponding size of the flakes and the droplets, respectively. In short more experimental data of atmospheric attenuations from different locations is required to build a global database of important meteorological parameters and corresponding extinctions and hence to draw more concrete results and conclusions for the FSO system. It was concluded that their observed attenuation characteristics are strongly dependent on the microphysics involved, and will be further investigated and explained in the next chapter.

4 ANALYZING THE FOG MICROPHYSICS (PHYSICAL PROPERTIES)

The observation of fog and clouds and the estimation or measurement of the thickness of their bases is necessary for the design of ground-space FSO links. The physical processes responsible for the formation and dissipation of fog are very complex and variable. Different microphysical mechanisms prevail depending upon the local thermodynamical conditions and hence lead to the development and growth of the different fog types which influence and determine the nature, strength, and the life cycle of the particular fog event. These microphysical processes are highly interactive and also tells about the thermodynamics, chemistry and dynamics of the ambient air. Typically, very thin fog does not require definite consideration on earth-space FSO links due to the fact that the vertical extent and the density of such fog are small. However, moderate and dense fog conditions pose a real challenge to the FSO links as the density of such fog is significant enough to completely or partially block the optical link for certain amount of time depending upon its spread and severity. The first section focuses on the microphysical characterization of the terrestrial FSO atmospheric channel especially for fog conditions and the microphysics behind the formation, maturity and dissipation phases of fogs is investigated and evaluated. The second section focuses on the fog density measurement system. The last section is based on liquid water content (LWC) and the fog density measurements and outlines some empirical models that relate liquid water content with the visibility range. Based on these empirical models some real attenuation measurement results are analyzed in detail.

4.1 The Phenomenon of Fog

Fogs are composed of very fine droplets of water produced by condensation of water vapors on a pre-existing aerosol distribution of different nature (dust, smoke, volcanic ash etc) suspended in the air near the surface of the earth under the effect of gravity. The presence of these droplets act to scatter the light and thus reduce the visibility near the ground. A fog layer is reported whenever the horizontal visibility is less than 1 km and the relative humidity of the air is brought to the saturation level (close to 100%) [121]. Usually the liquid water density in fog is typically around 0.05 g/m^3 having a visibility of about 300 m and 0.5 g/m^3 for the dense fog having visibility about 50 m [38]. A fog layer can extend vertically up also to a height of 300 m to 400 m above the ground surface up to the height of the layer where temperature inversion takes place. Optical attenuation is highly correlated with fog intensity, and it is particularly affected by the number density and the

size of fog droplets. As a general rule fog droplets tend to cluster around 5 μm to 15 μm in diameter [85].
Generally, fog is formed under a wide range of scenarios as a result of supersaturation generated by cooling, moistening and/or mixing of air parcels, near the ground surface, that have contrasting temperatures. The presence of small suspended water droplets and/or ice crystals can render an object undistinguishable to a distant observer and thus result in poor visibility conditions [91, 115]. During the fog formation stage, a concurrent increases in liquid water content, droplet concentration and mean droplet size have been observed to occur gradually. After the fog formation stage i.e., during the mature stage nearly constant mean droplet concentration and LWC, while a gradually decreasing mean droplet size has been observed. The fog dissipation stage typically occurs as the droplet concentration, mean droplet size, and LWC all decrease with the passage of time [122]. Droplet concentration and size dependent scattering losses of the propagating optical beam cause poor visibility that occurs through a reduction in the brightness contrast between an object and its background and through the blurring effect of forward scattering of light due to the presence of the water droplets/crystals [56, 85]. Fog is more likely to occur in climatic environments having large concentrations of aerosols characterized by a low activation supersaturation (level of supersaturation at which aerosol particles spontaneously grow to become cloud drops). It is very difficult to distinguish between unactivated and activated fog droplets in different fog types.
The presence of fog and its microphysical characteristics affect the capacity, availability and reliability of FSO systems by attenuating the power of transmitted optical signal propagating through it [12, 92, 123]. Optical signal attenuation through fog is mainly caused by scattering of electromagnetic wave on the spherical water droplets suspended in the air and interacting independently. The physical mechanism of fog attenuation is similar to rain attenuation, but since the typical fog droplet radius is much smaller than the rain droplet, therefore the impaired wavelengths are shorter in fog as compared to rain. The role of typical fog droplet radii is very important in case of terrestrial FSO links as there exist several types of fog in different regions and seasons. Typical fog droplet radii vary from environment to environment and hence the fog influence on the optical signal propagation varies. In order to predict the optical signal attenuations due to fog, the knowledge about evolution, dissipation of fog along with its spatial and temporal distribution and microphysical properties is quite useful.
Especially, among the microphysical properties of interest, the droplet size distribution (DSD) of fog and amount of liquid water content (LWC), average particle size and number per air volume are crucial. These properties together with the knowledge of the scattering properties of single droplets permits to estimate fog attenuation. The measurement of fog LWC and DSD is not trivial and dedicated data are still scarce in the literature. Additionally, these microphysical parameters undergo spatial and temporal changes and are dependent upon the atmospheric conditions like relative humidity, temperature, and the environment e.g. continental or maritime, and the microclimate.
Based on visibility range estimate Eldridge [121] defined three generalized types of shorter

visibility climatic conditions; fog for visibilities less than 500 m, mist for visibilities between 500 and 1000 m and haze for visibilities greater than 1000 m. These zones are based on changes in observed particle size distributions and changes in the wavelength selectivity of measured attenuation coefficients. Haze is primarily made of microscopic fine dust or salt or small droplets of a few microns to a few tenths of micron sizes. Nowadays, an international code of visibility is adopted in order to differentiate between different climatic conditions based on visibility range estimate as given in Table 4.1.

Intricate relationships exist between aerosols and fog. Fog may appear under the influence

Description	**Visibility Range (km)**	**Attenuation Loss (dB/km)**
Dense Fog	0.04-0.07	250-143
Thick Fog	0.07-0.25	143-40
Moderate Fog	0.25-0.5	40-20
Light Fog	0.5-1.0	20-9.3
Thin Fog	1.0-2.0	9.3-4.0
Haze	2.0-4.0	4.0-1.6
Light Haze	4.0-10.0	1.6-0.5
Clear Sky	10.0-25.0	0.5-0.1
Very Clear Sky	25.0-50.0	0.1-0.04
Extremely Clear Sky	50.0-150.0	0.04-0.005

Table 4.1: International code of Visibility Range

of particular aerosol characteristics like number concentration, size distribution and chemical composition that have a large impact on the occurrence of a particular type fog. These aerosol characteristics strongly influence fog microphysics and hence the overall life cycle of a particular type fog. Therefore, as a result the LWC, DSD, and visibility range of a fog layer are affected and modified according to the characteristics of the aerosols contained in the air mass. All the optical characteristics of aerosols and in particular those of fog are related to the particle size distribution, which is the most important parameter allowing us to compute the optical properties of a quantity of droplets. Generally, this distribution is represented by analytical functions such as log-normal distribution in the case of aerosols and the modified gamma distribution for fog, which is widely used to model the various types of fog and cloud [99] and is given by:

$$C(r) = N_0 r^m exp(-\Lambda r^\sigma) \tag{4.1}$$

In this equation, $C(r)$ gives the number of particles per volume unit and per increment unit of the particle radius r; N_0, m and Λ are parameters which characterize the particle size distribution. Fog is usually characterized by N_0, m and Λ with σ = 1 [99]. For dense fog these parameter values are 0.027, 3 and 0.3 respectively and for moderate continental fog the values are 607.5, 6 and 3.

4.1.1 Fog Types and their Classification

Radiative cooling and mixing or humidification are the two main physical mechanisms that result in fog formation. When radiative mechanism dominates the fogs are termed as radiative fogs and as advective fogs when the second mechanism is prominent. Many processes are involved in the fog formation and development, including the primary role of radiation, microphysics, turbulence, and moisture transport over heterogeneous terrain to produce the saturation of air [124]. The relative importance of each process varies from case to case and also temporally during a fog event. In terms of physical mechanisms, Jiusto [124] listed 14 factors that influence the formation and dissipation of a fog layer. The local scale factors mainly involve moisture availability, radiative balance of the clear and cloudy air, turbulent mixing, heat and moisture transfer in the soil medium and microphysical processes besides temperature and moisture horizontal advections and vertical motion associated with large scale and/or mesoscale circulations [112].
Fog occurs naturally in many different types dependent upon the mechanism of their formation, the location dependent climatic conditions and the geographical location. Some examples of major fog types are:

- Radiation or continental fog
- Advection or maritime fog
- Precipitation or frontal fog
- Upslope fog
- Valley fog
- Arctic or steam fog
- Cloud base lowering fog

Each type fog mentioned above have their particular physical characteristics and numerous researchers have devoted efforts to understand the relationship between the occurrence of a particular type of fog with the various mechanisms known to influence their evolution process. Moreover, each fog type has characteristic DSD that varies spatially and temporally and changes with the changes in relative humidity, temperature and the wind speed. Thereby making the forecast of formation, dissipation of fogs difficult and the attenuation prediction process even more difficult. Typical fogs (radiation and advection type) are composed of inactivated cloud droplets (haze particles) and activated Cloud Condensation Nuclei (CCN). The inactivated fog droplets are generally smaller than 2.5 microns in diameter, while activated droplets are usually much larger than 2.5 microns. But in comparison to droplets of different cloud types, the fog droplets (either radiation or advection) are generally smaller [99]. Since radiation fog and the advection fog are the two most prevalent

fog types that occur in most regions around the globe, therefore these two fog types will be discussed here and in the following chapters in further details.

Radiation or Continental Fog

Radiation fog in temperate areas mostly occur in winter and is formed near the ground surface under clear sky conditions in stagnant air in association with an atmospheric high pressure. The favorable conditions for radiation fog formation are very low speed winds, high humidity and clear sky. Under this scenario, radiation fog formation has been found to be sensitive to the coupled dynamical and thermodynamical structure of the evolving nocturnal boundary layer over land [112]. The typical fog droplets are considered spherical in shape having diameter ranges from 0.17 μm to 50 μm for any type of fog [62, 63] depending upon the geographical location. In the case of moderate continental fog droplets, the mode is about 2-4 μm, while for dense continental fogs the mode size is about 4-6 μm [99, 100]. As a comparison, a cloud may contain a good proportion of very small water droplets, but the radii of the drops that dominate extinction and scattering are in the range of 5 μm to 20 μm, whereas, the limiting liquid particle diameter of a cloud is of the order of 200 μm, larger drops than this comprise drizzle or rain. Fig. 4.1 gives an illustration of the formation mechanism of radiation or continental fog.

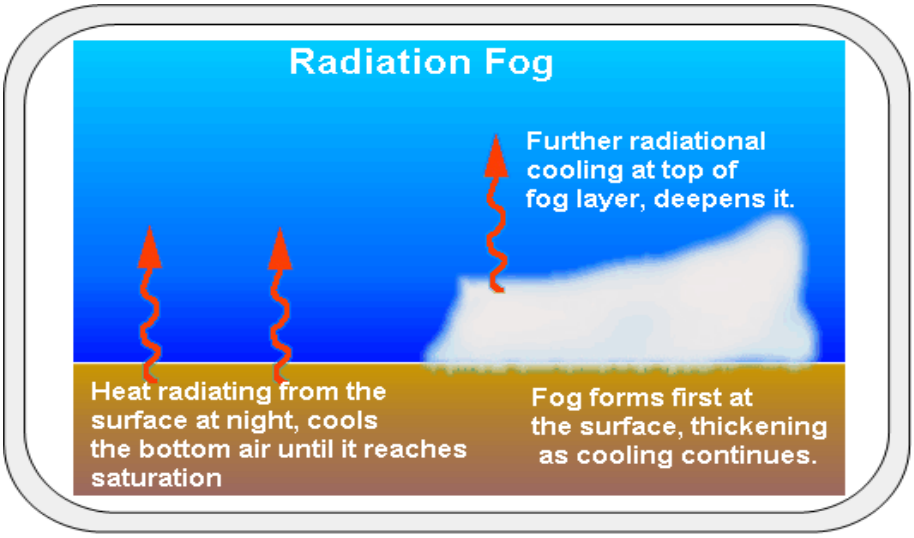

Figure 4.1: An illustration of radiation fog formation mechanism [125]

Advection or Maritime Fog

Advection fog is formed by the movement of wet and warm air masses having contrasting temperature properties above the colder maritime or terrestrial surfaces. The air in contact with the surface is cooled below its dew point, causing condensation of water vapor. It is characterized by a liquid water content reaching up to 0.5 g/m^3 against a visibility range of 50 m. The maritime fog particle diameter are normally larger in size to continental fog particles. The mode in case of moderate maritime fog lies around 8 μm and for dense maritime fog case it is around 10 μm with 20 fog particles in unit volume cm^3 for both types [99, 100]. Fig. 4.1 below gives an illustration of the formation mechanism of advection or maritime fog.

Studies have shown that the origin and history of air masses in the coastal areas are im-

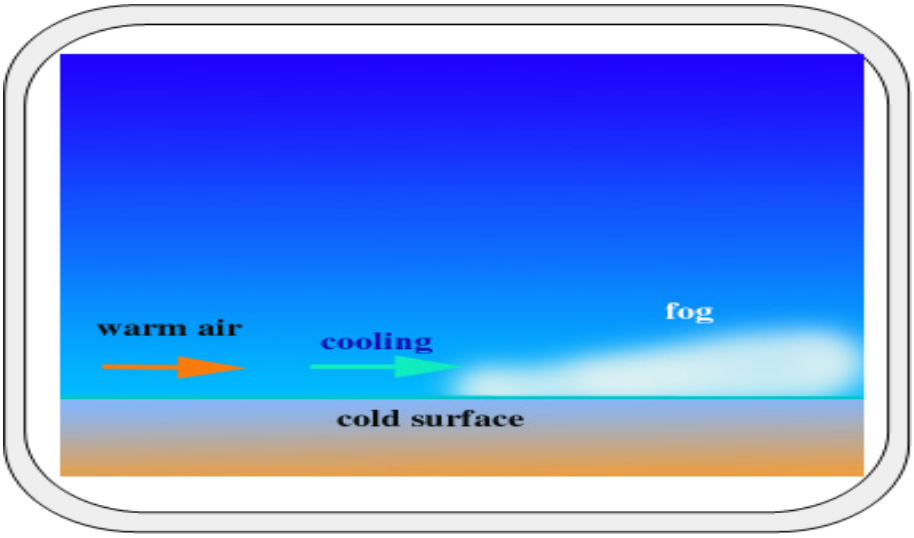

Figure 4.2: An illustration of advection fog formation mechanism [125]

portant factors in the observed variability and in the spatial distribution of maritime fog as well as to the fog microphysical characteristics [112]. The details about remaining fog types can be found in much detail in [97, 126, 127].

Fig. 4.3 shows the fog droplet distributions for the moderate maritime and continental fogs and dense maritime and continental fogs. The vertical axis shows the fog droplet distribution in units of number of droplets per cubic centimeter per micron and the horizontal axis shows fog droplets radius in microns. Fig. 4.4 below, shows the fog particle concentrations for the continental or radiation fog (on left) and maritime or advection fog (on right). The Y-axis shows the particle concentration in number per unit volume (cm^3). From the practical fog attenuation measurements it was observed that the attenuation of FSO links in the troposphere are in high correlation with the fog intensity, and optical attenuations are particularly affected by the density and distribution of the fog particles [27, 87].

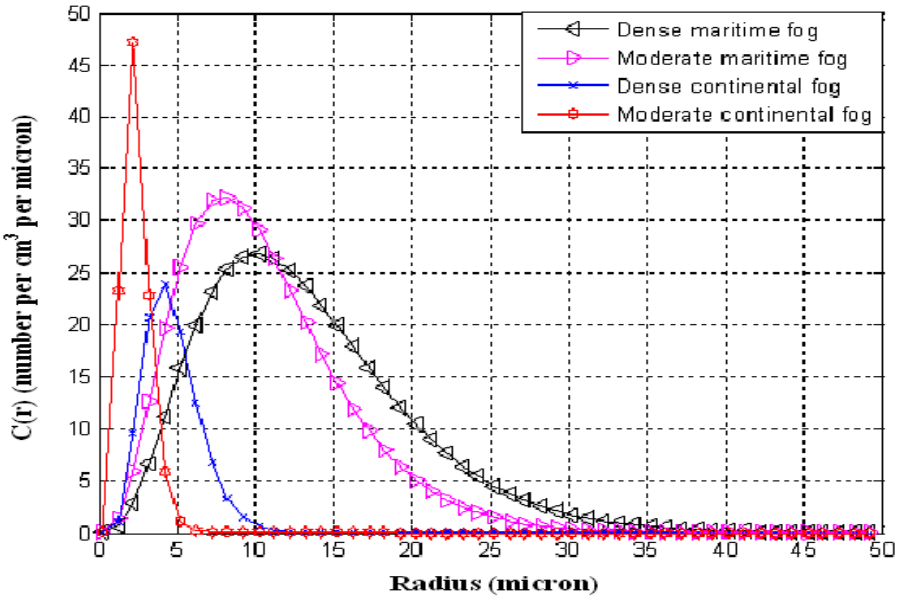

Figure 4.3: Typical droplet distribution for different kind of fogs [101]

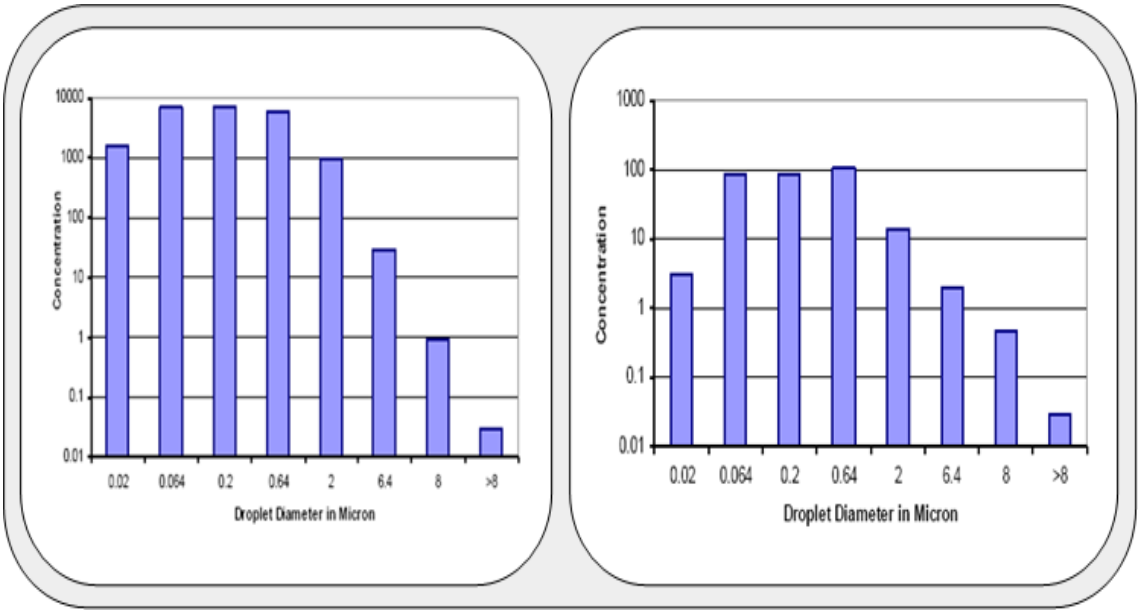

Figure 4.4: Typical fog particle concentration for radiation and advection fog

4.1.2 Formation and Dissipation of Fog and the Influencing Factors

Liquid water content, fog droplets size distributions, fog particle concentration and the chemical composition of the air mass aerosol constituents strongly affect the fog forma-

tion and dissipation. Typically, fog formation takes place as the difference (Δ) between temperature and dew point becomes (5 °F) 3 °C, or less and as a result water vapors in the air begin to condense into liquid water form while relative humidity reaches to 100%. When a moist air mass is cooled to its saturation point (dew point), the fog formation occurs. This apparent cooling can be the result of radiative processes for radiation fog, advection of warm air masses over cold maritime surfaces for advection fog, evaporation of precipitation for precipitation or frontal fog, due to the adiabatically cooling process of the air mass as it is forced up a mountain for a upslope fog. Simultaneous measurements of the FSO attenuation, relative air humidity and temperature are testifying that the appearance of the fog can be often detected with significant increase of the humidity (above 85 %) whilst the temperature is decreasing [128]. A typical effect of dissipation and evolution of moderate continental fog event of 11^{th} January 2005 measured on a 319 m FSO link installed at Milan is shown in Fig. 4.5. Radiation fog generally appears during the night and at the end of the day and is particularly common in the valleys. Normally, after sunset a strong cooling takes place near the earth surface through the divergence effect of long wave radiation. As the cooling increases, the relative humidity increases until fog droplets are activated over the haze particle nuclei.

Fog dissipates gradually and this process starts approximately after one hour to four hours after sunrise. An examination of Fig. 4.5 closely, reveals the continental fog dissipation process such that with the increase in solar radiation power, humidity is decreased and temperature is increased and hence as a result the visibility is improved [96]. Studies on fog formation and dissipation reveal that around the time of the termination of all fog events, approximately 72% are characterized by a decrease in relative humidity associated with increasing temperatures within a few hours after sunrise. While approximately 20% are characterized by a change of moist air mass with a drier air mass due to a shift in wind direction [112]. A typical dense maritime fog event measured on 28^{th} June 2004 on an 28 m FSO link installed at Nice, France is shown in Fig. 4.6. The major difference between a maritime fog event and the continental fog event is the variations of temperature and relative humidity values. One can clearly observe that during this particular maritime fog event, the temperature remained between + 20 - 30 °C, whereas the relative humidity values fluctuated between 10 - 100 %. According to this plot as shown in Fig. 4.6, it is clearly observed that with the onset of the dense maritime fog event the visibility range is improved with the increase in temperature while the relative humidity stayed approximately around 100 % (300 - 800 min) and visibility range was decreasing when temperature was decreasing but relative humidity was about 100% (800 - 1100 min). In situation, when the temperature was decreasing accompanied by a decrease in relative humidity, then the visibility range was also decreasing (as evident from 1100 - 1250 min time interval). At time interval between (1350 - 1440 min), the temperature remained around 22 -23 °C but the relative humidity was at its lowest value during this particular fog event. The link quality was significantly affected with the fog event and most of the time interval (400 - 1100 min) it stayed between 75 - 95 %). And when the optical attenuations reached above 150 dB/km, the link quality parameter could not be calculated due to the sensitivity of the

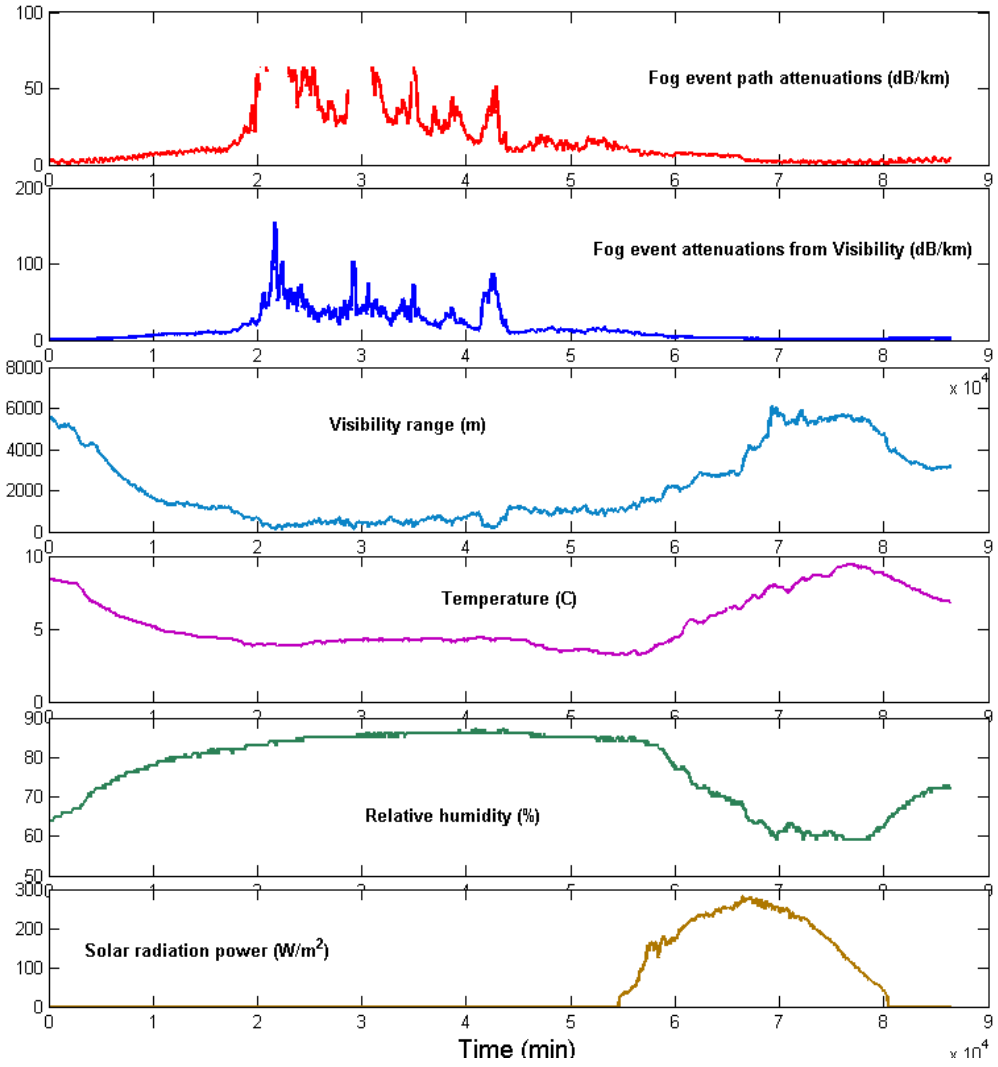

Figure 4.5: Typical continental fog event recorded on a FSO link at Milan

instrument.

4.1.3 The Identification of Fog Events and Frequency computation

Numerical models can be used for fog forecasting and to investigate the relative importance of the processes affecting fog formation and dissipation. Fog events can be identified easily by post-evaluation of the real attenuation measurement data by looking at the variations of visibility range. A particular fog event is identified if the visibility range is reduced to less than 1000 m distance besides, in general, increase in relative humidity and decrease

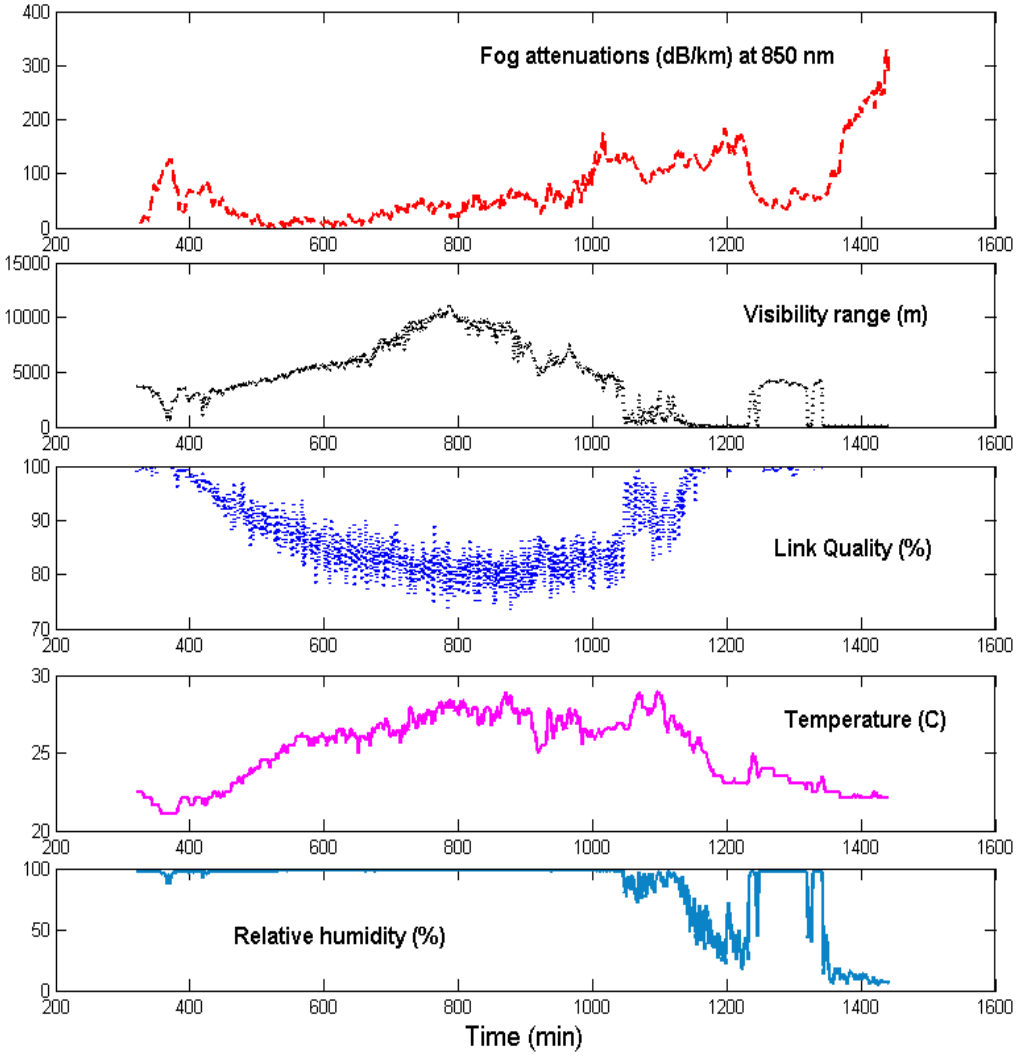

Figure 4.6: Typical maritime fog event recorded on a FSO link at Nice, France

in temperature. Based on the visibility range reduction the fog event can be classified as moderate fog event or dense fog event if the visibility range is several 100 meters but lesser than 1000 m and to few tens of meters but lesser than 100 m, respectively.
The character of a particular fog type is investigated by determining the spatial distribution of its frequency of fog events, as well as the seasonal and diurnal variations of fog evolution and dissipation frequencies. The frequency of fog events is calculated as:

$$F_{m,h} = \left(\frac{N_{m,h}}{N_t}\right) \times 100 \tag{4.2}$$

Where
$F_{m,h}$ is the frequency of fog events with evolution or dissipation started at hour 'h' during

month 'm'
$N_{m,h}$ is the number of fog events that started at hour 'h' in month 'm'
N_t is the total number of events that occurred during the measurement campaign.
The monthly frequency is then calculated, which is the sum of all the fog events that occurred in a particular month.

$$F_m = \sum_h F_{m,h} \tag{4.3}$$

Whereas, the hourly frequency which is the sum of all the fog events that occurred at a particular hour in a month is given by,

$$F_h = \sum_m F_{m,h} \tag{4.4}$$

The Table 4.2 below summarizes few major fog events that were measured during the measurement campaign in the winter 2005-2006 at Graz over a 80 m FSO link operating at 850 nm and 950 nm wavelengths [96]. Overall the fog attenuations at Graz, Austria were measured over 156 days almost 3711 hours, and the measurement data is available for about 3699 hours i.e., 13316400 readings. This means that there exist about 99.6% of the measurement values and the difference is explained by interruptions when these values are saved for compilation in a computer. Similarly, the Table 4.3 below summarizes the measurement campaign in dense maritime fog environment at La Turbie near Nice, France that lasted for eight days under COST 270 short term scientific mission (STSM). This measurement campaign took place in summer 2004 over a 28 m FSO link operating at 850 nm and 950 nm wavelengths. The maximum attenuations recorded against each date shows the maximum value of optical attenuation recorded on a second scale. During this measurement campaign three major dense fog events were recorded.

It is a well established fact now that there is a very high probability of continental fog occurrence whenever there is a decrease in temperature (approaching 0 °C) accompanied by an increase in relative humidity (more than 80%). Our experimental measurements against a continental fog event that is recorded on 11.01.2005 show that particularly around temperature of 4 ± 1°C and relative humidity 85 ± 3% the terrestrial FSO link suffers very high level of optical attenuations as visible through Fig. 4.7 and Fig. 4.8. Under such temperature and relative humidity conditions, a large number of transmission errors begin to appear thereby causing reduction in the reliability and availability of terrestrial FSO links.

Event Date	Event Start Time	Event End Time	Maximum Attenuation Recorded
29.09.2005	02.00	07.30	80 dB/km
25.10.2005	03.00	11.00	110 dB/km
26.10.2005	01.30	04.00	118 dB/km
10. - 11.11.2005	16.00	10.00	58 dB/km
11. - 12.11.2005	14.00	11.00	50 dB/km
22.11.2005	00.00	06.00	110 dB/km
25. - 28.11.2005	19.00	10.00	60 dB/km
28. - 29.11.2005	22.00	06.00	120 dB/km
30.11.2005	06.00	11.00	110 dB/km
02.12.2005	01.00	17.25	90 dB/km
13. -14.12.2005	21.00	12.00	80 dB/km
25. - 28.12.2005	19:32	13:30	35 dB/km
09.01.2006	05:00	10:00	110 dB/km
09. - 10.01.2006	22:00	05:00	116 dB/km
30. - 31.01.2006	21:00	10:00	135 dB/km
31. - 01.02.2006	15:00	09:00	150 dB/km
01. - 02.02.2006	20:00	10:20	140 dB/km
02. - 03.02.2006	21:00	08:00	143 dB/km

Table 4.2: Major fog events detected during continental fog attenuation measurement campaign at Graz that started at 27.09.2005 19:20 and ended at 01.03.2006 14.35

Event Date	Event Start Time	Event End Time	Maximum Attenuation Recorded
24.06.2004	15:36:55	23:59:59	560 dB/km
25.06.2004	00:00:00	23:59:59	490 dB/km
26.06.2004	00:00:00	23:59:59	460 dB/km
27.06.2004	00:00:00	23:59:59	190 dB/km
28.06.2004	00:00:00	23:59:59	480 dB/km
29.06.2004	00:00:00	23:59:59	540 dB/km
30.06.2004	00:00:00	23:59:59	535 dB/km
01.07.2004	00:00:00	23:59:59	540 dB/km

Table 4.3: Major fog events detected during dense maritime fog attenuation measurement campaign at Nice, France that started at 24.06.2004 15:36:55 and ended at 01.07.2004 23:59:05

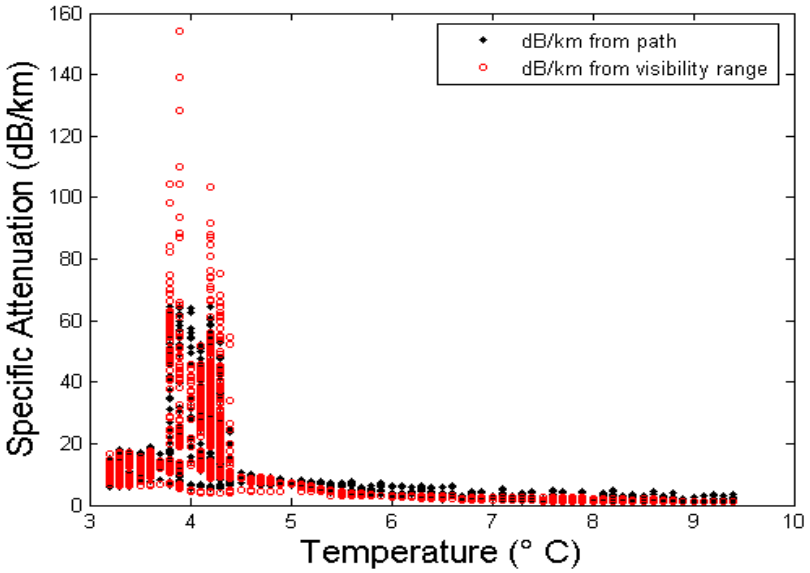

Figure 4.7: Effect of temperature variations on optical attenuations inside continental fog

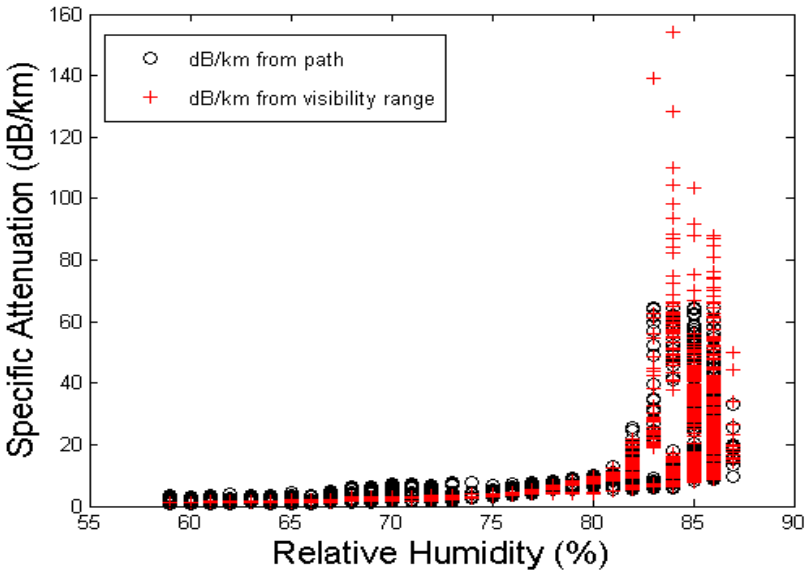

Figure 4.8: Effect of relative humidity variations on the optical attenuations inside continental fog

4.2 Fog Density Measurement Sensor

In order to estimate the path attenuation due to the fog conditions, the liquid water content per unit volume should be measured. The fog attenuations of the optical signals are highly dependent on the amount of LWC in the atmosphere. The measurement of the amount of LWC in the atmosphere is quite complicated and required expensive measurement devices [129]. However, for experimental purposes a simple and low-cost device has been developed through cooperation between Graz University of Technology and the Budapest University of Technology and Economics. This device detects fog events and provides a quantitative value of the LWC in the air. Besides the optical fog sensor the device is equipped with temperature and relative air humidity sensors. These parameters are providing also important information and they have characteristic values during foggy weather. The sensor is built into a rain and sunlight-shielded device box, but allows the free movement of the fog droplets to and from the sensor area. A built-in data processing unit is applied to form the data and transfer the measurement data to the indoor data collecting system.

4.2.1 Principles of the Fog Density Measurement

This fog sensor device is based on an optical sensor which transmits periodically short infrared light pulses and measures the squarely reflected impulses. The amplitude of the reflected light is correlated with the amount of the reflective material in the sensor area; therefore a good estimation of the LWC can be achieved. The construction of the optical sensor and its operation principle is depicted in Fig. 4.9 [96].
The sensor is calibrated to measure the density of the floating particles in the air. The sen-

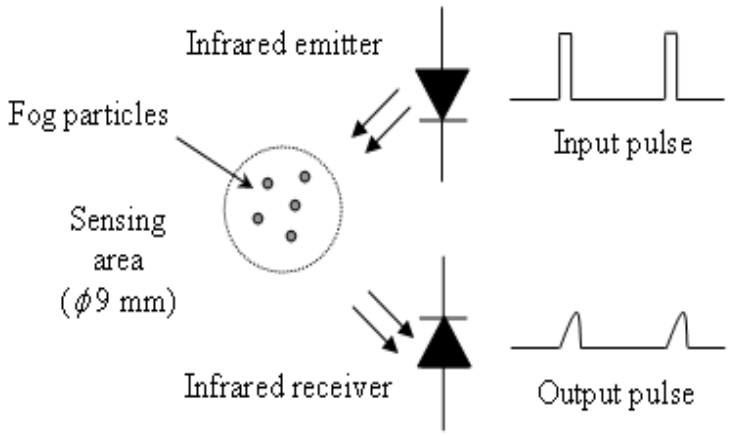

Figure 4.9: Operating principle of an optical sensor to measure the number concentration and the size of fog droplets [96]

sor can detect particles with the size of 1 μm or higher, therefore it will be appropriate to detect fog particles. A sequence of short optical pulses is transmitted through a sampling volume filled with fog droplets. As fog becomes denser, the shape of the received pulse sequence changes according to fog density. The peak voltage of the output pulse response carries the information of the fog density. Moreover, the pulse pattern informs about the size of the particles. The device is factory-calibrated to measure the mass density of the suspended particles in the air and gives this value in mg/m^3. The sensor should be operated continuously, driving the infrared emitting element with the recommended, 10 ms pulse cycle. The fog particles are reflecting the light pulse to the receiver element, and after amplification and shaping the output pulse the signal is ready for the further processing. The fog density can be determined in two ways. On the one hand the factory calibration of the sensor device ensures that the peak voltage of the output pulse varies linearly with the particle concentration in the air, and the concentration/voltage characteristic is also given. In addition, the sensorŠs pulse cycle is high enough to test the density by examining the variation of the consecutive output pulses. In case of moderate fog conditions the peak voltage falls down between two or more detections, while dense fog may cause constantly high output pulse peaks Fig. 4.10 [96]. Moreover, the pulse pattern yields information about the size of the particles. The pulsing of the infrared emitter will be uniformly performed with the recommended cycle and width. It can be foreseen, that the shape of the output pulse (rising and falling time, peak voltage) will be the function of the drop size, however the effective values can be determined only after the analysis of the measurement data, i.e. a calibration process is needed.

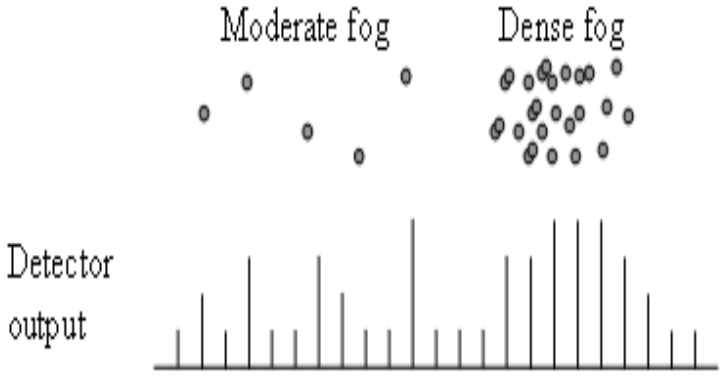

Figure 4.10: Fog density detection mechanism [96]

4.2.2 Hardware Elements of the Measurement System

The device consists of an outdoor and an indoor unit as shown in Fig. 4.11. The microcontroller-based outdoor unit has a serial communication interface (RS-422) and built-in sensors to measure the next properties:

- Density of floating particles in the air
- Temperature
- Relative humidity

The indoor unit receives the RS-422 line of the outdoor unit, converts it to RS-232 and connects the device to a standard PC serial line. The indoor unit also powers the outdoor unit, therefore the outdoor unit doesn't needs power source. The communication between the outdoor and indoor unit is an RS-422 serial line with the next parameters:

- 38400 kbit/sec, no parity, 1 stop bit, no hardware flow control
- Maximal cable length is approx. 1200 m

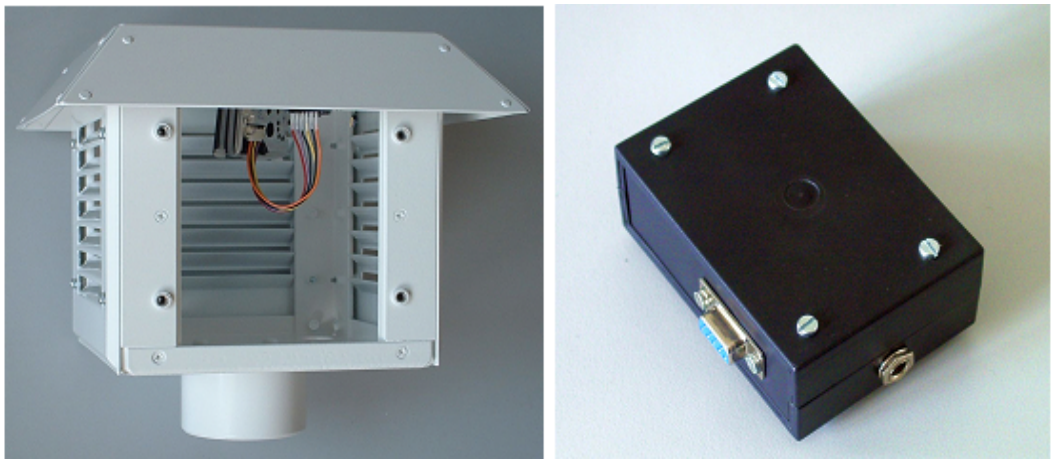

Figure 4.11: Fog sensor outdoor unit (left) and indoor unit (right)

4.2.3 Software Components

Fog sensor software components comprises of separate components for the outdoor and indoor units. Fog sensor data can be collected through software routines written in MATLAB code. A further detail of each unit is being mentioned in below subsections.

Outdoor Unit

The outdoor unit contains a microcontroller to perform data collecting and communication with the indoor unit. The firmware of the outdoor unit can be uploaded with a bootloader program: (http://www.etc.ugal.ro/cchiculita/software/picbootloader.htm, freeware). Fig. 4.12 shows the graphical user interface (GUI) of the fog sensors data handling software component. Usage of the bootloader:

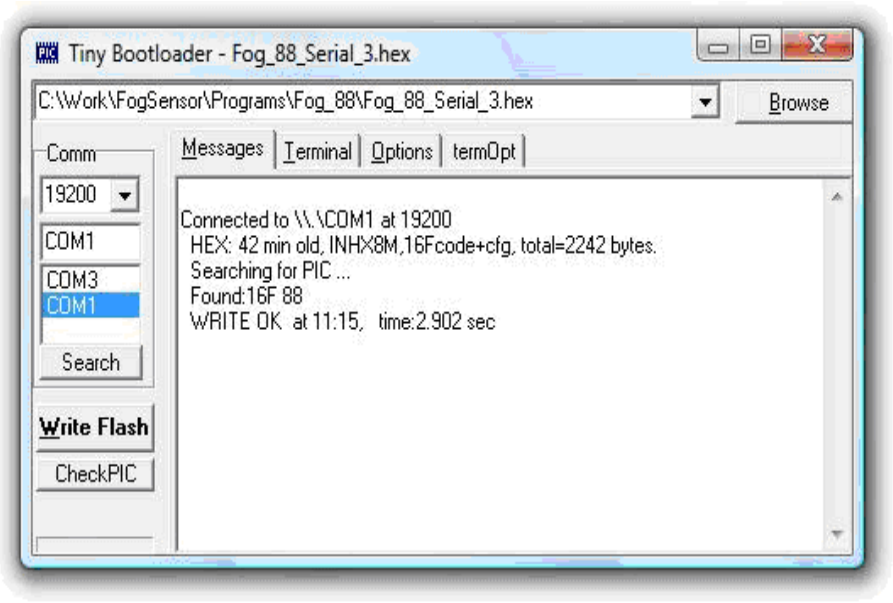

Figure 4.12: GUI of the fog sensor software component

- start Tiny bootloader
- select HEX file to upload
- power up the outdoor unit
- click Write Flash button

Indoor Unit

To receive and store measurement data from the outdoor unit a PC with MS Windows XP or Vista with serial communication port (RS-232) is needed. Required Windows settings for the data collecting computer:

- The time zone is set to GMT+0
- The 24 hour time format is adapted

- The PC is connected permanently to the internet and automatic internet time synchronization is made
- To enable the autostart utility of the program after reboot, "serial.exe com1" file is added in the startup menu

The serial.exe is the program to collect measurement data. It can be started without arguments or with com1/com2/com3/com4 to enable autostart with the selected serial port. The serial data collecting program receives and stores in a data file the measurement data. Fig. 4.13 shows the GUI of the software component that collects the data of the fog sensor. The data are sampled in the outdoor unit in every 10 msec, averaged by using the "Averaging No." value and sent via the serial line to the indoor unit in every second.

The data collecting program saves 1 sample/sec in the next file format as shown in the

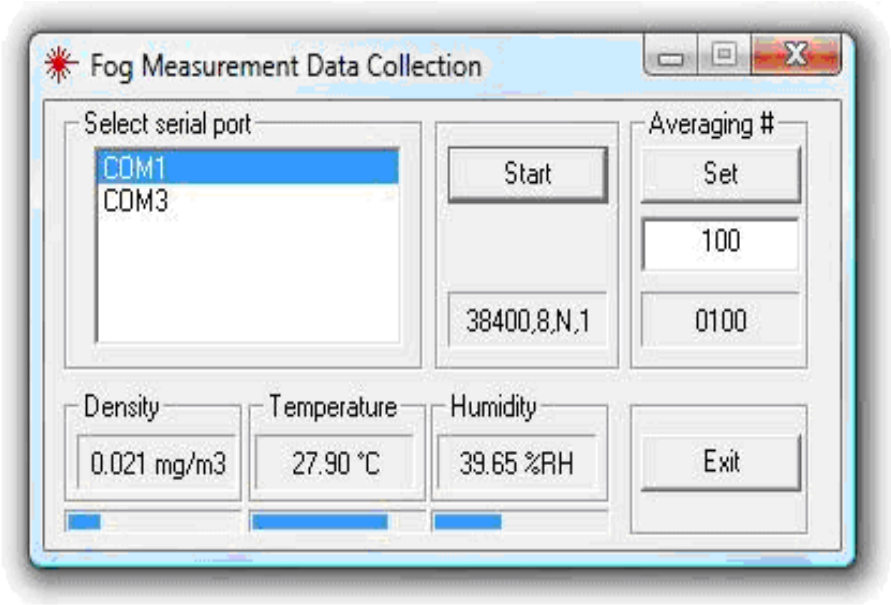

Figure 4.13: GUI of the fog sensor software component for data collection

Table 4.4 below, The decoding of the data can be done through a software routine written in MATLAB. The relative time is the serial number of seconds in the current day, starting with 0. The file is closed and new file opened at 24:00 o'clock. If the program is stopped and later restarted, the file of current day will be continued and data appended.

4.2.4 Fog Sensor Cabling

The fog sensor cabling consists of connections between indoor unit, interface unit and the outdoor cable unit of the fog sensor. The schematics diagrams of the each unit are mentioned in below subsections.

Fog Density	Temperature	Humidity	Averager	Relative Time
0169	4844	2354	0100	0
0167	4845	2355	0100	1
0168	4845	2356	0100	2
0171	4844	2357	0100	3
0171	4843	2358	0100	4
0171	4842	2359	0100	5
0170	4841	2360	0100	6
0168	4840	2361	0100	7
0168	4838	2361	0100	8
0170	4836	2362	0100	9
0170	4836	2363	0100	10
0167	4835	2363	0100	11
0167	4834	2363	0100	12
0167	4834	2363	0100	13
0171	4833	2366	0100	14
0166	4833	2367	0100	15

Table 4.4: Sample data format of the data received by a fog sensor

Fog Sensor Cabling - Indoor Unit

The cabling of the fog sensor indoor unit consists of cabling between interface unit to the outdoor unit via a 9 pol. DB9 Cannon female connector, to the 12 Volt power connector and to PC RS-232 9 pol. DB9 male connector as shown in Fig. 4.14.

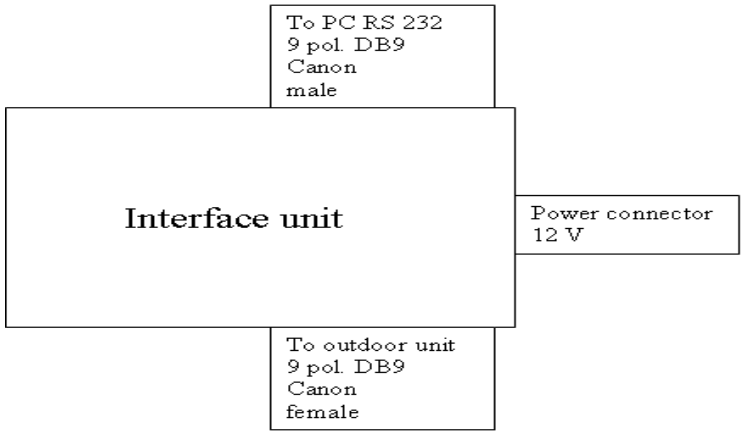

Figure 4.14: Schematic diagram of fog sensor cabling of the indoor unit

Fog Sensor Cabling - Interface Unit

The schematic diagram of the fog sensor's cabling interface unit is shown in Fig. 4.15. This cabling of the interface unit is is accomplished through connections of two 9 pol. DB9 female connectors between interface unit and the PC RS-232 connector.

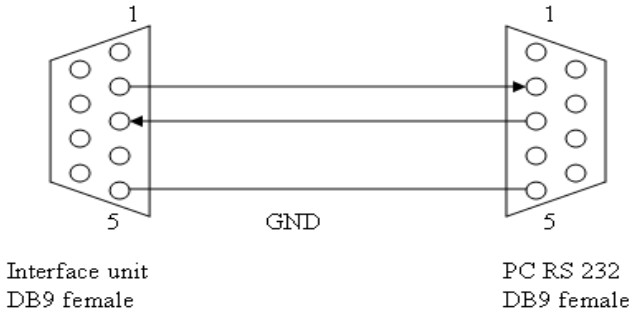

Figure 4.15: Schematic diagram of fog sensor interface unit

Fog Sensor Cabling - Outdoor Cable Unit

Fig. 4.16 shows the schematic of the fog sensor cabling of the outdoor cable unit. The connections are established through the use of twisted pair UTP cable between 9 pol. DB9 male connector of the interface unit and the 6 pinheader female connector of the outdoor unit.

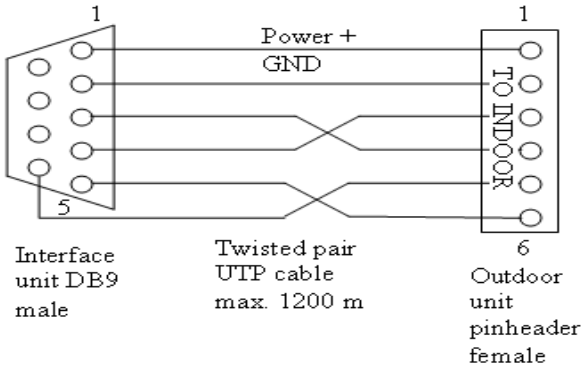

Figure 4.16: Schematic diagram showing fog sensor outdoor cabling unit

4.3 Fog Liquid Water Content and Density Measurement

Liquid water content (LWC) is the measure of the mass of the water in a fog or cloud to a specified amount of dry air. LWC is typically measured per volume of air (g/m^3) or mass of air (g/kg) [63]. This parameter is strongly linked to two variable: the fog or cloud DSD and the droplet number concentration. The amount of LWC in a particular volume of air is useful in determining which kind of fog or cloud formations is likely to occur and so is extremely useful for weather forecasting.
The main cause of the optical signal attenuations in free-space is the small sized spherical shape water droplets that are suspended in the air that contribute towards attenuations as a result of scattering and absorption effects. There exist several types of fog in different regions and seasons, having a typical droplet radius range and mode radius, that is inherent of the type of fog. So one should take the typical droplet radius of a particular type fog into account too while considering the effects of fog attenuation on the terrestrial FSO link. The physical mechanism of fog attenuation is therefore somewhat similar to the one of rain attenuation, but since the typical water droplet radius is much smaller in fog than in rain, the impaired wavelengths are shorter in fog when compared to rain. Considering this analogy between rain and fog attenuations, a question naturally arises if there is a microphysical parameter of fog that plays a role like that of rain intensity from the optical attenuations point of view. Liquid water content (LWC) of fog seems to be a suitable parameter in this respect, because it is related to a number of water droplets in the free-space propagation path. The liquid water content (LWC) is the mass of liquid water per unit volume of air. It is given by the following equation,

$$LWC = \rho_w \frac{4}{3} \int_0^\infty \pi r^3 C(r) dr \tag{4.5}$$

where,
ρ_w is the density of water ($\rho_w = 1.0 \times 10^6 g/m^3$)
r is the radius of the fog particles (m)
and C(r)dr is the number of fog particles per unit volume whose radius is between r and r + dr.

4.3.1 The Fog Density Measurement Results

The time series analysis of fog attenuations can provide interesting insight, and lead way to develop systems that can cope better with fog attenuations. For free-space optical communications, it is of high relevance to consider effects of changes in fog attenuation during short time intervals. One of the major aims of the measurement campaign in Graz in the winter of 2005, was to get better insight into the time domain analysis of the fog attenuations for the terrestrial free space optical links. Earlier in [27], some preliminary notions

on the importance of time domain analysis of fog attenuation were provided. The exact or more compact analysis of the attenuation behavior of fog can lead to design of better systems, with more throughput capabilities and enhanced performance. The current measurement campaign that started in September 2009 is aimed at studying the influence of fog density variations on the inflicted optical attenuations.
The occurrence of fog seriously affects the performance of a terrestrial FSO link by attenuating the power of the signal. The severity of fog is the direct consequence of the density of fog. The more severe the fog conditions the higher are the resultant optical attenuations. In order to characterize the optical attenuations due to fog conditions, it is important to investigate the density of fog and to see how optical attenuations vary with the variations in fog density. For the fog events detection and measurement of the corresponding amount of liquid water content, the fog sensor devices are installed near the FSO terminals at the two continental fog locations; Graz and Budapest. Several measurement result of detected fog events prove that the device is capable to sense the fog events and give a quantitative liquid content value, as it is shown in Fig. 4.17 [96]. The plot shows variations of relative humidity $(\%)$, temperature (°C) and the fog density in mg/m^3 against a sample fog event that occurred on 03rd Nov. 2008 at Budapest, Hungary. These observed variations are in high correlation with the occurrence of the moderate continental fog event at Hungary with density of fog approaching 0.5 mg/m^3.

In Fig. 4.18 is shown a typical continental fog event recorded at Budapest, Hungary on

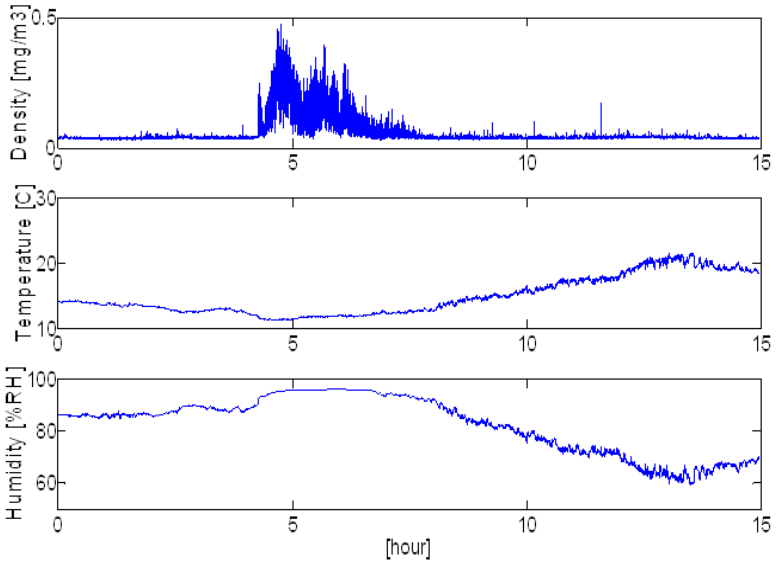

Figure 4.17: A sample fog event density measurement example

29th December 2008. It is clearly evident that the foggy periods are pairing with high humidity, but the air temperature was below the common 0 °C [120].

The prototype of the sensor is operating since October of 2008 at TUG, Graz and BME,

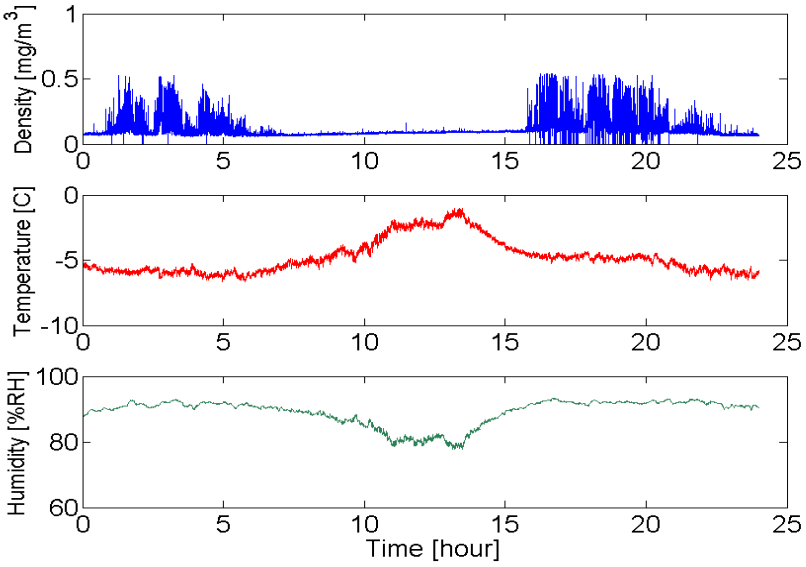

Figure 4.18: Fog density, temperature and humidity profile against a continental fog event at Budapest

Hungary. During this period several fog events have been detected at both locations. In addition to fog events at Graz, three very heavy snow events also occurred during this period. It would be interesting to look into the measured density, temperature and humidity profile related to snow events. The density profile related to fog and snow events at Graz, Austria and a fog event at Budapest, Hungary is discussed here. The plot as mentioned below in Fig. 4.19 corresponds to a fog event at Graz that occurred on 24^{th} January, 2009. This is a typical fog event with air humidity higher than 95% and low temperature close to 0 °C. It is well observable that during the lower-value periods of the humidity the fog has disappeared [120].

Our measurement results recorded at Budapest (as shown in Fig. 4.18) and Graz (as shown in Fig. 4.19) indicate that the fog sensor device is quite capable of detecting the fog events and in addition gives us a quantitative measure of the amount of liquid water content. Another measurement is shown in the next Fig. 4.20, against a snow event recorded on 02^{nd} Feb. 2009 at Graz.

In this case the density shows also a deviation from the zero-level, but comparing its value with the previous example, the order of magnitude is ten times lower. The levels of the humidity and the temperature are also non-typical for fog events. By analyzing the meteorological data recorded with another device close to our sensor, this event can be identified as the typical effect of snow event coupled with very low fog intensity. The parallel temperature and humidity values measured are in strong correlation with the fog density; however, detectable but very low level fog density could appear during snow events, as it is demonstrated in Fig. 4.20.

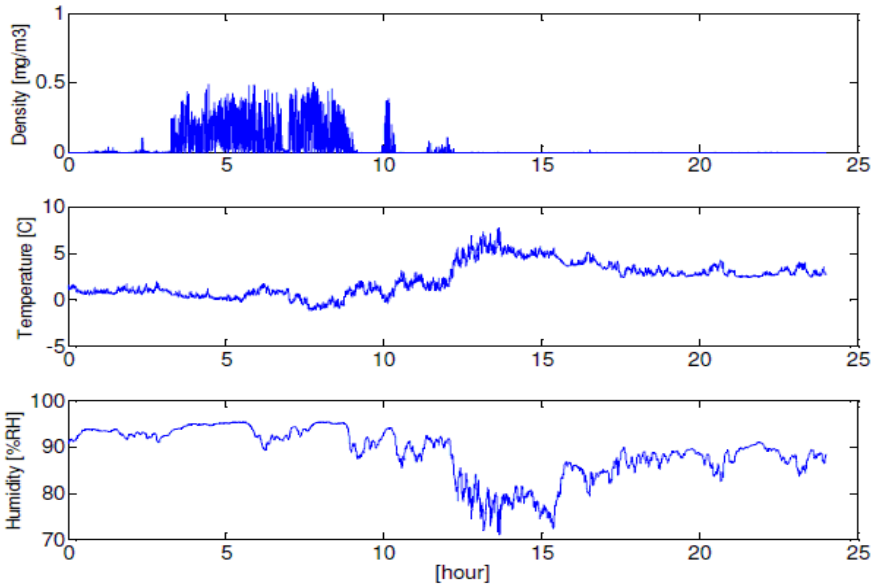

Figure 4.19: Density, temperature and humidity profile against a fog event at Graz

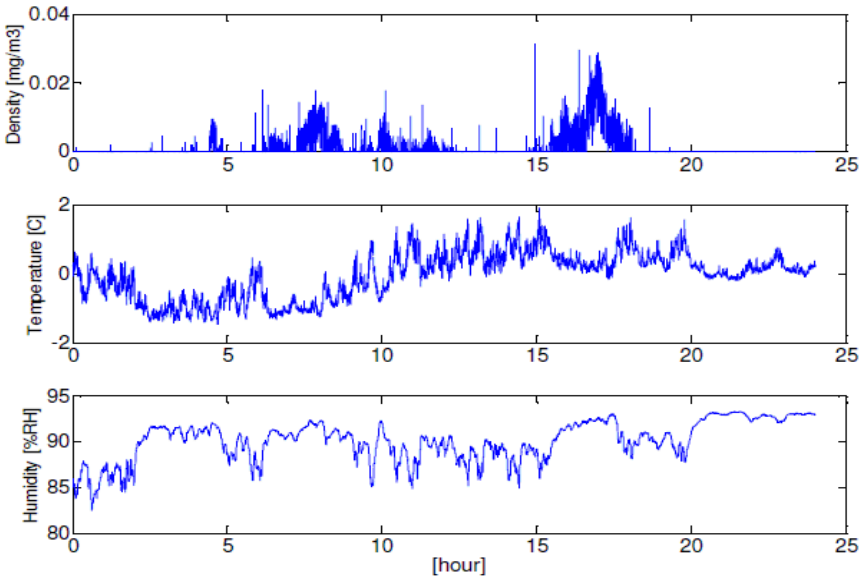

Figure 4.20: Density, temperature and humidity against a snow event at Graz

4.3.2 Empirical Relationship Between Relative Humidity and Temperature with Optical Extinctions

Relative humidity (RH) and temperature (T) play an important part in the formation and dissipation of continental fog. Measurement of RH and T are simple tasks and based on their values recorded, we can approximate corresponding attenuations. However, additional information in the form of parameters like fog drop size distribution, liquid water content and fog density would further enhance the accuracy in estimating the optical attenuations. We propose here an empirical relationship between temperature, relative humidity and optical attenuation values for an optical wireless link in continental fog environments. This relationship is developed using standard curve fitting technique by employing Gaussian model which is considered a best fit in our case. The relative humidity and temperature values are plotted along x-axis in Fig. 4.21 and Fig. 4.22, respectively, while measured specific attenuation values are plotted along y-axis in both plots [130].

The data values of RH-specific attenuation and temperature-specific attenuation are first

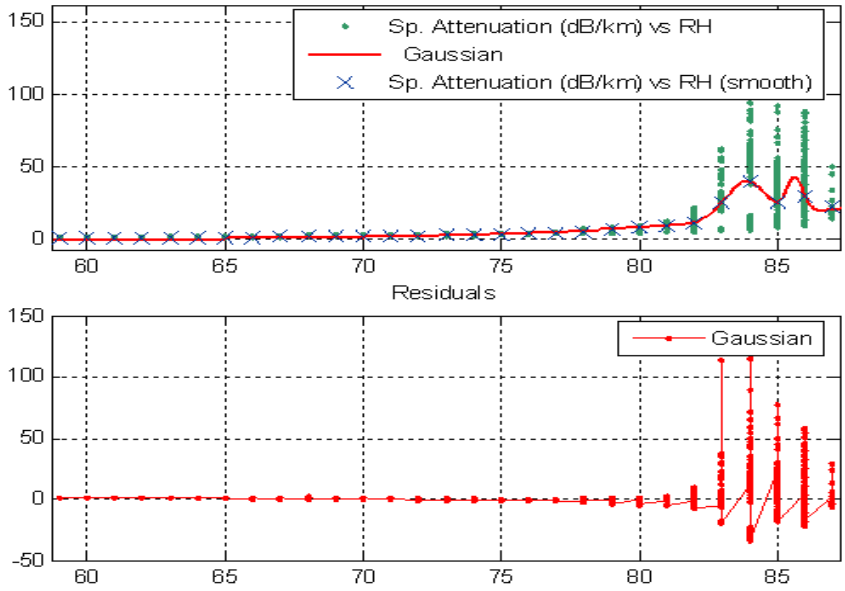

Figure 4.21: Gaussian fit for specific attenuations vs relative humidity

smoothed (averaged) and then non-linear least square Gaussian fit is applied. There is a large scatter of attenuation values for relative humidity values between $83\% - 87\%$ range and temperature values between 3.5 °C and 4.5 °C range, as evident from Fig. 4.21 and Fig. 4.22, respectively. As the interpolation technique mentioned can not go through all the data points so we first averaged out the instantaneous variations of specific attenuation. By this way the data points are smoothed and so we applied the non-linear least square Gaussian fit. We could expect large residual errors especially for the data points lying in

the above mentioned range for temperature and RH, and it is also evident from the residuals plots as shown in lower halves of Fig. 4.21 and Fig. 4.22. The Gaussian fitting plot after smoothing the temperature-specific attenuations values and additionally showing the residual errors is presented in Fig. 4.22 [130].

It is observed that for the above mentioned relative humidity and temperature values, mod-

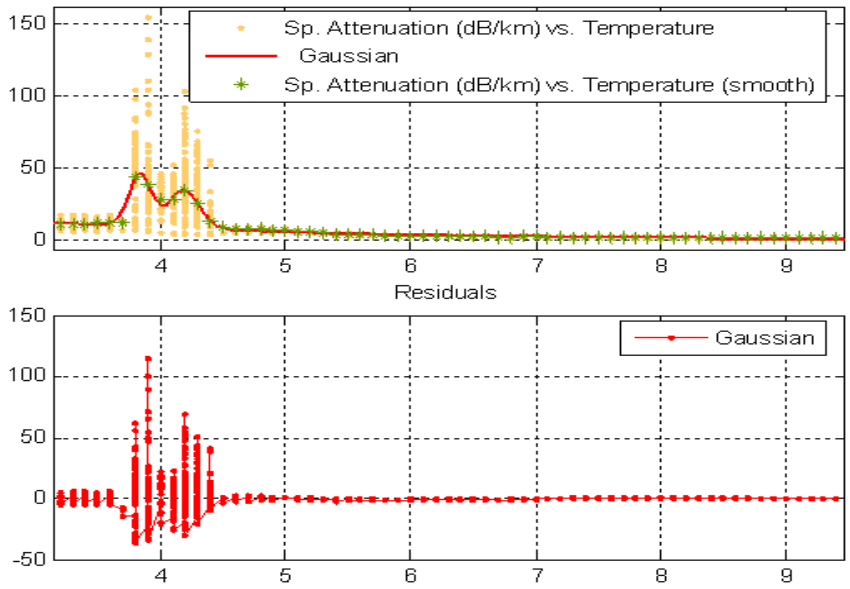

Figure 4.22: Gaussian fit for specific attenuations vs temperature

erate continental fog really establishes itself and results in significantly high variations in optical power attenuations. The possible explanation to these variations in specific attenuation values can be attributed to the complex microphysical processes that vary spatially and temporally during the life cycle of the continental fog with reference to a particular location with time. The combined effect of all microphysical processes results in comparatively large fluctuations of optical signal attenuations. Quantitatively this can be observed as sum of square value of the residual errors as evident in the lower halves of the plots mentioned in Fig. 4.21 and Fig. 4.22. We applied Gaussian fitting by employing the non-linear least squares method and used the trust-region reflective Newton algorithm for this Gaussian curve fitting. The model equation is given by the following relationship [130],

$$\beta_{att} = a_1 * \exp[-(\frac{x-b_1}{c_1})^2] + a_2 * \exp[-(\frac{x-b_2}{c_2})^2] + a_3 * \exp[-(\frac{x-b_3}{c_3})^2] \qquad (4.6)$$

Here β_{att} is the attenuation coefficient estimated from the recorded relative humidity value x. The corresponding coefficients having 95% confidence bounds are mentioned below,

$$\begin{cases} a_1 = 25.75(14.98, 36.52) \\ b_1 = 83.85(82.69, 85.01) \\ c_1 = 1.026(-0.7717, 2.824) \\ a_2 = 93.89(-2568, 2756) \\ b_2 = 113.8(-242.2, 469.9) \\ c_2 = 21.77(-80.5, 123.6) \\ a_3 = 24.46(-2.335 \times 10^5, 2.335 \times 10^5) \\ b_3 = 85.64(-903.2, 1075) \\ c_3 = 0.4174(-1501, 1502) \end{cases}$$

The sum of squared errors (SSE) and root mean squared errors (RMSE) arising from the residual errors is mentioned in Table 4.5 for relative humidity-specific attenuation values and in Table 4.6 for temperature specific attenuation values, respectively [130].

The same model (as already given in Equation (4.6)) can be applied for the temperature

SSE	Rsquare	DFE	Adjrsquare	RMSE
2.809×10^5	0.47594	1426	0.473	14.035

Table 4.5: Statistical parameters of fitting model between relative humidity and specific attenuations

and specific attenuation values [130]. The corresponding coefficients for temperature-specific attenuation relationship having 95% confidence bounds are,

$$\begin{cases} a_1 = 36.04(32.36, 39.72) \\ b_1 = 3.839(3.826, 3.852) \\ c_1 = 0.1298(0.09624, 0.1634) \\ a_2 = 26.16(23.65, 28.66) \\ b_2 = 4.189(4.171, 4.207) \\ c_2 = 0.1722(0.1428, 0.2017) \\ a_3 = 263.7(-7976, 8504) \\ b_3 = -12.74(-158.4, 132.9) \\ c_3 = 9.071(-28.11, 46.25) \end{cases}$$

4.3.3 Relationship between Fog Drop Size Distribution and Liquid Water Content

The size distribution of the fog droplets is usually described by modified gamma distribution as given by Equation (4.1). If N_d is the actual total concentration of the fog droplets

SSE	Rsquare	DFE	Adjrsquare	RMSE
2.4426×10^5	0.5443	1426	0.54175	13.088

Table 4.6: Statistical parameters of fitting model between temperature and specific attenuations

per cubic centimeter of air then the real profile of the fog droplets is given by multiplying C(r) by N_d [127]. Therefore, following Equation (4.1) the liquid water content in g/m^3 is defined as,

$$LWC = \rho_w N_d \frac{4}{3} \int_0^\infty \pi r^3 C(r) dr \tag{4.7}$$

where r is the particle radius. The values of LWC resulting from Equation (4.7) and the corresponding set of MGDSD parameters giving the best fit curves relative to eight size spectra of small water droplets for a visibility range of 1 km are given by Claudio Tomasi et. al [127]. Given the third power radius in Equation (4.7) suggest that water droplets smaller than 3 μm have a very little contribution towards LWC and therefore, could be neglected [131]. The effective extinction efficiency $\zeta(r)$ and effective droplet radius r_e in terms of DSD are given by Equations (4.8) and (4.9) below, respectively [132]:

$$\zeta_e = \frac{\int_0^\infty \zeta(r) r^2 C(r) dr}{\int_0^\infty r^2 C(r) dr} \tag{4.8}$$

$$r_e = \frac{\int_0^\infty r^3 C(r) dr}{\int_0^\infty r^2 C(r) dr} = 30000 \frac{LWC}{PSA} \tag{4.9}$$

It is important to mention that r_e is the radius of the fog particles of *single diameter droplet* having the same LWC and PSA. PSA is the fog particle surface area measured in (cm^2/m^3). LWC and PSA are both important parameters to estimate fog attenuations caused by scattering of fog particles. When fog particles are assumed spherical in shape then PSA is given by [132]:

$$PSA = 10^{-2} \times 4\pi \int_0^\infty r^2 C(r) dr \tag{4.10}$$

PSA and LWC of fog and clouds droplet size distribution can be estimated from MGDSD i.e., C(r). Assuming a modified gamma drop size distribution MGDSD (as given by Equation (4.1)), and provided m is specified, N_0 and Λ are given by,

$$N_0 = \frac{3 \times 10^6 (LWC \cdot \Lambda^{m+4})}{4\pi\Gamma(m+4)} \tag{4.11}$$

$$\Lambda = \frac{(m+3)}{r_e} \tag{4.12}$$

Here $\Gamma()$ is the gamma function. Figure 4.23 illustrates the influence of three DSD parameters of the modified gamma distribution (as shown on left), and the particle surface area (PSA) (as shown on right) of fog for a given value of LWC = 0.5 g/m^3 [132]. LWC

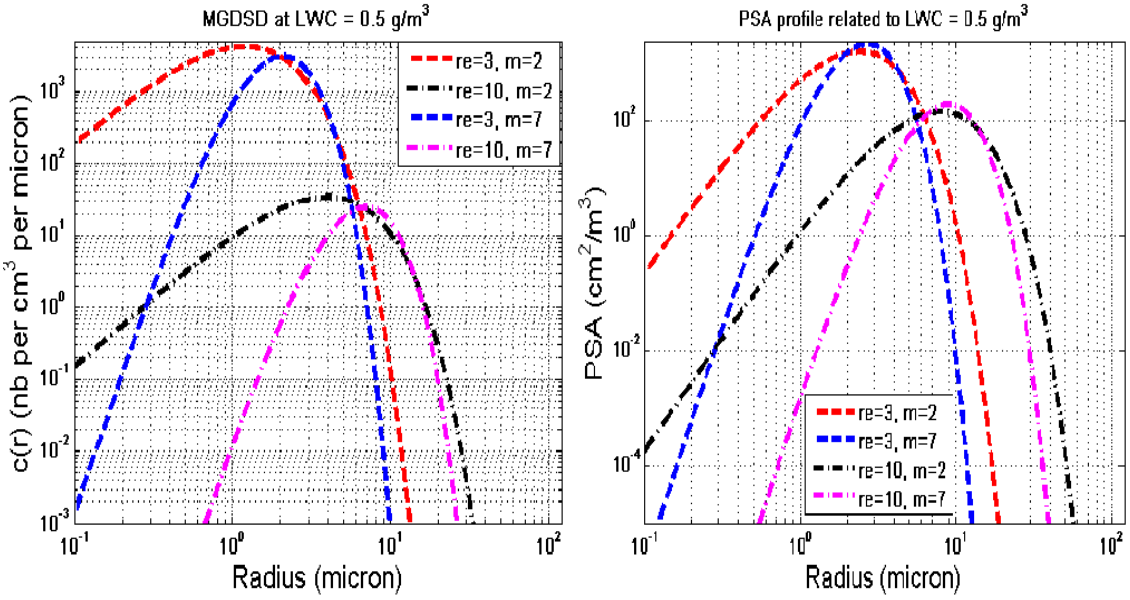

Figure 4.23: The MGDSD and PSA of fog for different MGDSD parameter values against LWC=0.5 g/m^3

varies significantly depending on the type of fog or cloud present in the atmosphere at a particular location. Their classification is highly related to the amount of LWC as well as to their origin. The combination of LWC and the origin allows to readily predict the types of conditions that will be most likely in the vicinity of the free-space optical link. Fog, having very low densities, contain very little amount of water and thus result in lower values of LWC around 0.05 g/m^3 for a moderate fog (visibility range around 300 m). While much higher values of LWC (around 0.5 g/m^3) usually means formation of thick or dense fog (visibility range of about 50 m) [133]. Similarly, clouds may have a LWC value of 0.06405 g/m^3 and 1-3 g/m^3 for Cirrus and Cumulonimbus clouds, respectively measured in the same amount of space [99]. Fog or cloud droplets of the maritime origin tend to have fewer water droplets having relatively larger size radius than the continental droplet size [96, 99]. The concentration of maritime origin droplets lies between 100 drops/cm^3 to about 200 drops/cm^3, whereas the concentration of continental origin droplets is about 900 drops/cm^3 [134].

4.3.4 Models Relating Liquid Water Content to Visibility Range

Many models exist that relate DSD of fog or clouds with the optical attenuations for the FSO links. Due to the complexity of computing the DSD of fog or clouds at a particular location, models that relate visibility range to the optical attenuations have been developed. It may not be straight forward to compute the visibility range because of availability of the transmissiometer system and their high installation costs involved. Hence, there is a need to find an alternate solution to predict visibility range from some microphysical properties of certain atmospheric conditions like fog, rain, snow and clouds. LWC seems a suitable option as it is easily computable and, moreover, existing empirical models could then be used that relate visibility range to the LWC.
The variability in the fog microstructure causes a considerable variability in the reduction of visibility range induced by the presence of small water droplets in the air. Numerous researchers have aimed at defining relationships between associated visibility range reduction and the overall characteristics of fog. Most of them have focused on the power law relationship between fog LWC and its associated extinction coefficient [121, 127]. The general form of LWC and visibility range relationship derived from the ample set of data related to fog evolutionary stages is given by [132],

$$V = b(LWC)^{-2/3} \tag{4.13}$$

Where V is the visibility range and LWC is the amount of liquid water content (g/m^3). Parameter b takes on specific values for different fog conditions as shown in Table 4.7.
Another relationship dealing with LWC and the corresponding optical extinctions is given

Fog Type	b	**Reference**
Dense Haze	0.013	Claudio Tomasi et. al
Continental fog (dry and cold)	0.034	Claudio Tomasi et. al
Maritime fog (wet and warm)	0.060	Claudio Tomasi et. al
Dense Haze and Selective fog	0.017	Eldridge et. al
Stable and evolving fog	0.024	Eldridge et. al
Advection fog	0.02381	Koester and Kosowsky

Table 4.7: Fog types and the values of coefficient b to estimate visibility range from LWC

by,

$$\beta_{ext} = p(LWC)^a \tag{4.14}$$

Here, β_{ext} is the optical extinction coefficient. The proportionality constant p is related to specific fog conditions. Experimental results show considerable variability, with values falling in the range of $65 \leq p \leq 178$ and $0.63 \leq a \leq 0.96$ [122]. A relationship for visibility range as a function of both liquid water content and the droplet size was proposed by J. E. Jiusto who showed that LWC is directly related to droplet size [124]. More recently

Gultepe et al. proposed a relationship between visibility range V and the product of droplet number concentration N_d and LWC [135] as given by Equation 4.15. This model recognizes the presence of variability in fog droplet sizes and their role in optical extinctions in different fog conditions by influencing the visibility range parameter.

$$V = 1.002(LWC \cdot N_d)^{-0.6473} \tag{4.15}$$

The maximum value for N_d and LWC used in derivation of Equation (4.15) are about 400 cm^{-3} and 0.5 g/m^3, respectively. Whereas the minimum values are 1.0 cm^{-3} and 0.005 g/m^3, respectively. This model recognizes the presence of variability in droplet sizes and their contribution towards reduction of visibility range in fog. Under a project named Fog Remote Sensing and Modeling (FRAM), a model have been developed from the empirical data to characterize different phases of maritime fog (e.g., formation, evolution and dissipation) that deals with marine fog and is given by [136],

$$V = 0.856(LWC \cdot N_d)^{-0.609} \tag{4.16}$$

Expression (4.16) suggests that when LWC is fixed, N_d should decrease to obtain large visibility range values e.g., during fog dissipation phase. In case of small droplets evaporation, some large droplets tend to be formed such that when these large droplets reach a critical size (diameter > 20 μmm) they drizzle out [136].
Fig. 4.24(a)-(d) shows simulation results for the visibility range for fixed values of N_d, fixed LWC, the continental and maritime fog models defined by Equations 4.15 & 4.16, and the simulation model of Equation 4.14, respectively [132].
It is evident from this plot that visibility range decreases with increasing N_d and LWC. In Fig. 4.24-(c), the model labelled as maritime (advection) fog is simulated using Equation 4.16, whereas, models labelled as continental fog and maritime fog are simulated using Equation 4.15 [132].
Furthermore, it is obvious that in situations when LWC is fixed and N_d increases, fog particle terminal velocity weighted over the spectra (V_t) becomes lower and hence results in decreased visibility range, thus suggesting higher density fog. In other words, if the droplet terminal velocities are low then the droplets stay longer in the air resulting in reduced visibility range and vice versa. Alternatively, during fog natural dissipation phase the droplet number concentration N_d should decrease. The terminal velocity of fog particles V_t is given by:

$$V_t = 178.984(\frac{LWC}{N_d})^{0.684} \tag{4.17}$$

Now in order to estimate the fog LWC (g/m^3) values directly from the fog density values (mg/m^3) the following procedure can be adopted. The fog density is measured with a simple optical device, whose output values may have big fluctuations as they are measured on the seconds time scale. So conversion from fog density values to LWC values first require smoothing of the data values since LWC can not change so rapidly. This can be achieved through averaging of the instantaneous values of LWC. Let W_k be the averaged

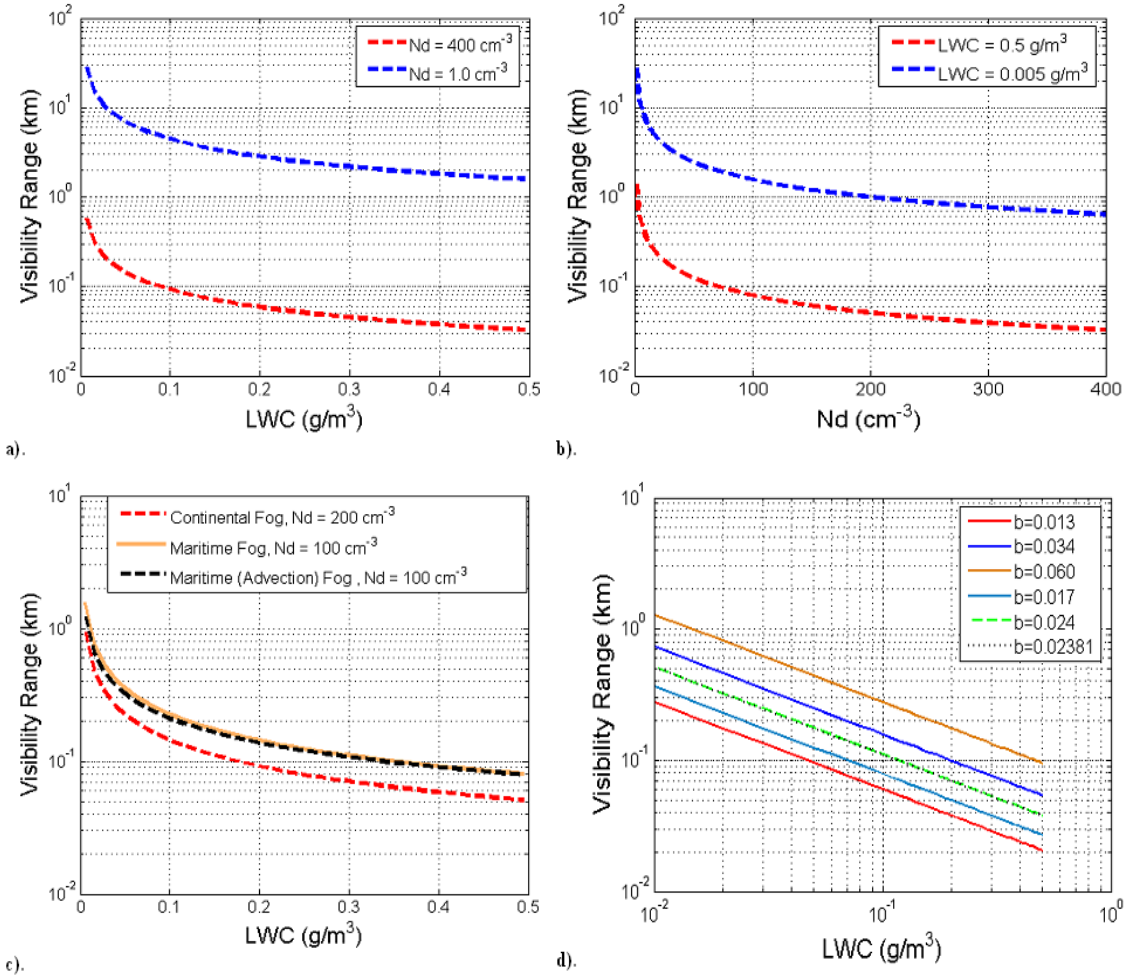

Figure 4.24: Simulations of relationship between LWC, N_d and visibility range

value of LWC and D_k is the output of the fog sensor between 0-0.5 relative values, therefore their ratio is represented by a constant C given by [137]:

$$C = \frac{\sum_{k=1}^{n} W_k}{\sum_{k=1}^{n} D_k} = 0.7384(g/m^3) \qquad k = 1,2,....,n \tag{4.18}$$

Where n is the total number of measurement samples during the whole fog event. The momentary value of LWC in the presence of fog is thus given by:

$$LWC_k = C \cdot D_k = 0.7384 \cdot D_k(g/m^3) \qquad k = 1,2,....,n \tag{4.19}$$

The optical extinctions can be predicted from LWC values either by the power law relationship as given by Equation (4.14), or by first predicting the visibility range from LWC instantaneous values using equations (4.15 & 4.16) for continental and maritime fog, respectively.

4.3.5 Impact of Fog Density and Liquid Water Content on the FSO link Performance

Figure 4.25(a)-(f) show results of LWC, temperature and relative humidity variations, LWC and fog density variations, variations of LWC on minute scale, variations of LWC on the hour scale, corresponding measured optical attenuations on the seconds scale and measured attenuations on minute scale, respectively against a continental fog event recorded at 950 nm over an 80 m FSO link at Graz on 18-19 Nov. 2009. A time series of all the above mentioned parameters is shown from 10 AM on 18 Nov. 2009 to 10 AM on 19 Nov. 2009. The total duration of this fog event was about 13 hours (started around 5 PM on 18 Nov. 2009 and lasted until 8 AM on 19 Nov. 2009. The optical attenuations recorded the maximum value of 140 dB/km averaged on a minute scale. The appropriate photographs taken by a CCD camera looking at the transmitted beam spot (at 950 nm) for the no fog condition, moderate fog condition with attenuations of 40 dB/km to very dense fog condition with attenuations as high as 140 dB/km, are also shown in Fig. 4.25-(f). The corresponding variations of temperature, relative humidity and the LWC (g/m^3) estimated from fog density (mg/m^3) are illustrated in Fig. 4.25-(a) and a comparison between fog density and the corresponding LWC is depicted in Fig. 4.25-(b) [132]. During dense fog event, the temperature is around 4-6 °C with the relative humidity at around 100%, see Fig. 4.25-(a). As the temperature increases, the relative humidity decreases and hence causes the fog dissipation, while the fog formation takes place as temperature decreases towards 0 °C and relative humidity increases towards 100%. A comparison between Figs. 4.25-(c) & 4.25-(f) reveals that maximum optical attenuation of 140 dB/km is achieved against LWC value of around 0.29-0.3 g/m^3 and around 0.19-0.2 g/m^3 averaged over a minute and on hourly scales, respectively. The LWC value stay around 0.1198 g/m^3 during the mentioned 24 hours when averaged either over seconds, or minutes or hourly scales. By comparison it can be seen that against the maximum value of LWC ($\sim$ 0.4 g/m^3) the corresponding optical attenuation value is 130 dB/km. The possible explanation of this observation may be due to a variation in N_d because of the sudden wind gusts or may be because of 1 m separation between the FSO receiver terminal and the fog sensor device. Overall, it is evident that optical attenuations are in high correlation with the fog density variations and the results indicate that both are directly proportional to the severity of fog.

The plot in Fig. (4.26) shows the comparison between the actual measured optical attenuations at 950 nm and the optical attenuations predicted from LWC momentary values. The procedure adopted to compute the predicted attenuations from LWC instantaneous values is as follows: firstly, the instantaneous values of fog density recorded by the fog sensor are converted to momentary LWC values averaged over minutes and hours time scale against the mentioned fog event using Equation 4.19. Then from these momentary values of LWC, visibility range is estimated using the relationship given by Equation 4.15. Once the visibility range is computed against the LWC values for the mentioned continental fog event, using Kruse and Kim model (approximations of visibility range) the corresponding spe-

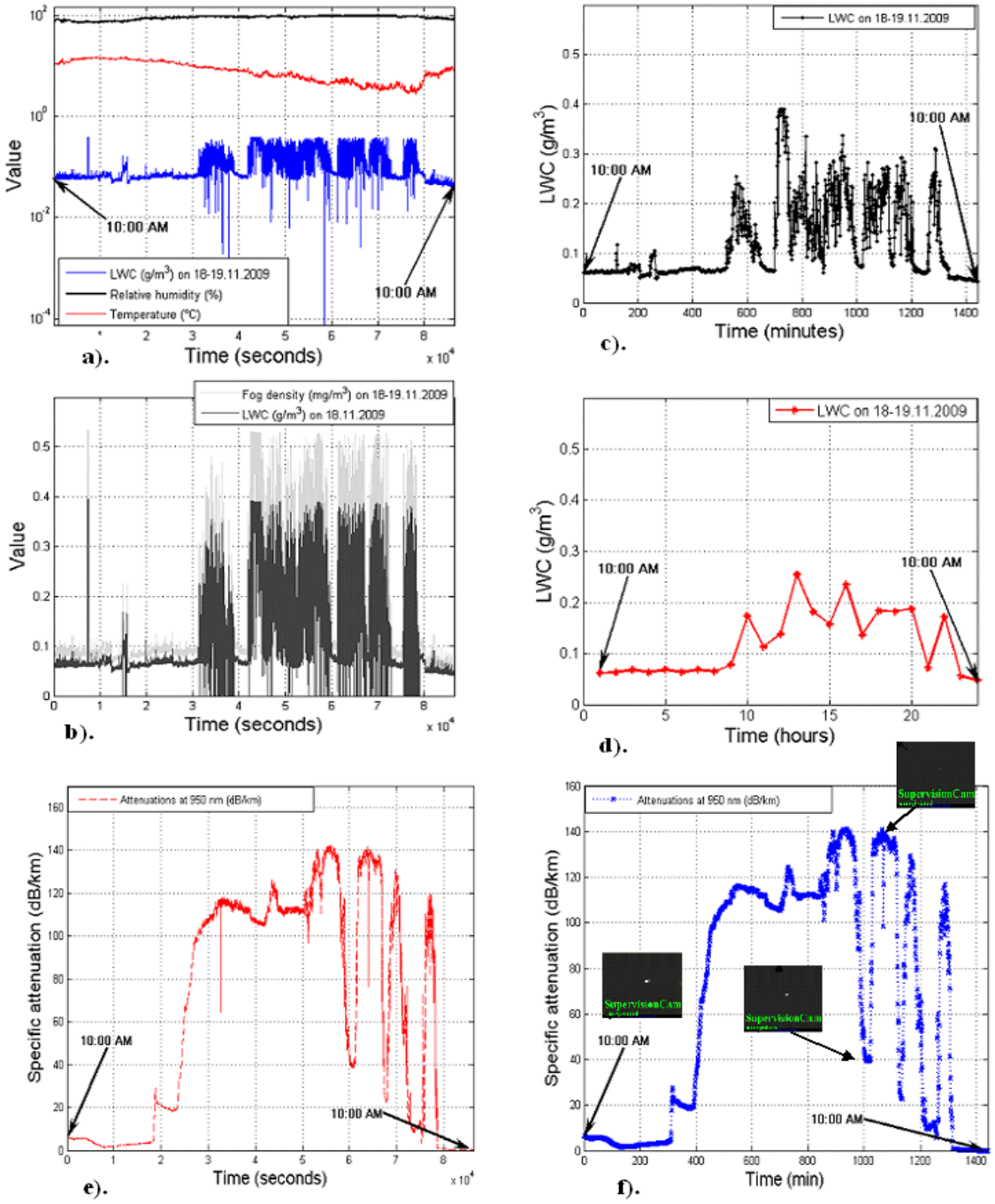

Figure 4.25: Results of LWC, temperature, relative humidity and fog density variations against a continental fog event recorded at Graz

cific attenuations are computed for attenuation values averaged over minutes and hours time scales for comparisons [132]. It is important to mention that the transmission thresh-

old was taken as 5% while predicting the visibility range values from LWC instantaneous values. The plots given in Fig. 4.26(a)-(b) show a comparison between the measured optical attenuations and the predicted attenuations for a range of N_d against Kruse and Kim model, respectively. Different values of N_d are compared in order to get a rough idea about the fog particles concentration during certain fog event. From Figs. 4.26(a)-(b), it appears as though the particle concentration roughly varies somewhat between 100-250 particles/cm^3 volume as the actual measured attenuations were more closer to this range values as compared to the other range values. In order to get a better impression between comparisons of attenuations, plots in Fig. 4.26(c)-(d) are compared on attenuation values averaged on a hourly time scale for both actual measured and the predicted attenuations using Kruse and Kim approximations, respectively. From these two plots, its clearer to see that the particle concentration remained in the above mentioned range during this fog event. In Figs. 4.26(e)-(f), the predicted (Kruse and Kim) and actual measured optical attenuations are compared against the CDF (%) exceeded for values averaged on a minute and hourly time scales, respectively. It is evident from these plots that the CDF of the measured and the predicted attenuations proves that the attenuation values are similarly distributed; validating the LWC estimation. Moreover, the predictions made through visibility range estimates by Kim model are closer to the actual measured attenuations as compared to the attenuations predicted by the Kruse model. This behavior is observed because the fog was a kind of dense continental type with visibility range well below 500 m most of the time and so the Kim model performs better in comparison to Kruse model and is thus more relevant to describe the effects of very low visibility range conditions [132].

In order to refine the precision of this technique further measurements would be preferable especially during dense fog conditions in different fog environments and geographical locations. The attenuation predictions generated through fog density and LWC are of prime significance in addition to visibility range for terrestrial as well as ground-space optical links. The significance of this method over prediction method based on visibility range is that this method is equally valid in order to predict attenuations for both terrestrial as well as ground-space optical links. Whereas, the prediction method based on visibility range is so far only applicable to horizontal terrestrial links. Moreover, it would be useful in improving the current and future FSO link designs in terms of their performance enhancements by mitigating the harmful attenuation effects caused by different fog types.

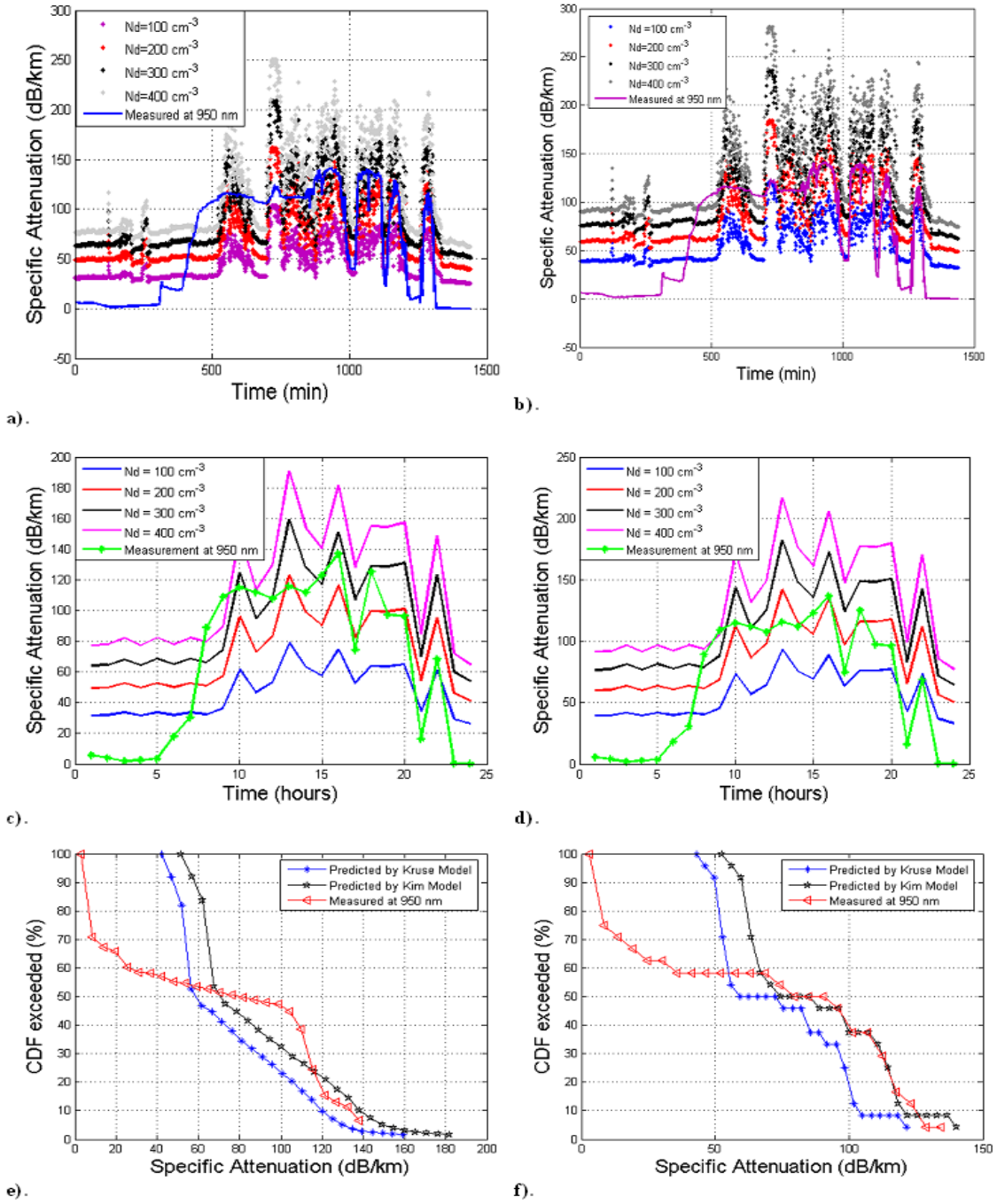

Figure 4.26: Comparison between actual measured optical attenuations and the predicted attenuations from momentary values of LWC

4.4 Summary about Fog Microphysics

An analysis of the environmental conditions associated with continental fog and maritime fog events has been presented using observations made at different locations around Europe. Preferred weather scenarios and physical processes influencing the formation and dissipation of fog were identified. Continental fog mostly occur as a result of radiative cooling over land with the decrease in temperature and increase in relative humidity under clear skies in stagnant air conditions. Maritime fog is associated with the advection of a moist air-mass with contrasting temperature properties with respect to the underlying surface. Intricate relationships exist between fog microphysics and the fog characteristics that influence the optical signals transmitted in free-space. LWC of fog seems to be a suitable parameter to predict optical attenuations besides droplet size distribution and visibility range, that is related to a number of fog particles in the propagation path. Since there exist several types of fog with different typical droplet radii dependent on the region and the season. Therefore, one should also take into consideration additional microphysical parameters of fog such as the droplet diameter and droplet number density. Moreover, it was seen through simulations that optical attenuations in fog conditions are highly dependent on the amount of LWC. In order to understand and properly parameterized the overall mechanism of interactions between the various processes that shape up the fog microstructure, a comparison of fog density measured through a simple fog sensor device installed at the location of FSO transceivers is made. It has been observed that fog density is in high correlation with the LWC and in turn to the resultant optical attenuations. However, there is not enough information available on the fog vertical structure, and its representation in the form of different models can be useful in the design of future ground-space FSO links. Also the process of fog droplet growth and different factors (like turbulent mixing) affecting it are not considered in most of the fog models and need further investigations. Reliable measurements of small size droplets of fog are also missing that add up to our incomplete understanding. Therefore, a multi-year data-set with consistent state of the art instrumentation is needed that could prove invaluable in efforts to characterize, understand and parameterize the considerable variability in fog microstructure within the various fog environments. However, on the basis of this limited set of available attenuation data we can propose some methods to predict optical attenuations that will be based on the computed DSD parameters from actual measurements, and are discussed in detail in the next chapter.

5 IMPLEMENTATION OF THE FOG ATTENUATION PREDICTION MODELS

Different fog conditions have been found to have a great impact on the performance of terrestrial FSO systems. In order to characterize the free-space atmospheric channel for different fog conditions, the biggest issue is the unavailability of measurement data of fog attenuations for different fog environments, seasons and climates. Conducting field tests in different atmospheric environments requires huge amount of money and a lot of difficulties in order to study the impact of different atmospheric conditions. In recent times, a number of attenuation prediction methods have been developed that allow to calculate propagation related important parameters and are useful in planning FSO systems operating in the visible and infrared spectrum. Such methods can be tested against available measurement data to check for their adequacy, efficiency and compatibility with the natural variability of propagation phenomena. In this section fog attenuation models are discussed that are developed based on measurement data recorded at three different continental fog locations Graz (Austria), Milan (Italy), and Prague (Czech Republic). These models are based on microphysical quantities like droplets drop size distribution (hereafter DSD) and liquid water content (hereafter LWC) and the Mie theory. The first model proposes a method to artificially simulate the fog DSD and is based on Marsaglia Method [138], and can be used to compute the Modified Gamma DSD (hereafter MGDSD) parameters for any location. The next prediction model is based on Maitra and Gibbins technique that employs standard iterative procedure to compute the DSD parameters [139]. Using this method an optimal set of DSD parameters corresponding to MGDSD and exponential drop size distribution (hereafter EDSD) are computed for the two locations Graz and Prague.

5.1 Prediction Model Based on Droplet Size Distribution

The FSO systems are suitable for certain terrestrial and space-based communications in near-Earth and deep space environments. Appropriate propagation prediction methods are required for the prediction of the most significant propagation related impacts to Earth-space systems. Such methods must yield an accuracy that is both compatible with the natural variability of propagation phenomena and adequate for most present applications.

5.1.1 Mie Scattering and Modified Gamma DSD Based Prediction Model

In case of terrestrial FSO links, fog particles introduce Mie scattering to the optical signals transmitted in free-space which causes significant attenuation of the optical energy. This attenuated energy is strongly dependent upon the fog particles distribution which is not routinely measured or reported in the standard meteorological data. The nature of fog droplets distribution may change drastically at a certain location with time and so is considered the major atmospheric element responsible for the attenuation of the optical signals. The prediction of fog droplets distribution and its behavior during fog formation, maturity and dissipation stages represent a challenging problem because it crosses many scientific areas: thermodynamics, cloud physics and boundary layer meteorology.
A number of aerosol models are used to predict particle concentration on the basis of actual meteorological conditions or according to climatology. It is admitted in meteorology that a given aerosol model cannot be used to predict wave attenuation under all atmospheric conditions, since the local meteorological conditions dominate the aerosol source function [2]. However, the size distribution of atmospheric particulates is commonly represented by three analytical functions: the exponential distribution, lognormal distribution and the modified gamma distribution (MGDSD). The gamma probability density function (PDF) is actually a general PDF that is used for nonnegative random variables. r is said to be a gamma random number with parameter α and β, if the following relationship holds,

$$\Gamma(\alpha) = \int_0^\infty r^{\alpha-1} e^{-r} dr \tag{5.1}$$

Let us assume that $\alpha = m+1$ and $\beta = \frac{1}{\Lambda}$, then Equation (5.12) becomes,

$$f(r) = \frac{r^m \Lambda^{m+1} e^{-r\Lambda}}{\Gamma(m+1)} \tag{5.2}$$

In meteorology, the DSD of fog can be more conveniently described by a frequency distribution c(r) than the probability distribution f(r), and MGDSD is the most commonly used for several types of fog and clouds [99]. If C(r) represents the fog particle concentration, then the number of particles per unit volume and per unit radius increment (r to $r+\Delta r$) is,

$$C(r) = N_0 r^m exp(-\Lambda r^\sigma)\Delta r, \qquad 0 \leq r \leq \infty \tag{5.3}$$

with

$$\Lambda = \frac{m}{\sigma \cdot r_{mod}^\sigma} \tag{5.4}$$

Here, m, σ, N_0, Λ are the four adjustable parameters characterizing the MGDSD. m is called the shape parameter and Λ is the slope or gradient. These parameters allow the MGDSD to fit a large variety of cases. r_{mod} is the mode radius (μm) of fog particles i.e.,

the radius r at which c(r) is a maximum. Multiplying Equation (5.2) and Equation (5.3) by N_T (total number of fog particles per unit volume), we get N_0 as,

$$N_0 = \frac{N_T \Lambda^{m+1}}{\Gamma(m+1)} \tag{5.5}$$

and

$$N_T = N_0 \sigma^{-1} \Lambda^{\frac{m+1}{\sigma}} \Gamma(\frac{m+1}{\sigma}) \tag{5.6}$$

5.1.2 Artificial Fog Droplet Simulation

By comparing the observed attenuation values with the ones obtainable by the DSD model previously described, one can state whether the model is suitable to describe fog process in Milan and/or Graz eventually after tuning of some parameters, or whether a different DSD model is necessary. To this aim we have simulated the fog process (DSD), as outlined in the following.
In simulating artificial fog droplets according to a MGDSD, no reference describes how to simulate random numbers from the modified gamma frequency distribution. However, several methods are available to simulate random numbers from a probability distribution such as the transformation method [138] and the rejection method [140]. The method proposed here is employed to generate modified gamma-distributed variables by considering a monotone transformation h(x). It can be shown that if x has density,

$$e^{g(x)} \cong \frac{h(x)^{a-1} c^{-h(x)} h'(x)}{\Gamma(a)} \tag{5.7}$$

then $y = h(x)$ follows the gamma density $\Gamma(a)$. Moreover, if g(x) is close to $c - \frac{x^2}{2}$ for some constant c, then a rejection method from a normal density can be developed. After generating a radius r that follows the probability gamma distribution, the fog droplet distribution is derived by using the following relationships:
$\int f(r)dr = 1$ and $\int c(r)dr = N_T$.
We can then calculate c(r) by binning r into several classes with bin width $\Delta(r)$. The probability density for each class is,

$$P(\Delta) = \frac{C_\Delta}{N_T} = \int_{D_1}^{D_2} f(r)dr = \int_{D_1}^{D_2} \frac{c(r)}{N_T} dr = \frac{c(\Delta)}{N_T} \cdot \Delta r \tag{5.8}$$

Where C_Δ and c(Δ) are the count and distribution of drops with radius $r_1 \leq r \leq r_2$ respectively. From Equation (5.8), it is robust that $C_\Delta = c(\Delta) \cdot \Delta r$ and the fog DSD is therefore given by,

$$c(\Delta) = \frac{C_\Delta}{\Delta r} \tag{5.9}$$

The fog DSD is correctly reproduced provided the following holds,

$$\sum_{i=1}^{n} c(\Delta) i \cdot \Delta r = N_T \tag{5.10}$$

5.1.3 DSD Parameters Analysis

The peak specific attenuation value predicted using the standard parameters of the MGDSD for moderate continental fog conditions and the Mie scattering theory results in specific attenuation of about 180 dB/km. whereas, the measured peak specific attenuation value at Graz was up to 224 dB/km and for Milan it was around 154 dB/km (deduced from visual range). It means that the standard parameter values are not always applicable to model fog attenuations for each place and each kind of fog environment as we observed in case of Graz (observed attenuations are higher than predicted by standard parameters) and Milan (observed attenuations are lesser than predicted by standard parameters). Moreover, we know that the DSD of fog particles may vary from location to location, and at a particular location with time [141]. Hence, the need arises to find a new set of MGDSD (average) parameters for each of these two continental locations to see how much the new parameters deviate than the standard parameters of MGDSD. This knowledge of the location dependent set of distribution parameters can be useful prior to installation of a the terrestrial FSO in order to get a realistic estimate of optical attenuation at a particular location. In addition, the information about the frequency of occurrence of a particular fog type along with its seasonal and diurnal dependence is also important in order to overcome the attenuation losses by adjusting a certain link margin.
In this effort here, it is tried to find the value of MGDSD parameter N_0 by keeping fix the values of other two parameters m and Λ to their standard values i.e., 6 and 3 for continental fog, respectively to match the observed peak, median and mean values of measured specific attenuation at Graz and Milan. The corresponding optical attenuations are obtained through Mie theory by keeping the mode size of fog droplets to 2 μm, which is assumed to adequately represent moderate continental fog. The fog droplets are simulated with sizes from 0.1 to 50 μm with a step size of 0.1 μm. The new sets of MGDSD parameters are plotted in Fig. 5.1 and Fig. 5.2, and are also presented in Table 5.1 [96].

The main reason for using this mentioned preliminary procedure is that the during the experimental measurements at both Graz and Milan only one measured data related to fog properties i.e., optical attenuations is recorded, therefore, only one DSD parameter can be computed. Upon measurement of more physical parameters related to fog like LWC a much better method, as proposed in the next sections, can be used to compute optimal set of DSD (e.g., EDSD and MGDSD) parameters.

The corresponding specific attenuation values are shown in Fig. 5.3 and Fig. 5.4 [96, 101]. It can be noticed that the contribution from 1 to 5 μm particles is about 96% of the overall attenuation, while 5 to 50 μm particles are responsible for only 4% of attenuation. It

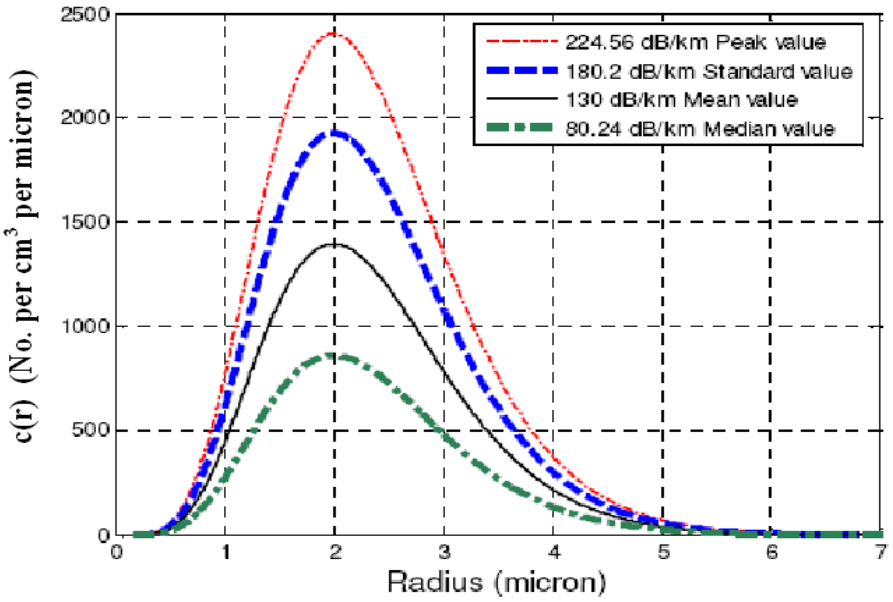

Figure 5.1: Estimated parameters of MGDSD for peak, standard, mean and median values of attenuations at Graz

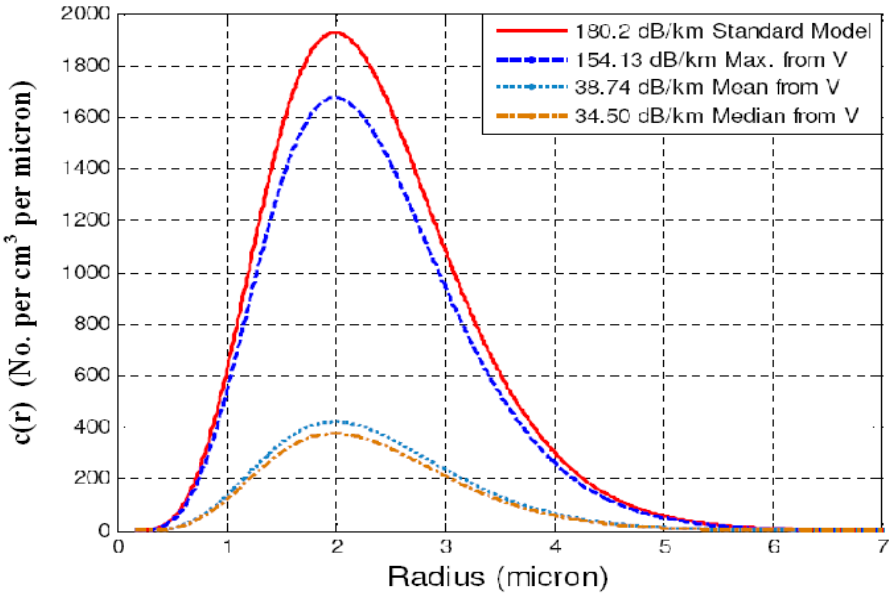

Figure 5.2: Estimated parameters of MGDSD for peak, standard, mean and median values of attenuations at Milan

means that smaller droplets play a critical role in attenuating the optical signal: as their size is comparable with normally used optical wavelengths, simple methods are inadequate and therefore use of Mie theory is mandatory. Furthermore, there are also temporal variations

Moderate Continental Fog Sp. Attenuation (dB/km)	Graz				Milan			
	m	N_0	Λ	$\gamma(dB/km)$	**m**	N_0	Λ	$\gamma(dB/km)$
Standard Value	6	607.5	3	180.2	6	607.5	3	180.2
Peak Value	6	757	3	224.56	6	528.2	3	154.13
Mean Value	6	440	3	130	6	132.8	3	38.74
Median Value	6	270.5	3	80.24	6	118.5	3	34.50

Table 5.1: Proposed modified gamma DSD parameters

during the life cycle of a fog event, as well as spatial variations at any given time instant. Therefore, the identical visibilities during fog formation and dissipation might correspond to different size distributions. This is the reason why we speak of average DSD parameters.

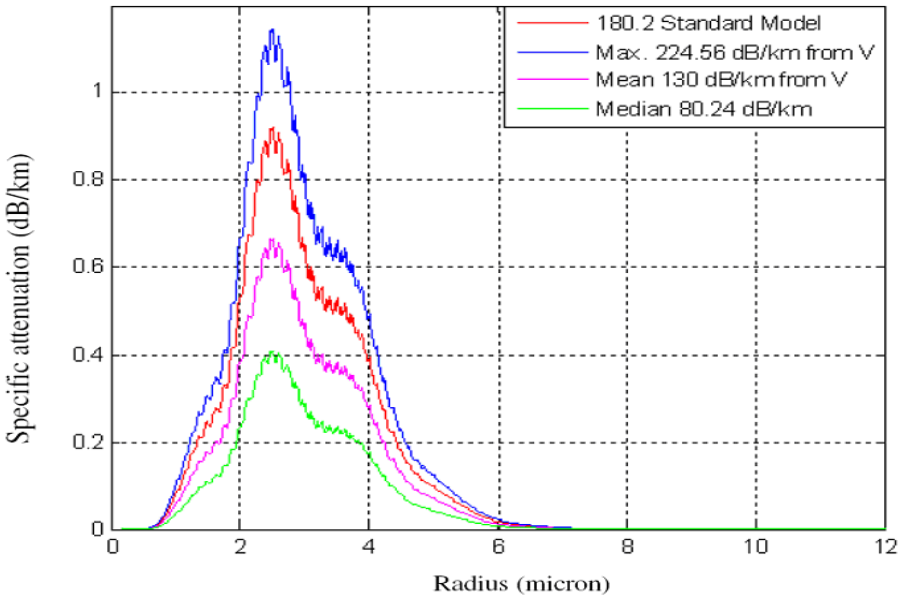

Figure 5.3: Predicted attenuations for Graz using MGDSD and Mie scattering

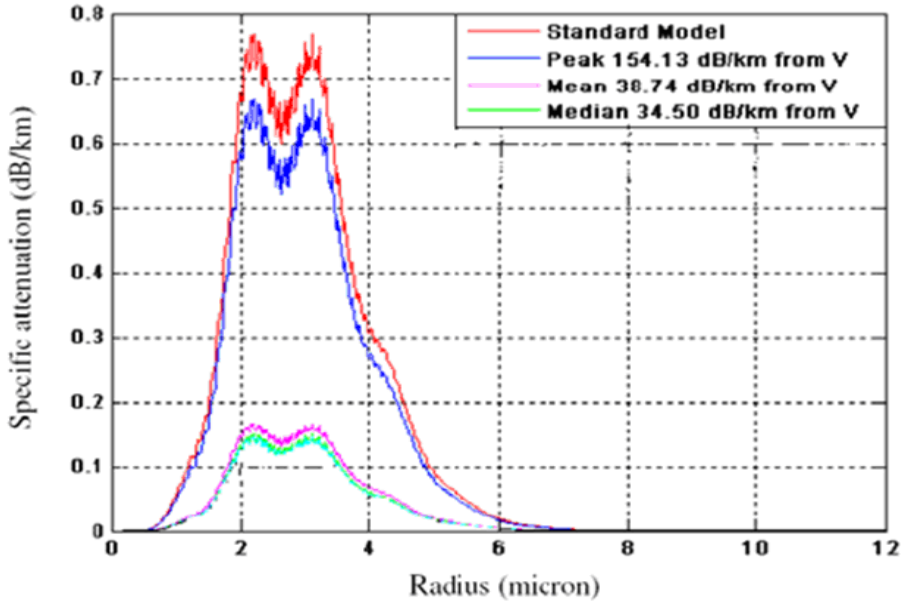

Figure 5.4: Predicted attenuations for Milan using MGDSD and Mie scattering

5.2 Methodology to Retrieve Fog Drop Size Distribution Parameters

The optimum scaling of the fog DSD leads to the fine tuning of the methods used for the prediction of attenuation over terrestrial FSO links, and for the reliable behavior of these transmission links under harsh environments. In the following sections two continental fog events will be discussed and analyzed while drop size distribution parameters will be estimated by considering EDSD and MGDSD, separately. The DSD parameters computation method is based on standard iterative procedure that selects those optimal parameters of a certain distribution for which the residual errors between the actual measured value and the computed value is minimum. The two representative fog events are selected from two different continental locations i.e., Graz (Austria) and Prague (Czech Republic).
While computing optimal distribution parameters of the EDSD and MGDSD parameters for the two selected continental fog events, radius r is considered as the independent variable of a size distribution as it prevails in the literature probably because it is favored in electromagnetic and Mie theory. The size of fog particles considered, while computing the DSD parameters, is in the range between 0.1 μm-50 μm with an interval size of 0.1 μm. And Mie scattering efficiency is calculated by employing the complex refractive index of a particular wavelength considered using Ray method [95]. The algorithm adopted to determine individual DSD parameters (for EDSD or MGDSD) is explained below under appropriate sections.

5.2.1 Methodology to Retrieve MGDSD Parameters

In 1964, Deirmendjian analyzed a large number of empirical size spectra of fog droplets by a computational method using three parameters MGDSD having a general form as given in the Equation (4.1) [142]. These three parameters completely determine the shape of a distribution curve. In 1971-73, Garland measured the parameter sets of the MGDSD of small water droplets corresponding to 1 km visibility range by giving the best-fit curves relative to eight size spectra, which are representative size distribution models of haze droplets [142, 143]. The corresponding mode radius r_c range of these small water droplets studied was between 0.038 μm and 0.734 μm. Later on in 1976, Tomasi and Tampieri listed parameters sets of MGDSD for fog droplets against 0.2 km horizontal visibility for different fog types [142]. The mode radius r_c for radiation fog water droplets case studied, was in the range between 2.13 μm and 12.22 μm. Then in 1989 Shettle and later on in 1995 by Harris listed the MGDSD parameters corresponding to moderate radiation fog case [99, 100]. The reference values of MGDSD parameters (m, N_0 and Λ) and the total actual concentration N_d for the radiation fog case from the above mentioned references are listed in the Table 5.2, below.
In the subsequent sections to follow, the methodology adopted to retrieve optimal MGDSD parameters related to the two selected representative fog events recorded at Graz and Prague, is explained separately.

Size distributions	m	N_0 $\mathbf{cm}^{-3} \cdot \mu\mathbf{m}^{-1}$	Λ $\mu\mathbf{m}^{-1}$	N_d $\mathbf{cm}^{-3}$	**Fog Type**
Garland [143]	1 - 7	0.54 - 1.28	1.362 - 184.2105	718.61 - 9230.25	Small water droplets
Tomasi and Tampieri [127]	4 - 5	7.54×10^{-6} - 4.32×10^{0}	0.3273 - 2.3474	15.90 - 249.93	Radiation fog
Shettle, Harris [99, 100]	6	2.37 - 607.5	1.5 - 3.0	20 - 200	Radiation fog

Table 5.2: Ranges of MGDSD parameters from literature survey

For Graz Fog Event

In order to compute MGDSD parameters N_0, m and Λ against the fog events recorded at Graz, Maitra and Gibbins procedure is adopted [139]. We modify this procedure to compute three parameters of MGDSD from two equations. The two considered Equations are Equation (3.3) & (4.7). It is important to remind here that the optical attenuations measured correspond to 950 nm wavelength and the measured attenuation data considered is taken averaged over a minute scale for the computation of MGDSD parameters here. The three MGDSD parameters, namely, m, N_0 and Λ can be computed theoretically by taking the ratio of the above mentioned two equations as [144],

$$\frac{\gamma_{exp}(950nm)}{LWC_{exp}} = \frac{10^5 \int_{0.1\mu m}^{50\mu m} Q_d(\frac{2\pi r}{\lambda}, n')\pi r^2 C(r)dr}{\rho_w \frac{4}{3} \int_{0.1\mu m}^{50\mu m} \pi r^3 C(r)dr}. \tag{5.11}$$

where "*exp*" denotes the experimentally measured values. Assuming the three parameters MGDSD distribution as given by Equation (4.1), then the ratio of two equations become,

$$\frac{\gamma_{exp}(950nm)}{LWC_{exp}} = \frac{10^5 \int_{0.1\mu m}^{50\mu m} C_{Ext} N_0 r^m exp(-\Lambda r) dr}{\frac{4}{3}\pi\rho_w \int_{0.1\mu m}^{50\mu m} r^3 N_0 r^m exp(-\Lambda r) dr} \tag{5.12}$$

Where

$$C_{Ext} = Q_d(\frac{2\pi r}{\lambda}, n')\pi r^2.$$

So

$$\frac{\gamma_{exp}(950nm)}{LWC_{exp}} = \frac{10^5 \int_{0.1\mu m}^{50\mu m} C_{Ext} r^m exp(-\Lambda r) dr}{\frac{4}{3}\pi\rho_w \int_{0.1\mu m}^{50\mu m} r^{3+m} exp(-\Lambda r) dr} \tag{5.13}$$

By this procedure parameter N_0 can be eliminated, and we are left with the only two parameter m and Λ. Now the iterative procedure is adopted to compute the two remaining MGDSD parameters. For the computation of these two parameters the values of parameters m and Λ are taken as m =0.1, 0.2, ..., 10 (100 values), and Λ=0.1, 0.2, ..., 10 (100 values). It seems appropriate not to restrict the MGDSD parameters, while computing them against the measured attenuation values against the radiation fog events at the two mentioned locations, in the reference ranges as existing in the previous literature since the fog DSD parameters characteristics vary from location to location. Therefore, the ranges mentioned for MGDSD parameters m and Λ between 0.1 to 10, for our computation here, seems reasonable. These ranges of the respective parameters are taken from Tomasi and Tampieri [127, 142]. Then for each combination of m and Λ, residuals of the computation are calculated out of 100x100 matrix combination. Finally, the residuals are compared and that optimal combination of m and Λ is taken for which the residual of ratio of attenuations at 950 nm and LWC (as given by Equation (5.13) is the minimum. After finding the optimal set of m and Λ, the third parameter N_0 can be computed from the ratio of the measured attenuation and the computed attenuation at a particular wavelength given by,

$$N_0 = \frac{\gamma_{exp}(950nm)}{\gamma_{thr}(950nm)}. \tag{5.14}$$

$$N_0 = \frac{LWC_{exp}}{LWC_{thr}}. \tag{5.15}$$

where "*thr*" denotes the theoretically computed values using the MGDSD parameters and the LWC_{exp} as mentioned in Equation (5.15) corresponds to LWC values computed from fog density values (see Equation 4.19) [96, 137].

For Prague Fog Event

To compute MGDSD parameters m and Λ against the selected fog event of Prague as well, the same procedure as we adopted in case of Graz fog event is used here. In case of Prague fog event we have an additional possibility of computing the MGDSD parameters from the ratio between two attenuations (at 1550 nm and 850 nm), besides taking the ratio of attenuation at a particular wavelength (either 850 nm or 1550 nm) and the LWC. It is important to mention here that we mainly considered attenuations at 1550 nm wavelength, because of the preference of this wavelength for future FSO link designs, to compute the three MGDSD parameters against the Prague fog event. Therefore, the final equation in case of taking the ratio between optical attenuations at 1550 nm and LWC thus become [144],

$$\frac{\gamma_{exp}(1550nm)}{LWC_{exp}} = \frac{10^5 \int_{0.1\mu m}^{50\mu m} C_{Ext} r^m exp(-\Lambda r) dr}{\frac{4}{3}\pi\rho_w \int_0^{\infty} r^{3+m} exp(-\Lambda r) dr}. \tag{5.16}$$

Finally, the third parameter N_0 can be computed by taking the ratio between measured and computed LWC values as given by the following equation,

$$N_0 = \frac{LWC_{exp}}{LWC_{thr}}. \tag{5.17}$$

The other possibility of computing the two MGDSD parameters (m and Λ) is to take the ratio between measured attenuations at 1550 nm and at 850 nm as given by the following equation,

$$\frac{\gamma_{exp}(1550nm)}{\gamma_{exp}(850nm)} = \frac{\int_{0.1\mu m}^{50\mu m} C_{Ext_{1.55\mu}} r^m exp(-\Lambda r) dr}{\int_{0.1\mu m}^{50\mu m} C_{Ext_{0.85\mu}} r^m exp(-\Lambda r) dr}. \tag{5.18}$$

Finally, the third parameter of MGDSD (N_0) in case of Prague's representative fog event can be computed by taking the ratio of measured and computed attenuations at 1550 nm wavelength as,

$$N_0 = \frac{\gamma_{exp}(1550nm)}{\gamma_{thr}(1550nm)}. \tag{5.19}$$

5.2.2 Methodology to Retrieve EDSD Parameters

The size distribution of fog droplets is not an easy function to quantify. It has been customary to express DSD in terms of distribution function. The distribution specified by negative exponential distributions (EDSD), such as those described by Marshal and Palmer [145], much attention has been focused on obtaining relatively simple analytical expressions involving as small number of parameters as possible to model measured drop size distributions. Marshal and Palmer approximated the drop size distributions with exponential

functions which can be written as,

$$C(r) = N_0 exp(-\Lambda r) \tag{5.20}$$

where C(r) is the number concentration of droplets of radius r (μm) per unit size interval for the fog case, N_0 ($\mu m^{-1} m^{-3}$) and Λ are the EDSD parameters i.e., concentration and size parameters, respectively. The exponential distribution has been used in many studies to describe the DSD before Ulbrich introduced the Gamma DSD (MGDSD) model [146]. EDSD is also a special case of the Gamma distribution DSD when m=0. In this section EDSD parameters have been computed for the two fog attenuation events selected (of Graz and Prague) and the results of the measured and computed quantities are compared and analyzed. The methodology adopted to retrieve EDSD parameters corresponding to the two sample fog event is discussed below, separately.

For Graz Fog Event Case

In order to compute EDSD parameters i.e., N_0 and Λ against the two fog events recorded at Graz and Prague, Maitra and Gibbins procedure is adopted [139]. This procedure considers three nonlinear equations to determine three parameters of the lognormal distribution in case of raindrops. This procedure is modified a little to compute two parameters of EDSD. Consider the two Equations (3.3) and (4.7) again. The first Equation (3.3) computes fog attenuation coefficient (dB/km) from Mie scattering efficiency and the respective DSD (either EDSD or MGDSD), and the second Equation (4.7) computes the LWC (g/m^3) from the respective DSD. It is important to mention here that the measured attenuation data considered is taken averaged over a minute scale for the computation of EDSD parameters. The two EDSD parameters, namely, N_0 and Λ can be computed theoretically by taking the ratio of these above mentioned two equations [147],

$$\frac{\gamma_{exp}(950nm)}{LWC_{exp}} = \frac{10^5 \int_0^\infty Q_d(\frac{2\pi r}{\lambda}, n')\pi r^2 C(r) dr}{\rho_w \frac{4}{3} \int_0^\infty \pi r^3 C(r) dr} \tag{5.21}$$

where "*exp*" denotes the experimentally measured values. Then again,

$$\frac{\gamma_{exp}(950nm)}{LWC_{exp}} = \frac{10^5 \int_0^\infty C_{Ext} C(r) dr}{\frac{4}{3}\pi\rho_w \int_0^\infty r^3 C(r) dr} \tag{5.22}$$

Now if considering EDSD (Equation 5.20), then N_0 can be eliminated and we are left to deal with the only one EDSD parameter Λ. So Equation (5.22) becomes,

$$\frac{\gamma_{exp}(950nm)}{LWC_{exp}} = \frac{10^5 \int_0^\infty C_{Ext} exp(-\Lambda r) dr}{\frac{4}{3}\pi\rho_w \int_0^\infty r^3 exp(-\Lambda r) dr} \tag{5.23}$$

This theoretically computed ratio between attenuations at 950 nm (γ) and the LWC can be compared with the ratio of the same two parameters measured experimentally (the optical attenuations measured at 950 nm and the LWC values approximated from fog density). After comparing the two ratios; one experimentally measured values and the other theoretically computed values (using EDSD) for each minute data, that optimal value of EDSD parameter Λ is taken for which the residual of ratios between attenuation and the LWC is minimum. Once, the instantaneous values of Λ are known for the whole fog event, then equating its instantaneous values over the minute scale to the Equation (4.7), would result in instantaneous values of N_0 for the whole fog event. By this procedure, the two parameters of the EDSD can be computed against a particular fog event.

For Prague Fog Event Case

In order to compute EDSD parameters for Prague fog event, two possibilities of taking the ratios exist. One possibility is to take ratio between the two measured attenuations i.e., at 1550 nm and 850 nm, or to take the ratio between one of the measured attenuations (at 1550 nm or at 850 nm) and the LWC measured since measurement data contains values for all these variables over a link distance of 100 m. We noticed an offset in the measured values of LWC for Prague due to the measurement sensor (see for detail Section 5.4.2), so the recorded values of LWC are not reliable. Therefore, for the computation of EDSD parameters against the selected fog event of Prague we consider the ratio between two measured attenuations i.e., 1550 nm and 850 nm. It is important to mention here that the values of parameters considered for the computation are averaged on a minute scale. Now in order to compute the ratios between the two attenuations (1550 nm and 850 nm) theoretically, the final equation becomes [147],

$$\frac{\gamma_{exp}(1550nm)}{\gamma_{exp}(850nm)} = \frac{\int_0^\infty C_{Ext_{1.55\mu}} exp(-\Lambda r)dr}{\int_0^\infty C_{Ext_{0.85\mu}} exp(-\Lambda r)dr} \tag{5.24}$$

where "exp" denotes the experimentally measured values and $\gamma_{exp}(1550nm)$ and $\gamma_{exp}(850nm)$ correspond to optical attenuations at 1550 nm and 850 nm, respectively. After comparing the measured and computed attenuation ratios, the optimal value of EDSD parameter Λ can be found so that the residuals of the two ratios is minimum. After knowing the values of parameter Λ, the instantaneous values of second EDSD parameter N_0 can be computed from Equation (3.3).

5.2.3 Evaluation of the Distribution Parameters

The newly found distribution parameters of EDSD and MGDSD need to be evaluated in terms of their suitability to accurately model a certain quantity. In order to determine how

closely our measured attenuation data conform to a linear relationship, R^2 test is conducted that determines how closely a certain function fits a particular set of experimental data. R^2 values range from 0 to 1, with 1 representing a perfect fit between the data and the line drawn through them, and 0 representing no statistical correlation between the data and a line. The R^2 value (often referred to as the goodness of fit) is computed as follows [147],

$$R^2 = 1 - \frac{\sum(Y_i - Y_i')^2}{\sum(Y_i - \bar{Y})^2} \tag{5.25}$$

or,

$$R^2 = 1 - \frac{Error - Sum - of - Squares(SSE)}{Total - Sum - of - Squares(SSTO)} = \frac{Regression - Sum - of - Squares(SSR)}{Total - Sum - of - Squares(SSTO)} \tag{5.26}$$

where Y_i represents an individual data point value, Y_i' represents the value obtained by when the independent coordinate of this data point is input into the best-fit function (a line in this case). Therefore, Y_i' represents the values of the data points projected onto the line of best fit (the ideal values). $\bar{Y}$ represents the average of the Y_i values.

5.2.4 Statistics of the Distribution Parameters

In order to describe the variation of some physically meaningful quantities like optical attenuations, LWC or ratio of optical attenuations etc., with some parameter like size of the droplets or time, statistics are computed and evaluated.

Mean Value

Considering an arbitrary function g(r) that applies over the domain of the size distribution C(r). The mean value of g is the integral of g over the domain of the size distribution i.e., 0.1 μm to 50 μm, and weighted at each point by the concentration of the fog particles,

$$\bar{g} = \int_{0.1}^{50} g(r)C(r)dr \tag{5.27}$$

Once C(r) is known, it is always possible to determine $\bar{g}$ for any desired quantity g.

Median Value

A median is a numeric value that separates the higher half of a sample or a probability distribution from the lower half. For an absolute continuous probability distribution with probability density function PDF denoted by f, we have

$$P(X \leq m) = P(X \geq m) = \int_{-\infty}^{m} f(r)dr = \frac{1}{2} \tag{5.28}$$

Standard Deviation

The standard deviation σ_r of a size distribution C(r) is the square root of the variance and it shows how much variation is there from the mean value,

$$\sigma_r = \sqrt{\sigma_r^2} \tag{5.29}$$

5.3 Analysis of Measured Fog Events

In this section, the two fog events are first discussed on the basis of their time series attenuation behavior and the corresponding histograms are given of the measured quantities in order to evaluate their behavior statistically. Finally, the measured statistics are provided in tabular form in each sub-section.

5.3.1 Graz's Fog Event of 18-19 Nov. 2009

The first fog event analyzed for the determination of optimum distribution parameters is recorded at Graz over an 80 m FSO link operating at 950 nm. This fog event started at 3:15 pm on 18 Nov. 2009 and lasted at 7:50 am on 19 Nov. 2009. The total duration of this fog event was about 990 minutes. Fig. 5.5 shows the time series of measured optical attenuations and LWC against this recorded fog event. The maximum value of attenuation reached up to 141 dB/km, with an average attenuation of about 93 dB/km and median attenuation of about 111 dB/km when averaged over a minute scale. The corresponding analysis of changes in attenuation shows that a maximum change of $\pm$ 37 dB/km was recorded with an average variation of about 0.003 dB/km.

Fig. 5.6(a)-(d) shows the histograms of optical attenuations and the corresponding changes in attenuations when measured over a second scale and averaged on a minute scale, respectively. The histogram in Fig. 5.6-(e) shows the variation behavior of LWC (g/m^3) measured, while the histogram as shown in Fig. 5.6-(f) depicts the behavior of ratio

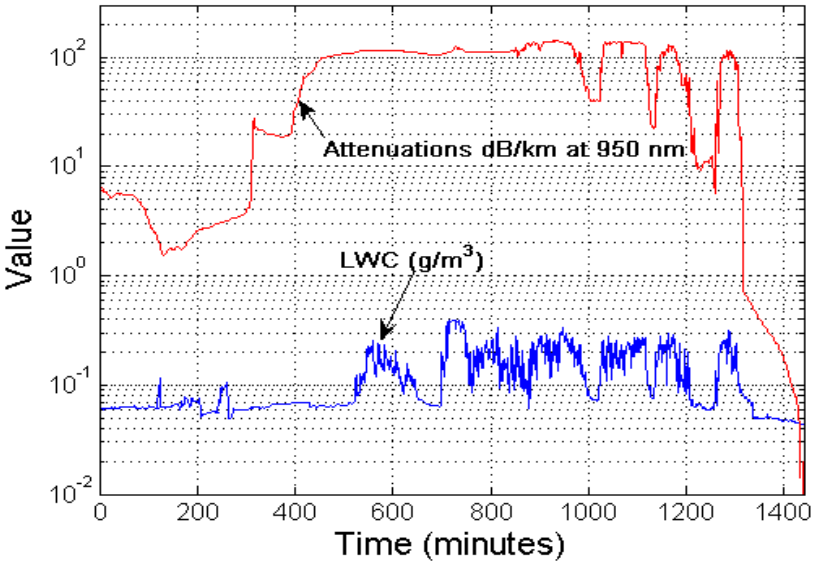

Figure 5.5: Time series of attenuations (dB/km) and LWC (g/m^3) at Graz

between measured optical attenuation and the LWC for the mentioned fog event. From the analysis of the measured LWC data, it was observed that the maximum value of LWC recorded against this fog event was about 0.394 (g/m^3), while the average and median values of LWC were about 0.1466 and 0.127 (g/m^3). Table 5.3 summarizes the relevant statistics of different parameters measured related to this fog event [144].

Parameters	**Attenuations (dB/km) seconds**	**Changes in Attenuation (dB/km) seconds**	**Attenuations (dB/km) minutes**	**Changes in Attenuation (dB/km) minutes**	**LWC (g/m^3) minutes**
Min.	-0.03477	5.884	5.7369	-37.923	0.058612
Max.	142.6	-5.894	140.99	37.117	0.39044
Mean	65.15	-0.001096	93.51	0.002724	0.1466
Median	77.08	0	110.935	-0.009	0.12718
Std. dev.	53.33	0.9575	39.47	4.594	0.08144
Range	142.6	11.78	135.3	75.04	0.3318

Table 5.3: Statistics of measured optical attenuation (dB/km) and LWC (g/m^3) against the fog event of 18-19 Nov. 2009 at Graz

5.3.2 Prague's Fog Event of 07 Feb. 2009

The second continental fog event selected was recorded at Prague on 07 Feb. 2009 over a 100 m FSO link established with two parallel links using 1550 nm and 850 nm wave-

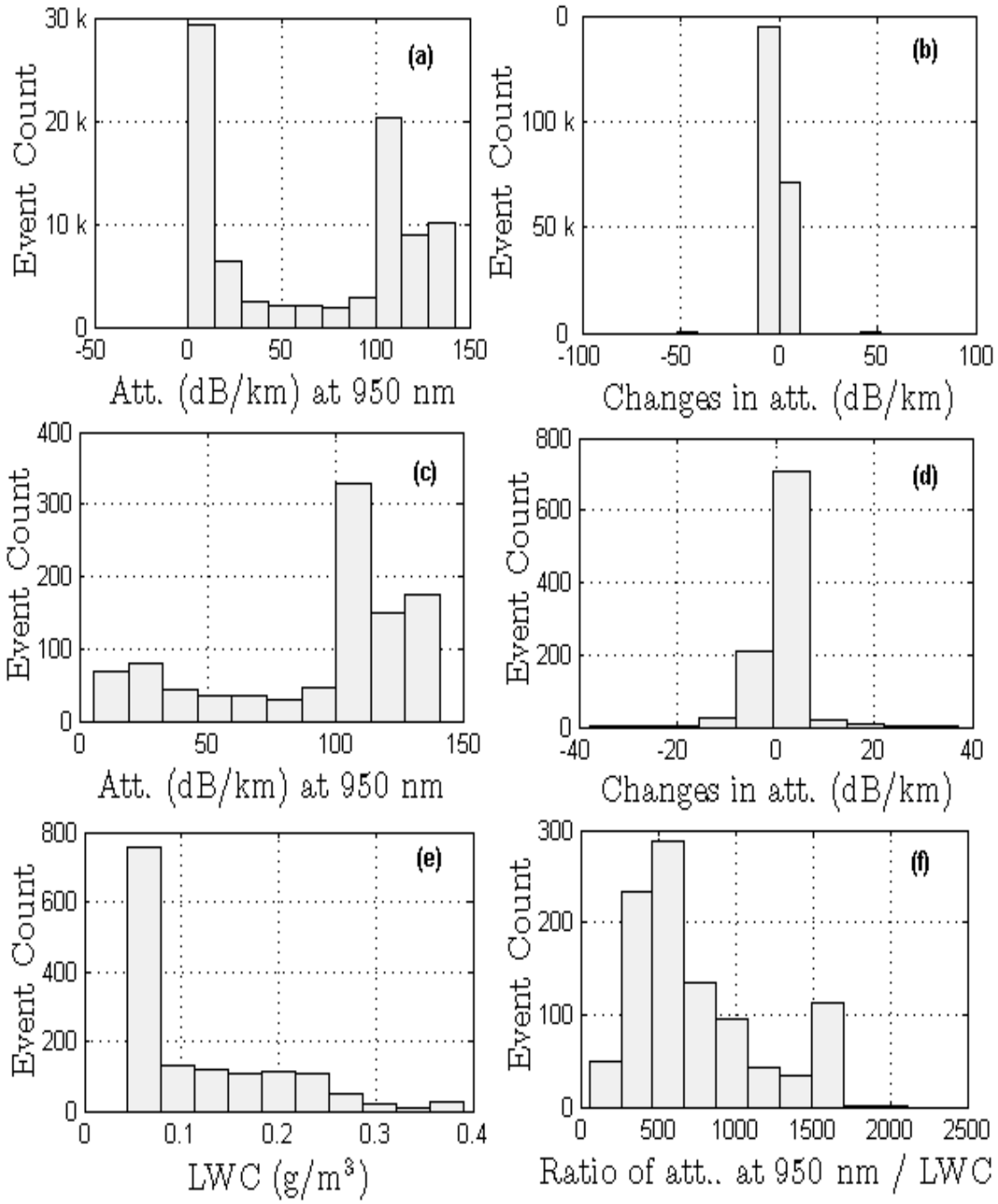

Figure 5.6: Histograms of measured optical attenuations (dB/km), the LWC and ratio of optical attenuations (dB/km) and LWC (g/m^3) at Graz

lengths. The total duration of this fog event was 480 minutes. Besides the measurement of optical attenuations and visibility range (m), liquid water content LWC (g/m^3) and particle

surface area PSA (cm^2/m^3) are also measured, in parallel, in order to demonstrate relation between microphysical parameters of fog and the optical attenuations as shown by a time series plot in Fig. 5.7(a)-(b). The LWC and integrated PSA are measured by the PVM-100 instrument during the duration of the fog event. From Fig. 5.7-(b) it is clearly visible that measured optical attenuations are higher in case of 850 nm as compared to 1550 nm. Fig. 5.7(c)-(f) shows the histogram of measured attenuations at 1550 nm, measured LWC, ratio between measured attenuations at 1550 nm to 850 nm, and the ratio between attenuations at 1550 nm to LWC, respectively. Table 5.4 summarizes the relevant statistics of the mentioned measured parameters related to this fog event [144].

The maximum value of attenuation over 1550 nm link reached up to 111 dB/km, while

Parameters	**Visibility Range meters minutes**	**Attenuations (1550 nm) (dB/km) minutes**	**Attenuations(850 nm) (dB/km) minutes**	**LWC (g/m^3) minutes**	**PSA (cm^2/m^3) minutes**
Min.	148	27.41	27.62	0.022	0
Max.	1521	110.7	154.6	0.14	551.3
Mean	317.5	71.92	89.96	0.06942	248.8
Median	265.5	74.56	90.59	0.0695	237.5
Std. dev.	160.1	17.2	25.19	0.03229	118.5
Range	1373	83.27	127	0.118	551.3

Table 5.4: Statistics of measured optical attenuation (dB/km) and other parameters against the fog event of 07 Feb. 2009 at Prague

on the parallel 850 nm FSO link the maximum value was about 155 dB/km. The average and median values of optical attenuations were about 72 dB/km and 75 dB/km over 1550 nm, and 90 dB/km and 91 dB/km. For the determination of MGDSD parameters the attenuation data measured with 1550 nm is only considered, and later on, using the same computed MGDSD parameters the attenuations at 850 nm are computed for our further analysis and comparisons.

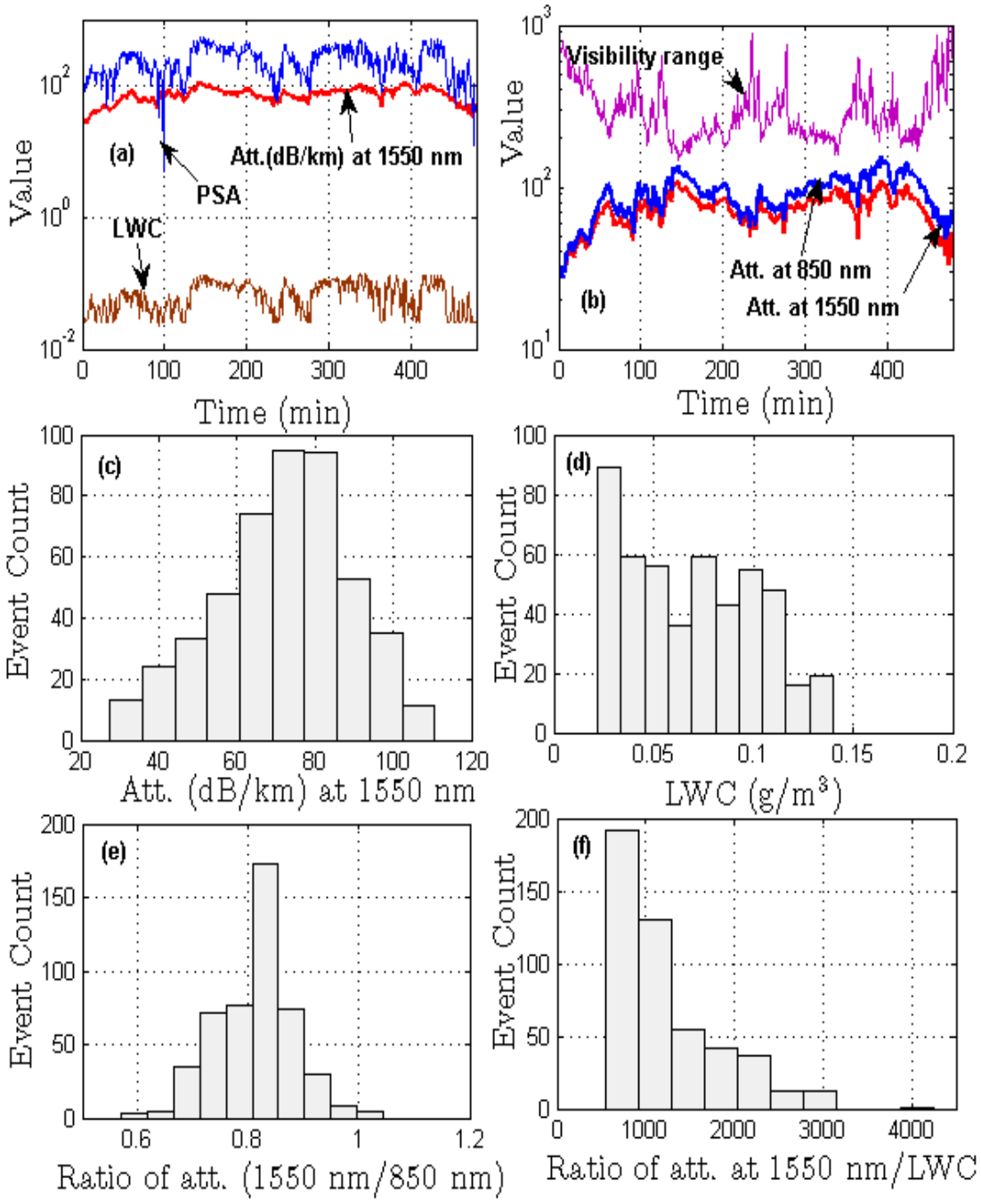

Figure 5.7: Time series of measured parameters against the fog event at Prague

5.4 Analysis of Modified Gamma Drop Size Distribution (MGDSD) Parameters

This section deals with the computation of three parameters m, Λ, and N_0 of the MGDSD by employing the iterative procedure to compute against the two fog events; Graz fog event recorded on 18-19 Nov. 2009 and the Prague fog event recorded on 07 Feb. 2009. The iterations of different combinations of two MGDSD parameters m and Λ are repeated unless the residuals of the respective parameters to model are minimized.

5.4.1 MGDSD Parameters for Graz Fog Event of 18-19 Nov. 2009

In this section, first the performance analysis of the newly computed three MGDSD parameters m, Λ, and N_0 will be presented by comparing the measured and computed optical attenuations (dB/km) at 950 nm, measured and computed LWC (g/m^3) and the ratio of measured and computed attenuations (dB/km) at 950 nm to the LWC (g/m^3). For the representative Graz fog event, the computed quantities are attenuations at 950 nm, the LWC and the ratio between attenuations at 950 nm to the LWC. These quantities are computed from newly computed MGDSD parameters, by employing iterative procedure, using Equations (3.3), (4.7) & (5.21). This will be followed by an analysis of the computed quantities and the respective three parameters of the MGDSD.

Performance Analysis of the Method

The DSD parameters corresponding to representative fog event of Graz are obtained by Equations. (5.13) & (5.14). Fig. 5.8 shows the performance analysis of the newly computed parameters of the MGDSD in terms of their computation of optical attenuations (dB/km), LWC (g/m^3) and the ratio between optical attenuations (dB/km) to the LWC (g/m^3). In the plot as shown in Fig. 5.8-(a), the optical attenuations computed are compared with the actual measured attenuations at 950 nm. A strong correlation between measured and computed optical attenuations exists as visible through R^2 test and the corresponding linear fitting applied. The equations related to linear fit along with the respective value of R^2 in case of measured and computed optical attenuations at 950 nm is [144],

$$Y = 1.0007 * X - 0.0813, \qquad R^2 = 0.9999 \tag{5.30}$$

Fig. 5.8-(b) shows a comparison between the measured LWC (g/m^3) (from fog density) and computed values LWC (g/m^3) (using MGDSD parameters). Here, again it is evident that a very strong correlation exists between the measured and the computed values of the

LWC as visible through the R^2 test and the linear fitting applied. The resultant equation in case of linear fitting with same R^2 value is,

$$Y = 1.00 * X + 1.1284 \times 10^{-05}, \qquad R^2 = 0.9999 \tag{5.31}$$

Same performance test was conducted in case of ratio between measured and computed attenuations at 950 nm and the respective LWC as shown by Fig. 5.8-(c). It is clearly evident that here again the behavior of newly computed MGDSD parameters is sufficiently acceptable as evident through R^2 values obtained and the linear fit equation as given below,

$$Y = 1.00 * X - 0.0084807, \qquad R^2 = 1 \tag{5.32}$$

It is to remind that "Y" denotes the quantity computed and "X" denotes the quantity measured. On the basis of the performance analysis presented for the radiation fog event at Graz, it is clearly evident that the proposed method performs exceptionally well in order to retrieve MGDSD parameters corresponding to attenuations (dB/km), LWC (g/m^3) and the ratio between attenuations (dB/km) and LWC (g/m^3). Since, the retrieved parameters are in excellent agreement with the attenuations and LWC obtained from measurements, therefore, this method can be quite useful in the study of fog microphysics and in modeling the optical attenuations for terrestrial FSO links in radiation fog environments.

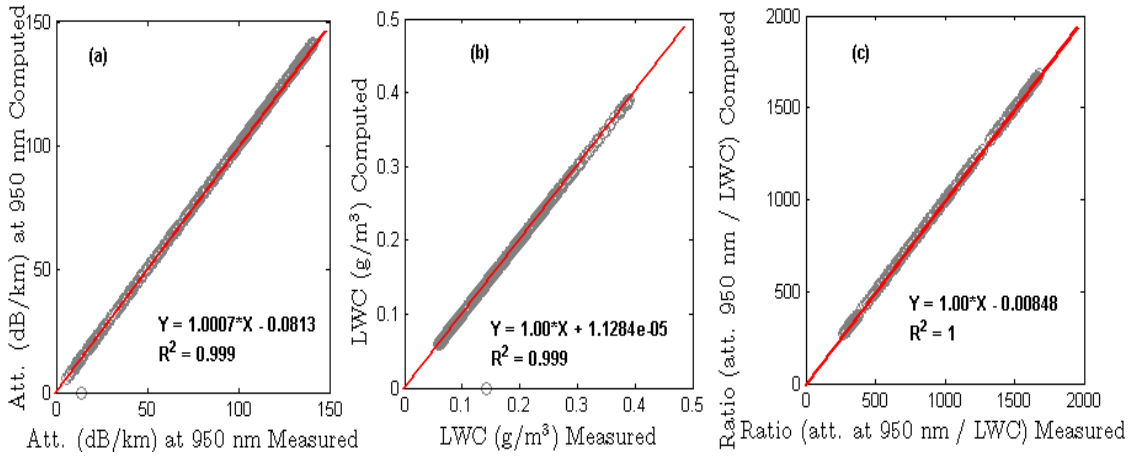

Figure 5.8: Performance test of measured and computed quantities based on newly computed MGDSD parameters against the fog event at Graz

Analysis of the Computed Quantities and MGDSD Parameters

In Fig. 5.9 the histograms of residuals of the computed quantities (attenuations at 950 nm, LWC and the ratio between attenuations at 950 nm and the corresponding LWC values

computed from newly retrieved MGDSD parameters), and MGDSD parameters are presented that shows the behavior of these computed quantities and the MGDSD parameters during the whole fog event of Graz. As visible through histograms of residual of computed optical attenuations (dB/km) at 950 nm as shown in Fig. 5.9-(a), computed LWC (g/m^3) as shown in Fig. 5.9-(b), and the ratio between computed attenuations at 950 nm and the LWC values as shown in Fig. 5.9-(c), the retrieved MGDSD parameters were quite excellent in modeling the optical attenuations, and the corresponding value of LWC for a radiation fog event. The mean and median values of computed optical attenuations at 950 nm are 93.49 dB/km and 110.9 dB/km with a standard deviation of about 39.51 for the whole fog event. The analysis of the computed LWC values shows that the mean and median values are about 0.1465 and 0.1268 (g/m^3), respectively with a standard deviation of about 0.08157 for the complete fog event. Similarly, by analyzing the ratio of computed attenuations at 950 nm and the computed LWC, we observe a value of 737.0 and 598.4 for the mean and median values with a standard deviation of about 423.3, respectively. The histograms as presented in Figs. 5.9-(d) to 5.9-(f) describe the behavior of the three MGDSD parameters (Λ, m and N_0) that are retrieved by the standard iterative procedure. The mean, median values are 3.547 and 3.2 for Λ, 6.135 and 6.6 for m, and 3.834 and 4.01 for N_0, respectively. Whereas, the values of the standard deviation corresponding to this fog event are 1.935, 2.692 and 2.239 for Λ, m and N_0, respectively. An analysis of the computed MGDSD parameters m reveal that about 14.70 % of the its values are below 3.0, and about 26.73 % are about within the range of 3.0 and 6.0, while major portion of its values about 58.57 % are above a value 6.0. Analysis of the the computed values, for this whole fog event, in case of second MGDSD parameter lambda (Λ) shows that about 11.62 % are below a value of 1.5, about 32.34 % are within the range between 1.5 and 3.0, while a major portion about 56.04 % lies above a value of 3.0. Similarly, analyzing the values obtained for the third MGDSD parameter i.e., N_0, it was observed that about 22.14 % values are below 2.37 and remaining values about 77.86 % are all within the range between 2.37 and 607.5 [144].

Fig. 5.10 presents a comparison of newly computed MGDSD parameters with the measured attenuation (dB/km) for this fog event through a time series analysis. It is evident through this plot that all these parameters of the MGDSD have a strong correlation with the formation stage, maturity and the dissipation phase of this fog event. An increase in attenuation, results in an increase in all three MGDSD parameters and vice versa. The Table 5.5 summarizes the computed quantities and the three parameters of the MGDSD for this fog event [144].

5.4.2 MGDSD Parameters for Prague Fog Event of 07 Feb. 2009

In this section, first the performance analysis of the newly computed three MGDSD parameters m, Λ, and N_0 will be presented by comparing the measured and computed optical attenuations (dB/km) at 1550 nm and 850 nm, measured and computed LWC (g/m^3), the

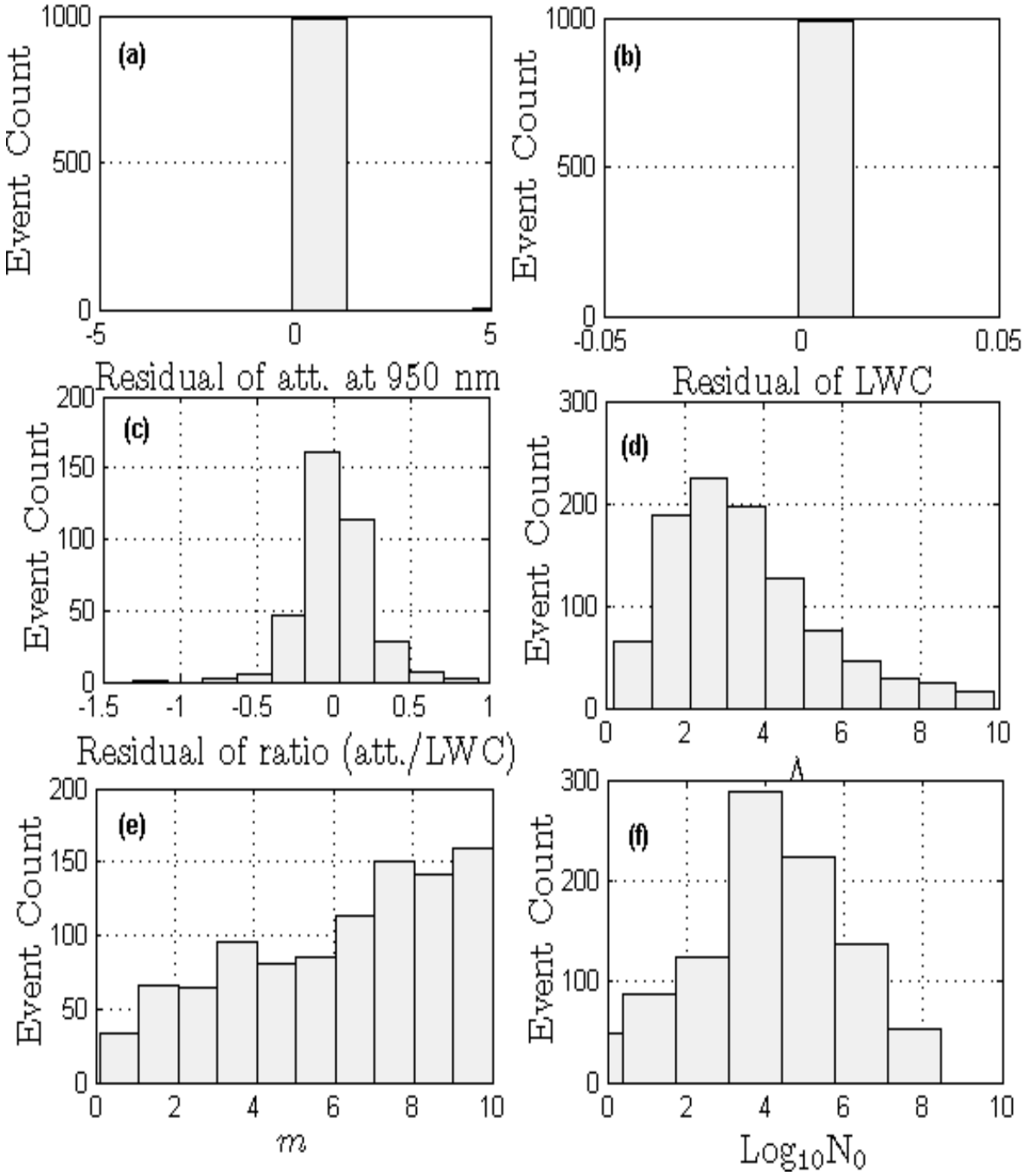

Figure 5.9: Histograms of residuals of computed quantities and the computed MGDSD parameters Λ, m, and $\mathrm{Log}_{10}(N_0)$ against the fog event at Graz

ratio of measured and computed attenuations (dB/km) at 1550 nm to the LWC (g/m^3), and the ratio of measured and computed attenuations (dB/km) at 1550 nm to attenuations

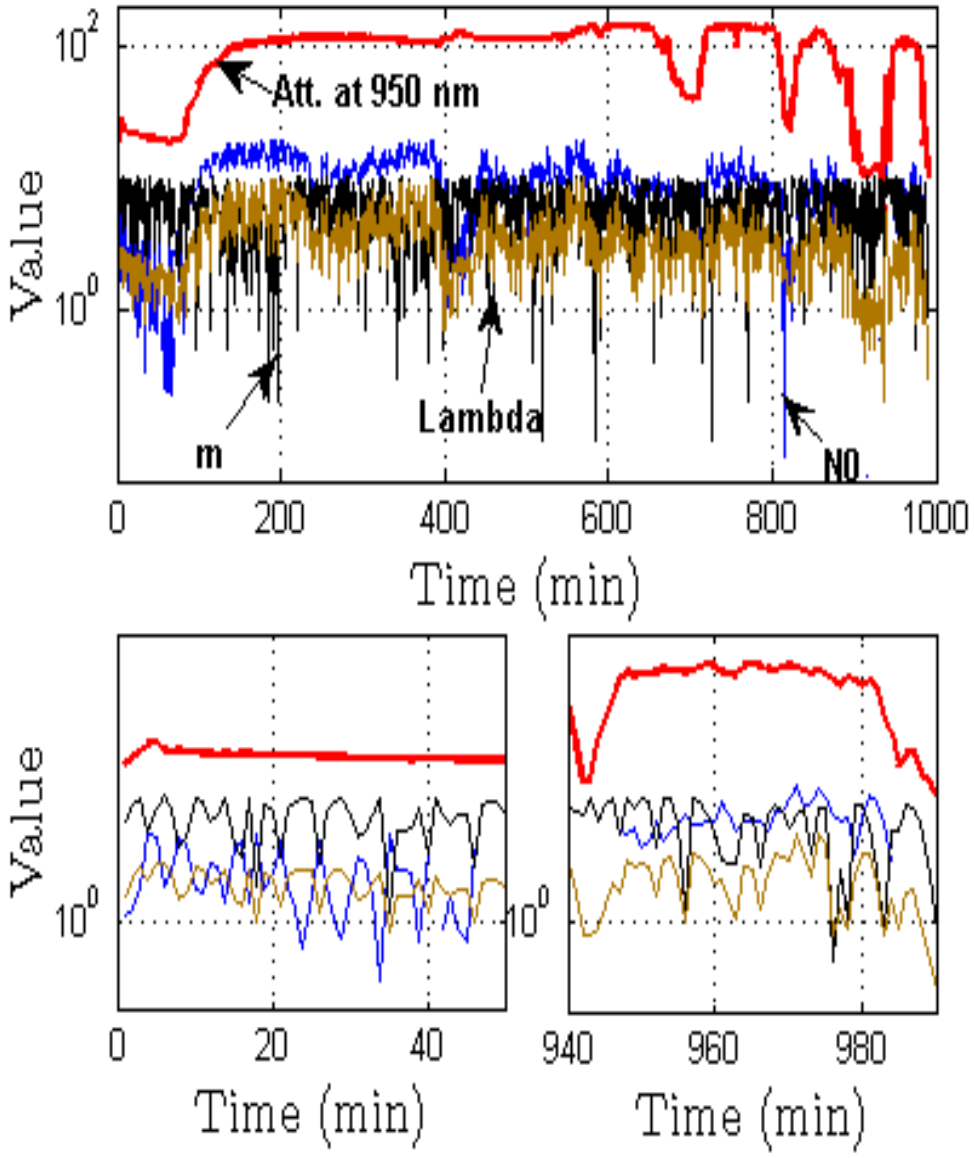

Figure 5.10: Time series of measured optical attenuation (dB/km), and the newly computed MGDSD parameters Λ, $\mathrm{Log}_{10}N_0$, and m against the fog event at Graz

(dB/km) at 850 nm. This will be followed by an analysis of the computed quantities and the respective three parameters of the MGDSD corresponding to this fog event.

Parameters	**Attenuations (dB/km) minutes**	**LWC (g/m^3) minutes**	Λ μm^{-1}	N_0 $cm^{-3} \cdot \mu m^{-1}$	m
Min.	0	0	0.2	-5.0	0.1
Max.	140.99	0.3904	9.9	8.44	10
Mean	93.49	0.1465	3.547	3.834	6.135
Median	110.9	0.1268	3.2	4.01	6.6
Std. dev.	39.51	0.08157	1.935	2.239	2.692
Range	141	0.3904	9.7	13.44	9.9

Table 5.5: Statistics of computed optical attenuation (dB/km), LWC (g/m^3) and corresponding MGDSD parameters against the fog event of 18-19 Nov. 2009 at Graz.

Performance Analysis of the Method

After the retrieval of DSD parameters using Equations (5.16) and (5.17) from the ratio of optical attenuations at 1550 nm to the LWC, we first analyze the performance of computed attenuations at 1550 nm, at 850 nm, computed LWC and the ratio between computed attenuations at 1550 nm to the LWC on the basis of newly computed three MGDSD parameters by this method for the selected fog event recorded on 07 Feb. 2009 at Prague. Fig. 5.11(a)-(d) shows the scatter plots between measured and computed attenuations at 1550 nm, at 850 nm, LWC and the ratio between attenuations at 1550 nm to the LWC, respectively. The linear fit equations obtained along with their respective R^2 values, by above mentioned two equations, for the case of measured and computed attenuations at 1550 nm, at 850 nm, measured and computed LWC and the ratio between measured and computed attenuations at 1550 nm to the LWC are given below, respectively [144].

$$Y = 0.9894 * X + 0.7428, \qquad R^2 = 0.9797 \tag{5.33}$$

$$Y = 0.5636 * X + 13.265, \qquad R^2 = 0.8758 \tag{5.34}$$

$$Y = 0.9 * X + 0.0083, \qquad R^2 = 0.9345 \tag{5.35}$$

$$Y = 0.6 * X + 4.2 \times 10^{+02}, \qquad R^2 = 0.8383 \tag{5.36}$$

It is to remind that "Y" denotes the quantity computed and "X" denotes the quantity measured. We observe that the R^2 values, as obtained in the above mentioned four equations, are not as good as they are in case of Graz fog event, even after removing the outliers in the measured attenuations and LWC values. Upon analyzing the data, it seems that there was a slight offset in the values of LWC measured by the measuring device and so requires proper calibration. We noticed, that on the average, a difference of about 1 % exists between the actual measured LWC values and the values of LWC computed by MGDSD parameters.

Due to this offset the LWC measurement device measured LWC values which were about 1 % lesser than the actual values, on the average, when compared with the LWC values computed using MGDSD parameters. That is why a relatively weaker correlation existed between the measured and the computed LWC values and as a consequence it affected the computed attenuation values at 850 nm and the ratio between attenuations at 1550 nm to the LWC, as evident through R^2 test values obtained in above mentioned equations.

Due to the above mentioned problem, we again retrieved DSD parameters for this se-

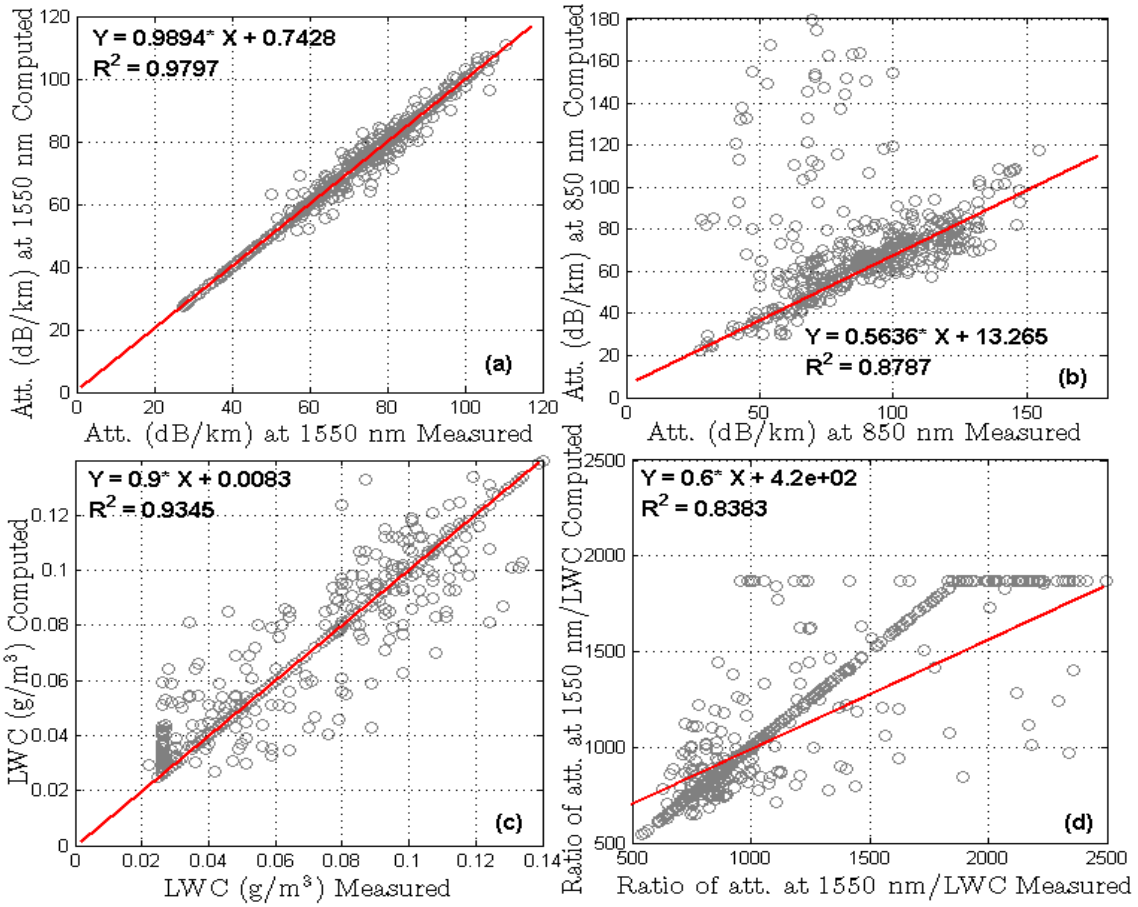

Figure 5.11: Performance test of measured and computed quantities based on newly computed MGDSD parameters from ration between measured and computed attenuations at 1550 nm to the corresponding LWC against the fog event at Prague

lected fog event (by the same iterative procedure) but now from the ratio of attenuations at 1550 nm to 850 nm by using Equations (5.18) and (5.19) given above. The linear fitting equations, along with respective R^2 values, obtained now for optical attenuations at 1550 nm, attenuations at 850 nm and the ratio between attenuations at 1550 nm to 850 nm are

given below in order [144].

$$Y = 1.00 * X - 2.8 \times 10^{-14}, \qquad R^2 = 1.0 \tag{5.37}$$

$$Y = 1.00 * X + 0.00043, \qquad R^2 = 1.0 \tag{5.38}$$

$$Y = 1.00 * X - 0.0001, \qquad R^2 = 1.0 \tag{5.39}$$

We observe now a very good correlation between the measured and computed attenuation values and their ratio, duly evident by respective R^2 values obtained and the corresponding linear fit applied over the scatter plots between measured and computed attenuations at 1550 nm, at 850 nm, and the ratio between attenuations at 1550 nm to 850 nm as shown in plots shown in Fig. 5.12(a)-(c). Thus, in general it is quite evident that the proposed method based on standard iterative technique performs exceptionally well towards the retrieval of MGDSD parameters from the optical attenuations (dB/km) and the LWC (g/m^3). The proposed method can be quite useful towards the study of fog microphysics at a particular place and in modeling the optical attenuations for terrestrial FSO links in different fog environments.

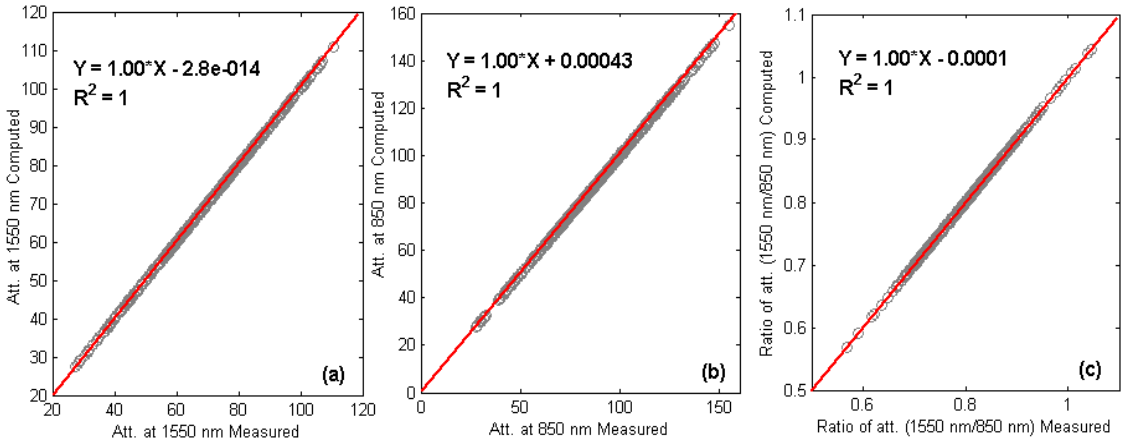

Figure 5.12: Performance test based on newly computed MGDSD parameters the ratio of attenuations at 1550 nm to 850 nm, between measured and computed quantities against the fog event at Prague

Analysis of the Computed Quantities and MGDSD Parameters

In order to perform analysis of the computed parameters of MGDSD for the Prague fog event case, histograms of residuals of actual measured and computed quantities (optical attenuations (dB/km) at 1550 nm, at 850 nm, the ratio of measured and computed attenuations at 1550 nm to 850 nm), and the three computed MGDSD parameters m, Λ and

N_0 (using standard iterative procedure) are shown in Fig. 5.13. As evident through the histograms of residuals of measured and computed optical attenuations at 1550 nm as shown by Fig. 5.13-(a), residual of measured and computed attenuations at 850 nm as shown by Fig. 5.13-(b), and the residual of measured and computed ratio of attenuations (1550 nm/850 nm) as shown by Fig. 5.13-(c), the retrieved MGDSD parameters are quite accurate in modeling the optical attenuations for this representative radiation fog event. Excellent results are achieved for the selected fog event at Prague as were achieved in the case of representative fog event of Graz, and thus the proposed method is accurate enough to model the optical attenuations in radiation fog environments.
Just for the sake of comparison, Fig. 5.14(a)-(f) shows the residuals of computed attenuations at 1550 nm, LWC, ratio between attenuation at 1550 nm to corresponding LWC and the three MGDSD parameters Λ, m, and the Log10N_0, respectively. From the comparison of Figs. 5.13 and 5.14, it is quite clear that for Prague the proposed iterative procedure (i.e., comparing attenuations over LWC) that is used to retrieve the MGDSD parameters performs equally well in the similar fashion as it was for the selected fog event for Graz. However, because of a small offset in the LWC measuring device and flexibility of having another measured quantity (attenuations at 850 nm), we slightly modified the procedure and then again retrieved MGDSD parameters from ratio of attenuations at 1550 nm to 850 nm. It was quite clear that the proposed iterative procedure performs exceptionally well towards the retrieval of MGDSD parameters [144].
An analysis of the computed optical attenuations reveals that the maximum attenuation value, for the 1550 nm wavelength, using retrieved MGDSD parameters is about 110.7 dB/km, whereas the mean and median values are about 71.92 and 74.56 dB/km, respectively with a standard deviation of about 17.2. An analysis of the computed attenuations at 850 nm shows that the maximum value reached is about 154.5 dB/km and the mean and median values are about 89.96 and 90.59 (dB/km) with a standard deviation of about 25.19. The histograms as shown in Fig. 5.13-(d) to 5.13-(f) reveal the behavior of the three computed MGDSD retrieved by iterative procedure against this representative fog event. The mean and median values are 3.933 and 3.9 for m, 6.669 and 6.8 for Λ, and 6.81 and 6.918 in case of Log10(N_0). A further analysis of these three parameters shows that in case of parameter m, about 35.20 % values are less than 3.0, about 45.20 % are within the range 3.0 and 6.0 and about 19.58 % are above a value of 6.0. Similarly, analyzing the values of Λ retrieved against the whole fog event show that about 0.4 % are below a limit of 1.5, about 2.5 % are within the range 1.5 and 3.0, while a major portion of the computed values for Λ, about 97.08 %, are above a value of 3.0. A similar analysis of the 3rd parameter N_0 reveals that about 0.833 % are below a value of 2.37 and the remaining values about 99.16 % lie within the range between 2.37 and 607.5 [144].

In order to study the behavior of these three computed MGDSD parameters during the whole fog event, Fig. 5.15 shows the time series of plot between the measured attenuation and the three retrieved MGDSD parameters. During the early phase of the representative fog event (fog formation stage) and the last phase (fog dissipation stage) of the fog event there exist a strong correlation between all three MGDSD parameters and the measured

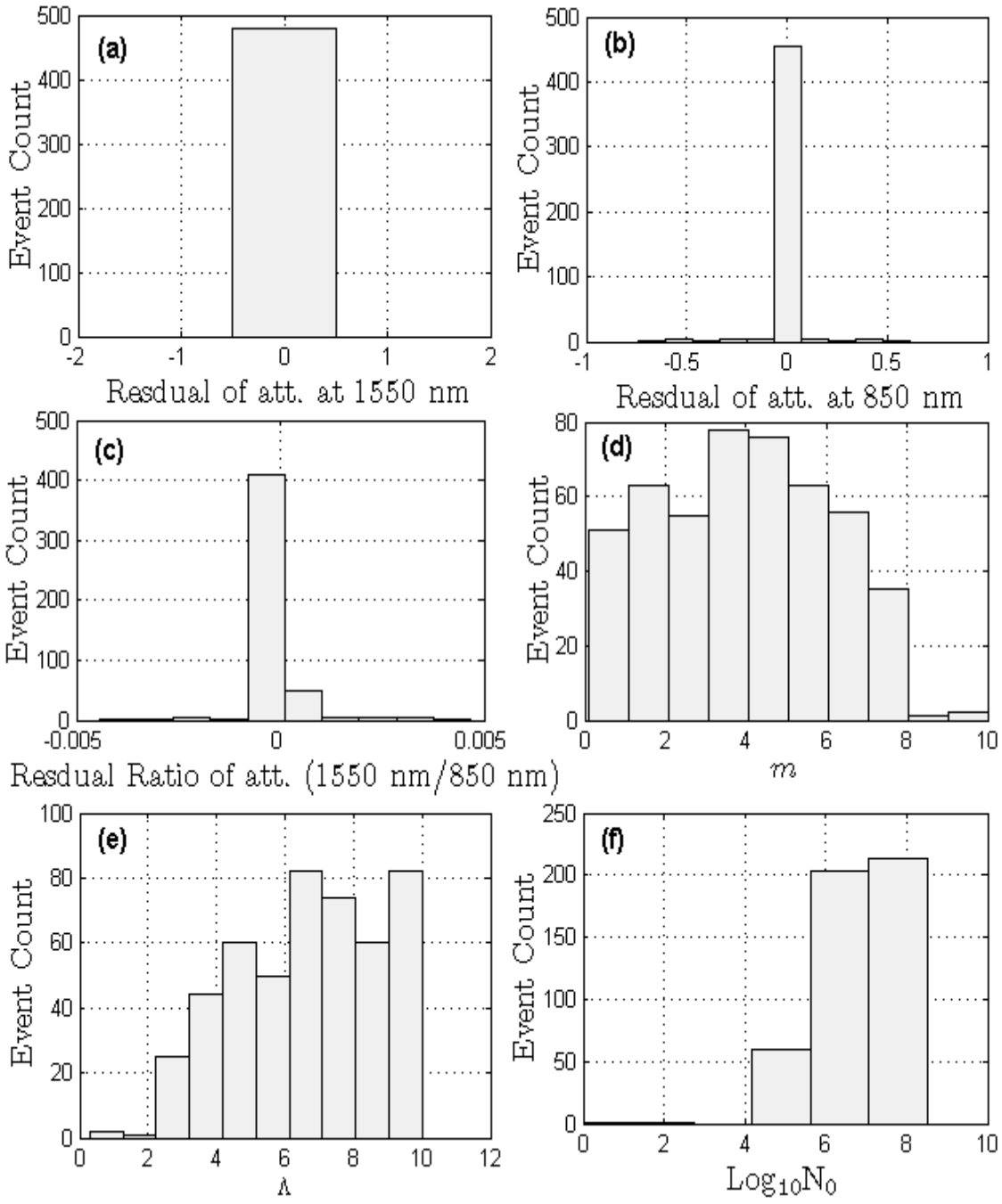

Figure 5.13: Histograms of residuals of computed quantities and the newly computed MGDSD parameters m, Λ, and $\mathrm{Log}_1 0 N_0$ retrieved by taking ratio of attenuations at 1550 nm to 850 nm, against the fog event at Prague

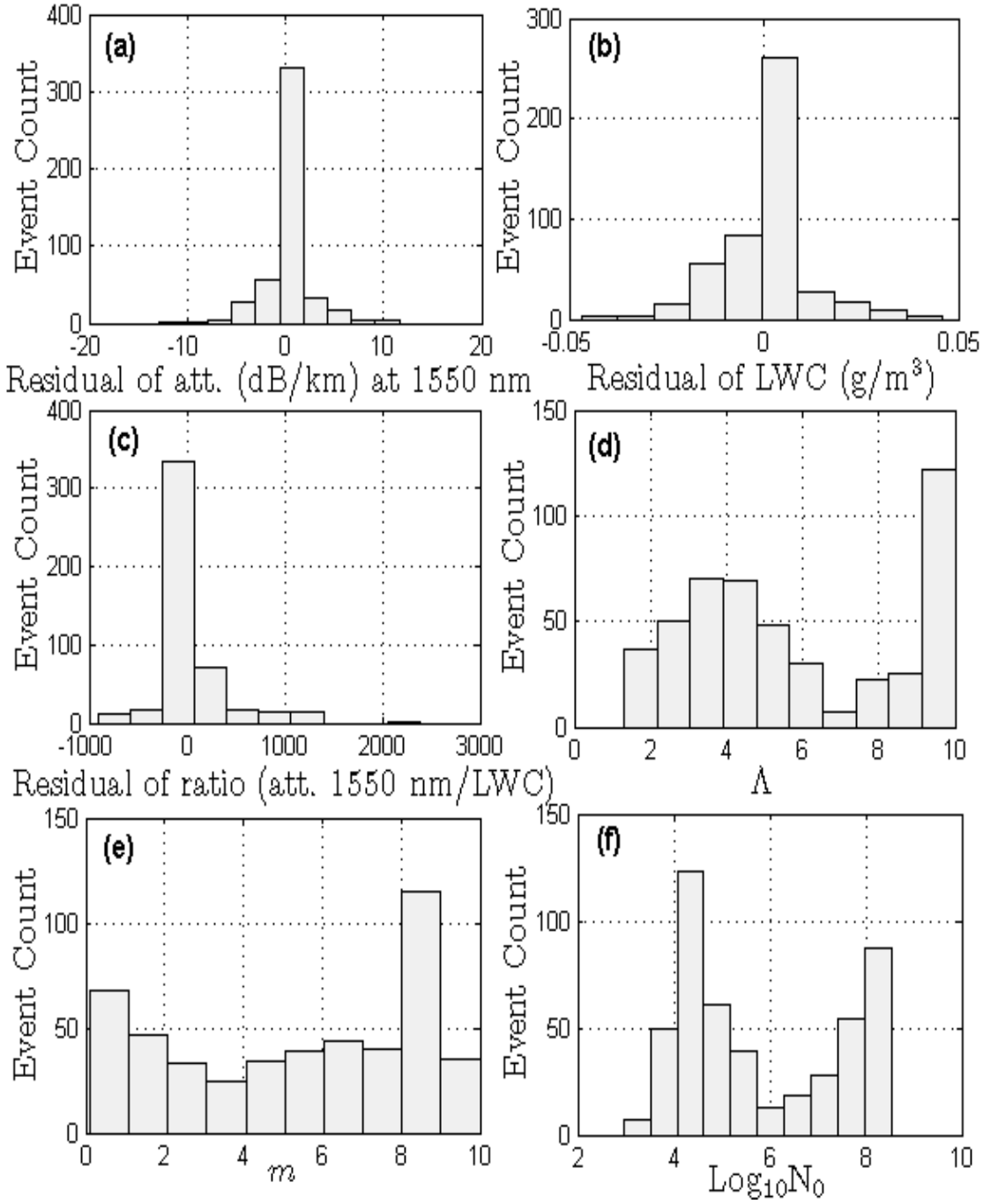

Figure 5.14: Histograms of residuals of computed quantities and the newly computed MGDSD parameters Λ, m, and Log_10N_0 retrieved by taking ratio of attenuations at 1550 nm to LWC, against the fog event at Prague

attenuations at 1550 nm. With the increase in attenuation, a corresponding increase in all these three parameters of MGDSD is observed and vice versa. Whereas, during the maturity stage of the fog event, fog attenuations are in high correlation with parameter N_0 as compared to the other two parameters. This time series behavior of the three parameters of MGDSD is exactly the same as observed in case of their influence for the Graz fog event case. Thus it can be safely concluded that the fog distributions at the two locations Graz and Prague are closely the same and they behave in the similar fashion during different phases of the continental fog event. Moreover, it may also be concluded that the MGDSD parameters for similar kind of fog environments may have the same behavior of DSD parameters. The Table 5.6 summarizes the computed quantities and the three parameters of MGDSD for the representative fog event of Prague [144].

Hence, we may safely conclude that the observed behavior of the three parameters of

Parameters	**Attenuations at 1550 nm (dB/km) minutes**	**Attenuations at 850 nm (dB/km) minutes**	**Ratio of Attenuations (1550 nm / 850 nm) minutes**	Λ $\mu\mathbf{m}^{-1}$	N_0 $\mathbf{cm}^{-3} \cdot \mu\mathbf{m}^{-1}$	m
Min.	27.41	27.62	0.5693	0.3	-5.953	0.1
Max.	110.7	154.6	1.045	10.0	8.515	10.0
Mean	71.92	89.96	0.8124	6.669	6.81	3.933
Median	74.56	90.59	0.8194	6.8	6.918	3.9
Std. dev.	17.20	25.19	0.07235	2.071	1.221	2.128
Range	83.27	127.0	0.4753	9.7	14.47	9.9

Table 5.6: Statistics of computed optical attenuation (dB/km), LWC (g/m^3) and corresponding MGDSD parameters against the fog event of 07 Feb. 2009 at Prague.

MGDSD for the two selected continental locations is closely the same. The behavior of these three parameters is found in a very high correlation with the measured and computed attenuations. Therefore, it may also be concluded that the MGDSD parameters for similar kind of fog environments may use the same DSD model in order to characterize a particular type of fog for the terrestrial FSO links.

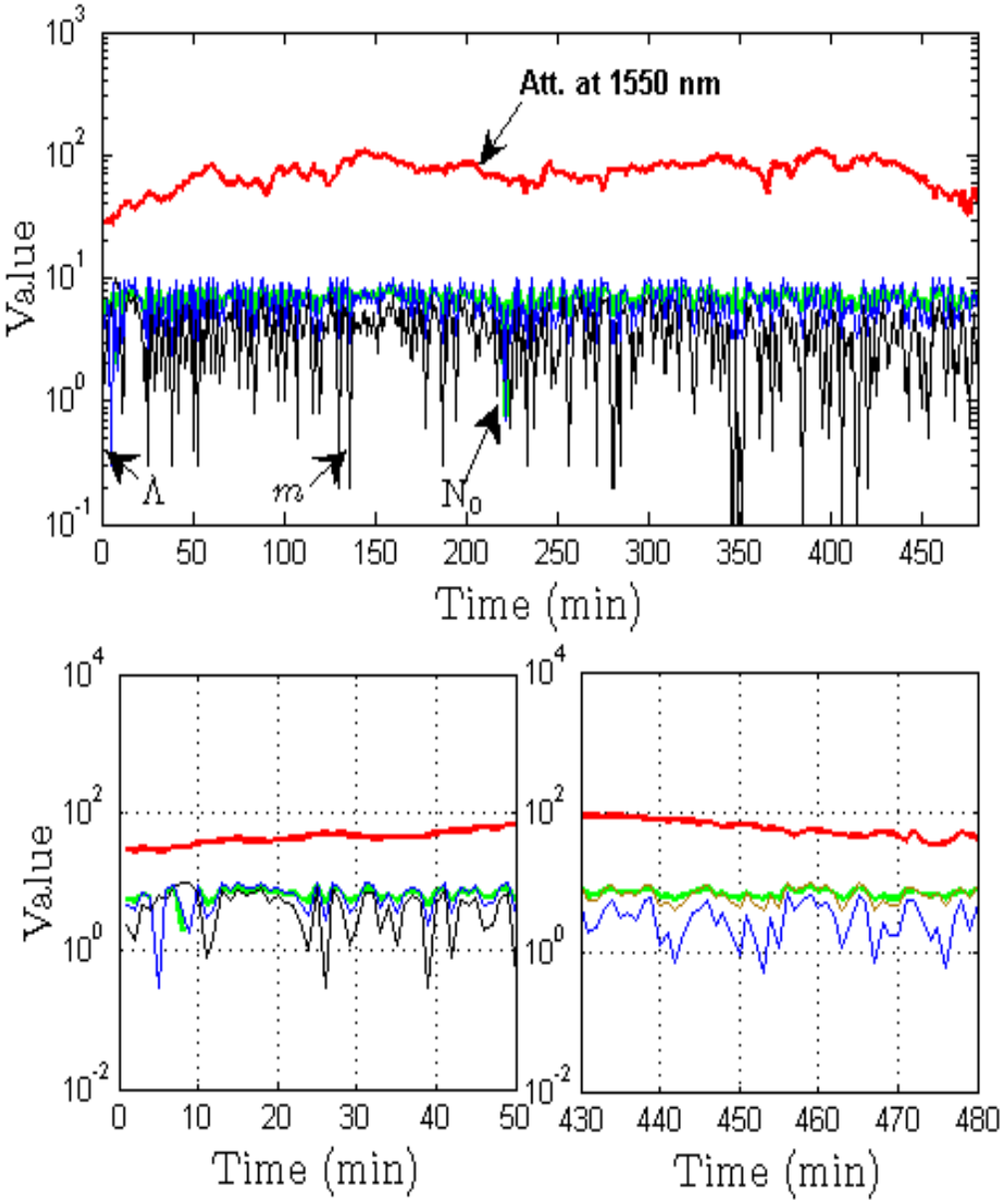

Figure 5.15: Time series of measured optical attenuations (dB/km), and the corresponding newly computed MGDSD parameters Λ, $\mathrm{Log}_1 0N_0$ and m against the fog event at Prague

5.5 Analysis of Exponential Drop Size Distribution (EDSD) Parameters

In this section the analysis of computed EDSD parameters is being discussed for the two mentioned fog events. First the histograms are shown of the computed quantities and then the time series of computed EDSD parameters is compared with the measured optical attenuations for Graz and Prague at 950 nm and 1550 nm, respectively. The measured statistics are given in tabular form for each fog event, and the computed EDSD parameters goodness is evaluated through R^2 fitting between the measured and computed quantities.

5.5.1 EDSD Parameters for Graz Fog Event of 18-19 Nov. 2009

In the first part of this section the performance analysis of the proposed method is presented on the basis of comparison between measured and computed quantities. The computed quantities are the optical attenuations (dB/km) at 950 nm, the LWC (g/m^3) and the ratio between attenuations at 950 nm to the LWC as given by Equations (3.3), (4.7) and (5.21), respectively. The DSD considered now is the EDSD as given by the Equation (5.20). These mentioned quantities are computed by considering the newly computed EDSD parameters, which are computed by standard iterative procedure (see Section 5.2.2). The performance analysis of the proposed method based on comparison between measured and computed quantities is presented under the performance analysis section. This is followed by a detailed statistical analysis of the behavior of computed quantities and the EDSD parameters [147].

Performance Analysis of the Method

To test the performance of measured EDSD parameters for the Graz fog event, a scatter plot between measured and computed attenuations (dB/km), the LWC (g/m^3), and the ratio between attenuation and LWC is drawn as shown in Fig. 5.16. In Fig. 5.16(a)-(c) based on the performance test, the plots between measured and computed optical attenuations (dB/km) at 950 nm, the LWC, and ratio between optical attenuations/LWC is shown respectively. It is important to remember that the optical attenuations at 950, and the LWC against the fog event of 18-19 Nov. 2009 at Graz are computed by utilizing the Equations (3.3) & (4.7), from those two EDSD parameters for which the difference between ratio of measured and computed quantities (consider Equation (5.21) is minimum. The linear curve fitting is applied on all three quantities and a very accurate results are obtained for R^2 test as for measured and computed attenuations its value is R^2=0.9957 as shown in Fig. 5.16-(a), for the case of measured and computed LWC its value is R^2=1 as shown in Fig. 5.16-(b), and for the ratio between measured and computed attenuations to LWC its value

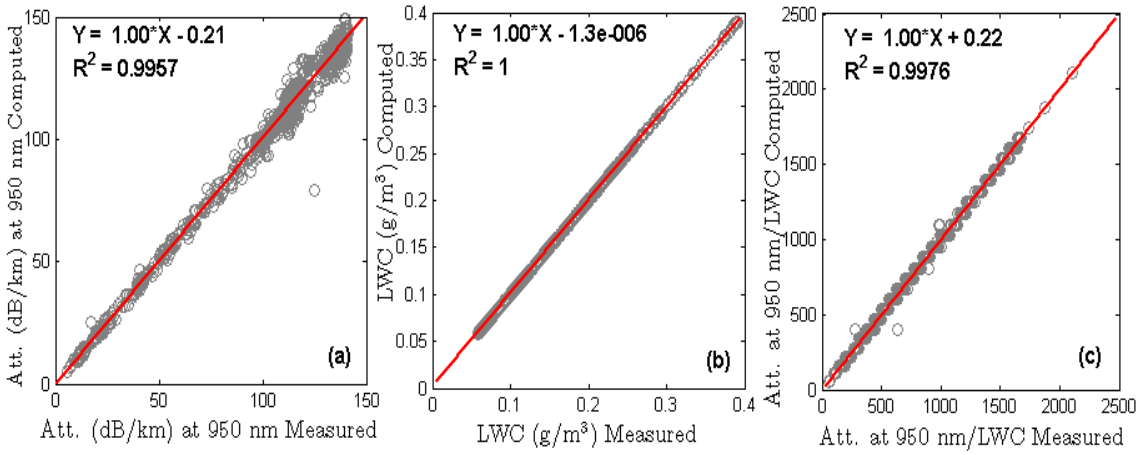

Figure 5.16: Performance test of measured and computed quantities for a fog event at Graz

is R^2=0.9976 as shown in Fig. 5.16-(c). The resultant equations of the linear fit applied over the three quantities i.e., measured and computed optical attenuations, LWC and the ratio between optical attenuations and the LWC are [147],

$$Y = 1.00 * X - 0.2131, \qquad R^2 = 0.9957 \tag{5.40}$$

$$Y = 1.00 * X - 1.3 \times 10^{-6}, \qquad R^2 = 1 \tag{5.41}$$

$$Y = 0.9974 * X + 0.22, \qquad R^2 = 0.9976 \tag{5.42}$$

Here "Y" denotes the quantity computed and "X" denotes the quantity measured.

Analysis of the Computed Quantities and EDSD Parameters

Fig. 5.17(a)-(f) shows the histograms of the computed optical attenuations, residual of optical attenuations at 950 nm, residual of LWC, residual of ratio between optical attenuation to the corresponding LWC, and the two computed EDSD parameters (Λ and $Log_{10}N_0$) against the fog events of Graz. It is visible through histogram as shown in Fig. 5.17-(a) that the average and median attenuations values for the computed attenuation are about 93.62 dB/km and 108.6 dB/km, and has a standard deviation of about 39.79 dB/km in comparison to mean and median of measured attenuations about 93 dB/km and 111 dB/km and having standard deviation of about 53.3 dB/km. The histogram in Fig. 5.17-(b) shows the residual of measured and computed attenuations at 950 nm. Similarly, Fig. 5.17-(c) reveals that residual of measured and computed LWC. In case of computed LWC, the mean and median values of LWC are about 0.1466 g/m^3 and 0.1272 g/m^3 with a standard deviation of about 0.08144 g/m^3. Whereas, in case of measured LWC, these values were about 0.1466 g/m^3, 0.12718 g/m^3, and 0.0814 g/m^3, respectively. The histogram as shown in Fig. 5.17-(d) shows the residual of ratio between measured and computed attenuation

at 950 nm to the LWC. Finally, the histograms as shown in Figs. 5.17(e)-(f) correspond to the newly computed EDSD parameters Λ and $Log_{10}N_0$, respectively. An analysis of these two parameters reveal that the mean, median and standard deviation values of these parameters were 3.75, 3.89, 0.9012, and 1.179, 1.0 and 0.6034, respectively. Analyzing the computed values of the two EDSD parameters, it is observed that in case of parameter Λ, about 72.2% of values computed are less than a value of 1.5, about 26.9 % are between 1.5 and 3.0, while about 0.1 % are greater than a value of 3.0. Similarly, for the parameter $Log_{10}N_0$ it is observed that about 10.10 % values are less than 2.37, while about 89.90 % values are within the range of 2.37 and 607.5 [147].

It would be interesting to see the behavior of the computed EDSD parameters for this whole fog event. Fig. 5.18 shows the time series of the two EDSD parameters Λ and N_0 along with the measured attenuation (dB/km) at 950 nm. As evident from Fig. 5.18 that the two newly computed EDSD parameters are generally in good correlation with the measured attenuations at 950 nm. Overall, the value of the correlation coefficient in case of comparison between measured attenuation at 950 nm and EDSD parameters Λ and N_0 for the whole fog event is about 0.4284 and 0.7493, respectively. While during formation, maturity and dissipation phases the values of the correlation coefficient between parameter Λ and measured attenuations at 950 nm are 0.7859, 0.3570, 0.7358, respectively. Similarly, the values of correlation coefficient between measured attenuations at 950 nm and the EDSD parameter N_0 during formation, maturity and dissipation phases of the mentioned fog event are 0.7975, 0.6990 and 0.8935, respectively. This shows that optical attenuations are in relatively in stronger correlation with the EDSD parameter N_0 as compared to the parameter Λ. Table 5.7 summarizes the statistics of the computed attenuations (dB/km), LWC (g/m^3), their ratio and of the two computed EDSD parameters [147].

From the analysis and study of the selected Graz fog event, it is quite evident that the

Parameters	**Attenuations (dB/km) minutes**	**LWC (g/m^3) minutes**	**Attenuations / LWC (dB/km)/(g/m^3) minutes**	Λ	N_0
Min.	5.182	0.05861	55.68	0.08	-0.4074
Max.	149.10	0.3904	2107	3.2	5.406
Mean	93.62	0.1466	736.9	1.179	3.754
Median	108.6	0.1272	599	1.0	3.892
Std. dev.	39.79	0.08144	422.8	0.6034	0.9012
Range	143.9	0.3318	2051	3.12	5.814

Table 5.7: Statistics of computed optical attenuation (dB/km), LWC (g/m^3) and corresponding EDSD parameters against the fog event at Graz

proposed method is quite accurate while computing the EDSD parameters against the measured attenuations. This suggests that the same method can be used to predict, from fog attenuations of other fog events, the EDSD parameters with quite high accuracy. More-

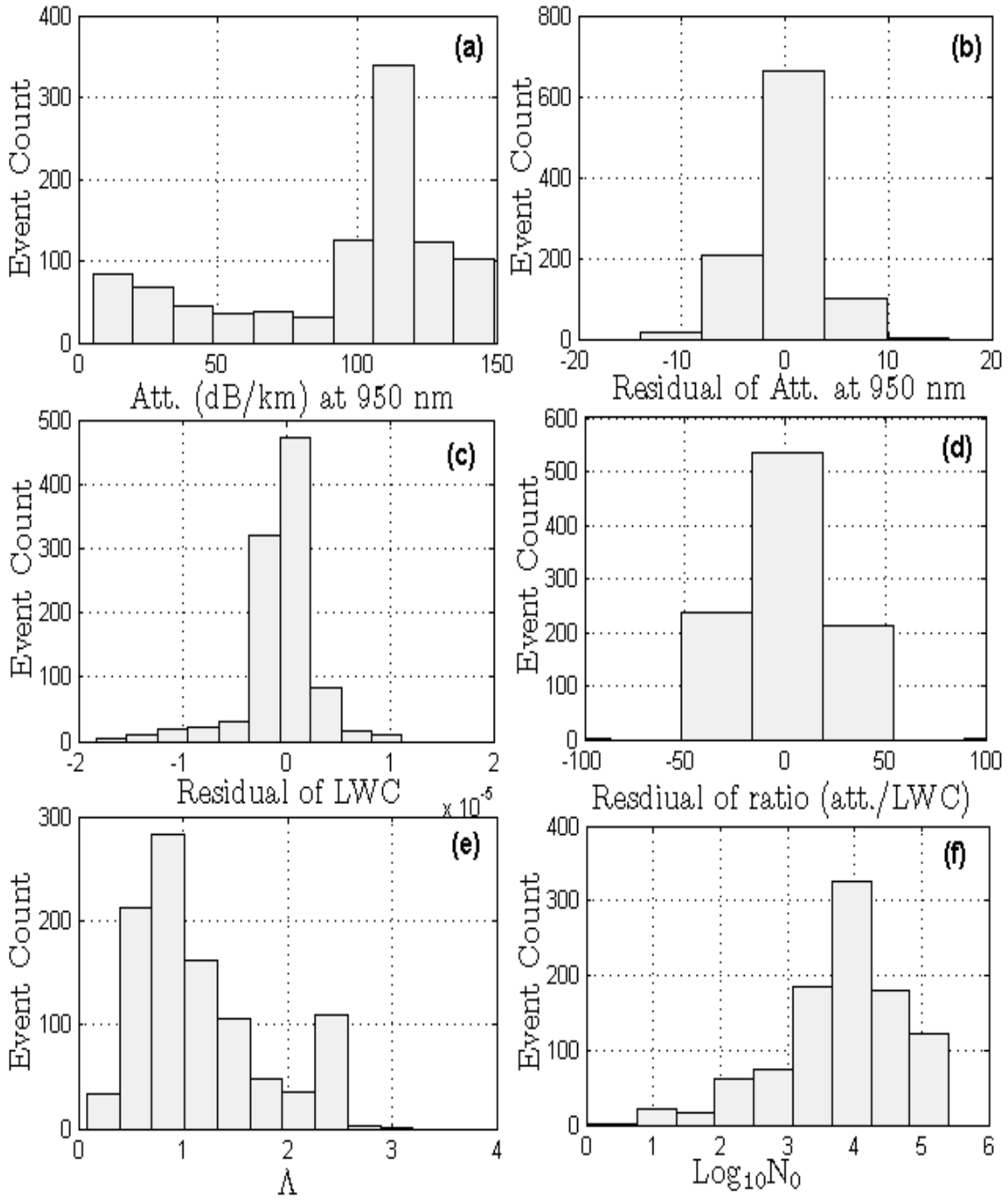

Figure 5.17: Histograms of computed quantities and parameters against the fog event at Graz

over, the computed EDSD parameters can be useful for the scientists interested in the understanding of fog microphysics and the related meteorological processes for providing

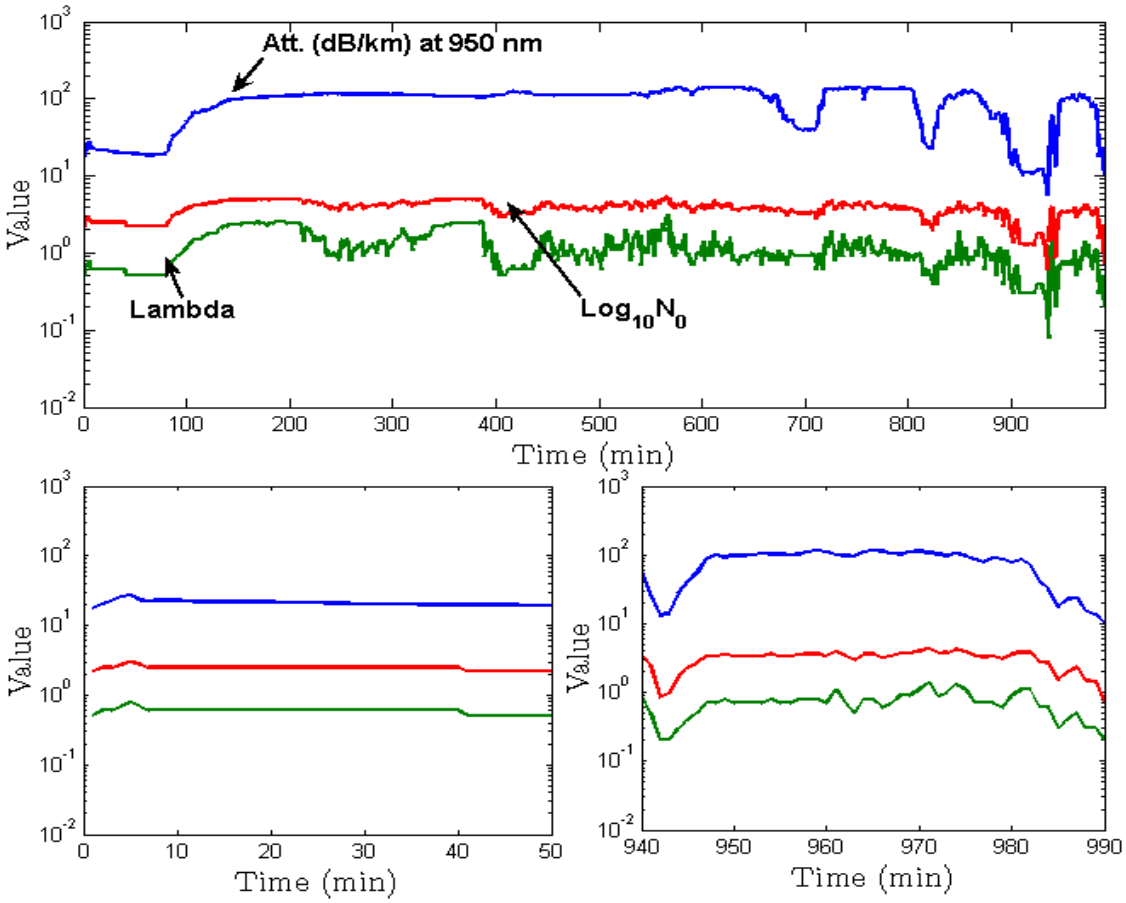

Figure 5.18: Time series of measured attenuation and the newly computed EDSD parameters Λ and $\mathrm{Log}_{10}(N_0)$ against the fog event at Graz

improved diagnostics of fog attenuation potential for the terrestrial FSO links. By this way, the computed DSD parameters can be used in the simulation models to predict fog attenuations to know about the level of attenuations and then adjusting appropriate link margin so that sufficiently high level of availability and quality of service of FSO links may be guaranteed for a particular environment like fog.

5.5.2 EDSD Parameters for Prague Fog Event of 07 Feb. 2009

The same procedure, as adopted in case of computation of EDSD parameters for Graz fog event, is used in case of Prague fog event of 07 Feb. 2009. The optical attenuations (dB/km) at 1550 nm and 850 nm and their ratios are computed by considering Equations (3.3) and (5.24). The DSD considered here is the EDSD as given by the Equation (5.20). These computed quantities are then compared to their corresponding actual mea-

sured quantities, in order to evaluate the performance of newly computed EDSD parameters under the performance analysis section. The performance analysis section is followed by statistical analysis of the computed quantities and the EDSD parameters.

Performance Analysis of the Method

The plot as shown in Fig. 5.19 represents the performance analysis of the newly computed EDSD parameters and compares the results of measured and computed attenuations at 1550 nm and 850 nm as shown by Fig. 5.19(a)-(b), while compares the ratio between attenuations at 1550 nm and 850 nm in Fig. 5.19-(c) for the Prague fog event. It is clearly evident from this plot that the newly computed EDSD parameters perform sufficiently well as represented by the value attained through performance analysis test (R^2 test) for the mentioned fog event.

For the representative fog event of Prague, the linear equations obtained in case of com-

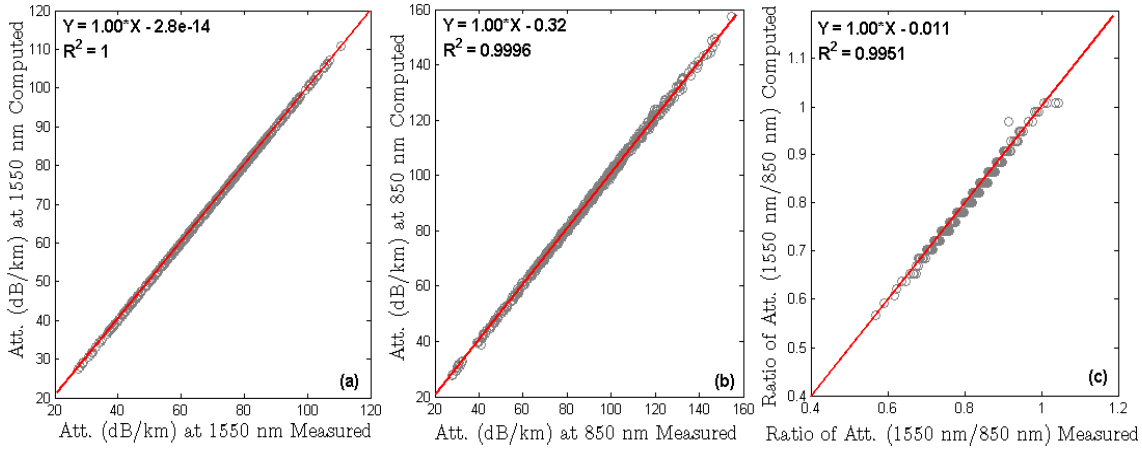

Figure 5.19: Performance analysis of measured and computed quantities against the fog event at Prague

parison between the measured and computed attenuations at 1550 nm and at 850 nm are given by Equations (5.43) and (5.44), respectively [147].

$$Y = 1.00 * X - 2.8e - 14, \qquad R^2 = 1 \tag{5.43}$$

$$Y = 1.00 * X - 0.32, \qquad R^2 = 0.9996 \tag{5.44}$$

Here "Y" denotes the quantity computed and "X" denotes the quantity measured. While the linear fit equation in case of the ratio between attenuations at 1550 nm to 850 nm is given by,

$$Y = 1.00 * X - 0.011, \qquad R^2 = 0.9951 \tag{5.45}$$

Analysis of the Computed Quantities and EDSD Parameters

Fig. 5.20 shows the histograms of the residuals of measured and computed attenuations at 1550 nm and the ratio between measured and computed attenuations at 1550 nm and 850 nm, and the two newly computed EDSD parameters Λ and $\mathrm{Log}_{10}(N_0)$ for the Prague fog event. The histogram as shown by Fig. 5.20-(a) represents the residual of measured and computed attenuations in dB/km at 1550 nm. While the histogram as shown in Fig. 5.20-(b) represents the behavior of the residual of ratio between measured and computed attenuations in dB/km at 1550 nm to 850 nm. It was observed that the mean and median values of ratio between the two attenuation are about 0.00710 and 0.00715 with maximum ratio reaching up to 0.0363 while the value of standard deviation for the whole fog event is about 0.007195. Fig. 5.20-(c) and Fig. 5.20-(d) represents the behavior of the computed EDSD parameter Λ and $\mathrm{Log}_{10}(N_0)$, respectively. It is observed that the mean and median values of the Λ parameter are about 2.891 and 2.9 for the whole fog event with maximum value of this parameter reaching to about 4.3. The standard deviation is about 0.3649 for the whole fog event. While for N_0 the mean and median values are about 11.71 and 11.74, respectively with a standard deviation of about 0.6395. The minimum and maximum values of parameter N_0 are 9.369 and 12.97, respectively [147].

It would be interesting to see the behavior of the two EDSD parameters related to this whole fog event also. Fig. 5.21 shows the time series of measured attenuations at 1550 nm and the two EDSD parameters for the whole duration of the fog event. As can be seen that, like the case of Graz fog event, generally the two parameters are in good correlation with the measured attenuations at 1550 nm. Particularly, the measured optical attenuations at 1550 nm has comparatively stronger correlation with EDSD parameter N_0 compared to parameter Λ during formation, middle and dissipation phases of the mentioned fog event. It is observed that the value of the correlation coefficient in case of parameter N_0 for formation, maturity and dissipation phases is 0.8892, 0.7375 and 0.5695, respectively. While for the case of parameter Λ, the values of correlation coefficient for formation, maturity and dissipation stages are 0.7468, 0.4068 and 0.2202, respectively. For this mentioned fog event, Table 5.8 summarizes the computed results and the corresponding EDSD parameters [147].

From the analysis of the newly computed EDSD parameters of the Prague fog event case, it was observed that most of the computed values of parameter Λ about 63.12 % lie within the range between 1.5 to 3.0. While the rest of the values about 36.87 % are greater than the value of 3.0. This is contrary to the Graz fog event where most of the values about 72.2 % were below the value of 1.5. And the values of the 2nd EDSD parameter N_0, all lie within the range between 2.37 and 607.5. This behavior of parameter N_0 is similar to the behavior of this parameter for the Graz fog event, where about 90 % of the values of this parameter lie within this mentioned range [147].

From the analysis of the two selected fog events recorded from two different locations and the comparison of their computed EDSD parameters computed with the measured at-

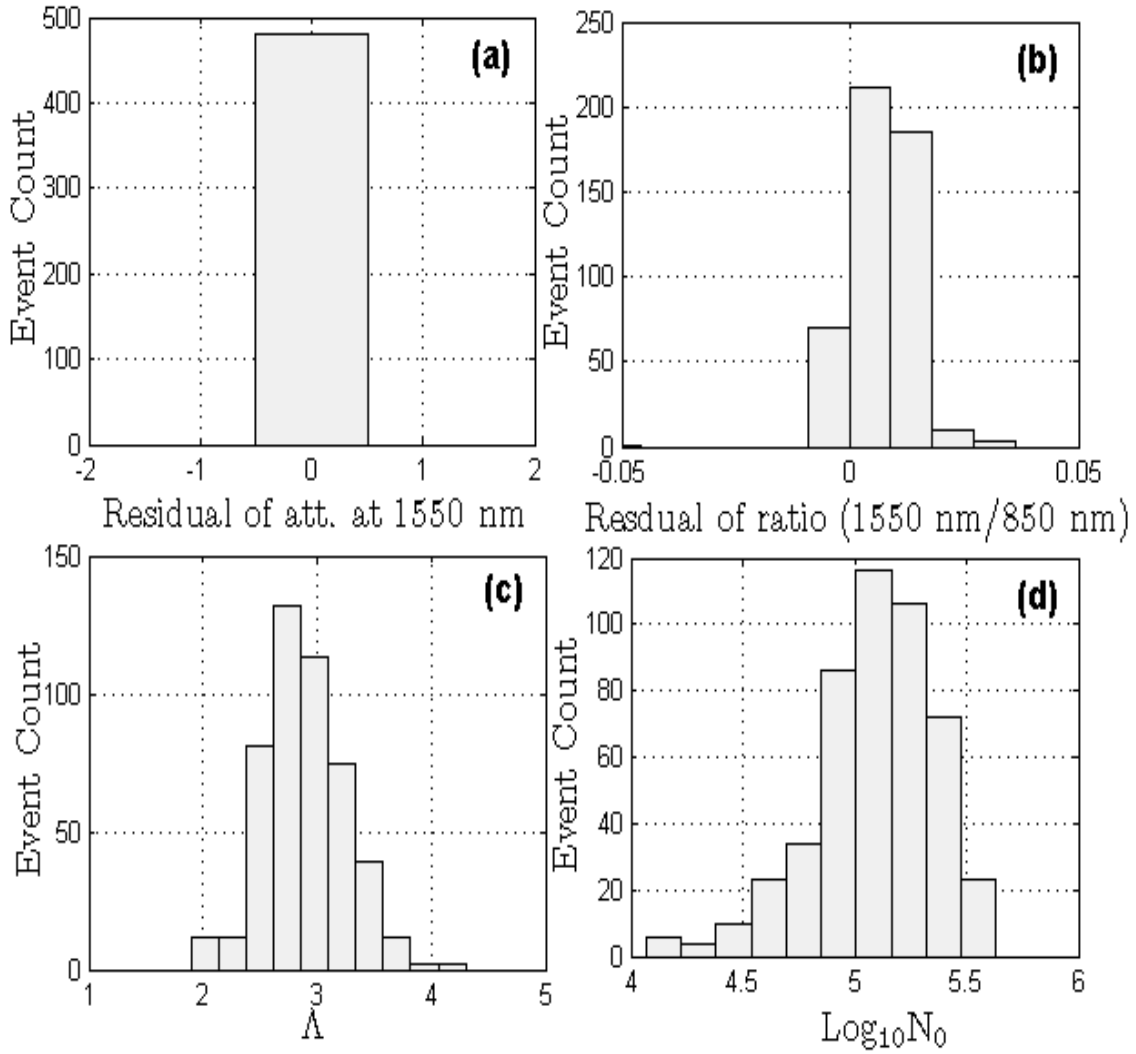

Figure 5.20: Histograms of residual of measured and computed quantities and the newly computed EDSD parameters Λ and $\mathrm{Log}_{10}(N_0)$ against the fog event at Prague

tenuations (see Figures 5.18 & 5.21), it is quite visible that the time series behavior (trend) of the two EDSD parameters during the formation phase (early stage), the maturity phase (middle stage) and the dissipation phase (last stage) is closely the same for the two locations. Moreover, the computed parameters are in high correlation with the measured attenuations. Up to the best of my knowledge, no prior record of the standard EDSD parameters exists in the literature related to continental fog conditions. Therefore, its difficult to compare the computed results with some standard models as we observe a difference in the observed mean and median values of the two EDSD parameters for Graz and Prague, especially the parameter N_0 (see Table 5.7 & Table 5.8 for comparison). This behavior is expected as the measured attenuations are not the same. The difference in the distribution

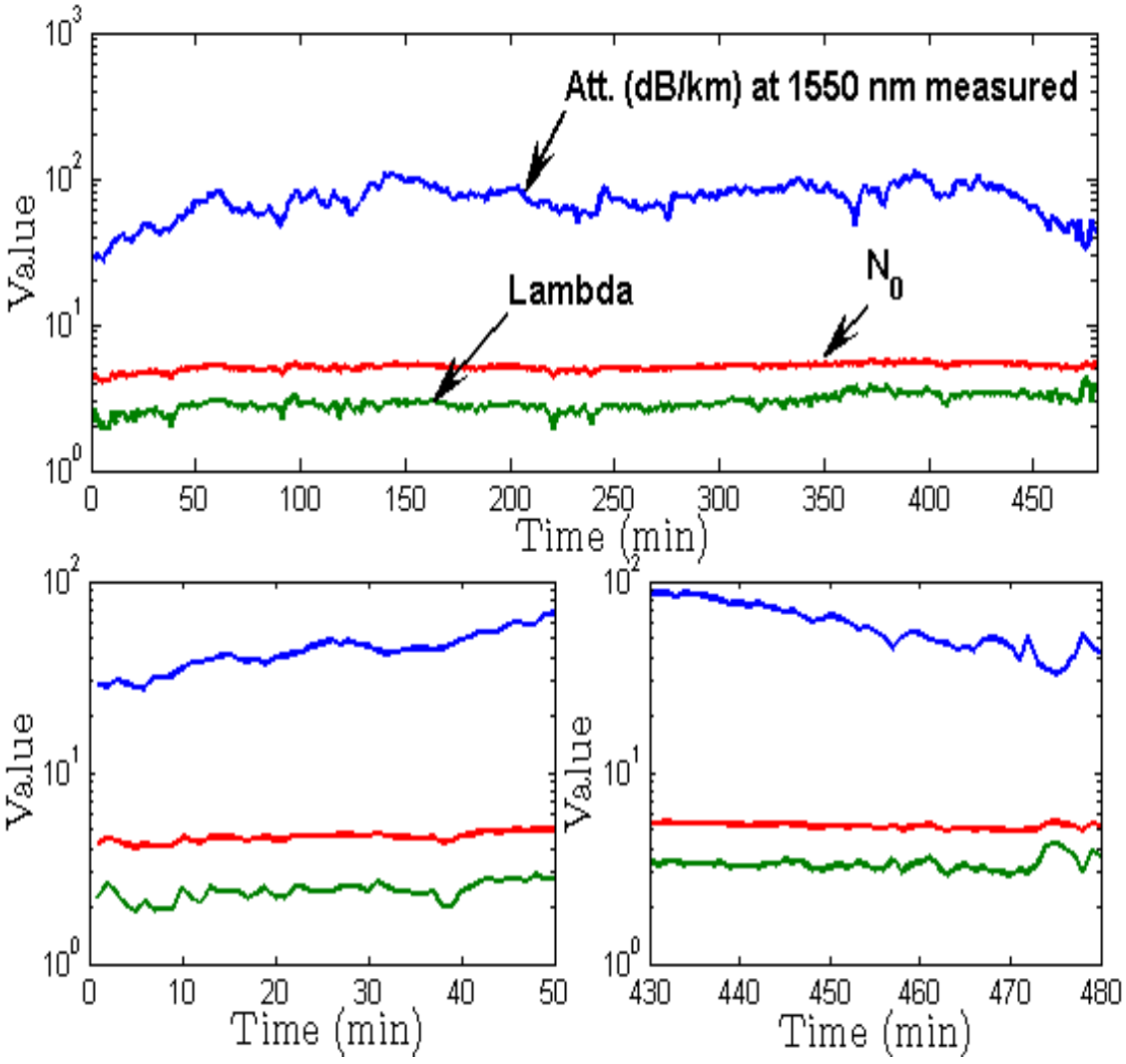

Figure 5.21: Time series of measured optical attenuation at 1550 nm, and the EDSD parameters Λ, and $\mathrm{Log}_{10}(N_0)$ against the fog event at Prague

parameter values may be attributed to the range of attenuation values recorded for the both locations, since the sample data corresponding to Graz fog event contains attenuation values that are mostly in the higher range approaching 100 dB/km for the major portion of time as compared to the Prague fog event. It is to be noted that the Graz fog event contains attenuation data of about 990 minutes with mean and median of 65.15 dB/km and 77.08 dB/km, respectively. Whereas Prague data has only 480 minutes of attenuation data with mean and median around 71.92 dB/km and 74.56 dB/km, respectively [147].
Although, the statistics showing the behavior of continental fog at two locations are derived from a limited samples from two fog events, one fog event from Graz and one from Prague. Hence, they do not necessarily represent the true behavior of continental fog microphysics

Parameters	Ratio of Attenuations (1550 nm/850 nm) Measured	Ratio of Attenuations (1550 nm/850 nm) Computed	Λ	N_0
Min.	0.5692	0.5663	1.9	9.369
Max.	1.045	1.008	4.3	12.97
Mean	0.8124	0.8053	2.891	11.71
Median	0.8194	0.8007	2.9	11.74
Std. dev.	0.07234	0.07302	0.3649	0.6395
Range	0.4753	0.4421	2.4	3.603

Table 5.8: Statistics of computed EDSD parameters against the fog event of 07 Feb. 2009 at Prague

and its modeling with EDSD. The main focus of the work presented in this thesis is on the method to retrieve DSD parameters corresponding to EDSD and MGDSD, and not on the values of the DSD parameters computed. The proposed method yields excellent results towards the computation of EDSD parameters from this study and gives us a slight insight of the EDSD parameters behavior corresponding to the selected fog events. More sample data is thus required from different locations in order to refine the EDSD parameters computed related to continental fog that truly represent the continental fog microphysics and its influence on the optical signal transmissions.

5.6 Final Discussion

The results presented in this thesis related to the computation of optimal set of DSD (EDSD and MGDSD) parameters are derived from a very limited sample data set (only two representative fog events). The statistical results from this research may not represent the true behavior of the fog microphysics at Graz, Prague and Milan. However, more data is needed from different locations in order to draw some concrete results that represent the actual cloud/fog microphysics and modeling its influence on the optical signal transmissions for terrestrial FSO links.

Apart from the obtained statistical results related to continental fog at Graz and Prague, the performance of the proposed method is quite excellent in computing optimal set of DSD parameters from optical attenuations and the LWC values. This method may be useful for the meteorologists and engineers who want to study fog/cloud microphysics but do not have the instruments to directly measure the fog related physical parameters and have only FSO links related attenuation data. Moreover, this proposed method is equally useful in order to compute optimal set of DSD parameters (EDSD and MGDSD) related to any fog type, snow, rain and clouds from corresponding optical attenuations, provided there exists some physical parameter (like Liquid water content or particle surface area etc.,) related

data.
Although, we obtained excellent results for the selected continental fog events with the proposed procedure to compute EDSD and MGDSD parameters, as the performance of both drop size distributions is exactly alike. However, in situ measurements related to fog and cloud suggests that MGDSD is more better than any other distribution to characterize the fog and cloud size distributions [99, 148]. Hence it is better to use MGDSD model in order to study the fog microphysics and its related characteristics.

5.7 Summary about Implementing Attenuation Prediction Models

In order to study the characteristics of fog using the free-space optical wireless links, we adopted Maitra and Gibbins technique, that employs iterative procedure, to compute three distribution parameters of a modified gamma distribution. For the mentioned purpose two individual radiation fog events were analyzed, one each at Graz and Prague, mainly to indicate the effectiveness of the technique adopted to obtain near-instantaneous radiation fog droplets size distribution in terms of modified gamma distribution. Based on the performance analysis of the mentioned techniques, it was observed that this technique is quite useful in terms of simplicity and efficiency and yield excellent results while computing optimal parameters for the MGDSD. The newly computed three parameters of the modified gamma distribution, both for Graz and Prague locations, are consistent with the previously computed distribution parameters existing in the literature and are in a very strong correlation with the actual measured quantities like optical attenuations and the LWC. Hence it may safely be inferred that the behavior of computed MGDSD parameters at both mentioned locations is quite similar which implies that the radiation fog behavior at both locations is somewhat similar. This proposed techniques seems to be very useful in computing the distribution parameters at some particular location, for the FSO links, in situations where the measurement of most of the microphysical parameters is not feasible besides measurement of optical attenuations. The computation method of retrieving MGDSD parameters using Marsaglia method is somewhat difficult to simulate and may not yield accurate results in comparison to Maitra and Gibbins method based on iterative procedure to accurately compute the EDSD and MGDSD parameters.

6 CONCLUSIONS

Free-space optics is an assertive access technology, installed in telecommunications networks basically for the last mile access, provides very high data rates comparable to fiber optics with greater economic efficiency. The FSO has successfully established itself in several areas of the world of telecommunications such as secure connections for military applications, high definition television and temporary broadband connections ("Fiber backup"). However, this technology is subject to certain number of constraints and challenges imposed mainly by the environmental factors, that degrade its link performance, and hence limit its spread to most telecommunications networks. Although in the last few decades, much research work has been done on various aspects of modeling the atmospheric free-space channel for different environmental factors, but significant breakthrough could not be achieved in overcoming, especially, the deleterious fog effects. The main difficulties towards theoretical characterization of the free-space atmospheric channel are

- the unavailability of extensive and accurate weather parameters database
- the need to identify main influencing parameters of the meteorological effects and study of their impact on the propagation of optical signals in free-space
- the unavailability of enough experimental data of optical attenuations (especially for different fog environments)

Further difficulty is experienced in the validation of empirical models through some microphysical models: comparisons between models and measurements cannot be explicitly made mainly due to the unavailability of simultaneous measurement of microphysical parameters along with the measured fog attenuations at the site of FSO deployment. Moreover, the microphysical characteristics of a particular fog type change with the location to location, and even at a particular location it change with time. Thus to optimize the design methodologies for future FSO systems, there is a need to construct a statistical-dynamical channel model for optical wireless communications especially for different fog environments, which is reliable enough generally in counteracting the dynamic channel impairments in an efficient manner.

6.1 Achieved Work

The free-space optics work in the field of optical waves in the visible and near infrared spectral range for which the optical components used to provide broadband. To enhance the robustness of FSO link improved atmospheric effect (attenuation and scintillation) mitigation is required. So, we are interested to study the attenuation of optical radiations (in this spectral range) during propagation through the free-space atmosphere in general and through fog in particular. Different aspects of optical wireless communication systems have been investigated in depth in this thesis. In s *chapter 2*, the influence of Earth atmosphere on the transmission of optical signals, its composition, characteristics and those particles that may be present have been revised. The physical phenomena that occur during propagation of radiation through the atmosphere and causing the extinction, namely the absorption and scattering were detailed from a theoretical point of view. In particular, the problem of scattering of light by spherical particles was studied from the theory of Mie scattering. We have evaluated various models that allow us to calculate the attenuation of optical radiation in the atmosphere, especially in the presence of fog (visibility range less than 1 kilometer). Few deterministic (Mie scattering and Ray tracing models) and the empirical models (Kruse, Kim, Al Naboulsi, and Bataille models), that are either a functions of wavelength or the visibility range, are discussed. These models can be employed to model optical attenuations under reduced visibility range conditions (such as fog, snow and rain) for optical signals lying in the 0.5 μm to 2.4 μm wavelength range. Furthermore, for the sake of completion of discussion other atmospheric channel effects like atmospheric absorption, turbulence or scintillation, solar influence, effect of background radiation, beam wander and beam spreading are also discussed in sufficient detail.

As it is reported, fog remains the most important problem that limits the availability of terrestrial FSO links. The performance of a terrestrial FSO system and its ability to overcome the presence of fog in the atmosphere are strongly related to the spectral dependence of attenuation on the transmitted optical signals. In studies on the spectral dependence, opinions remain divergent choosing the best suited wavelength for a particular type of FSO transmission and hence there remains a disagreement between the designers of these systems. In *chapter 3*, the important results of fog attenuation studies conducted at different locations in Europe (Graz, Milan, Prague and Nice) and their comparisons on the basis of well established empirical models (mainly Kruse and Kim models) have been reviewed. The detailed analysis and comparison of radiation fog and advection fog has proved their distinctly different behavior and it reveals that the Kim model describes well the reality than the Kruse model. It was observed that while employing Kruse model the attenuation decreases as the wavelength increases regardless of visibility range (i.e., FSO system operating at 10 micron is more efficient than a system operating at 950 nm). Whereas, Kim model states there is no spectral dependence of optical attenuation for values of visibility below 500 m. Upon experimental verification of these models using radiation fog

attenuation data (collected at Graz, Milan and Prague) and advection fog data (recorded at Nice), it was noticed that for the case of moderate fog conditions (radiation as well as advection fog) both Kim and Kruse models are equally acceptable and, therefore, we cannot prefer one model over the other. But in case of dense fog conditions (radiation as well as advection fog) for visibility range lesser than 500 m, Kim model performs better than the Kruse model. The results indicate that for stable fog conditions (like those in Graz, Milan and Prague) no availability of the FSO link can be improved with channel coding mechanism, however, for advection fog case, appropriate coding schemes can be used in order to improve the FSO link availability. But in any case very high attenuations cannot be compensated by employing higher state coded-modulation schemes alone. A brief but comprehensive analysis of measured optical attenuations corresponding to dry snow and rain conditions reveals that rain attenuations are not much significant in terms of their impact on terrestrial FSO links even for the case of heavy rain. However, dry snow attenuations are quite significant and in situations the corresponding optical attenuations can exceede quite easily the maximum allowable link margin of the FSO systems. The dry snow attenuations are highly dependent on the snowflake size, and the snowflake fall rate.

Since intricate relationships exist between fog microphysics and the fog characteristics, therefore, microphysical properties that shape up the fog microstructure like especially fog droplets number density and liquid water content alongside dependence on fog temperature and the relative humidity, were investigated in *chapter 4*. For that reason an analysis of the environmental conditions associated with radiation and advection fog has been presented using observations made at different locations around Europe. Preferred weather scenarios and physical processes influencing the formation and dissipation of fog were also identified. A preliminary empirical model that predicts optical attenuations from the dynamic surface observations of radiation fog temperature and relative humidity has been proposed. This model is based on applying Gaussian fitting (using the non-linear least squares method) and employing the trust-region reflective Newton algorithm. The model can be further improved by incorporating the effects caused by microphysical processes like nucleation, condensation and turbulent mixing etc. The usefulness of this model lies in situations when no data other than temperature and relative humidity is available at a particular continental fog location. Furthermore, in order to study the relationship between fog density and the corresponding optical attenuations, a fog sensor device device was installed near the vicinity of the FSO link. From the surface observations of fog density, the corresponding liquid water content (LWC) of fog has been computed. LWC of fog seems to be a suitable parameter to predict optical attenuations besides droplet size distribution and visibility range that is related to a number of fog particles in the propagation path. The computed LWC is then compared with the measured optical attenuations and optical attenuations computed with the existing empirical models that relate visibility range to the corresponding LWC. It has been observed that fog density is in high correlation with the LWC and thus in turn to the recorded optical attenuations. Through simulations it has also

been observed that optical attenuations in different fog conditions are a strong function of the LWC, as the LWC increases so are the corresponding optical attenuations, and vice versa. The results presented suggest that fog density measurements carried out are an accurate representation of the fog intensity and the attenuation predictions generated through the computed LWC closely match the actual measured optical attenuations. The computations of optical attenuations from LWC is an additional useful tool, besides visibility range and particle size distributions, to predict and compare optical attenuations in the presence of different fog types. Moreover, there is not enough information available on the fog vertical structure and its representation in the form of different models can be useful in the design of future ground-space FSO links.

In order to characterize the free-space atmospheric channel for radiation fog conditions, three different techniques of modeling the size distribution of fog droplets, in terms of exponential and modified gamma distribution from fog attenuation measurements at infrared wave bands have been demonstrated in *chapter 5*. Two techniques were proposed; first one uses Marsaglia method (that considers rejection technique to compute three modified gamma distribution parameters), and the other technique uses Maitra and Gibbins technique (that considers standard iterative procedure to compute three distribution parameters of modified gamma distribution for Graz and Prague). While computing two parameters of the exponential distribution for radiation fog at locations Graz (Austria), and Prague (Czech Republic), the same Maitra and Gibbins procedure (that considers iterative procedure) was adopted. For the mentioned purposes two individual representative radiation fog events were analyzed, one at each location, mainly to indicate the effectiveness of the technique adopted to obtain near-instantaneous radiation fog droplets size distribution in terms of exponential as well as modified gamma distribution. Based on the performance analysis of the mentioned techniques, it was observed that Maitra and Gibbins technique is the better one in terms of simplicity and efficiency and yield excellent results as compared to Marsaglia method. The two parameters of exponential distribution computed for Graz and Prague are the first ever computed distribution parameters from the experimental results. From the analysis of the computed exponential distribution parameters, against the representative radiation fog events at Graz and Prague, it is found out that the agreement between measured attenuations and the calculated attenuations is good and comparable to the modified gamma distribution. The newly computed parameters of exponential distribution against the fog events at Graz and Prague are also in high correlation with the measured quantities (attenuations, LWC and the ratio between attenuation or ratio between attenuation and LWC), and hence provide an additional option of modeling the fog related attenuations using two parameter EDSD. In case of modified gamma distribution, the newly computed distribution parameters for Graz and Prague locations are consistent with the previously computed distribution parameters as available in the literature. Furthermore, it was demonstrated that the three MGDSD parameters computed for Prague and Graz are also in very strong correlation with the actual measured quantities like optical attenuations

and the LWC. Hence we may safely infer that the behavior of these parameters against the selected continental fog events, at both mentioned locations, is almost similar and they behave exactly alike. Therefore the same MGDSD model can be used at both locations. The usefulness of the Maitra and Gibbins techniques is that this techniques is quite handy in predicting optical attenuations at locations where measurement related to most of the microphysical parameters is not possible or feasible and thus only optical attenuations are measured.

6.2 Future Work

For a terrestrial FSO link at a particular site, the predictions of optical attenuations levels remain significantly inaccurate. This is because of the high variability in the fog microphysical characteristics and because too few reliable measurements are today available. Only a vast measurement campaign where the statistics of fog microphysical characteristics and the localized weather parameters along the path are simultaneously measured could state on the validity of certain theoretical results. If one further assumes that empirical propagation results keep on agreeing satisfactorily with future attenuations measurements for different locations in different fog environments, then it would be worth putting efforts in the implementation of a powerful simulation tool. Moreover, it would be worthwhile to extend the model that relates LWC with visibility range for ground-space optical links by considering meteorological data obtained from satellites.

Like for the weather forecast, one can imagine in the future the existence of an extensive dynamic database rendering in real-time the evolution of the different fog types and layers in the atmosphere. These fog related configurations would then serve as inputs to simulations of beam propagation. In turn, the results of these propagation simulations will permit the assessment of conceivable atmospheric links or the watch of the performance of the currently operating terrestrial optical links.

REFERENCES

[1] O. Bouchet, H. Sizun, C. Boisrobert, F. D. Fornel, and P. Favennec. *Free-Space Optics: Propagation and Communication*. ISTE, Great Britain, 2006.

[2] A. K. Majumdar and J. C. Ricklin. *Free-Space Laser Communications, Principles and Advantages*. Springer Science, LLC, 233 Spring Street, New York, NY 10013, USA, 2008.

[3] S. Glisic. *Advanced Wireless Communications 4G Technologies*. John Wiley and Sons Ltd, University of Oulu, Finland, 2004.

[4] H. Hemmati (Edited). *Near-Earth Laser Communications*. CRC Press, Taylor and Francis Group, 6000 Broken Sound Parkway NW, Suite 300, 2009.

[5] M. Gebhart. Optical Space Communication, Masters Thesis, Department of Space Science, Graz University, 2007.

[6] S. Bloom, E. Korevaar, J. Schuster, and H. Willebrand. Understanding the performance of free space optics (Invited paper). *Journal of Optical Networking*, 2(6):178–200, June 2003.

[7] C. A. Thompson, S. C. Wilks, J. M. Brase, R. A. Young, G. W. Johnson, and A. J. Ruggiero. Horizontal path laser communications employing mems adaptive optics correction. *SPIE Proceedings*, 4494:89–95, 2002.

[8] R. W. Burch. Technology needs for next-generation space-borne lasercom systems. *SPIE Proceedings*, 7199:719902.1–719902.9, 2009.

[9] E. Leitgeb, M. Gebhart, A. Truppe, U. Birnbacher, P. Schrotter, and A. Merdonig. Hybrid wireless networks for civil-military-cooperation (cimic) and disaster management. *SPIE Proceedings*, 5614:139–150, 2004.

[10] M. Toyoshima. Trends in satellite communications and the role of optical free-space communications. *Journal of Optical Networking*, 4 (6):300–311, 2005.

[11] Tzung-Hsien Ho, S. Trisno, A. Desai, J. Llorca, S. D. Milner, and C. C. Davis. Performance and analysis of reconfigurable hybrid fso/rf wireless networks. *SPIE Proceedings*, 5712:119–130, 2005.

[12] K. W. Fischer, M. R. Witiw, J. A. Baars, and T. R. Oke. Atmospheric laser communication: New challenges for applied meteorology. *Bulletin of the American Meteorological Society*, 85(5):725–732, May 2004.

[13] D. Giggenbach, J. Horwath, and M. Knapek. Optical data downlinks from earth observation platforms. *SPIE Proceedings*, 7199:719903.1–719903.14, 2009.

[14] T. Tolker-Nielsen and G. Oppenhaeuser. In orbit test result of an operational optical intersatellite link between artemis and spot4, silex. *SPIE Proceedings*, 4635:1–15, 2002.

[15] M. Al Naboulsi, H. Sizun, F. de Fornel, M. Gebhart, and E. Leitgeb. Availability prediction for free space optical communication systems from local climate visibility data. *COST 270 Short Term Scientific Mission Report*, pages 1–30, 2004.

[16] A. Pavelchek, R. Trissel, J. Plante, and S. Umbrasas. Long wave infrared (10 micron) free space optical communication system. *SPIE Proceedings*, 5160:247–252, 2004.

[17] A. Soibel, M. Wright, W. Farr, S. Keo, C. Hill, R. Q. Yang, and H. C. Liu. Mid-infrared interband cascade lasers for free-space laser communication. *SPIE Proceedings*, 7199:71990E.1–71990E.8, 2009.

[18] Y. Arimoto. Compact free-space optical terminal for multi-gigabit signal transmissions with a single mode fiber. *SPIE Proceedings*, 7199:719908.1–719908.9, 2009.

[19] ISI Satcom Initiative. `http://www.isi-initiative.org`. website visited in Sept. 2009.

[20] E. Korevaar, I. Kim, and B. McArthur. Debunking the recurring myth of a magic wavelength for free-space optics. *SPIE Proceedings*, 4873:155–166, 2002.

[21] E. Leitgeb, M. Gebhart, U. Birnbacher, W. Kogler, and P. Schrotter. High availability of hybrid wireless networks. *SPIE Proceedings*, 5465:238–249, 2004.

[22] C. Grigorov. Evaluation of coarse- and fine-pointing methods for optical Free Space Communication, 2007.

[23] N. Perlot, D. Giggenbach, H. Henniger, J. Horwath, M. Knapek, and K. Zettl. Measurements of the beam-wave fluctuations over a 142-km atmospheric path. *SPIE Proceedings*, 6304:63041O.1–63041O.10, 2006.

[24] N. Perlot. *Characterization of Signal Fluctuations in Optical Communications with Intensity Modulation and Direct Detection through the Turbulent Atmospheric Channel*. PhD thesis, School of Electronique, Université de Valenciennes, 2005.

[25] F. David, D. Giggenbach, R. Landrock, K. Pribil, E. Fischer, R. Buschner, and D. Blaschke. Preliminary results of a 61km ground-to-ground optical im/dd data transmission experiment. *SPIE Proceedings*, 4635:16–23, 2002.

[26] B. Flecker, M. Gebhart, E. Leitgeb, S. Sheikh Muhammad, and C. Chlestil. Results of attenuation-measurements for optical wireless channels under dense fog conditions regarding different wavelengths. *SPIE Proceedings*, 6303:63030P.1–63030P.11, 2006.

[27] M. Gebhart, E. Leitgeb, S. Sheikh Muhammad, B. Flecker, C. Chlestil, M. Al Naboulsi, F. de Fornel, and H. Sizun. Measurement of light attenuation in dense fog conditions for fso applications. *SPIE Proceedings*, 5891:58910K.1–58910K.12, 2005.

[28] C. Capsoni and R. Nebuloni. Effect of rain on free space optics. pages PR5.11–PR5.17, 2007.

[29] R. Nebuloni and C. Capsoni. Laser attenuation by falling snow. *Proceedings CSNDSP 2008*, pages 265–269.

[30] H. Hemmati. *Deep Space Optical Communications*. Wiley-Interscience, Jet Propulsion Laboratory California Institute of Technology, 2006.

[31] J. A. Baars, M. Witiw, A. Al-Habash, and K. W. Fischer. The effects of low clouds on terrestrial free space optics availability. *SPIE Proceedings*, 4635:171–178, 2002.

[32] F. Moll and M. Knapek. Wavelength Selection Criteria and Link Availability due to Cloud Coverage Statistics and Attenuation affecting Satellite, Aerial, and Downlink Scenarios. *SPIE Proceedings: Free-Space Laser Communications VII*, 6709(670916):670916.1–670916.12, 2007.

[33] S. Arnon and N. S. Kopeika. Adaptive suboptimum detection of an optical pulse-position-modulation signal with a detection matrix and centroid tracking. *Journal of Optical society of America*, 15(2):511–515, February 1998.

[34] M. S. Awan, E. Leitgeb, F. Nadeem, and C. Capsoni. A new method of predicting continental fog attenuations for terrestrial optical wireless link. *NGMAST 2009*, 2009.

[35] S. A. Dvoretsky, V. S. Varavin, N. N. Mikhailov, Y. G. Sidorov, T. I. Zakharyash, V. V. Vasiliev, V. N. Ovsyuk, G. V. Chekanova, M. S. Nikitin, I. Y. Lartsev, and A. L. Aseev. Mwir and lwir detectors based on hgcdte/cdznte/gaas heterostructures. *SPIE Proceedings*, 5694:59640A.1–59640A.12, 2005.

[36] F. Courvoisier. Ultraintense light filaments transmitted through clouds. *Applied Physics Letters*, 83(2):213–215, 2003.

[37] M. Achour. Simulating atmospheric free-space optical propagation: Part i, rainfall attenuation. *SPIE Proceedings*, 4635:192–201, 2002.

[38] M. Achour. Free-space optics wavelength selection: 10 micron versus shorter wavelengths. *SPIE Proceedings*, 5160:234–246, 2004.

[39] D. A. Rockwell and G. S. Mecherle. Wavelength selection for optical wireless communications systems. *SPIE Proceedings*, 4530:27–35, 2001.

[40] I. I. Kim and E. Korevaar. Availability of free space optics (fso) and hybrid fso/rf systems. *SPIE Proceedings*, 4530:84–95, 2001.

[41] J. Llorca, A. Desai, E. Baskaran, S. Milner, and C. Davis. Optimizing performance of hybrid fso/rf networks in realistic dynamic scenarios. *SPIE Proceedings*, 5892:52–60, 2005.

[42] A. Sana, H. Erkan, S. Ahmed, and M. A. Ali. Design and performance of hybrid fso/rf architecture for next generation broadband access networks. *SPIE Proceedings*, 6390:63900A.1–63900A.8, 2006.

[43] A. Geiger, C. Ting, E. J. Burlbaw, J. Ding, and Shinn-Der Sheu. 3.5 micron free-space laser communications. *SPIE Proceedings*, 6304:63041L.1–63041L.9, 2006.

[44] F. Fidler. *Optical Communications from High-Altitude Platforms*. PhD thesis, Fakultat fur Elektrotechnik und Informationstechnik, Technischen Universitat Wien, 2007.

[45] V. V. Nikulin, R. M. Khandekar, and J. Sofka. Agile acousto-optic tracking system for freespace optical communications. *SPIE Proceedings, Optical Engineering*, 47(6):064301.1–064301.7, 2008.

[46] Y. Takayama, T. Jono, M. Toyoshima, H. Kunimori, D. Giggenbach, N. Perlot, M. Knapek, K. Shiratama, J. Abe, and K. Arai. Tracking and pointing characteristics of oicets optical terminal in communication demonstrations with ground stations. *SPIE Proceedings*, 6457:645707.1–645707.9, 2007.

[47] Z. Hajjarian and M. Kavehrad. Using mimo transmissions in free space optical communications in presence of clouds and turbulence. *SPIE Proceedings*, 7199:71990V.1–71990V.12, 2009.

[48] H. Henniger. Packet-layer forward error correction coding for fading mitigation. *SPIE Proceedings*, 6304:630419.1–630419.8, 2006.

[49] B. Moision and J. Hamkins. Constrained coding for the deep-space optical channel. *SPIE Proceedings*, 4635:127–137, 2002.

[50] F. Nadeem, V. Kvicera, M. S. Awan, E. Leitgeb, S. Sheikh Muhammad, and G. Kandus. Weather effects on hybrid fso/rf communication link. *IEEE JSAC*, 27(9):1687–1697, 2009.

[51] R. M. Sova, J. E. Sluz, D. W. Young, J. C. Juarez, A. Dwivedi, N. M. Demidovich, J. E. Graves, M. Northcott, J. Douglass, J. Phillips, D. Driver, Andy McClarin, and D. Abelson. 80 gb/s free-space optical communication demonstration between

an aerostat and a ground terminal. *SPIE Proceedings*, 6304:630414.1–630414.10, 2006.

[52] H. Hemmati and Y. Chen. Compensation of large-diameter optical system aberrations with spatial light modulators and deformable mirrors. *SPIE Proceedings*, 7199:71990D.1–71990D.7, 2009.

[53] G. Baister and P. V. Gatenby. Pointing acquisitionand tracking for optical space communications. 6(6):271–280, December 1994.

[54] S. Betti, V. Carrozzo, and E. Duca. Over-Stratospheric-Altitude Optical Free Space Links : System Performance Evaluation. pages 170–173, 2007.

[55] U. Ketprom, S. Jaruwatanadilok, Y. Kuga, A. Ishimaru, and J. A. Ritcey. Channel modeling for optical wireless communication through dense fog. *Journal of Optical Networking*, 4(6):291–299, June 2005.

[56] F. G. Smith. *Atmospheric Propagation of Radiation Volume 2: The infrared and electro-optical systems handbook*. Infrared Information Analysis Center and SPIE Optical Engineering Press, Washington, 1993.

[57] S. Hranilovic. *Spectrally Efficient Signalling for Wireless Optical Intensity Channels*. PhD thesis, Department of Electrical and Computer Engineering, University of Toronto, 2003.

[58] CCIR Recommendations and Reports. Attenuation of the visible and infrared radiation. pages 1–11, 1986.

[59] M. Aharonovich and S. Arnon. Performance improvement of optical wireless communication through fog with a decision feedback equalizer. *JOSA A*, 22(8):47–54, August 2005.

[60] V. V. Ragulsky and V. G. Sidorovich. On the availability of a free-space optical communication link operating under various atmospheric conditions. *SPIE Proceedings*, 4530:96–103, 2001.

[61] V. Sidorovich. Optical counter-measures and security of free-space optical communication links. *SPIE Proceedings*, 5614:97–108, 2004.

[62] H. C. van de Hulst. *Light Scattering by Small Particles*. Dover Publications, Leiden Observatory, 1981.

[63] C. F. Bohren and D. R. Huffman. *Absorption and Scattering of Light by Small Particles*. Wiley-Interscience, first edition, 1998.

[64] L. Castanet. *Influence of the Variability of the Propagation Channel on Mobile, Fixed Multimedia and Optical Satellite Communications*. Shaker Verlag GmbH., 2008.

[65] X. Zhu, J. M. Kahn, and J. Wang. Mitigation of Turbulence-Induced Scintillation Noise in Free-Space Optical Links using Temporal-Domain Detection Techniques. *IEEE Photonics Technology Letters*, 15(4):623–625, April 2003.

[66] X. Zhu and J. M. Kahn. Markov Chain Model in Maximum-Likelihood Sequence Detection for Free-Space Optical Communication Through Atmospheric Turbulence Channels. *IEEE Transactions on Communications*, 51(3):509–516, March 2003.

[67] M. A. Al-Habash and L. C. Andrews. New mathematical model for the intensity pdf of a laser beam propagating through turbulent media. *SPIE Proceedings*, 3706:103–110, 1999.

[68] A. Al-Habash, L. C. Andrews, and R. L. Phillips. Mathematical model for the irradiance probability density function of a laser beam propagating through turbulent media. *SPIE Proceedings*, 40(8):1554Ű1562, 2001.

[69] R. L. Philips L. C. Andrews and C. Y. Hopen. *Laser Beam Scintillation with Applications*. SPIE Press, SPIE Press, Bellingham Washington USA, 2001.

[70] R. L. Philips L. C. Andrews. *Laser Beam Propagation through Random Media*. SPIE Press, SPIE Press, Bellingham Washington USA, first edition, 1998.

[71] W. Leeb. Communications to and from haps Űwith laser beams. *COST 297 HAPCOS Meeting*, 2008.

[72] S. Sheikh Muhammad. *Investigations in Modulation and Coding for Terrestrial Free Space Optical Links*. PhD thesis, IBK TU Graz, Infeldgasse 12, Graz, Austria, 2007.

[73] E. Leitgeb, M. Gebhart, P. Fasser, J. Bregenzer, and J. Tanczos. Impact of atmospheric effects in free space optics transmission systems. *SPIE Proceedings*, 4976:86–97, 2003.

[74] J. A. Anguita, M. A. Neifeld, and B. V. Vasic. Multi-beam space-time coded systems for optical atmospheric channels. *SPIE Proceedings*, 6304:63041B.1–63041B.9, 2006.

[75] K. Kiasaleh. Hybrid arq receiver for packet communications over free-space optical channels. *SPIE Proceedings*, 6304:630407.1–630407.12, 2006.

[76] W. Stallings. *Wireless Communications and Networks*. Prentice Hall, Pearson Education International, Upper Saddle River, NJ USA, second edition, 2005.

[77] J. Horwath. Optical free-space communication under atmospheric impacts. *Seminar presentation at TU Graz*, 2005.

[78] V. G. Sidorovich. Solar background effects in wireless optical communications. *SPIE Proceedings*, 4873:133–142, 2002.

[79] Solar Spectrum. `http://org.ntnu.no`. website visited in Dec. 2009.

[80] S. Sheikh Muhammad, B. Flecker, E. Leitgeb, and M. Gebhart. Characterization of fog attenuation in terrestrial free space optical links. *Journal of Optical Engineering*, 46(6):066001 1–10, June 2007.

[81] H. R. Anderson. A ray tracing propagation model for digital broadcast systems in urban areas. *IEEE Transactions on Broadcasting*, 39(3):309–317, 1993.

[82] N. J. Davis K. S. Schaubach and T. S. Rappaport. A ray-tracing method of predicting path loss and delay spread in microcell environments. *Proceeding of the 1992 Vehicular Technology Society Conference*, 1992.

[83] Z. Kolka, O. Wilfert, R. Kvicala, and O. Fiser. Complex model of terrestrial fso links. *SPIE Proceedings*, 6709:67091J.1–67091J.8, 2007.

[84] M. Z. Jacobson. *Fundamentals of Atmospheric Modeling*. Cambridge University Press, The Edinburgh Building, Cambridge CB2 2RU, UK, 2nd edition edition, 2005.

[85] R. M. Pierce, J. Ramaprasad, and E. Eisenberg. Optical attenuation in fog and clouds. *SPIE Proceedings*, 4530:58–71, 2001.

[86] P. W. Kruse and et al. *Elements of Infrared Technology: Generation, transmission and detection*. J. Wiley and sons, New York, 1962.

[87] M. Al Naboulsi, H. Sizun, and F. D. Fornel. Fog attenuation prediction for optical and infrared waves. *SPIE Proceedings*, 43 (2):319–329, 2004.

[88] P. Bataille. *Analyse du comportement d'un systeme de telecommunications optique fonctionnant a 0,83 ţm dans la basse atmosphere*. PhD thesis, University of Rennes 1, 1992.

[89] S. Sheikh Muhammad, P. Kohldorfer, and E. Leitgeb. Channel Modeling for Terrestrial Free Space Optical Links. *ICTON 2005*, 2005.

[90] E. J. McCartney. *Optics of the Atmosphere*. John Wiley, New York, 1977.

[91] E. Brookner. Atmospheric propagation and communication channel model for laser wavelengths. *IEEE Transactions on Communication Technology*, 1970.

[92] M. Al Naboulsi, F. de Fornel, H. Sizun, M. Gebhart, E. Leitgeb, S. Sheikh Muhammad, B. Flecker, and C. Chlestil. Measured and predicted light attenuation in dense coastal upslope fog at 650, 850, and 950 nm for free-space optics applications. *SPIE Proceedings, Optical Engineering*, 47(3):036001.1–036001.14, 2008.

[93] B. Flecker, E. Leitgeb, M. Gebhart, S. Sheikh Muhammad, C. Chlestil, E. Duca, and V. Corrozzo. Measurement of Light Attenuation in Fog and Snow Conditions for Terrestrial FSO Links. 2006.

[94] V. Kvicera, M. Grabner, and O. Fiser. Visibility and attenuation due to hydrometeors at 850 nm measured on an 850 m path. pages 270–272.

[95] P. S. Ray. Broadband complex refractive indices of ice and water. *Applied Optics*, 11(8):1836–1844, August 1972.

[96] M. S. Awan, R. Nebuloni, C. Capsoni, L. Csurgai-Horvath, S. Sheikh Muhammad, E. Leitgeb, F. Nadeem, and M. S. Khan. Prediction of drop size distribution parameters for optical wireless communications through moderate continental fog. *International Journal on Satellite Communications and Networks*, 28(05), 2010.

[97] T. S. Chu and D. C. Hogg. Effects of precipiation on propagation at 0.63, 6.5, and 10.6 microns. *Bell system technical journal*, 47(5):723–769, May-June 1968.

[98] S. Arnon, D. Sadot, and N. S. Kopeika. Simple mathematical models for temporal, spatial, angular, and attenuation characteristics of light propagating through the atmosphere for space optical communication: Monte carlo simulations. *Journal of Modern Optics*, 41(10):1955–1972, 1994.

[99] E. P. Shettle. Models of Aerosols, Clouds, and Precipitation for Atmospheric Propagation Studies. *AGARD conference Proceedings*, 454(15), 1989.

[100] D. Harris. The Attenuation of Electromagnetic Waves Due to Atmospheric Fog. *International Journal of Infrared and Millimeter Waves*, 16(6):1091–1108, 1995.

[101] M. S. Awan, E. Leitgeb, S. Sheikh Muhammad, Marzuki, F. Nadeem, M. Saeed Khan, and C. Capsoni. Distribution function for continental and maritime fog environments for optical wireless communication. *CSNDSP 2008*, 2009.

[102] H. Weichel. Laser beam propagation in the atmosphere. *SPIE Proceedings, SPIE Press, Bellingham, Washington USA*, TT3, 1990.

[103] T. H. Carbonneau and D. R. Wisely. Opportunities and challenges for optical wireless: the competitive advantage of free space telecommunications links in today's crowded marketplace. *SPIE Proceedings*, 3232:119–128, 1998.

[104] G. S. Mecherle. Mitigation of atmospheric effects on terrestrial free space optical communication systems. *SPIE Proceedings*, 5338:102–118, 2004.

[105] P. F. Szajowski, G. Nykolak, J. J. Auborn, H. M. Presby, G. E. Tourgee, E. Korevaar, J. Schuster, and I. I. Kim. 2.4 km free space optical communication 1550 nm transmission link operating at 2.5 gb/s-experimental results. *SPIE Proceedings, Optical wireless communications*, 3532:29–40, 1998.

[106] I. Kim, B. McArthur, and E. Korevaar. Comparison of laser beam propagation at 785 nm and 1550 nm in fog and haze for optical wireless communications. *SPIE Proceedings*, 4214, 2001.

[107] R. Nebuloni. Empirical relationships between extinction coefficient and visibility in fog. *Applied Optics*, 44(18):3795–3804, June 2005.

[108] I. Gultepe and J. A. Milbrandt. Probabilistic parmeterization of visibility using observations of rain precipitation rate, relative humidity and visibility. *Journal of Applied Meteorology and Climatology*, pages 1–11, 2009.

[109] M. S. Awan, C. Capsoni, O. Koudelka, E. Leitgeb, F. Nadeem, and M. S. Khan. Diurnal variations based fog attenuations analysis of an optical wireless link. *IEEE Photonics Global 2008*, 2008.

[110] M. S. Awan, C. Capsoni, O. Koudelka, E. Leitgeb, F. Nadeem, and M. S. Khan. Evaluation of fog attenuations results for optical wireless links in free space. *IWSSC 2008*, 2008.

[111] C. Capsoni and R. Nebuloni. Optical Wave Propagation through the Atmosphere in a Urban Area. pages 335–338, 2006.

[112] R. M. Tardif. *Characterizing Fog and the Physical Mechanisms Leading to its Formation during Precipitation in a Coastal Area of the Northeastern United States*. PhD thesis, Department of Atmospheric and Oceanic Sciences, University of Colorado, 2007.

[113] ITU-R P.837-3. Characteristics of precipitation for propagation modelling. *International Telecommunication Union, Recommendation ITU-R P.837-3, Geneva, Switzerland*, 2001.

[114] D. Atlas. Shorter contribution optical extinction by rainfall. *Journal of Meteorology*, 10, 1953.

[115] T. Oguchi. Electromagnetic wave propagation and scattering in rain and other hydrometeors. *Proceedings of the IEEE*, 71(9):1029–1079, Septmber 1983.

[116] J. Joss, J. C. Thams, and A. Waldvogel (editors.). The variation of raindrop size distribution at locarno. *Proceedings of international conference on cloud physics, Toronto, Canada*, 1968.

[117] M. S. Awan, Marzuki, E. Leitgeb, F. Nadeem, M. S. Khan, and C. Capsoni. Weather effects impact on the optical pulse propagation in free space. *VTC 2009-Spring*, 2009.

[118] M. S. Awan, E. Leitgeb, R. Nebuloni, F. Nadeem, and M. S. Khan. Optical wireless ground- link attenuation statistics of fog and snow conditions. *WOCN 2009*, 2009.

[119] H. W. OŠBrien. Visibility and light attenuation in falling snow. *Journal of Applied Meteorology*, 9:671–683, 1970.

[120] M. S. Awan, L. Csugai-Horvath, R. Nebuloni, P. Brandl, F. Nadeem, and E. Leitgeb. Transmission of high data rate optical signals in fog and snow conditions. *Wireless Vitae 2009*, 2009.

[121] R. G. Eldrige. Mist - the transition from haze to fog. *Bull. Am. Meteorological Society Journal*, 50, 1969.

[122] I. Gultepe, R. Tardif, S. C. Michaelides, J. Cermak, A. Bott, J. Bendix, M. D. Müller, M. Pagowski, B. Hansen, G. Toth G. Ellrod, W. Jacobs, and S. G. Cober. Fog research: A review of past achievements and future perspectives. *Pure Applied Geophysics*, 164:1121–1159, 2007.

[123] D. Kedar and S. Arnon. Optical Wireless Communication Through Fog in the Presence of Pointing Errors. *Applied Optics*, 42(24):4946–4954, August 2003.

[124] J. E. Jiusto. *Fog structure. Clouds, Their Formation, Optical Properties, and Effects*. Academic Press, P. V. Hobbs and A. Deepak, Eds., 1981.

[125] `http://www.rap.ucar.edu`. website visited in Jan. 2008.

[126] F. Tampieri and C. Tomasi. Size distribution models of fog and cloud droplets and their volume extinction coefficients at visible and infrared wavelengths. *Pure and Applied Geophysics*, 114(4):571–586, July 1976.

[127] C. Tomasi and F. Tampieri. Features of the proportionality coefficient in the relationship between visibility and liquid water content in haze and fog. *Atmosphere*, 14(2):61–76, 1976.

[128] J. Bendix. A satellite-based climatology of fog and low-level stratus in Germany and adjacent areas.

[129] R. G. Knollenberg. Comparative Liquid Water Content Measurements of Conventional Instruments with an Optical Array Spectrometer. *Journal of Applied Meteorology*, 11(3):501–508, 1972.

[130] M. S. Awan, L. Csurgai-Horvath, S. Sheikh Muhammad, E. Leitgeb, F. Nadeem, and M. S. Khan. Characterization of fog and snow attenuations for free-space optical propagation. *Journal of Communications*, 4(8):533–545, 2009.

[131] M. Achour. Simulating atmospheric free-space optical propagation, part ii: Haze, fog and low clouds attenuations. *SPIE Proceedings*, 4873:1–12, 2002.

[132] Sheikh S. Muhammad, M. S. Awan, and A. Rehman. Pdf estimation and liquid water content based attenuation modeling for fog in terrestrial fso links. *Radio Engineering 2010*, 18(01), 2010.

[133] ITU-R P.840-3. Attenuation due to clouds and fog. *International Telecommunication Union, Recommendation ITU-R P.840-3, Geneva, Switzerland*, 1999.

[134] J. M. Wallace and P. V. Hobbs. *Atmospheric Science: An Introductory Survey*. Elsevier Inc., U.K, 2nd edition edition, 2006.

[135] I. Gultepe, M. D. Muller, and Z. Boybeyi. A new warm fog parameterization scheme for numerical weather prediction models. *Journal of Applied Meteorology*, 45:1469–1480, 2006.

[136] I. Gultepe and G. A. Isaac. A natural fog dissipation process in a marine fog event during fram. *Ninth WMO Scientific Conference on Weather Modification*, Antalya, Turkey, 22- 24 October 2007, 2007.

[137] L. Csurgai-Horwath and J. Bito. Fog attenuation on v band terrestrial radio and a low-cost measurement setup. *accepted for presentation at Future Network and MobileSummit 2010, 16 - 18 June 2010, Florence - Italy*, 2010.

[138] G. Marsaglia and W. W. Tsang. A simple method for generating gamma variables. *ACM transactions on mathematical software*, 26(3):363–372, September 2000.

[139] A. Maitra and C. J. Gibbins. Modeling of raindrop size distributions from mutliwavelength rain attenuation measurements. *Radio Science*, 34(3):657–666, 1999.

[140] A. Papoulis and S. U. Pillai. *Probability, Random variables and Stochastic Processes*. Tata McGraw-Hill, Polytechnic University, fourth edition, 2002.

[141] D. A. Stewart and O. M. Essenwanger. A survey of fog and related optical propagation characteristics. *Review of Geophysics and Space Physics*, 20(3):481–495, August 1982.

[142] C. Tomasi and F. Tampieri. Infrared radiation extinction sensitivity to the modified gamma distribution parameters for haze and fog droplet polydispersions. *Applied Optics*, 15(11):2906–2912, 1976.

[143] J. A. Garland. Some fog droplet size distributions obtained by an impaction method. *Quarterly Journal of the Royal Meteorological Society*, 97(414):483–494, 1971.

[144] M. S. Awan, E. Leitgeb, Marzuki, and T. Plank. A study of fog characteristics using free-space optical wireless links (invited paper). *Radio Engineering Journal*, 2010.

[145] J. S. Marshall and W. M. Palmer. The distribution of raindrops with size. *Journal of Meteorology*, 5:165–166, 1948.

[146] C. W. Ulbrich. Natural variations in the analytical form of the raindrop size distribution. *Journal of Applied Meteorology*, 22:1764–1775, 1983.

[147] M. S. Awan, Marzuki, E. Leitgeb, and M. S. Khan. Optical attenuation modeling of continental fog using exponential distribution. *CSNDSP 2010, Newcastle Upon Tyne, UK*, 21-23 July, 2010.

[148] A. Harris and T. A. Giuma. Minimization of acquisition time in a wavelength diversified fso link between mobile platforms. *SPIE Proceedings*, 6551:655108.1–655108.10, 2007.

[149] H. Hemmati. Optical systems for free-space laser communications. *SPIE Proceedings*, 5173:64–68, 2003.

[150] A. Alonso, M. Reyes, and Z. Sodnik. Performance of satellite-to-ground communications link between artemis and the optical ground station. *SPIE Proceedings*, 5572:372–383, 2004.

[151] OGS-Artemis Link. `http://www.esa.int`. website visited in Sept. 2009.

[152] W. Dan Williams, M. Collins, D. M. Boroson, J. Lesh, A. Biswas, R. Orr, L. Schuchman, and O. S. Sands. Rf and optical communications: A comparison of high data rate returns from deep space in the 2020 time frame. *NASA/TMŰ2007-214459*, pages 1–14, 2007.

[153] OCTL. `http://www.jpl.nasa.gov`. website visited in Sept. 2009.

[154] G. G. Ortiz, S. Lee, S. Monacos, M. Wright, and A. Biswas. Design and development of a robust atp subsystem for the altair uav-to-ground lasercomm 2.5 gbps demonstration. *SPIE Proceedings*, 4975:103–114, 2003.

[155] H. Hemmati. Free-space optical communications at jpl/nasa. *Presentation*, 2009.

[156] J. Horwath, M. Knapek, B. Epple, M. Brechtelsbauer, and B. Wilkerson. Broadband backhaul communication for stratospheric platforms: The stratospheric optical payload experiment (stropex). *SPIE Proceedings*, 6304:63041N.1–63041N.12, 2006.

[157] J. Horwath. Optical free-space communication under atmospheric impacts. *Master Thesis Presentation at TU Graz*, 2005.

[158] V. Cazaubiel et al. Le terminal optique aeroporte sur lola. *Proc. of OPTRO 2005 Conference, Paris*, 2005.

[159] LOLA. `http://www.astrium.eads.net`. website visited in Sept. 2009.

[160] N. Perlot et al. Results of the optical downlink experiment kiodo from oicets satellite to optical ground station oberpfaffenhofen (ogsop). *SPIE Proceedings*, 6457:645704.1–645704.8, 2007.

[161] D. Giggenbach. Mobile optical communication projects at dlr and prospects on future developments. *"BroadSky Workshop", in conjunction with the 13th Ka and Broadband Communications Conference, 24.09.2007, Turin, Italy*, 2007.

[162] J. Horwath et al. Coherent transmission feasibility analysis. *Proc. Free-Space Laser Communication Technologies XVII, San Jose CA, 25-26*, 2005.

[163] TerraSAR-X LCT-ATM Laser Link. `http://www.tesat.de`. website visited in Sept. 2009.

[164] G. Baister, K. Kudielka, T. Dreischer, and M. Tuchler. Results from the dolce (deep space optical link communications experiment) project. *SPIE Proceedings*, 7199:71990B.1–71990B.9, 2009.

[165] Lagrangian points. `http://de.wikipedia.org/wiki/Lagrange-Punkt`. website visited in Sept. 2009.

[166] ROSA Final Presentation. Rf-optical system study for aurora. *ESA Contract No. 20371/07/NL/EK*, 2008.

[167] ksdensity function. `http://www.mathworks.com`. website visited on May. 2010.

APPENDIX A: PUBLICATIONS

The work presented in this thesis has been published, in part, in the following journals and refereed conference proceedings.

As First Author

1. ***M. S. Awan***, E. Leitgeb and et al., *"Analysis of Free Space Optical Links under Moderate Fog Conditions in Graz and Milan and Behaviour of the Drop Size Distribution Parameters"*, presented at 2nd SatNEx International Propagation Workshop 2008, Oberpfaffenhofen, Munich, Germany, 17-18 April 2008.

2. ***M. S. Awan***, Marzuki, et al. *"Distribution Function for Continental and Maritime Fog Environments for Optical Wireless Communication"*, IEEE CSNDSP 2008, pp. 260-264, Graz, Austria, 23-25 July 2008.

3. ***M. S. Awan***, C. Capsoni, E. Leitgeb, et al. *"FSO-Relevant New Measurement Results under Moderate Continental Fog Conditions at Graz and Milan"*, IEEE ASMS 2008, pp. 111-115, Bologna, Italy, 26-28 August 2008.

4. ***M. S. Awan***, E. Leitgeb, C. Capsoni, et al. *"Attenuation Analysis for Optical Wireless Link Measurements under Moderate Continental Fog Conditions at Milan and Graz"*, IEEE VTC 2008-Fall, pp. 1-5, Calgary, Canada, 21-24 September 2008.

5. ***M. S. Awan***, E. Leitgeb, C. Capsoni, et al. *"Evaluation of Fog Attenuations Results for Optical Wireless Links in Free Space"*, IEEE IWSSC 2008, pp. 112-116, Toulouse, France, 1-3 October 2008.

6. ***M. S. Awan***, C. Capsoni, O. Koudelka, E. Leitgeb, F. Nadeem, M. S. Khan, *"Diurnal Variations Based Fog Attenuations Analysis of an Optical Wireless Link"*, IEEE Photonics Global 2008, pp. 1 - 4, 8-11th December 2008, Singapore.

7. ***M. S. Awan***, Marzuki, E. Leitgeb, F. Nadeem, M. S. Khan, C. Capsoni, *"Weather Effects Impact on the Optical Pulse Propagation in Free Space"*, IEEE VTC 2009-Spring, pp. 1-5, 26-29 April 2009, Barcelona, Spain.

8. ***M. S. Awan***, E. Leitgeb, R. Nebuloni, F. Nadeem, M. S. Khan, *"Optical Wireless Ground- Link Attenuation Statistics of Fog and Snow Conditions"*, IEEE WOCN 2009, pp. 1-5, April 28 -30, 2009, Cairo, Egypt.

9. ***M. S. Awan***, L. Csugai-Horvath, R. Nebuloni, P. Brandl, F. Nadeem, E. Leitgeb, *"Transmission of high data rate optical signals in fog and snow conditions"*, IEEE Wireless Vitae 2009, pp. 702-706, 17-20 May, 2009, Aalborg, Denmark.

10. ***M. S. Awan***, E. Leitgeb, *"Results in an Optical Wireless Ground link Experiment in Continental Fog and Dry Snow Conditions"*, IEEE ConTel 2009, pp. 45-49, 8-10 June 2009, Zagreb, Croatia.

11. ***M. S. Awan***, Marzuki, E. Leitgeb, B. Hillbrand, F. Nadeem, M. S. Khan, *"Cloud Attenuations for Free-Space Optical Links"*, IEEE IWSSC 2009, 10-11 September 2009, Sienna, Italy.

12. ***M. S. Awan***, E. Leitgeb, F. Nadeem, C. Capsoni, *"A new method of predicting continental fog attenuations for terrestrial optical wireless link"*, IEEE NGMAST 2009, pp. 245-250, 15-18 September 2009, Cardiff, UK.

13. ***M. S. Awan***, E. Leitgeb, M. Loeschnig, F. Nadeem, C. Capsoni, *"Spatial and time variability of fog attenuations for optical wireless links in the troposphere"*, IEEE VTC 2009-Fall, September 20 - 23, 2009, Anchorage (Alaska), USA.

14. ***M. S. Awan***, et al., *"Characterization of Fog and Snow attenuations for Free-Space Optical Propagation"*, Journal of Communications (JCM), VOL. 4, NO. 8, pp. 533-545, September 2009.

15. ***M. S. Awan***, Marzuki, E. Leitgeb, M. S. Khan, *"Optical Attenuation Modeling of Continental Fog using Exponential Distribution"*, accepted to CSNDSP 2010, July 21 - 23, 2010, Newcastle, UK.

16. ***M. S. Awan***, R. Nebuloni, C. Capsoni, L. Csurgai-Horwath, S. Sheikh Muhammad, E. Leitgeb, F. Nadeem, M. S. Khan, *"Prediction of Drop Size Distribution Parameters for Optical Wireless Communications through Moderate Continental Fog"*, International Journal on Satellite Communications and Networks (IJSCN), pp. , Vol. 28, No. 5, August 2010.

17. ***M. S. Awan***, E. Leitgeb, Marzuki, T. Plank, *"A Study of Fog Characteristics using Free-Space Optical Wireless Links (Invited Paper)"*, Radio Engineering 2010 Journal, pp. - , Vol.19 , No. 02, 2010.

18. Sheikh S. Muhammad, ***M. S. Awan***, A. Rehman, "PDF Estimation and Liquid Water

Content Based attenuation modeling for Fog in Terrestrial FSO links", Radio Engineering Journal, pp. -, Vol. 19, No. 02, June 2010.

19. ***M. S. Awan***, E. Leitgeb "Evaluation of Weather parameters for Ground-Space Optical Links", Input document to COST Action IC0802 WG3 Propagation tools and data for integrated Telecommunication, Navigation and Earth Observation systems, 26-28 April 2010 NTUA, Athens, Greece.

As Co-author

1. E. Leitgeb, ***M. S. Awan***, T. Plank, N. Perlot, et. al, *"Investigations on Free-Space Optical Links within SatNEx II"*, (SatNEx II Invited paper) IEEE Eucap 2009, pp. 1707-1711, 23-27 March 2009, Berlin, Germany.

2. E. Leitgeb, ***M. S. Awan***, P. Brandl, T. Plank, C. Capsoni, R. Nebuloni, T. Javornik, G. Kandus, S. Sheikh Muhammad, F. Ghassemlooy, M. Löschnigg, F. Nadeem, *"Current Optical Technologies for Wireless Access"*, (Invited paper) IEEE ConTel 2009, pp. 7-17, 8-10 June 2009, Zagreb, Croatia.

3. E. Leitgeb, P. Brandl, T. Plank, M. Löschnigg, F. Ozek, ***M. S. Awan***, M. Wittig, *"Reliable Optical Wireless Links used as Feeder Links between Earth and Satellite"*, Invited Paper, IEEE ICTON 2009, pp. 1-7, June 28 - July 2, 2009, Island of Sao Miguel, Azores, Portugal. (Invited paper)

4. W. Popoola, F. Ghassemloy, ***M. S. Awan***, E. Leitgeb, *"Atmospheric channel effects on terrestrial laser communication"*, (invited paper) at 3rd IEEE International Conference on Electronics, Computers and Artificial Intelligence, (ECAI 2009), pp. 17-23, Jul 2 - 5, 2009, Pitesti, Romania. (IEEE, best paper award)

5. F. Nadeem, E. Leitgeb, M. S. Khan, ***M. S. Awan***, *"Availability simulation of Switch over for FSO and MMW"*, International Conference on Information and Emerging Technologies, ICIET 2007, pp. 95-99, Karachi, Pakistan. (IEEE)

6. F. Nadeem, E. Leitgeb, ***M. S. Awan***, M. S. Khan, *"Simulation of Switch over for FSO and MMW for four years measured data of FSO availability"*, presented at 2nd SatNEx International Propagation Workshop 2008, Oberpfaffenhofen, Munich, Germany, 17-18 April 2008.

7. F. Nadeem, E. Leitgeb, M. S. Khan, ***M. S. Awan***, et al. *"Comparing the Fog Effects on Hybrid Network using Optical Wireless and GHz Links"*, CSNDSP 2008, pp. 278-282, Graz, Austria, 23-25 July 2008. (IEEE)

8. F. Nadeem, E. Leitgeb, M. S. Khan, ***M. S. Awan***, et al., *"Throughput efficient solution for hybrid wireless network"*, IWSSC 2008, pp. 316-320, Toulouse, France, 1-3 October 2008. (IEEE)

9. F. Nadeem, M. Gebhart, E. Leitgeb, W. Kogler, ***M. S. Awan***, M. S. Khan, G. Kandus, *"Simulations and analysis of bandwidth efficient switch-over between FSO and mmW links"*, (SoftCOM 2008), pp. 356-351, Split-Dubrovnik, Croatia, 25-27 September 2008. (IEEE, best paper award)

10. F. Nadeem, M. Henkel, B. Geiger, E. Leitgeb, ***M. S. Awan***, G. Kandus, *"Implementation and Analysis of Load Balancing Switch over for Hybrid Wireless Network"*, WCNC 2009, pp. 1 - 6, 5-8 April 2009, Budapest, Hungary. (IEEE)

11. F. Nadeem, B. Geiger, M. Henkel, E. Leitgeb, M. Loeschnig, ***M. S. Awan***, A. Chaman Motlagh, G. Kandus, *"Switch over implementation and analysis for hybrid wireless network of optical wireless and GHz links"*, WTS 2009, pp. 1-6, 22-24 April, 2009, Prague, Czech Republic. (IEEE)

12. F. Nadeem, B. Geiger, M. Henkel, E. Leitgeb, ***M. S. Awan***, M. Gebhart, G. Kandus, *"Comparison of wireless optical communication availability data and traffic data"*, VTC2009-Spring, pp. 1-5, 26-29 April 2009, Barcelona, Spain.

13. F. Nadeem, B. Geiger, E. Leitgeb, ***M. S. Awan***, G. Kandus, *"Evaluation of Switch-over Algorithms for Hybrid FSO-WLAN Links"*, Wireless Vitae 2009, pp. 565-570, 17-20 May, 2009, Aalborg, Denmark. (IEEE)

14. F. Nadeem, E. Leitgeb, V. Kvicera, M. Grabner, ***M. S. Awan***, G. Kandus, *"Simulation and analysis of FSO/RF switch over for different atmospheric effects"*, ConTel 2009, pp. 39-43, 8-10 June 2009, Zagreb, Croatia. (IEEE)

15. F. Nadeem, E. Leitgeb, ***M. S. Awan***, S. Chessa, *"Comparing the life time of terrestrial wireless sensor networks by employing hybrid FSO/RF and only RF network technology"*, ICWMC 2009, pp. 134-139, 23-29 August 2009, Cannes, France. (IEEE)

16. F. Nadeem, E. Leitgeb, ***M. S. Awan***, G. Kandus, *"FSO/RF hybrid network availability analysis under different weather conditions"*, NGMAST 2009, pp. 239-244, 15-18 September 2009, Cardiff, UK. (IEEE)

17. F. Nadeem, E. Leitgeb, ***M. S. Awan***, G. Kandus, *"Comparison of different models for prediction of attenuation from visibility data"*, IWSSC 09, Sienna, Italy. (IEEE)

18. F. Nadeem, E. Leitgeb, ***M. S. Awan***, G. Kandus, *"Forward Prediction of FSO re-*

ceived signal for FSO/RF hybrid network", IWSSC 09, Sienna, Italy. (IEEE)

19. F. Nadeem, E. Leitgeb, ***M. S. Awan***, T. Javornik, G. Kandus, *"Comparing the Snow Effects on Hybrid Network Using Optical Wireless and GHz Links"*, IWSSC 09, Sienna, Italy. (IEEE)

20. F. Nadeem, E. Leitgeb, ***M. S. Awan***, G. Kandus, *"Optical Wavelengths Comparison for Different Weather Conditions"*, IWSSC 09, Sienna, Italy. (IEEE)

21. F. Nadeem, E. Leitgeb, ***M. S. Awan***, G. Kandus, *"Comparison of FSO 10 micrometer availability with FSO 850 nm/RF hybrid network availability"*, VTC 2009 fall, Alaska, USA. (IEEE)

22. F. Nadeem, M. Gebhart, E. Leitgeb, ***M. S. Awan***, B. Geiger, M. Henkel, G. Kandus, *"Performance Analysis of Throughput Efficient Switch-over between FSO and mmW Links"*, Journal of Communications Software and Systems (JCOMSS 2009) (IEEE technically cosponsored Journal), Vol. 5, No. 1, March 2009.

23. F. Nadeem, V. Kvicera, E. Leitgeb, ***M. S. Awan***, S. Sheikh Muhammad, G. Kandus, *"Weather Effects on Hybrid FSO/RF Communication Link"*, IEEE IJSAC, pp. 1687-1697, Vol. 27, No. 9, December 2009.

24. F. Nadeem, ***M. S. Awan***, E. Leitgeb, M. S. Khan, S. Sheikh Muhammed, G. Kandus, "Comparing the Cloud Attenuation for Different Optical Wavelengths", ICET 2009, October 19-20, 2009, Islamabad, Pakistan.

25. F. Nadeem, B. Geiger, E. Leitgeb, ***M. S. Awan***, S. Sheikh Muhammad, M. Loeschnig and G. Kandus, *"Comparison of Link Selection Algorithms for FSO/RF Hybrid Network"*, sumbitted to IEEE IET Communications Journal.

26. M. S. Khan, ***M. S. Awan***, E. Leitgeb, F. Nadeem, I. Hussain, "Selecting a Distribution Function for Optical Attenuation in Dense Continental Fog Conditions", ICET 2009, October 19-20, 2009, Islamabad, Pakistan.

27. E. Leitgeb, T. Plank, ***M. S. Awan***, P. Brandl, W. O. Popoola, Z. Ghassemlooy, F. Ozek, M. Wittig, "Analysis and Evaluation of Optimum Wavelengths for Free-Space Optical Transceivers", ICTON 2010, June 27 - July 1, 2010, Munich, Germany. (Invited paper) (IEEE)

APPENDIX B: OPTICAL WIRELESS EXPERIMENTS AND COMMUNICATION SCENARIOS

Taking benefits from the progress made for optical transmission through fibres, tremendous advances in electro-optics and optoelectronics components and systems design are made and these developments were incorporated and disseminated into today's FSO systems mainly for military applications. The aerospace and defence activity established a strong foundation upon which today's commercial FSO systems are based. There is a strong need to exploit the huge bandwidth offered by FSO technology, as the future broadband access needs will pose stringent requirements on the communication links between gateways and telecom satellites, classically located in GEO orbit [149]. Successful experiments like SILEX (Semiconductor inter-satellite link), the link between OGS (Optical Ground Station) and ARTEMIS (Advanced Relay Technology Mission Satellite) and the earth reconnaissance low earth orbit (LEO) satellite SPOT-4 proves the operability of long distance FSO. On the military side, the US has been working on optical satellite-ground and air-ground links with transmission of high power laser beams for their Strategic Defence Initiative (SDI) program. Table .1 summarizes some very important optical experiments successfully conducted in recent years.

	Ground	**LEO Satellite**	**GEO Satellite**
Ground	Many Experiments	KODEN (2006) TerraSAR-X (2008)	ETS-VI (1994) GeoLITE (2006) SILEX (2001)
LEO Satellite	KODEN (2006) KIODO (2006) TerraSAR-X (2008)	TerraSAR-X-NFIRE (2008)	SILEX (2001) OICETS (2005)
GEO Satellite	ETS-VI (1994) GeoLITE (2006) SILEX (2001)	OICETS (2005)	No Experiment

Table .1: Important optical wireless experiments

In this section we provide a brief and comprehensive survey of seven very important FSO system designs and the experiments to establish ground-space laser communication links through the earth atmosphere. The experiments date from 2001 with the bi-directional laser link experiment between the ARTEMIS satellite and the optical ground station on the Canary Islands until the successful test of a high data rate laser link from the LEO

TerraSAR-X satellite to the DLR ground station in Oberpfaffenhofen. Orbit / platform types investigated are GEO / LEO and high altitude platforms. The optical parameters of the experimental configuration of all these below mentioned seven experiments are tabulated in Table.

OGS - ARTEMIS

Experiments for investigation of atmospheric turbulence statistics have been carried out using an atmospheric bi-directional laser link between the OPALE laser terminal onboard the ARTEMIS satellite and ESA's optical ground station (OGS) at the Observatorio del Teide on the Canary Islands. The objective of this experiment was to perform optical communication experiments by sending the Earth observation data produced by SPOT4 to ARTEMIS satellite and then relayed to Earth station (Fig. .1). Within the ESA study 'Artemis Laser Link for Atmospheric Turbulence Statistics' a number of 45 bi-directional links have been established during a measurement campaign that was started in Nov. 2001. In [150], a number of 80 successful sessions is reported since then with average bit error rates of 10^{-6} achieved for durations of 20 min. In some occasions BERs of at least 10^{-9} to 10^{-10} have been achieved for 5 to 30 min duration. The test data transmitted at a rate of 50,000,000 bits per second (50 Mbps). A very high accuracy of data stream confirmed at ESA's test station in Redu (Belgium) and the SPOT4 receive station in Toulouse.

Figure .1: Illustration of OGS - Artemis experiment [151]

JPL Optical Communication Telescope

The Optical Communications Telescope Laboratory (OCTL) is a optical communications ground terminal by the NASA/JPL Telecommunications and Mission Operations. It supports bi-directional optical links for research and high bandwidth optical communications with spacecraft and deep space missions (Fig. .2). The telescope is a 1-m coude-focus system designed for high precision pointing and tracking. In a coude-focus telescope the light from a primary mirror is reflected along the polar axis to focus at a fixed place separate from the moving parts of the telescope. At JPL also a three tier laser safety monitoring system has been developed that defines safety zones in the airspace around the ground station using sensors for each exclusion zones enabling an automatic beam shutter interruption in case air traffic is detected (Fig. .3) [152].

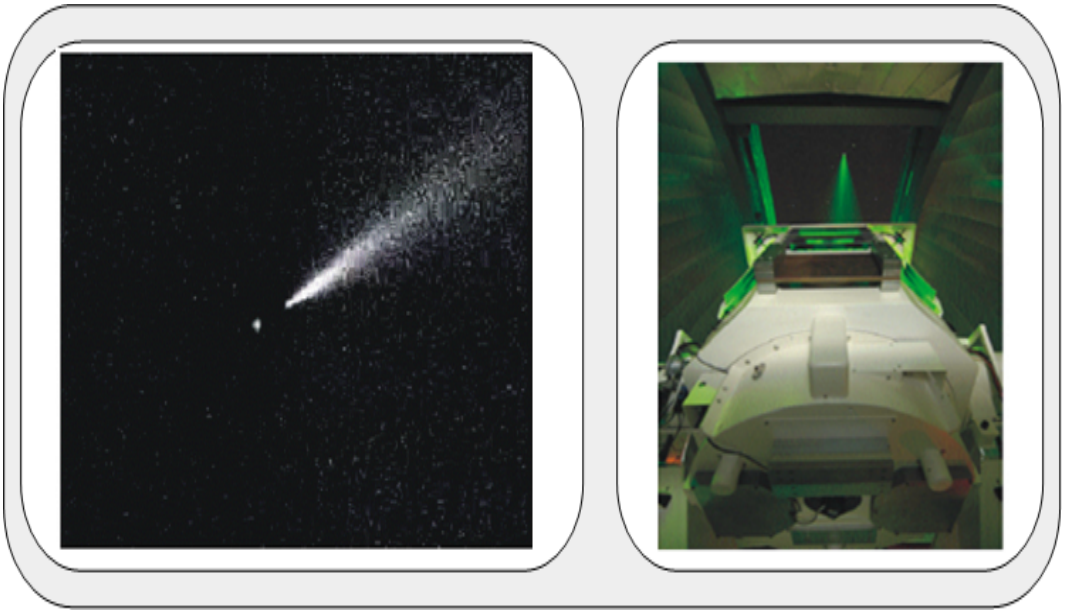

Figure .2: Laser beam transmitted from the main OCTL telescope (right); Sun-illuminated EGP-1 satellite at the end of the Rayleigh backscattered light (left) [153]

Altair UAV-to-Ground Lasercomm Demonstration

NASA JPL (Jet Propulsion Laboratory) designed and implemented a 2.5 Gbps optical link between a ground station and a UAV, described by Ortiz in (Fig. .4) [154]. Main topic of the experiment was to demonstrate the 2.5 Gbps optical link on the UAV and to study atmospheric fades and pointing uncertainties due to the flying behavior. To overcome vibration problems a Angular Vibration Test Fixture (AVTF) was designed. Also a robust acquisition, tracking and pointing (ATP) subsystem was developed at JPL. Link distance

Figure .3: Three JPL-defined safety tiers for ground-to-space laser beam propagation [153]

was 50 km while the altitude of the UAV was 18 km. The UAV was remote controlled using a c-band communication link. The listed optical link parameters are to be understood as design values. With 200 mW TX power the laser operated at a wavelength of 1550 nm gaining a BER of 10^{-9}The experiment is described in [154].

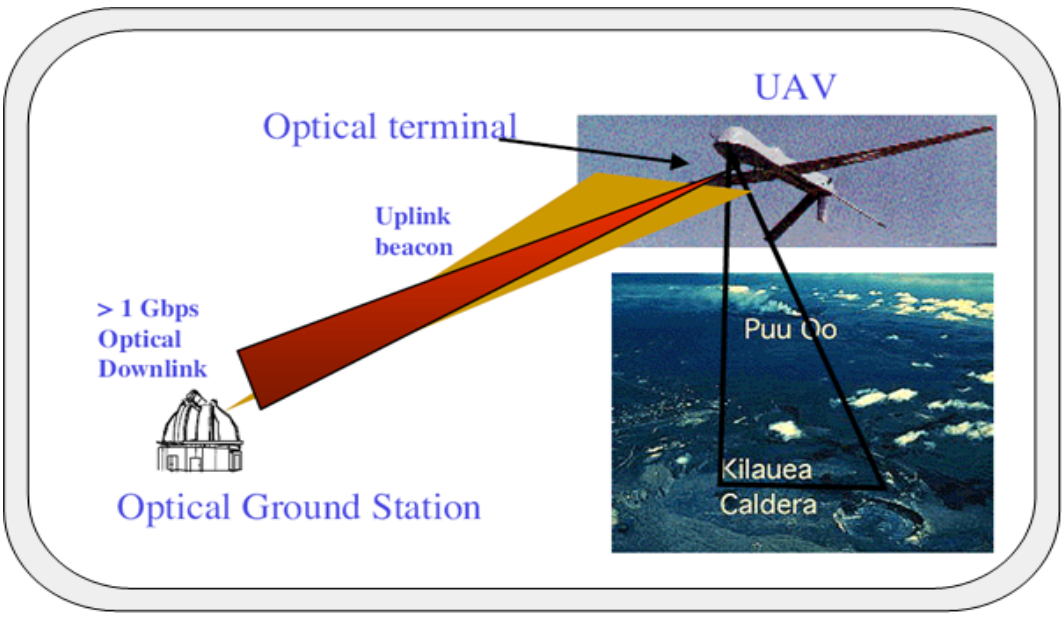

Figure .4: Altair UAV-to-Ground Lasercomm Demonstration [155]

Stratospheric Optical Payload Experiment STROPEX (CAPANINA Project)

The stratospheric optical payload experiment (STROPEX) was a high bit rate optical downlink experiment performed within the EU CAPANINA project (Fig. .5). The experiment used the airborne free-space experimental laser terminal (FELT). The terminal was carried by a high altitude platform (HAP) in a height of 24 km. A transportable optical ground station was used and operated during a measurement campaign at ESRANGE near Kiruna, Sweden. The FELT was carried by a stratospheric balloon. Among the design goals of FELT was to operate in stratospheric environmental conditions with temperatures down to -70 deg and near vacuum conditions.
The DLR established a 622 Mbit/s downlink and the bit error probability (BEP) was better than 10^{-9}. From the stratosphere to the ground the link distance amounted 64 km. Additionally, a 1.25 Gbit/s downlink was set up, but no bit error measurement was performed. As transmission scheme they have applied intensity modulation (IM) with direct detection (DD) at a communication wavelength of 1550 nm. A laser diode driven by pseudo-random bit-sequence with an output power of 1mW acted as the data source. Optical amplification was done by Erbium-doped fiber amplifier (EDFA) to receive 100 mW. The experiment is described in [156].

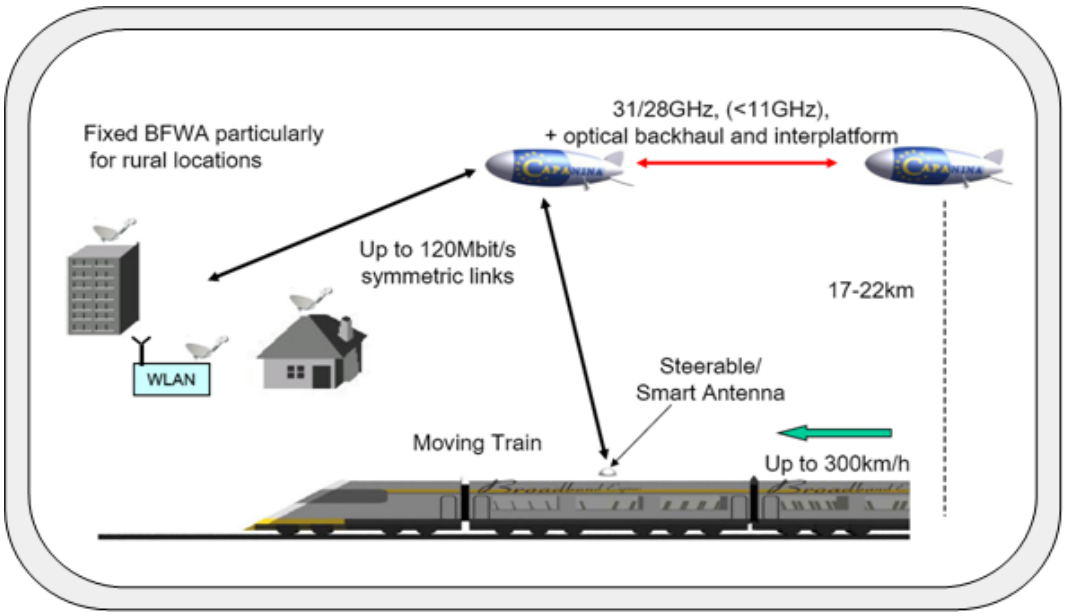

Figure .5: The CAPANINA Scenario [157]

Airborne Laser Optical Link - LOLA

LOLA (Liaison Optique Laser Aéroportée) was a French national demonstration program. The experiment performed in Dec 2006 was the first demonstration of a two-way optical link between a GEO satellite (ARTEMIS) and an aircraft flying at 9 km altitude (Mystère 20) (Fig. .6). This experiment showed an optical link between airborne terminals like UAVs (Medium Altitude Long Endurance (MALE); High Altitude Long Endurance (HALE)) in lower altitudes compared to Artemis, the geostationary communications satellite of ESA. The aircraft optical terminal was developed by EADS Astrium. Details of the terminal design were:

- Silicon Carbide used for high mechanical stability
- Accurate hemispherical broadband pointing mechanism for satellite acquisition.
- CMOS sensor for detection and tracking of the Satellite
- Less than 1 sec for link acquisition
- Pointing accuracy better 1 μrad.

The experiment is described in [158] and EADS brochures. The Objectives of this experiment were:

- Exploration of light propagation in the atmosphere
- Proof of link system power
- Ensure secure transmission of UAVs data

Optical Downlink Experiment - KIODO

The experiment performed in 2006 was the first optical downlink performed from a LEO satellite in Europe (Fig. .7). The satellite carrying the laser transmitter was the Japanese OICETS at a sun-synchronous orbit in 610 km altitude. The OICETS satellite is optically compatible with ARTEMIS regarding used wavelengths and OOK modulation. The KIODO experiment (Kirari Optical Downlink to Oberpfaffenhofen) performed link trials corresponding with a particular pass of the satellite. This required some planning of the attitude configuration for each test. The ground station received a 50-Mbit/s OOK signal at 847 nm on its 40-cm Cassegrain telescope. From eight performed trials five could be performed successfully. During three trials cloud blockage occurred. A bit error rate of 10^{-6} was achieved.
Also uplink test were performed sending two spatially displaced beacon beams towards

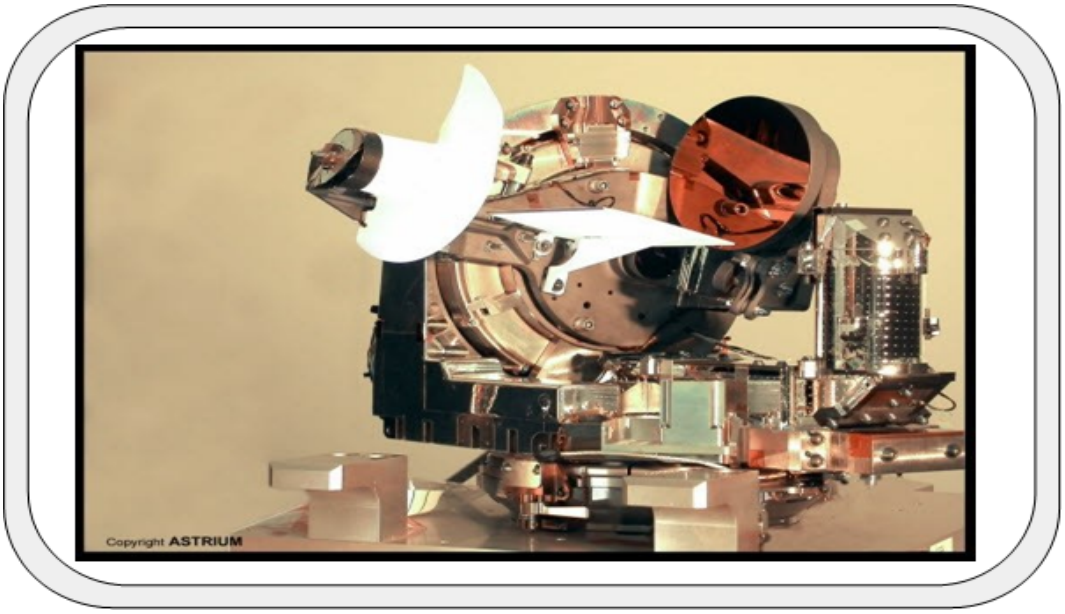

Figure .6: LOLA (Liaison Optique Laser Aéroportée) terminal [159]

the LUCE terminal onboard the OICETS. Because of the optical power range of the onboard sensors the beacon transmit power had to be adjusted as a function of the link elevation angle. The beacon power received was recorded and evaluated for atmospheric attenuation and scintillation. The experiment is described in [160]. The Optical Inter-orbit

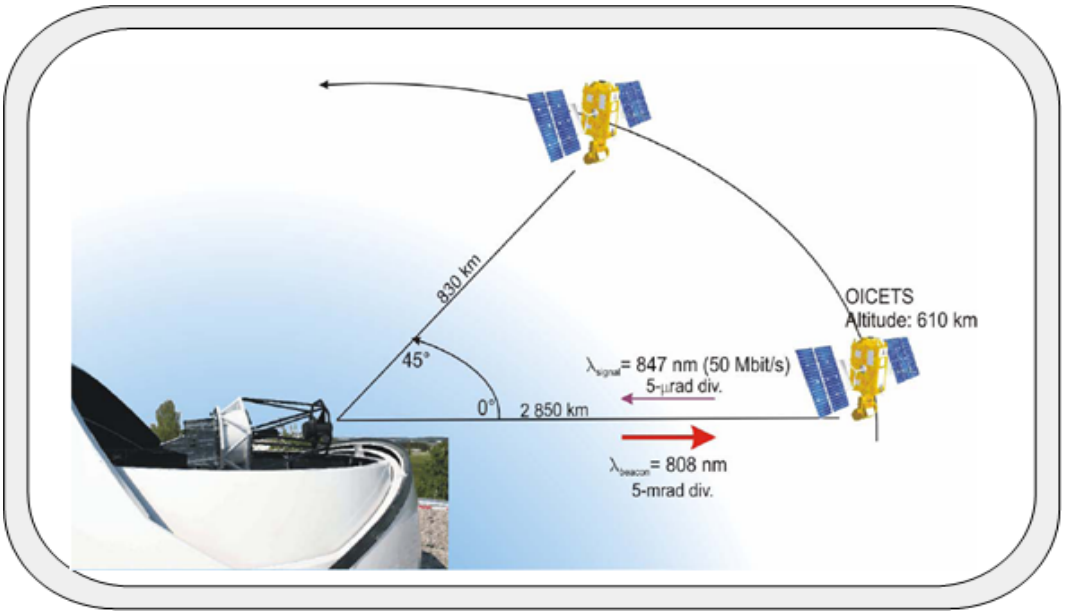

Figure .7: KIODO - Parameters [161]

Communication Engineering Test Satellite (OICETS, Japanese name *KIRARI*), was developed by the Japan Aerospace Exploration Agency (JAXA). It was launched into low earth sun-synchronous orbit at an altitude of 610 km and an inclination of 97.8 degree on 23rd August 2005. A main objective of OICETS was to demonstrate the free-space inter-orbit laser communications by using a laser communications terminal called the Laser Utilizing Communications Equipment (LUCE). Some major achievements of this experiment were; JAXA had success with the optical link in December 2005. In March 2006, a link was in operation between OICETS and a Japanese ground station. Simultaneously it was the first time between a fixed ground station and an LEO satellite. Three months later, a further link was pointed to a mobile ground station operated by the DLR.

TerraSAR-X LCT-ATM Laser Link

In 2008 an optical downlink experiment was performed between the Tesat LCT terminal onboard the LEO TerraSAR-X Earth observation satellite and the DLR optical ground station in Oberpfaffenhofen (Fig. .8). The OGS in Oberpfaffenhofen has a RX aperture of 40 cm. In fact, a broadband data transmission was established between the German TerraSAR-X and the U.S.-Satellite NFIRE, reaching a data rate of about 5.5 Gbit/s bidirectional using BPSK modulation at a wavelength of 1064 nm and a TX power of 1 W. Due to the tracking of the LEO satellite the link elevation is between 30 and 90 deg. The experiment carries instruments for atmospheric turbulence profiling. The link distance is specified with 500 - 1000 km. In those altitudes a link is only available for approximately 20 minutes duration, whereas the range between was about 5,000 km and the speed of the satellites amounted about 25,000 km/h. Important to mention is that no real science data transmission was performed, there were just bit sequences transmitted and received.
A scenario with a different ground station at Calar Alto in southern Spain and a link distance of approx. 510 km is described in [162]. The following link parameters are taken from the feasibility study. The RX aperture described in the study is 65 mm and is therefore smaller than the atmospheric coherence length.

Oerlikon DOLCE study

The Swiss company Oerlikon started in 1995 to develop the OPTEL family, a kind of optical terminals whose usage spreads over several areas of interest like:

- Commercial optical satellite cross links
- Deep space optical links
- Optical links between airborne platforms

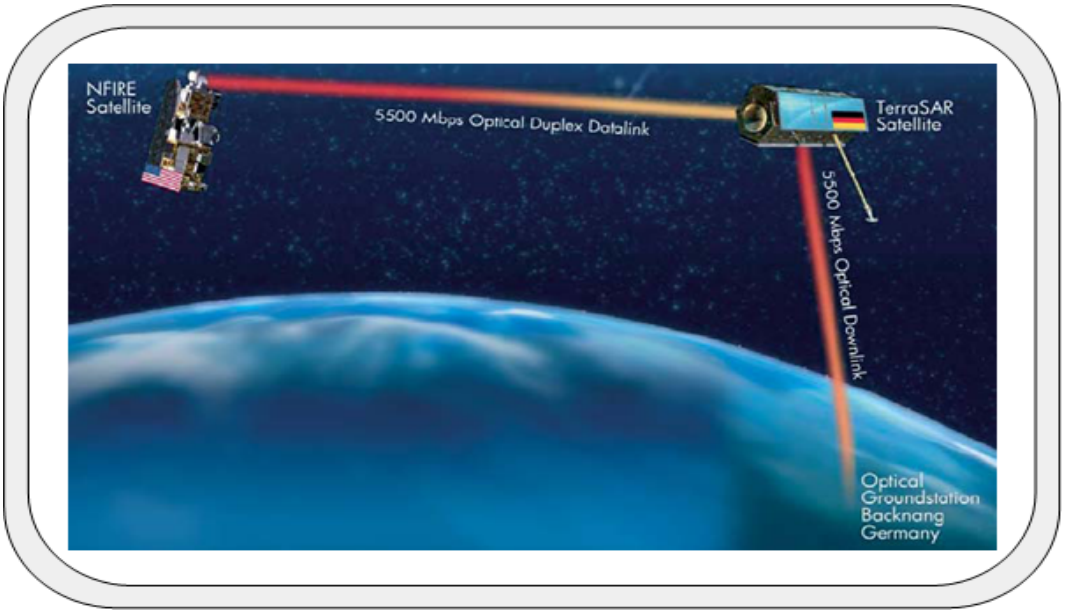

Figure .8: Illustration of TerraSAR-X LCT-ATM Laser Link [163]

Two studies performed under an ESA contract are somewhat deeper examined here. Dolce study experiment was an inter-island test between La Palma and Tenerife done in the year 2007 (Fig. .9). Over that line of 142 km a distance corresponding to 1,500,000 km was simulated as this is the route from Earth to the Lagrangian point L2 (L1 is as far away, but on the opposite side). On the transmit side, a MOPA (Master Oscillator Power Amplifier) laser was taken, with one Watt transmit power. As modulation scheme, 32-PPM (Pulse Position Modulation) was in use. On Tenerife, the 1m OGS with a Si-APD and a measured sensitivity of -70.9 dBm played the role of the receiver side. Finally, the user data rate was set to 10 Mbps [164].

Oerlikon ROSA study

This was again an inter island test between La Palma and Tenerife (Fig. .10) performed in the years 2007/08. Main goal was the investigation of Optical Telemetry for the MSR (Mars Sample Return) mission. During the test a simultaneous presence of atmospheric turbulence and sky radiance was detected. Due to the fact, that the link was over a horizontal line with a length of 142 km, worse conditions compared to a (near) vertical link to space were encountered. The long term link testing provided results for genuine day and night conditions. For this distance, as Mars is up to 400,000,000 km away, only PPM can be used as modulation scheme. Q-switched lasers provide only a low pulse repetition frequency, but very high power in the emitted pulses. Variable PPMs were examined; as a consequence, variable data rates were achieved. The targeted data rate of 1 Mbit/s was

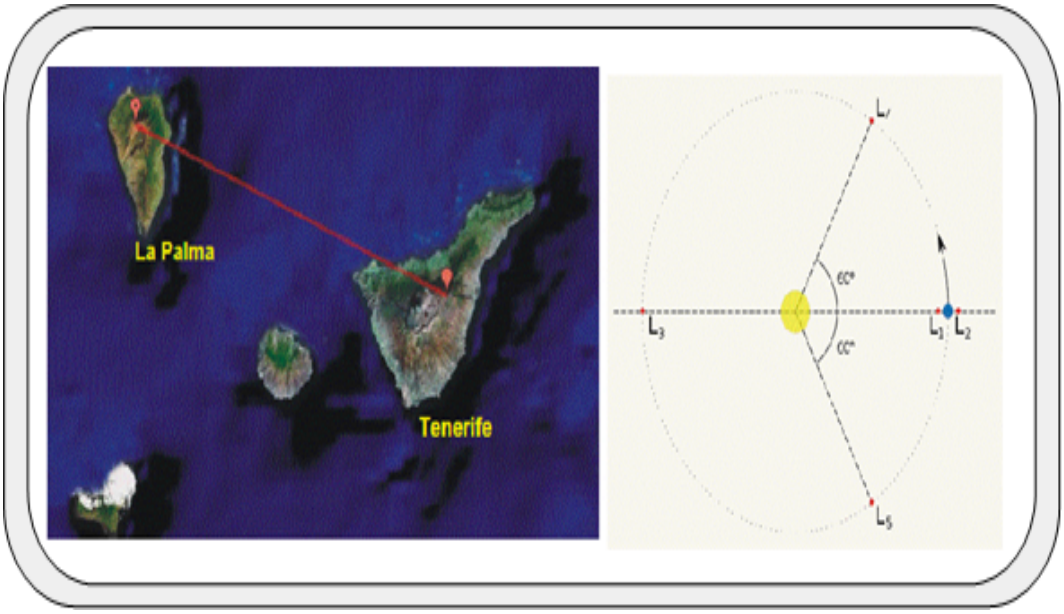

Figure .9: Dolce study optical link locations (left); Lagrangian points (right) [165]

not reached due to several reasons. As a conclusion, improvements of the laser technology would lead to the desired data rate [166].

Figure .10: Oerlikon: Locations of ROSA study experiment [151]

Parameters	Optical Experiments						
	OGS-ARTEMIS	JPL-OCTL	Altair UAV-to-Ground	STROPEX	LOLA	KIODO	TerraSAR-X LCT-ATM Laser link
Date	2001	2003	2003	2005	2006	2006	2008
Orbit of Platform	GEO	LEO-Deep Space	UAV (HAP)	HAP	Airborne to GEO	Sun-sync LEO	LEO
Link Distance	38000 km		50 km	64.3 km		2640 km	500 km
Link Direction	Uplink and Downlink	Uplink and Downlink	Downlink	Downlink	Bi-directional	Downlink	Downlink
Bit Rate	49 Mbps Uplink 2 Mbps Downlink	- -	2.5 Gbps	1.25 Gbps	50 Mbps	50 Mbps	5.6 Gbps
Modulation	NRZ Uplink 2-PPM Downlink	- -	-	OOK	OOK	OOK	BPSK
BER	10^{-3} Uplink 10^{-6} Downlink	- -	10^{-9}	10^{-9}	10^{-9}	10^{-6}	10^{-9}
Optical unit Mass	- -	- -	42 kg	17.5 kg	-	-	-
Wavelength	1016 nm Uplink 250 nm Downlink	532 nm Uplink 1064 nm Downlink	1550 nm	1550 nm	800 nm	847 nm	1064 nm
Optical Power	300 mW Uplink 10 mW Downlink	12.8 W Uplink 29.7 W Downlink	200 mW	100 mW	160-320 mW	-	1 W
RX-Mirror	250nm Uplink 1 m Downlink	- -	-	-	-	40 cm	65 mm
Beam Divergence	87.3 μrad Uplink 70 μrad Downlink	490 μrad Uplink 1000 μrad Downlink	200 μrad	1 mrad	-	-	7.5 μrad
Link Elevation Angle	- -	- -	25 deg	-	-	2-45 deg	30-90 deg
TX-Mirror	1 m Uplink 250 mm Downlink	1 m Uplink 1 m Downlink	-	-	-	-	12.4 cm
Laser Technology	Argon laser pumped Ti:sapphire laser GaAlAs laser diode, single mode	Nd-Yag Nd-Yag	-	Laser diode + optical amplifier	Laser diode	-	-

Table .2: Important parameters of optical link experiments

APPENDIX C: EYE SAFETY AND OPTICAL WIRELESS NETWORKS

Laser eye safety issue becomes of increased significance with the proliferation of FSO products that direct optical beams into potentially populated areas. Lasers are potentially hazardous due to their intense brightness (W/m^2). Many factors like laser-eye tissue interaction, laser pulse duration, laser power, and the transmission wavelengths can cause damage to the human eye as a result of several mechanisms like photochemical, thermal and acousto-thermal reactions [20, 6, 39]. Photochemical process occurs as a result of absorption of photon by a molecule and result in a chemical reaction causing permanent damage to the eye retina. The thermal interaction could result in the thermal deposition of heat to a local area which can be either lens or retina or cornea. Whereas, acousto-thermal process results in a damaging shock wave due to the rapid deposition of heat. Usual FSO systems operate predominantly in two wavelength bands; systems that operate near 800 nm wavelength band (the near-infrared band) and thus radiate invisible radiations while the other operate near 1550 nm. Fig. .1 shows the eye response against different optical wavelengths. The bold curve in the middle represents the human eye's response (photo-optic eye response) at the ambient light level. This curve peaks at 550 nanometers, which means the eye is most sensitive to yellowish-green color at this light level. While the dotted line represents the response of human eye in terms of total absorption across near-infrared wavelengths [6]. This total absorption response applies to visible and near-infrared wavelengths in the range of 400 nm to 1400 nm.

Near-infrared wavelength band light like visible wavelengths pass through the cornea and lens and ultimately focuses on the tiny spot on the retina. Such a collimated laser beam can concentrate by a factor of 100,000 times upon striking the retina and since retina has no pain sensors so it does not induce eye blink reflex action and thus could permanently damage it. Whereas, the optical beams operating outside the near-infrared band at 1550 nm wavelength do not focus onto the retina as they are absorbed by the cornea and the lens. This significantly different behavior of the two wavelength bands allows 50 times more eye safe allowable power to be used with optical transmitters operating at 1550 nm than 800 nm wavelength. This gain of 50 times is very important from the communication system designer point of view as it allows him to send information data at comparatively much higher data rates over longer distances through heavier attenuation conditions.

Table .1 mentions a list of the primary eye safety classes under which an optical radiator can fall [57]. Outdoor LOS optical wireless systems generally use high power lasers (Class 3B) to achieve a good power budget against different atmospheric impairments. So eye safety standards suggest to install such systems at locations where the optical beams

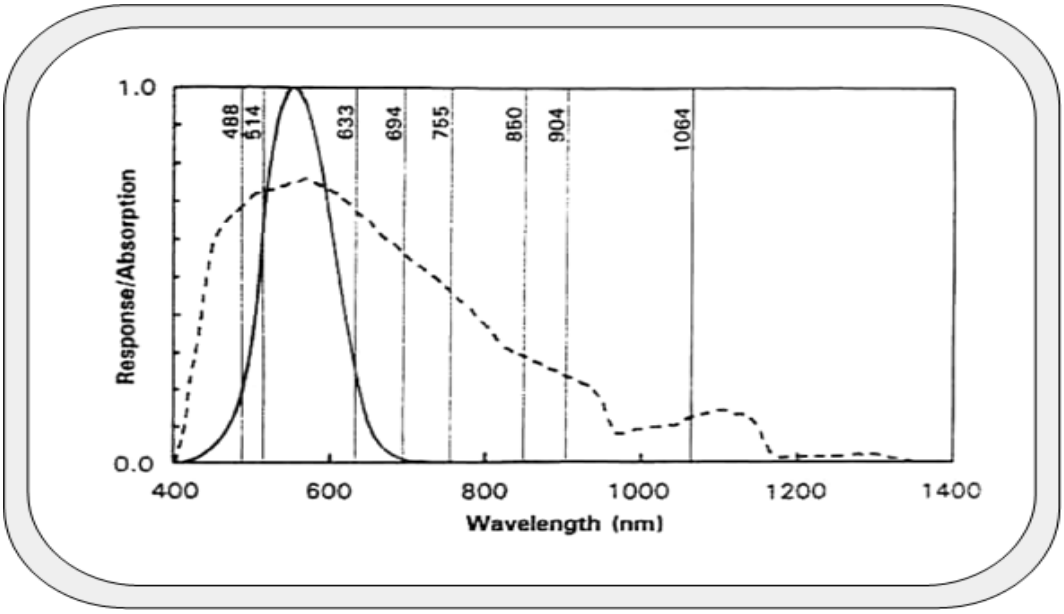

Figure .1: Eye response against different optical wavelengths [6]

Safety Class	**Description**
Class 1	Safe under reasonably foreseeable conditions of operation
Class 2	For visible sources $\lambda = 0.4$ μm - 0.7 μm, eye protection is afforded by aversion responses including eye blink reflex
Class 3A	Safe for viewing with unaided eye. Direct intra-beam viewing with optical aids may be dangerous
Class 3B	Direct intra-beam viewing with optical aids is always dangerous. Viewing diffuse reflections through holographic techniques is normally safe

Table .1: IEC 60825 safety classification for optical sources and their interpretation

cannot be interrupted or viewed inadvertently by a human [20]. Whereas, indoor systems usually employ Class 1 lasers such that transmitted powers must not exceed 0.5 W in any case. Class 3B laser for use in the outdoor applications can be rendered Class 1 eye safe laser by passing their beam through a hologram (sealed within the overall laser enclosure); the hologram breaks up the optical beam wavefront and diffuses the image of the beam spot on the eye retina in order to prevent serious damage to it. Table .2 summarizes the allowable average optical power limits calculated by assuming that the source is a point emitter and there is a very small divergence as is the case in laser diodes [57].

Communication systems transmit information from a transmitter to a receiver through the construction of a time varying physical signal and the transmitted signal is corrupted by deterministic and random distortions due to the environment. The goal of communication

Safety class	650 nm visible	880 nm infrared	1310 nm infrared	1550 nm infrared
Class 1	$<$ 0.2 mW	$<$ 0.5 mW	$<$ 8.8 mW	$<$ 10 mW
Class 2	0.2 - 1 mW	N.A	N.A	N.A
Class 3A	1.0 - 5.0 mW	0.5 - 2.5 mW	8.8 - 45.0 mW	10.0 - 50.0 mW
Class 3B	5.0 - 500 mW	2.5 - 500 mW	45.0 - 500 mW	50.0 - 500 mW

Table .2: Limits for the average transmitted optical power for the IEC 60825 classes at four different wavelengths

system design is to develop signalling techniques which are able to transmit data reliably and at high rates over these distorting channels. For efficient design, a detailed knowledge of the channel characteristics is necessary. The transmission of information using optical intensity channels differs significantly from the conventional RF channel. Unlike the RF technologies, where the carrier amplitude, phase or frequency are varied, the information sent on most optical channels lies in the intensity of the transmitted signal. This electro-optical conversion process is termed optical intensity modulation and is usually accomplished by a light emitting diode (LED) or a laser diode (LD). Using incoherent, diffuse light sources (for eye safety reasons), only the intensity of the optical signal can be varied, which must remain positive [57]. The photodiode detector is said to perform direct detection of the incident optical intensity signal and its response is the integration of tens of thousands of wavelength of incident light. The photodiode detector, thus, produces an output electrical current which is a measure of the optical power impinging on the device. Let $x(t)$ denote the intensity of the transmitted optical signal and let $ry(t)$ be the photodetector current at the receiver, where the constant r is the photodetector responsivity. When the intervening channel has impulse response $h(t)$, $y(t)$ is given by,

$$y(t) = \int_{-\infty}^{+\infty} x(\tau)h(t-\tau)d(\tau) + n(t) \tag{.1}$$

The input $x(t)$ represents power, not amplitude and this leads to two unusual constraints on the transmitted signal; firstly, $x(t)$ must be positive, and secondly, the average amplitude of $x(t)$ is limited. If the average of the transmitted light wave is constrained to a value denoted by P (which satisfies safety regulations), then the input $x(t)$ of the baseband channel must satisfy,

$$x(t) \geq 0 \tag{.2}$$

$$\lim_{T \longrightarrow \infty} \frac{1}{2T} \int_{-T}^{T} x(t)dt \leq P \tag{.3}$$

The first constraint implies that any modulation scheme for an optical intensity channel must have a DC component which transmits no information but consumes energy and

the second constraint is in marked contrast to conventional electrical channels in which the constraint is on the average squared amplitude of the transmitted signal [57]. The allowable exposure limit (AEL) depends on the wavelength of the optical source, the geometry of the emitter and the intensity of the source. In general, the constraints are placed on both the peak and average optical power emitted by a source.

APPENDIX D: PDF ESTIMATION OF RECEIVED SIGNAL STRENGTH

A novel approach of achieving a tractable probability density function of the received signal strength under fog attenuation has been investigated. The continental fog has characteristics which allow us to model the received signal strength by standard curve fitting techniques. In this section the results achieved through analysis of data acquired through measurement campaigns at the continental city of Graz are provided. A fog event measured in Graz, Austria on 31st January, 2006 has been analyzed. The RSS of transmitted optical signals having 850 nm and 950 nm wavelengths, over a link distance of approximately 800 m, were recorded by a unidirectional FSO link. Fig. .1(a)-(d) shows the distribution of the received power (dBm) for the complete fog event that spanned around 14 hours, for a 1 hour, for one minute and for 30 seconds, respectively [132]. These plots are drawn using *Kernel smoothing density estimate i.e., [f,xi] = ksdensity(x)* function in MATLAB. This function computes a probability density estimate of the sample in some vector x, while f is the vector of density values evaluated at the points in xi. The density estimate is based on a normal kernel function and the density is evaluated at 100 equally spaced points that cover the range of the data in x [167]. The distribution clearly exhibits a multimodal PDF with a spread of 1 dBm. The constituent parameters of fog including the drop size distribution undergoes significant changes over large spans of time resulting in the mean of the distribution of attenuation shifting to different values and thus creating a multimodal probability density function.

To analyze the distribution of the RSS on hourly scale, the PDF of received power for this selected fog event as shown in Fig. .1(b) is provided. As clearly evident that the PDF has a bimodal shape with two distinct modes around - 23.2 dBm and - 22.8 dBm of the received power. For the further analysis, the PDFs have been drawn on a minute and 30 seconds scales (as shown in Figs. .1(c) and .1(d)), respectively. It is quite interesting to note that the PDFs now take the shape of a standard Gaussian curve once the time span is reduced to a minute or less.

To further investigate the trend of RSS in continental fog, we analyze another continental fog event that is also recorded in Graz on 18-19th Nov. 2009. The total duration of this fog event was about 13 hours (started around 5 PM on 18 Nov. 2009 and lasted until 8 AM on 19 Nov. 2009). The optical attenuations recorded a maximum value of 140 dB/km averaged on a minute scale. The received power distribution for this selected whole fog event is given in Fig. .2(a). This is followed by received power distribution on 1 hour, 10 minute, 1 minute, and 30 seconds time intervals as shown in Figs. .2(b), .2(c), .2(d), and .2(e), respectively [132]. It is clearly evident that a multimodal behavior is observed

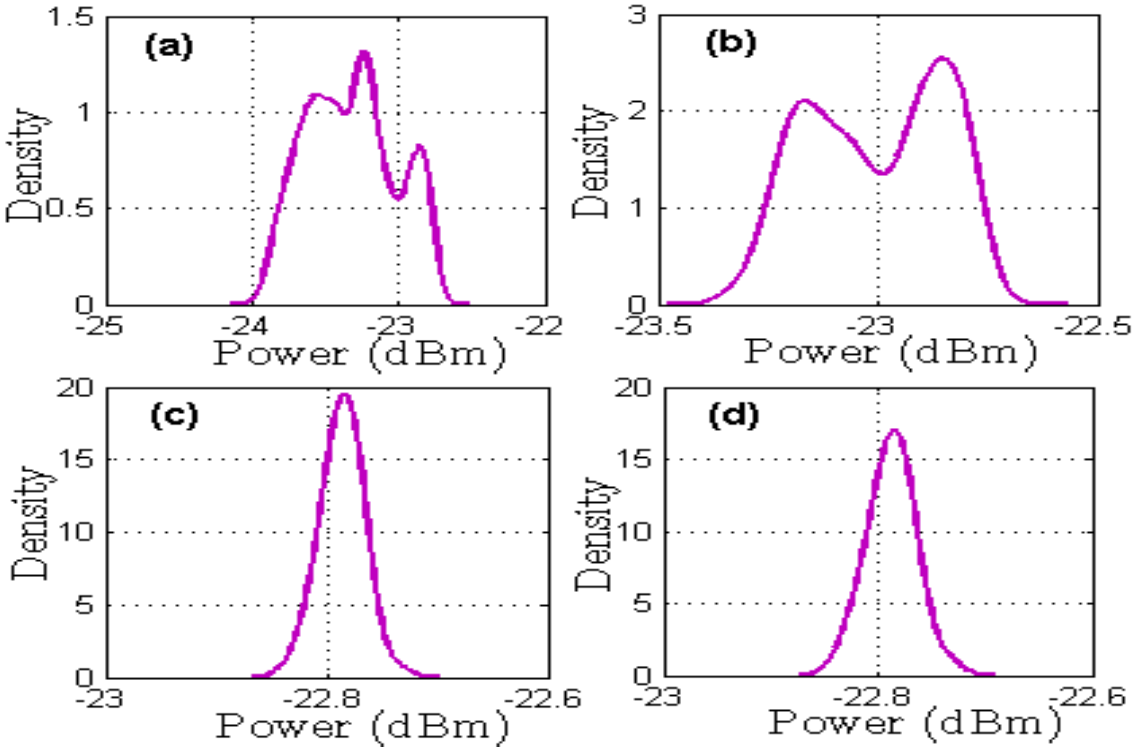

Figure .1: Received power distribution of a selected fog event recorded in Graz on 31.01.2006 for different time durations

for longer time intervals (on hourly basis). As we move down to shorter time intervals the curves depict a trend towards Gaussian distribution. The slight differences observed in terms of the details of the PDF's shape acquired by the RSS in the two events (Figs 1 and 2) can be attributed to the fog characteristics of the particular event. The overall trend is that of multimodal distribution over large time scales (see Figs. .1(b) and .2(b)) and a trend towards Gaussian or a skewed Gaussian PDF when measured on smaller time intervals in both the representative fog events. The results analyzed over smaller time intervals are more significant as they can then be suggestive towards signal estimation, selection of forward error correction codes and thus an improved FSO system design. For further statistical analysis of the fog attenuations, the statistical parametric values for the two fog events are summarized in Table .1. The variance of continental fog data recorded a sharp decrease when measured at reduced time scales. At smaller time intervals like 1 minute and 30 seconds, the variance became really small depicting that the attenuation almost becomes stable. This sharp decrease in variance on smaller time intervals suggests a rather stable characteristic of the continental fog as compared to other fog types like maritime (advection) fog. In other words, it means that the continental fog retains its attenuation characteristic once it sets in. It shall be noted that the link distance was about 800 m for

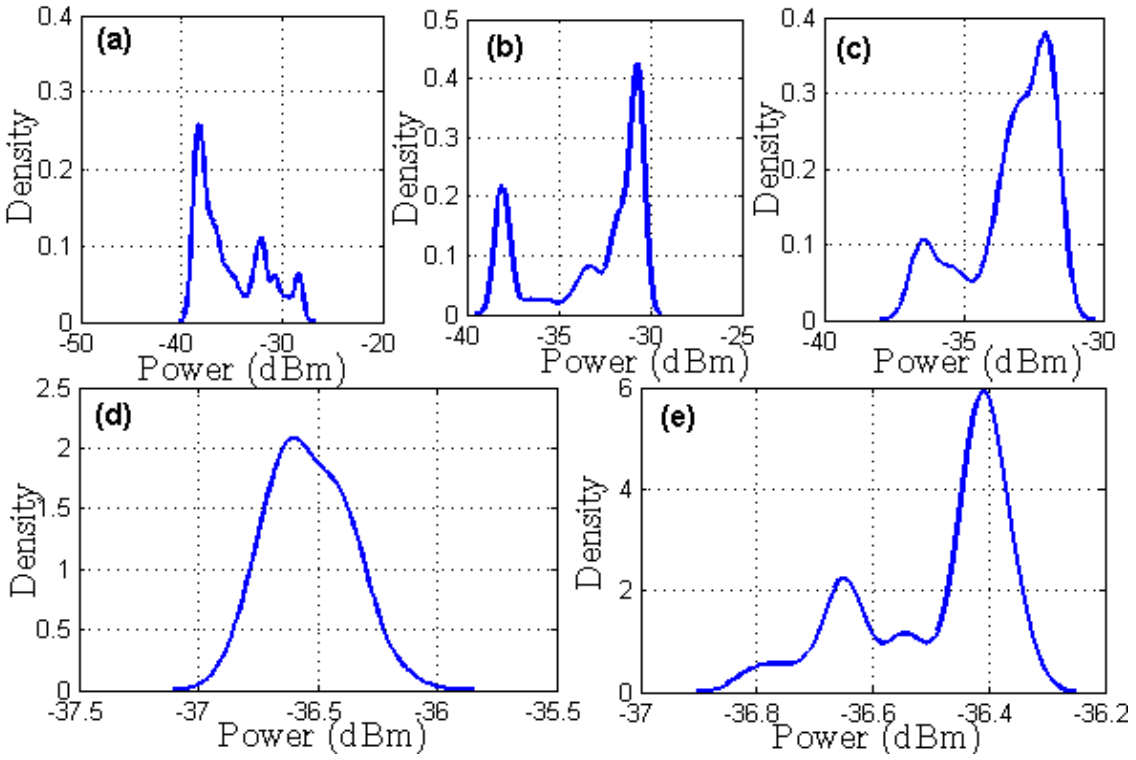

Figure .2: Received power distribution of a selected fog event recorded in Graz on 18-19.11.2009 for different time durations

the winter 2006 fog event, and about 80 m for winter 2009 fog event [132].
The comparison of Skewness reveals interesting insight in the fog attenuation analysis. The received power for winter 2006 interval has Skewness approaching zero for shorter intervals (1 hour and lesser). However, for larger time intervals ($>$ 3 hours) the curve is skewed to the right; indicating that the signals with lesser power are received more frequently than higher powered signals. Similar trend is observed for the winter 2009 fog event. The high kurtosis and small variance signifies a stable link. Higher variance alongside high kurtosis would depict infrequent extreme deviations in the received power. The generic trend in the data analyzed is a higher kurtosis than for a Gaussian distribution [132].

Probability density function fitting has been tried to the PDF estimates of the complete fog events recorded and the results have been summarized in Table .2. The sum of the square error (hereafter SSE) difference at each of these curves with the original nonparametric density estimates was evaluated and clearly the best fit shall have the least number of squared errors. The lognormal PDF has been found to be the closest fit for the continental Graz fog event of 2006, and Gamma PDF for Graz 2009 fog event. However, as evident from the complete fog event's real PDFs (Figs. .1(a) and .2(a)), it can be concluded that the attempts to find the best fit do not really reveal the true picture [132].

Fog event dated 31.01.06						Fog event dated 18-19.11.09					
Duration	**Mean**	**Variance**	**Range**	**Skewness**	**kurtosis**	**Duration**	**Mean**	**Variance**	**Range**	**Skewness**	**kurtosis**
14 hours	-26.578	6.3662	6.3662	0.0148	1.3356	**16.5 hours**	-35.1410	10.7702	11.4670	0.6593	2.1170
1 hour	-23.0037	0.0236	0.6520	-0.141	1.6875	**1 hour**	-33.2381	8.7600	7.8820	-0.7646	1.9026
10 minutes	-22.8052	0.0006	0.1680	-0.0561	2.8762	**10 minutes**	-33.2881	2.3010	5.3510	-1.0226	2.8677
1 minute	-22.7874	0.0003	0.0930	-0.0919	3.5764	**1 minute**	-36.5382	0.0233	0.6610	0.2697	2.4208
30 seconds	-22.7876	0.0004	0.0930	0.038	3.3312	**30 seconds**	-36.4930	0.0166	0.4550	-0.8895	2.4994

Table .1: Statistical parameter values (dB) of two representative fog event recorded in Graz

Density functions	**Fog event dated 31.01.06**				**Fog event dated 18-19.11.09**			
	Mean	**Variance**	**Distr. parameters**	**SSE**	**Mean**	**Variance**	**Distr. parameters**	**SSE**
Lognormal	-26.5784	6.46165	μ=-3.27555, σ=0.095423	0.6212	-34.1332	17.2807	μ=-3.52291, σ=0.12134	0.2796
Gamma	-26.578	6.40128	a=110.351, b=0.240849	0.6217	-34.1273	16.7069	a=69.7118, b=0.489548	0.2733
Exponential	-26.578	706.391	None	1.2388	-34.1273	1164.67	None	0.5367

Table .2: Statistics of three best fit density functions of two representative fog events at Graz